ALIGNMENT STRATEGIES FOR FULLERENES AND THEIR DIMERS USING SOFT MATTER

A Dissertation
Presented to
The Academic Faculty

by

Katie Campbell

In Partial Fulfillment
of the Requirements for the Degree
Doctor of Philosophy in the
School of Material Science and Engineering

Georgia Institute of Technology
August 2011

ALIGNMENT STRATEGIES FOR FULLERENES AND THEIR DIMERS USING SOFT MATTER

Approved by:

Dr. David G. Bucknall, Co-advisor
School of Material Science and Engineering
Georgia Institute of Technology

Dr. Yonathan S. Thio, Co-advisor
School of Material Science and Engineering
Georgia Institute of Technology

Dr. Haskell W. Beckham
School of Material Science and Engineering
Georgia Institute of Technology

Dr. Meisha Shofner
School of Material Science and Engineering
Georgia Institute of Technology

Dr. John Ankner
Liquid Reflectometer, Spallation Neutron Source
Oak Ridge National Lab

Date Approved: 8 June 2011

To Mom and Daddio…

For all your endless love and support.

ACKNOWLEDGEMENTS

First and foremost, I would like to thank my advisors, David Bucknall and Yonathan Thio, for the opportunity to work for them and their support and guidance over the last four years. I have thoroughly enjoyed my experience as a graduate student at Georgia Tech working in their labs and fruitful discussions about research.

Additionally, I would like to thank Dr. Beckham, Dr. Shofner, and Dr. John Ankner for serving on my dissertation committee and their insight and support. I would particularly like to thank Dr. Beckham for allowing me to use his lab space, and John for his support with the neutron reflectivity beamline at Oak Ridge National Lab (ORNL). Also at ORNL, I would like thank Dr. Jim Browning and Candice Halbert for their support and assistance with reflectivity experiments, particularly Candice who took the night shift on numerous experiments.

I would also like to express my gratitude to our collaborators both here at GT and with QIPIRC at Oxford University. I have had the pleasure of working closely with Ryan Kincer in the Beckham laboratory at GT on this project, and his insight and assistance has been invaluable. I would specifically like to thank Dr. Kyriakos Porfyrakis and Dr. Martyn Jevric at Oxford for the synthesis of fullerenes and helpful discussions. Many thanks to my former group members Hannah and Bilge for all their assistance, support, and advice.

Special thanks is due to Dr. Tsukruk and the SEMA lab at GT for access to equipment such as Langmuir trough, ellipsometer, AFM. In particular, I would like to thank Kyle

Anderson, Zachary Combs, and Ikjun Choi for direct assistance with training and use of equipment.

I would like to thank the PTFE/MSE administrative staff, especially Dan, Mike, Angie, Hope, and Linda for all their assistance with lab setup, paperwork, and travel.

I would like thank my family. My mom and dad have shown endless love and support, not just over the last 4 years, but throughout my life. I could not have made it here without them. Their phone calls and visits have provided me with the moral support I needed, and I love them dearly. My grandmother and my sister also deserve thanks for all their support.

Last but not least, I would like to thank Jakub Proszowski, love of my life, for all his support and for dealing with my stress over the last few months. I could not have done this without him.

TABLE OF CONTENTS

LIST OF TABLES

LIST OF FIGURES

NOMENCLATURE

γ	Surface tension in absence of monolayer
γ_0	Surface tension with monolayer
λ	Wavelength
Π	Surface pressure (mN/m)
Π-A isotherm	Pressure-area isotherm
θ	Angle of incidence (reflectivity)
χ	Flory-Huggins χ parameter
1D	1-dimensional
2D	2-dimensional
3-APTES	3-aminopropyltriethoxysilane
3D	3-dimensional
^{1}H	Hydrogen
^{2}H	Deuterium
^{14}N@C$_{60}$	Endohedral fullerene encapsulating ^{14}N
^{15}N@C$_{60}$	Endohedral fullerene encapsulating ^{15}N
P@C$_{60}$	Endohedral fullerene encapsulating phosphorous
AFM	Atomic Force Microscopy
Ag	Silver
Au	Gold
BAM	Brewster angle microscopy
C$_{60}$PS$_6$	C_{60} functionalized with 6 polystyrene chains
C$_{60}$PS2	C_{60} functionalized with 6 polystyrene chains with M_n: 2 kg/mol

C_{60}PS6	C_{60} functionalized with 6 polystyrene chains with M_n: 6 kg/mol
CA	Contant angle
CS_2	Carbon disulfide
CT complex	Charge-transfer complex
DFT	Density Functional Theory
DSC	Differential scanning calorimetry
ESR	Electron Spin Resonance
[F]	Concentration of free fluorophore
$[F]_0$	Initial fluorophore concentration
[FQ]	Concentration of fluorophore-quencher complex
HOPG	Highly oriented pyrolytic graphite
HPLC	High-performance Liquid Chromatography
HRTEM	High resolution transmission electron microscopy
dPS	Deuterated polystyrene
dPS-PMMA	poly(deuterated styrene-*b*-methylmethacrylate)
h-PMMA	Poly(methylmethacrylate) homopolymers
I	Fluorescence intensity at quencher concentration [Q]
I_0	Fluorescence intensity of pure fluorophore solution
$I_{ref}(Q)$	Reflected beam intensity
$I_{inc}(Q)$	Incident beam intensity
K	Association constant for complex formation
K_{sv}	Stern-Volmer constnat
L_0	Natural period of block copolymer

LB	Langmuir-Blodgett
LS	Langmuir-Schaefer
MMA	Mean molecular area
M_n	Number-average molecular weight
NR	Neutron reflectivity
ODT	Order-disorder temperature
OPVs	Organic photovoltaic devices
P1VA	Poly(1-vinylanthracene)
P2VN	Poly(2-vinylnaphthalene)
P4CS	Poly(4-chlorostyrene)
P4VP	Poly(4-vinylpyridine)
P9VP	Poly(9-vinylphenanthrene)
PCBM	[6,6]-phenyl-C_{61}-butyric acid methyl ester
PDMS	Poly(dimethylsiloxane)
PEG	Poly(ethylene glycol)
PMMA	Poly(methylmethacrylate)
PPE	Poly(phenylene ethynylene)
PQ^{+2}	Paraquat
PS	Polystyrene
PS_6	Polystrene with M_n~6 kg/mol
PS_{41}	Polystrene with M_n~41 kg/mol
PS_{100}	Polystrene with M_n~100 kg/mol
PS-P2VP	Poly(styrene-*b*-2-vinylpyridine)

PS-P4VP	Poly(styrene-*b*-4-vinylpyridine)
PS-PDMS	Poly(styrene-*b*-dimethylsiloxane)
PS-PEP	Poly(styrene)-*b*-poly(ethylene-*alt*-propylene)
PS-PI	Poly(styrene-*b*-isoprene)
PS-PMMA	Poly(styrene-*b*-methylmethacrylate)
PTFE	Polytetrafluoroethylene
Q	Wave transfer vector
[Q]	Free quencher concentration
$\mathbf{[Q]_0}$	Quencher concentration in a pure quencher solution
$\mathbf{r_M}$	Chain length ratio
R(Q)	Q-dependent reflectivity
SAM	Self-assembled monolayer
Si	Silicon
SiOx	Silicon oxide
STM	Scanning Tunneling Microscopy
SV	Stern-Volmer
TEM	Transmission electron microscopy
$\mathbf{T_g}$	Glass transition temperature
THF	Tetrahydrofuran
TR	Transfer ratio
WAXS	Wide angle x-ray scattering
XPS	X-ray photoelectron spectroscopy

SUMMARY

Since their discovery in 1985, fullerenes have been widely studied due to the unique chemical, electronic, and photophysical properties offered by the fullerene cage; research has led to fullerene application in numerous technological areas, including well publicized use in organic photovoltaic devices (OPVs), artificial photosynthesis, supramolecular assemblies, and potential use in quantum computing. This thesis research was largely motivated by the potential quantum computing applications for fullerenes encapsulating spin-active atoms. The overall goal of this research was to achieve alignment of endohedral fullerene dimers defined as covalently linked pairs of fullerene cages where each fullerene cage encapsulates a spin-active atom; however, the research discussed herein encompasses both monomer and dimer C_{60} behavior.

Devices where quantum effects dominate have a variety of potential uses in both classical and quantum computation, addressing issues with both decreasing size and increasing complexity. Buckminster fullerenes are ideal cages for spin-active atoms used for quantum computing such as atomic nitrogen ($^{14}N@C_{60}$, $^{15}N@C_{60}$) as the carbon cage provides almost total isolation of atomic properties as well as the ability for arrangement of spins with respect to one another. However, large aligned arrays of endohedral fullerenes are required to successfully achieve quantum computation. Self-assembled molecular networks are ideal for developing large because the spacing and geometry are typically well-defined by non-covalent interactions. Three self-assembly approaches will be discussed in depth here including (1) block copolymer templates as guides for

fullerene alignment; (2) Langmuir-Blodgett (LB) deposition of monolayers and multilayers; and (3) surface-directed assembly of fullerene monolayers.

The first section will discuss polymer-fullerene interactions from the point of view of determining how various polymer functional groups enhance or hinder the miscibility of C_{60}. The solubility and aggregation behavior as well as charge-transfer (CT) complex formation of C_{60} in solution have been studied extensively. Despite the wealth of empirical data, it is arguable that the fundamental nature of molecular interactions with fullerenes is not well understood, particularly with regard to polymer-fullerene interactions. In order to successfully incorporate fullerenes into a block copolymer system, we first need to understand the basic interactions that occur between polymers and fullerenes to anticipate the upper limit of fullerenes that may be incorporated in a given polymer and potential approaches to increase this quantity. In particular, studies conducted using wide angle x-ray scattering (WAXS) of vinyl polymer-fullerene blends indicated that an increasing number of phenyl rings in the vinyl side group of the polymer leads to an increase in the miscibility. In particular, poly(9-vinylphenanthrene) (P9VPh), having three phenyl rings in the side group, showed a 6-fold improvement in miscibility limit compared to the other systems studied, polystyrene (PS) and poly(2-vinylnaphathalene) (P2VN). The degree of increase in miscibility observed with P9VPh is attributed to the ability of the vinyl aromatic structure to essentially conform to the curvature of a fullerene molecule rather than the increased potential for π-π interactions. These results importantly suggest that a block copolymer system can be tuned to maximize fullerene content, particularly by considering the geometry of functional groups with respect to the fullerene cage and will be discussed further in Chapter III.

Second, the use of block copolymers as templates for creating ordered arrays of fullerenes is discussed. The initial goal was to disperse the fullerenes in one block of a block copolymer system and by aligning the microphase separation structure, also align the incorporated fullerenes. There are several major challenges associated with incorporating fullerenes into a block copolymer including the limited miscibility discussed in Chapter III. Furthermore, overcoming the strong inter-fullerene interactions that lead to aggregation also proves to be challenging; aggregates can disrupt the microphase structure in a block copolymer and make alignment difficult to obtain. One potential method generically used to solubilize nanoparticles within a block copolymer is modification of the nanoparticles by grafting polymer chains to the surface to solubilize the nanoparticle in a specific block. There are additional challenges associated with using polymer-modified nanoparticles including changes in microphase structure associated with swelling of the solubilizing block. However, the ability to tailor the size of the nanoparticle based on the length of the covalently attached polymer arms allows for control over the location of the particle within the solubilizing block. Because the C_{60} cage itself is quite reactive, we have investigated the addition of six polystyrene arms of different molecular weights to the fullerene cage and the behavior of these hard-core stars in a symmetric deuterated polystyrene-*b*-poly(methyl methacrylate) (dPS-PMMA) diblock copolymer. As discussed in Chapter IV, the effects of nanoparticle size and concentration on the phase behavior of lamellar-forming dPS-PMMA systems as well as the location of the fullerene star within the dPS block were studied using neutron reflectivity (NR). The NR results show that a full layer of fullerene stars forms in the dPS block; the loading of star where this occurs is size dependent. It was determined that in

both cases the fullerene star segregates to the center of the dPS block where distortion of the chain ends occurs to accommodate the presence of the star. Results of these studies are provided in more detail in Chapter IV. Using these PS-modified fullerene systems we showed that we can disperse and selectively assemble C_{60} within a lamellae-forming diblock copolymer system.

The scheme above has the disadvantage that modification of the fullerene cage with polymer arms dilutes the overall quantity of fullerene in the system and in the case of endohedral systems, would dilute and severely limit the overall quantity of spins available for measurement in quantum computing. For this reason we chose to investigate the formation of monolayers of amphiphilic fullerene dimers at the air/water interface using the Langmuir technique. We also studied the behavior of these materials when transferred as monolayers and multilayers to solid substrates as Langmuir-Blodgett (LB) films. The fullerene dimers in this case were modified to have at least one hydrophilic, polyethylene glycol-based ligand to balance the inherently hydrophobic nature of the fullerene cage and allow for a molecule that more closely resembled typical LB materials. Results of these studies indicated that we can form stable, close-packed monolayers and also control the orientation of the dimer at the air/water interface as well as on solid substrates by tuning the ligand chemistry as shown in Chapter V.

The final approach used to achieve alignment of fullerene materials involves the interaction of fullerenes with a chemically-modified substrate either covalently or non-covalently. Solid substrates were functionalized with amine-terminated molecules, and fullerene materials were then studied for their monolayer formation on these substrates. Results indicate that monolayers of fullerenes can be obtained on both silicon and mica

using this technique. Monolayers formed between fullerenes (either monomer or dimer) and amine-terminated surfaces are covalently bound, either through reaction with functional groups or direct addition to the fullerene cage. Endohedral systems were also studied using this approach and results are provided in Chapter VI for studies using this method.

In summary, we have shown that fullerenes can be selectively assembled using numerous approaches that can be tailored for the specific end application. Particular success was seen using block copolymers, monolayer formation at the air/water interface, and surface-directed assembly. Combining self-assembly with fullerenes has been shown to have a great deal of promise for development of functional nanomaterials using the techniques described above.

CHAPTER I: INTRODUCTION

1.1 Motivation and Approach

The development of a quantum computer has been an intense area of study for the last two decades due to the incredible computing power and problem solving capabilities possible with a working quantum computer. To date, a working quantum computer has not yet been developed, but study continues worldwide to identify ideal materials and approaches to designing such a system. While there a variety of nanoscale approaches to achieving the development of a quantum computer, our focus has been on combining molecular self-assembly with endohedral fullerenes [1-5]. This approach has the potential to lead to the alignment of spin-active functional carbon-based materials and the development of components for a practical, working quantum computer [6, 7].

Endohedral fullerenes are defined as having an additional atom, ion, or cluster of atoms isolated in the center of the inner fullerene cage. Particularly interesting for our applications are endohedral systems were the fullerene cage encapsulates a noble gas atom such as nitrogen ($N@C_{60}$) or phosphorous ($P@C_{60}$) [1, 8-10]. Atomic nitrogen is highly reactive but has been shown to be stable at room temperature when encapsulated by the C_{60} fullerene cage as the cage provides a totally isolated environment; the inner fullerene cage surface has also been shown to be inert [8-10]. Additionally, the atomic nitrogen is spin-active, and the isolated environment allows electronic spin to be maintained while also allowing control over interaction with neighboring spins. Maintaining and controlling the electronic spin interactions is highly important to quantum computing as the functional unit, known as a *qubit* and comparable to the classical computation bit, is carried in the form of the electron spin [6, 7].

Because repeatable and controllable spin interactions are necessary, one possible approach is using an endohedral fullerene dimer as discussed in this dissertation. The fullerene dimer, simply a covalently bonded pair of fullerene cages, allows for the position of one spin to be well defined with respect to another spin in a two-qubit system if both cages encapsulate a spin-active atom. Using a dimer allows for further control over the distance between spins as the bridge chemistry between fullerene cages can be manipulated to allow for an ideal spacing between spins within one dimer.

Initial approaches to the development of a quantum computer required each spin or qubit to be addressed individually, posing a number of challenges to practical and feasible implementation of components. However, recently it was determined that it is possible to address an entire linear chain or array of qubits at once using an approach termed global control [11-17]. Global control has been shown to be effective using a 3-qubit system [11], a system of alternating spin types [12-14], and with a chain composed of only one spin type [15-17]. Regardless of the type of qubit system used, alignment of the qubits in linear arrays is required with controlled spacing between neighboring qubits. In the case of endohedral fullerene systems, alignment of the fullerene cages leads to alignment of the spins, and this requirement for alignment has been the motivation for the experiments discussed in this thesis.

A number of approaches have been investigated for templating fullerene monomers, specifically C_{60} and functionalized C_{60} such as insertion into single-walled carbon nanotubes or self-assembled monolayers via sublimation. Techniques such as these do lead to aligned fullerenes with pristine C_{60}, but the high temperatures involved with sublimation are problematic in terms of the endohedral element as well as maintaining

the covalent linkage between cages in a dimer system. In addition to the challenges associated with elevated temperature, the limited miscibility of fullerenes and strong aggregation tendency also need to be considered when selecting experimental approaches for alignment of endohedral fullerenes. A final consideration in selecting a method is the minimum spin requirement of ~10^{12} spins for detection using electron spin resonance (ESR) measurements; to achieve this quantity of spins, a monolayer of high spin purity material would be sufficient, or multilayers of a lower purity material would be required.

With this in mind, we have decided to take advantage of the inherently strong force of self-assembly on the nanoscale of materials such as that with block copolymers and strong intermolecular interactions to direct the alignment and order of fullerenes. Three specific approaches will be discussed: using block copolymer microphase separation structure [18], and selective incorporation of fullerenes into one block, and subsequent alignment of the block copolymer structure; self-assembly of fullerene monolayers at the air/water interface using the Langmuir technique and transfer of the monolayer to a solid substrate [19]; and lastly, substrate-directed assembly of fullerene monolayers where a solid substrate is chemically functionalized to specifically attract and bind fullerene molecules [20].

1.2 Scope of Dissertation

This dissertation will discuss our approach to achieving the alignment of fullerenes and fullerene dimers for applications related to quantum computing using three major techniques: block copolymer alignment, Langmuir and Langmuir-Blodgett films, and surface-directed monolayer assembly. Chapter II provides a discussion of the relevant

literature pertaining to quantum information processing; material properties of fullerenes; and various fullerene alignment strategies along with the advantages and disadvantages to each method. Specific and detailed analysis of work related to the three alignment strategies discussed herein is also provided in this chapter for comparison purposes. Because fullerene miscibility has a strong influence on the choice of alignment strategy, it was important for us to characterize and fundamentally understand fullerene interactions with polymers and the structural factors and types of molecular interactions that most effectively increase the strength of polymer-fullerene interactions. These studies are discussed in Chapter III including fullerene interaction with conjugated polymers and polymers with vinyl aromatic groups. Chapters IV, V, and VI include the methods, characterization, and results of experiments involving the alignment of fullerenes using block copolymers, LB films of amphiphilic fullerenes, and functionalized substrates respectively. Finally, this dissertation concludes with a discussion of the alignment strategies in terms of the overall success in moving towards the ultimate goal of using endohedral fullerene dimers in quantum computing applications as well as recommendations for future work.

CHAPTER II: LITERATURE REVIEW

2.1 Quantum Information Processing

Development of quantum computers dates back to 1994 when a quantum algorithm for factoring large numbers was shown to be capable of breaking encryptions typically used in internet communication and commerce [21]. Although a working practical quantum computer does not yet exist, its development is being actively studied worldwide, particularly due to the immense implications such computation capability would have to defense applications including cryptography.

Devices where quantum effects dominate have a variety of potential uses in both classical and quantum computation [6, 7, 22]. These devices would address issues with decreasing size and increasing complexity as related to classical computation as well as quantum computing [6] and have important application regarding secure communications and information encoding/decoding [6, 21]. Analogous to a classical computation bit, the qubit is defined in quantum computing as the information carrier in the form of electron spin [6, 7]. Quantum computing typically requires local control over interactions between neighboring qubits. However, local control has many disadvantages as the typical approach involves one electrode per pair of qubits. This results in difficulties associated with fabrication and leads to a minimum spacing requirement for qubit separation [12]. Therefore, alternative approaches for controlling qubit interactions are required.

We are currently investigating the use of *global control* of qubit interactions [12]. Using two varieties of qubits allows for all of one variety to be addressed at once instead of

addressing each qubit individually [6]. Instead of switching on/off qubit interactions independently, global control allows for switching off many interactions at the same time using global fields [12]. Molecular structures are highly useful for global control applications as individual spin-active atoms can be inserted into molecular scaffolding to form an array [7].

Buckminster fullerenes are ideal cages for spin-active atoms as the carbon cage provides almost total isolation of atomic properties as well as the ability for arrangement of spins with respect to one another [1, 7]. With a high degree of symmetry and cage-like structure, fullerenes are of particular interest in quantum computing applications due to their unique properties [23]. Endohedral complexes are C_{60} fullerenes with atomic elements in their ground state encapsulated by the C_{60} cage. The fullerene cage has been shown to provide an isolated environment with the atomic element located within the cage and no covalent interactions with its inner surface [8-10]. In particular, $N@C_{60}$ and $P@C_{60}$ with nitrogen and phosphorous located in the center of the fullerene respectively are desirable systems for use in quantum computing [1, 8-10]. C_{60} and $N@C_{60}$ are chemically similar, as evidenced by the retention of the purple color in toluene solutions for both systems and the identical UV-visible spectroscopy spectra. Purified $N@C_{60}$ has also been shown to be inert and stable at room temperature in both solution and solid state [24]. The electron spins of endohedral fullerenes have a long lifetime which also makes them ideal for use as qubits in quantum computing [9].

Fullerene dimers, specifically a bonded pair of fullerenes, provide the potential for a two-qubit system if both fullerenes encapsulate spin-active material. Endohedral fullerene dimers allow for a variety of two-qubit combinations to be used such as a $^{14}N/^{15}N$ dimer

system. There are a variety of factors that are important in these dimer systems including the spacing between qubits which can be controlled via the covalent linkages between C_{60} cages in a dimer.

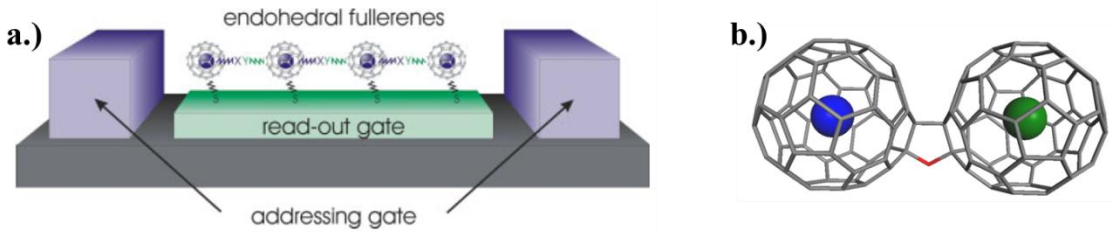

Figure 1. Quantum computing using endohedral fullerenes; a.) potential scheme for a solid-state spin quantum computer using linear arrays of endohedral fullerenes as proposed by Harneit et al (reproduced from [9]); b.) example of an endohedral fullerene dimer where the covalent linkage between fullerene cages can be manipulated to control spacing.

However, endohedral fullerene research has been limited to date by major technical difficulties associated with synthesis and purification of endohedral fullerenes. $N@C_{60}$ in particular can only be synthesized in usable quantities via ion implantation, resulting in a ratio of $N@C_{60}$ to C_{60} of 10^{-4}. Ion implantation is then followed by enrichment using high-pressure liquid chromatography (HPLC). Enrichment with HPLC is a slow, tedious technique as only small quantities of material can be processed at a time. Furthermore, HPLC is a multi-step process as C_{60} and $N@C_{60}$ are virtually chemically indiscernible as shown by Figure 2. As an example of the difficulties associated with this process, greater than 100 L of $C_{60}/N@C_{60}$ in toluene solutions have to be run through a standard HPLC

column in microliter injection quantities to get milligram amounts of purified $N@C_{60}$ [24].

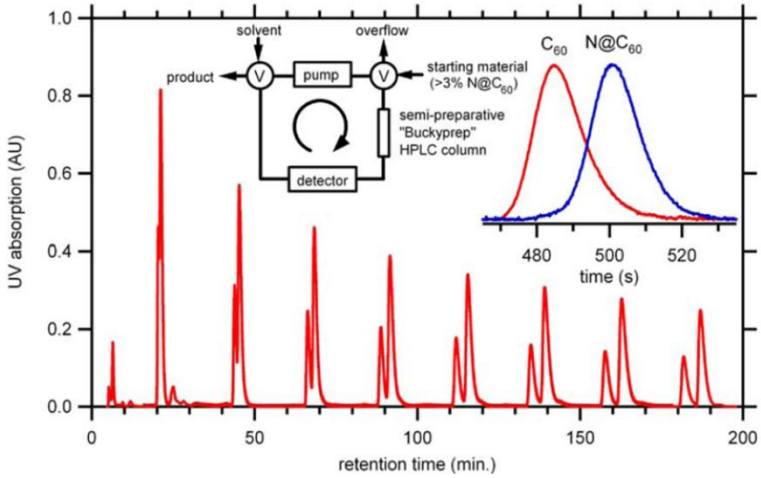

Figure 2. Representative HPLC process for the multi-step enrichment of $N@C_{60}$ with a schematic representation of the HPLC process included in the inset (reproduced from [24]).

To realize quantum computing, large arrays of spin-active atoms are required. For this reason, self-assembled molecular networks are advantageous where the spacing and geometry are well-defined, typically by non-covalent interactions [7]. In the case of endohedral fullerenes, alignment of the spins can be achieved by templating the fullerene cages.

Numerous methods have been proposed to achieve arrays of endohedral fullerenes for these applications, including use of single-walled carbon nanotubes (SWNT) [6, 25, 26]. These “peapod” structures can be prepared in high-yield with high densities of fullerenes within the SWNT with any fullerene structure via sublimation at 200 to 520 °C [25, 26].

Self-assembled monolayers (SAMs) of functionalized fullerenes have also been achieved with a high degree of alignment using low temperature (520K) sublimation on (111) oriented silver (Ag) thin films [27]. Porphyrin monolayers sublimated on Ag(100) substrates have also been used to direct self-assembly of fullerenes, and monomeric porphyrins were shown to lead to highly stable organized fullerenes over several square nanometers [28]. Representative results from the SWNT peapod and SAM techniques discussed above are shown in Figure 3.

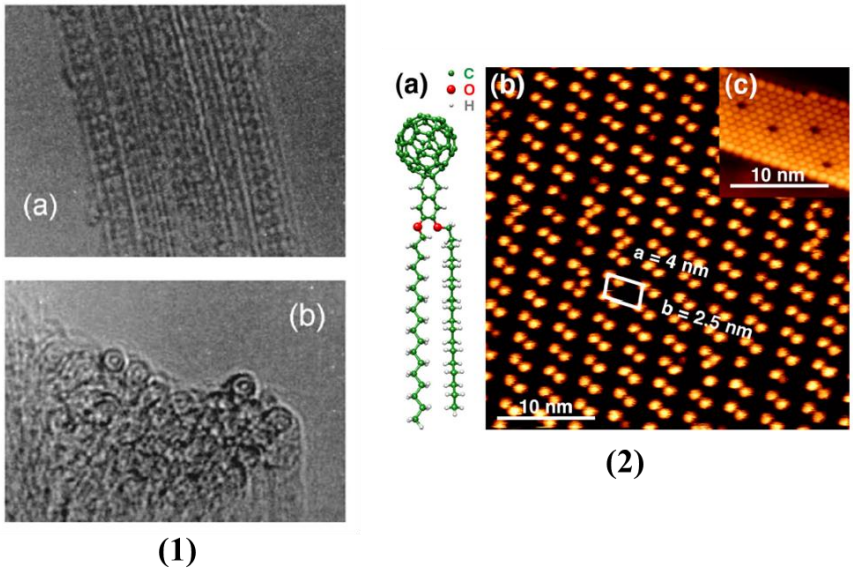

Figure 3. Techniques for alignment of fullerenes using sublimation; (1) high resolution transmission electron microscope (HRTEM) images of C_{70} peapod structures (a) from a side view and (b) a bundle of peapods (reproduced from [25]); (2) scanning tunneling microscope (STM) images of functionalized fullerenes aligned on an Ag(111) surface (reproduced from [27]).

The high temperatures involved with the sublimation process are problematic however as they adversely affect the number of endohedral atoms in the system. Endohedral complexes have been shown to have low thermal stability where above 50 to 100 °C the enclosed atom begins to form bonds with the interior of the C_{60} cage [9, 24]. These temperatures are well below the sublimation temperature of fullerenes, so alternative approaches at lower temperatures are required for achieving linear fullerene microstructures.

Perfectly straight nanowires of fullerenes have also been achieved by depositing fullerenes modified with long alkyl chains on highly oriented pyrolytic graphite (HOPG) by spin coating [29] or solution casting [30]. With this technique, the alkyl chains on the fullerene cage are used as the driving force for directional alignment on the graphite substrate. The alkyl chain length was shown to greatly influence the spacing of the nanowires as well as the placement/arrangement of the fullerenes with respect to one another [29]. The advantage of processes such as this is that the alignment of the fullerenes occurs at room temperature without thermal annealing or high temperature deposition. Alignment approaches that will be specifically addressed in this dissertation include the use of block copolymer microphase separation structures to align fullerenes by selective incorporation into one domain [31, 32] and surface directed assembly of fullerenes including Langmuir-Blodgett (LB) deposition [33-43] and self-assembled monolayers (SAMs) [36, 44-54] (Figure 4).

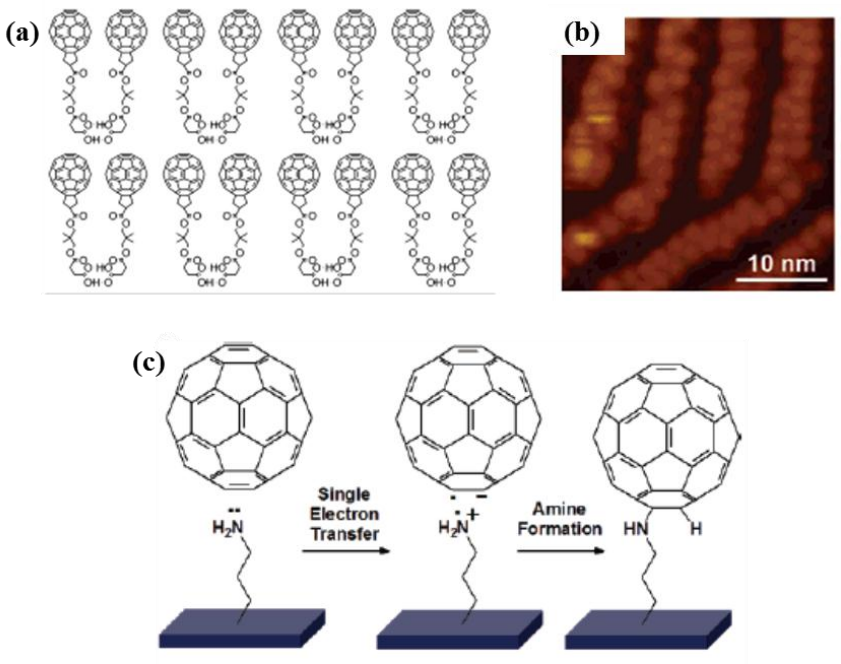

Figure 4. Examples of fullerene patterning using (a) Langmuir-Blodgett transfer from the air/water interface to solid substrates (reproduced from [52]), (b) highly oriented pyrolytic graphite (reproduced from [29]), and (c) an amine-terminated self-assembled monolayer (reproduced from [55]).

2.2 Fullerenes

2.2.1 Overview of Fullerenes

The shape and chemistry of buckminsterfullerene is unique in the chemistry world. With its spherical structure and the highest symmetry of any known molecule, the C_{60} cage is made up of sixty carbon atoms with chemical bonds resembling that of the stitching on a soccer ball. Buckyballs are a stable form of carbon, first discovered in 1985 and only produced in large enough quantities for study beginning in 1990 [56, 57]. Buckminster fullerenes are just one structure in an entire family of molecules composed entirely of carbon ranging in shape from the perfectly spherical cage of C_{60} to ellipsoid-shaped and

even tubular. Of the fullerenes, however, C_{60} is the most commonly found naturally-occurring form consisting of 20 hexagons and 12 pentagons where each carbon is covalently bonded to three others. In fact, C_{60} is the smallest fullerene where no two pentagons share an edge, lending to the stability of the molecule [56-58].

The discovery that fullerenes are soluble in benzene played a pivotal role in their continued study as fullerenes must be dissolved to successfully extract them from soot for further use. Subsequent studies regarding the dependence of fullerene solubility on temperature and organic solvent allowed for the separation of different members of the fullerene family and purification of the resulting materials [58]. While fullerene solubility has been intensely studied over the last twenty years, there is still no systematic method to explaining and predicting fullerene solubility in different solvents or even the differences in solubility between various fullerene structures. The limited solubility continues to be a challenge to widespread use of fullerenes in a variety of applications as discussed in the next section, but it is necessary to achieve a better understanding to take advantage of the massive potential offered by the unique physical and chemical properties of fullerenes.

2.2.2 Fullerene Solubility and Complex Formation

Fullerenes have been relatively limited in their use thus far due to their low solubility in common organic solvents. The solubility behavior [58-69] and aggregation tendencies [70-83] of fullerenes in solution have been thoroughly investigated. Miscibility behavior of fullerenes with polymers has not been probed as extensively, although factors important to good solubility in solvents also apply to polymer-fullerene interactions [59].

The charge-transfer behavior of C_{60} fullerenes and both small molecules [84-89] and polymers [31, 90-92] has also been examined.

Solubility for C_{60} has been measured in a variety of solvents using UV-visible spectroscopy [58, 61-63, 68, 69] as well as analyzed extensively using theoretical simulation [59, 60, 64, 66, 67]. Both theory and experiment agree in terms of factors that improve solubility in solvents. Both aromatic rings and atoms that are much larger than carbon such as chlorine lead to better solubility as evidenced by the series of naphthalenes shown in Figure 5, particularly when comparing the methylnaphthalene to the 1-chloronapthalene [59, 61, 63].

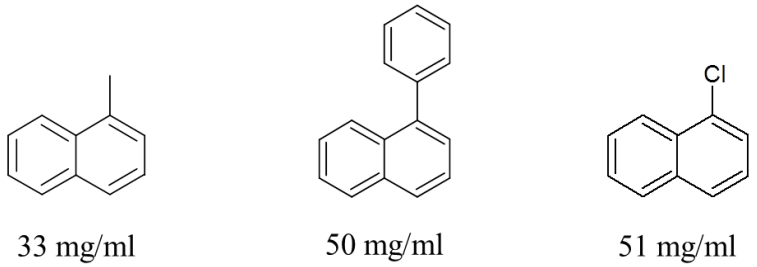

Figure 5. Solubility of C_{60} fullerenes with small molecule, organic solvents including (left to right): methylnaphthalene, phenylnaphthalene, and chloronaphthalene. As indicated by the solubilities reported, aromatic rings and large atoms improve the solubility of fullerenes in a given solvent.

Solubility is measured using UV-visible spectroscopy by taking a series of solutions of known concentration and measuring the absorbance spectra. Ruoff et al examined a wide range of solvents with fullerenes, and it is evident from their results that fullerenes show low solubility in alkanes and polar solvents. Fullerenes are most soluble with benzene-related solvents as well as naphthalenes as expected based on the presence of aromatic

rings [58, 61]. However, due to the limited solubility of fullerenes with most organic solvents, C_{60} molecules tend to aggregate in solution, even at dilute concentrations [70-83]. Studies have shown that fullerene aggregates form in a variety of solvents including toluene [77, 78] and N-methylpyrrolidone (NMP) [80, 81].

Methods for improving the solubility and dispersion of fullerenes, particularly with polymers, have also been employed including modification of the fullerene cage with polymer arms [32, 93-95]. These investigations have examined the improved miscibility offered specifically with polystyrene-based polymers with the addition of polystyrene (PS) arms to the fullerene cage. The addition of just two PS arms has been shown to drastically improve the miscibility of C_{60} with a PS matrix using UV-visible spectroscopy on blend films. PS-modified fullerenes were shown to disperse either as single molecules or small aggregates depending on the chain length of polymer and the blend composition [95]. Fullerenes with up to six polymer arms have been successfully included in PS-based block copolymer systems, and the addition of PS arms to the C_{60} cage has been shown to force the fullerenes into the PS block [32, 93].

Charge-transfer complex formation is important to the work discussed here due to the complex formation with block copolymers that has been shown to have a variety of effects including shifts in microphase separation morphology [31]. Because C_{60} is willing to accept up to six electrons, it readily forms charge-transfer complexes with a variety of materials. The strength of the complexes formed between C_{60} and several small molecules has been determined by the association constant, K, from Benesi-Hildebrand Theory [96]. Table 1 below summarizes the results found by several groups regarding this complex formation with small molecules. Complexes formed with short cyclic

polymers were shown to be several orders of magnitude stronger based on the size of the association constant, K, as discussed by Yamahuchi and coworkers [92].

Table 1. Examples of charge-transfer complex strengths between fullerenes and small molecules [84-89].

Name	Structure	K (M^{-1})
Methylnaphthalene (in toluene)		0.08±0.02
Napthalene (in toluene)		0.08±0.015
Diphenylaniline (in toluene)		0.08
Benzene		0.18±0.04
Diethylaniline		0.18 0.29±0.04
Triethylamine		0.18±0.06
N,N-dimethylaniline		0.04 0.20 0.28±0.04

Name	Structure	K (M^{-1})
tri-n-amylamine	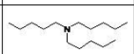	0.25±0.10
n-butylamine		0.3±0.08
Propylethylamine		0.34±0.10
Phenanthrene (in toluene)		0.37±0.07
n-heptylamine	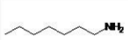	0.58±0.1
Pyrene (in toluene)		1.1±0.2
Ethylenediamine		1.16±0.16

2.2.3 Techniques for Alignment of Fullerenes

As mentioned briefly, the majority of applications in which fullerenes have potential use require ordered arrays of fullerenes. Many approaches have been taking to achieving just that, with successful methods including sublimation of fullerenes onto substrates [27]; incorporation of fullerenes into carbon nanotubes to create peapod structures [6, 25, 26]; and various self-assembly methods such as incorporation into block copolymer microphase structure [31, 32], monolayer formation at the air/water interface [33-43], and surface directed assembly taking advantage of the reactivity of the fullerene cage with

terminal functional groups [36, 44-54]. These last three methods will be discussed in detail in CHAPTERS IV-VI, as these are three approaches we have undertaken to achieve ordered arrays of fullerenes, fullerene dimers, and endohedral fullerenes for potential use in quantum computing applications.

2.3 Block Copolymers

2.3.1 Overview of Block Copolymers

Block copolymers are defined as two or more different polymer chains covalently linked and span a wide range of applications from enhancing toughness to templates for nanoparticles [18, 97]. Separation of incompatible blocks occurs on the nanometer length scale, resulting in complex nanoscale structures [18, 98]. A wide variety of chemical structures can be synthesized and are separated into two major classifications based on the number of different polymer blocks and linear versus branched structures. Different combinations and even attachment order result in different microphase separation morphologies as well as differences in material properties [18].

Chemical dissimilarities between blocks, however minor, results in increased free energy in the system that is unfavorable for mixing, particularly at higher molecular weights. Non-ideal mixing is typically defined using the "Flory Huggins χ Parameter" which quantifies the free energy requirement for monomers of polymer A to contact monomers of polymer B. Larger values of χ, particularly positive values are indicative of larger non-ideal mixing energies and phase separation while negative values of χ signify polymer mixing. In general the χ-parameter has an inverse relationship with temperature as mixing

is more likely to occur at higher temperatures but lower values of χ [18, 97]. Block copolymers with highly dissimilar blocks favor separation. However, the covalent link between blocks prevents macrophase separation and results in microphase separation where various structures form depending on the number of repeat units and relative weight fraction of each block along with the χ-parameter [18, 97-99]. Inherent in the χ-parameter as mentioned is an inverse temperature dependence. For this reason the block copolymer is a disordered, miscible melt above the order-disorder transition (ODT) temperature but forms microphase structures below the ODT temperature [99] and above the glass transition temperature, T_g. The scale and microphase separation morphology are determined by minimization of the free energy. Film thickness has also been shown to be an important experimental parameter for microphase structure development and orientation. Knoll et al showed that the microphase structure changes systematically with film thickness in thin films of cylinder-forming poly(styrene-*b*-butadiene-*b*-styrene) (SBS) block copolymers [100]. Figure 6 below depicts the classic theoretical phase diagram for diblock copolymer systems with the resulting structures shown below [18].

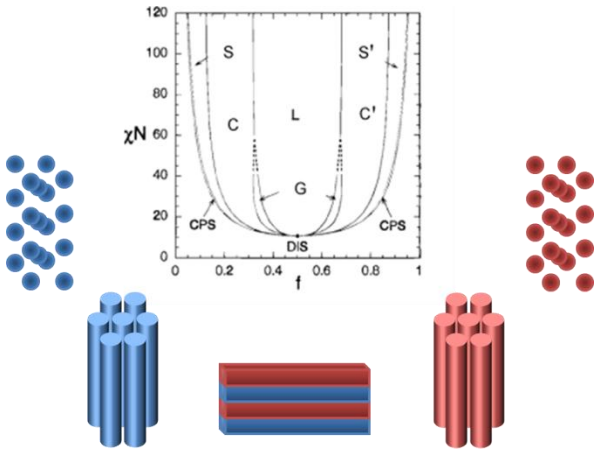

Figure 6. Microphase separation structures that may result from diblock copolymer microphase separation depending on the relative weight fraction of each block, degree of polymerization, and Flory-Huggins χ-parameter.

Morphologies shift from spheres to cylinders to lamellae of the minor block with a gyroid phase between the cylindrical and lamellar microphases. Spheres form cubic structures, cylinders form hexagonally packed structures, and lamellae can organize in a layered architecture [18, 98]. Triblock copolymers allow for the potential of even more distinctly unique microphase separation morphologies where simple in changes in block sequence can drastically change the morphology, particularly when comparing AB diblock and ABA triblock systems to ABC triblock copolymers. Variation of block molecular weight is an added variable that increases the number of morphologies that can be achieved [18, 98].

2.3.2 Techniques for Alignment of Block Copolymers

Long-range order in block copolymer thin films is important to a variety of applications ranging from nanolithography and patterning [97, 101] to incorporation of nanoparticles [97], and controlling the positioning and orientation of the microphase in block

copolymer thin films has thus far limited block copolymer use in these applications [101]. Several techniques have been used for developing long-range order in block copolymer thin films including electric fields [101, 102], applied shear [103-105], thermal annealing (with and without gradient) [106], solvent annealing [107-114], droplet pinning with solvent evaporation[115], directional crystallization of a solvent [116], topographic substrates [117-119], and soft molding techniques [120]. Of particular interest in this research is the use solvent annealing in conjunction with applied to shear to induce long-range order in cylindrical morphology block copolymers.

The application of shear as a method for ordering block copolymer thin films has been achieved using elastomer pads dragged across the polymer surface [103], the use of soft molds on the thin film surface [120] and topographic substrates [117-119], and flow of a non-solvent fluid across the surface [104, 105]. Angelescu and coworkers developed a method for ordering single-layer thin films of poly(styrene)-*b*-poly(ethylene-*alt*-propylene) (PS-PEP) cylindrical forming diblock copolymers with PS as the minor phase in a matrix of PEP using uni-directional shear as follows. Monolayer thin films were heated using a hotplate while an un-patterned PDMS pad was pressed on the film using a weight. A controlled lateral force was then applied to the weight, and the displacement was monitored. Monitoring of the displacement indicated that the immediate displacement of the weight caused elastic deformation of the PDMS pad followed by slow linear displacement indicative of viscous flow of the polymer thin film [103]. Figure 7 provides a diagram of the experimental setup and illustrates the results seen with uni-directional shear by Angelescu and coworkers.

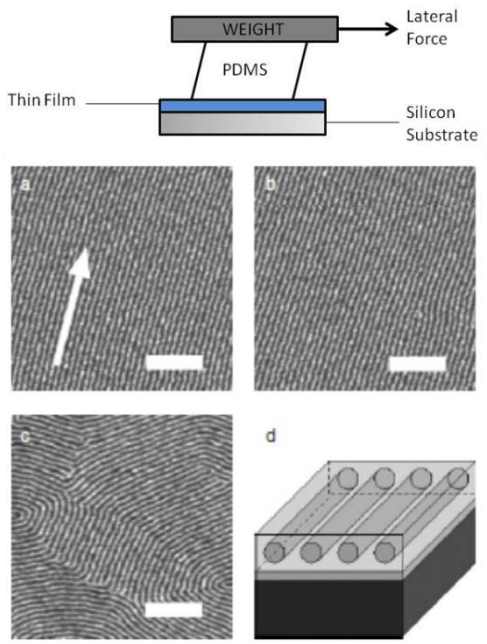

Figure 7. Application of uni-directional shear to monolayer block copolymer thin films and results achieved by Angelescu and coworkers using this method where (a) and (b) are the AFM results at different locations on the surface after shearing, (c) is a thermally annealed sample without shearing, and (d) is a pictorial representation of a single layer of PS cylinders in a PEP matrix. The arrow in (a) indicates the direction of shear, and scale bars are 250 nm (reproduced from [103]).

Shear applied through fluid flow of a non-solvent over a heated block copolymer thin film through a channel causes local alignment over several mm. Complex alignment patterns can be generated through the path of the channel across the surface, with alignment along the direction of fluid flow/applied shear [104]. A similar method using a rheometer has also been used to align block copolymer thin films with viscous fluid flow also at elevated temperature [105].

The use of patterned and un-patterned soft molds as a form of shearing to align single-layer cylindrical morphology thin films has also been shown to be effective in aligning areas as large as 1cm x 1cm. Figure 8 depicts the step-by-step process for achieving this

alignment where a patterned elastomeric (PDMS) mold is pressed to the heated thin film and the pattern is transferred to the thin film surface.

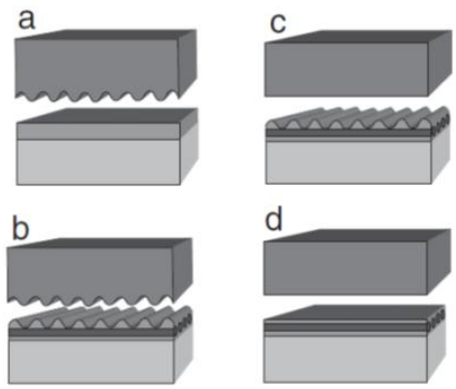

Figure 8. Soft molding method for alignment of block copolymer thin films: a) grated PDMS mold pressed to surface, b) pattern transferred from mold to thin film, c) flat PDMS mold pressed to surface, d) well aligned, flat thin film (reproduced from [120]).

The movement induced in the block copolymer by heating results in shear flow in the direction perpendicular to the grating and alignment of the cylindrical domains perpendicular to the gratings. Application of a flat PDMS mold to the surface while heating the thin film removes the grating pattern while still maintaining the alignment of the block copolymer [120]. Similarly, topographic or patterned silicon substrates have been used to achieve long range order of block copolymer thin films, a method known as graphoepitaxy [117]. The order in these cases is achieved over an area of several cm^2 either parallel or perpendicular to the groove depending on the microphase separation morphology [117-119]. Long-range ordering behavior in graphoepitaxy is affected by the groove dimensions and thermal annealing times as well as other factors [117]; smaller

grooves lead to better alignment than wider grooves, with a decrease in the number of defects, particularly when the grain size and groove are of similar sizes [117-119]. Longer thermal annealing times improve the order as do channels with flat, vertical sides [117].

Applied shear, fluid flow, and topographic substrate techniques all use thermal annealing to induce movement in the polymer chains. As mentioned previously, the endohedral element of the endohedral fullerene dimer is unstable with heating, so typical thermal annealing methods for alignment are not useful in terms of the final goal of work in this dissertation. However, solvent annealing has also been shown to be effective in creating long-range order in block copolymer thin films at room temperature [107-114].

Solvent evaporation from a thin film creates a directional solvent gradient that induces flow of the block copolymer and leads to well-ordered microdomains as shown in Figure 9. Experimentally, the sample is placed in solvent vapor at room temperature where the film is swollen. The film is then removed from the solvent vapor and as the solvent evaporates, the block copolymer shows long-range order. Because the order achieved is independent of the substrate, the process must begin at the surface and propagate through the entire film.

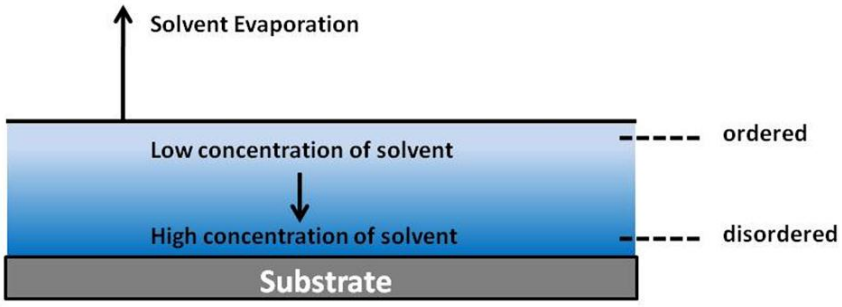

Figure 9. Mechanism of long-range order in block copolymer thin films via solvent annealing. Ordering begins at the air/film interface and propagates downward through the film to the substrate.

Solubility differences between the different blocks can be used to control domain size and spacing. There is a time-dependence shown by Kim and coworkers where the number of defects decreases rapidly with the exposure time with dewetting of the film occurring at long exposure times. This method has also been shown to be applicable on topographic substrates where the polymer dewets outside the channel but is trapped within the channel, and the ordering process occurs within the channel along the wall [109].

Symmetric PS-PMMA systems have been thoroughly investigated using solvent annealing in previous studies and are of particular interest to us as results with PS-PMMA/fullerene systems will be discussed later in this work [121-125]. Using AFM, TEM, XPS, and contact angle measurements, Peng and coworkers investigated symmetric PS-PMMA thin films by varying solvent/solvent selectivity, film thickness, and solvent anneal time to observe the various morphologies that develop [122]. Acetone has been investigated as a PMMA-selective solvent, and the morphology has been shown to evolve from the worm-like structure of an as-cast film to spheres with little long-range order (1 hour), well-ordered array of spheres (5 hours), and a mixed sphere and striped

morphology after 36 hours [121]. Further experimentation showed that after 48 hours of solvent annealing in acetone both the striped morphology and hexagonal array of spherical depressions continue to exist. With annealing time increased to 60 hours, the morphology consists completely of striped, surface perpendicular lamellae, and increasing the time to 85 hours results in striped morphology where the stripes show a directional preference [123]. The degree of swelling using acetone vapor was also shown to be important as films with a high degree of swelling dewetted while less swollen films showed hills and valleys with stripes on the hills and hexagonally packed spheres in the valleys after 26 hours of solvent annealing. The lower degree of swelling is thought to disturb the film less because the attraction of PMMA to the surface is weaker, so dewetting does not occur [125].

Solvent annealing studies with chloroform, also PMMA-selective, and PS-PMMA systems showed a similar evolution of structure with time. The morphology developed from a flat, featureless PS surface (10 hours) to a disordered microphase separated structure with no long-range order (20-40 hours) to well-ordered hexagonally packed nanocylinders (60 hours) to a combination of nanocylinders and stripes (80 hours) to fully striped morphology (100 hours) and back to a featureless, flat surface composed of PMMA after 120 hours. Film thickness effects were also determined using solvent annealing for 60hours in chloroform vapor. It was shown that well-ordered, hexagonally packed cylinders develop in thin films with thickness less than $\frac{1}{2}L_0$ where L_0 is the natural period of the block copolymer. At film thicknesses greater than $\frac{1}{2}L_0$, lamellae oriented perpendicular to the surface form [122]. In the case of PMMA-selective solvent annealing, XPS and contact angle measurements indicate that PMMA migrates to the air

interface with solvent annealing while PS block aggregate to minimize contact with acetone vapors [121]. Peng et al also investigated the effects of solvent selectivity using neutral (THF) and PS-selective (CS_2) vapors for solvent annealing over 23 hour periods. After annealing in THF vapor, a stepped morphology with lamellae aligned parallel to the plane of the film develops while annealing in PS-selective CS_2 results in a flat thin film with a disordered micellar structure as revealed by AFM. The micellar structure results from aggregation of PMMA blocks which are then surrounded by PS blocks to limit contact with the CS_2 solvent [125].

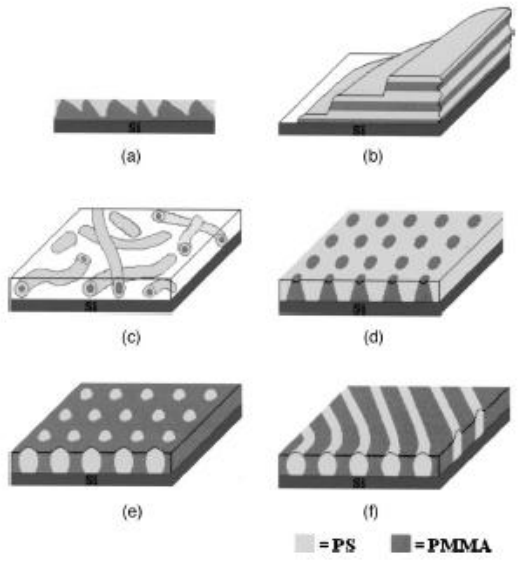

Figure 10. Schematic representation of the structure of symmetric PS-PMMA diblock copolymer thin films on silicon under different annealing conditions: a.) as spin coated where PS is shown to wet the silicon substrate; b.) after THF exposure (neutral solvent), lamellae are oriented parallel to the substrate; c.) after CS_2 exposure (PS-selective), results in a micellar structure with a PS "shield" around a PMMA core; d.) after a high degree of swelling in acetone (PMMA-selective), PMMA cylinders form perpendicular to the substrate; e.) after solvent annealing in acetone with a low degree of swelling, PS spheres form in a PMMA matrix; and f.) after acetone exposure at a low swelling degree at longer time, PS spheres merge to form PS cylinders (reproduced from [125]).

2.3.3 Block Copolymer/Homopolymer Blends

As briefly discussed above, block copolymer/homopolymer blends have been widely investigated for the effects of homopolymer addition on the phase behavior and microphase separation morphology of block copolymer systems [124, 126-128] [129]. Homopolymer additions have been shown to clearly influence the block copolymer structure; for example, Orso et al showed the intermolecular spacing in symmetric diblock copolymers increases for low and high molecular weight homopolymers, although less so for low molecular weight chains [128]. These systems have some relevance to the experimental work discussed here as polymer-modified fullerenes systems, expected to behave similarly to homopolymer addition to a block copolymer, have been investigated with symmetric PS-PMMA systems.

Block copolymer/homopolymer blends can be classified as being in either a "wet" or "dry" brush regime, first introduced by de Gennes [126, 130]. The behavior of an AB block copolymer blended with either A or B homopolymer is dependent on both the volume fraction ratio and the chain length ratio, r_M, of number-average molecular weight of the homopolymer to the corresponding block copolymer segment. With an $r_M<1$, where the homopolymer length is shorter than that of the block copolymer length, the homopolymer segregates to the interfaces, and there is an increasing interfacial curvature associated with increasing concentration in these systems [124, 126]. This region is defined as the wet brush region where the homopolymers addition causes a change in microphase structure [124]; Holoubek and coworkers showed with a symmetric dPS-PMMA diblock copolymer of molecular weight of 15-*b*-15 kg/mol with 8 kg/mol PS incorporated, the homopolymer causes a change in morphology from lamellar to

spherical in the wet brush regime [126]. Contrastingly, the dry brush region occurs when r_M~1 where the homopolymers segregates to the center of the block at the chain ends and only induces a swelling of the domain thickness but no change in morphology [124]. When r_M>1, macrophase separation occurs, as shown with a 35 kg/mol PS homopolymer in the same dPS-PMMA diblock copolymer described above. The macrophase separation results in distinct regions of ordered lamellae and distinct regions of disordered homopolymer [126]. Furthermore, Matsen and coworkers showed that the minority component can only accommodate a limited amount of homopolymer before macrophase separation occurs, but the majority block can swell indefinitely.

Peng and coworkers also investigated the effects of the addition of a PMMA homopolymer (h-PMMA) of low and high molecular weight and short, symmetric PS-PMMA block copolymers to higher molecular weight symmetric PS-PMMA systems when combined with solvent annealing. Thin films with 10 and 20 wt% short and long h-PMMA were annealed for 3.5-4.5 hours in acetone vapor at room temperature and compared to a pure thin film annealed for the same amount of time. Addition of both short and long h-PMMA results in an increase in the size and spacing of cylindrical microdomains as compared to the pure thin film. However, between 10 and 20 wt% the spacing remains the same while the diameter of the cylinders increases for short h-PMMA. Cylinder diameter and spacing increase when comparing 10 and 20 wt% long h-PMMA after solvent annealing in acetone. To identify the distribution of h-PMMA in the microdomains, the films were washed with acetic acid to remove the h-PMMA. The long h-PMMA chains were found to localize to the center of the PMMA cylinders throughout the thickness of the film. However, the addition of short h-PMMA results in PMMA

homopolymers that are evenly distributed throughout the PMMA block. These results are in agreement with the expectations expected based on bulk behavior. The addition of a short PS-PMMA block copolymer to the long PS-PMMA system results in a contraction of the cylinders with increasing weight percent of short PS-PMMA but an increase in the spacing. Both and theory and experiment suggest that short, symmetric block copolymers segregate to interfaces to act as compatiblizers. Because the cylindrical microdomain contracts in this case, it is assumed that the short PS-PMMA chains have localized to the interfaces [124].

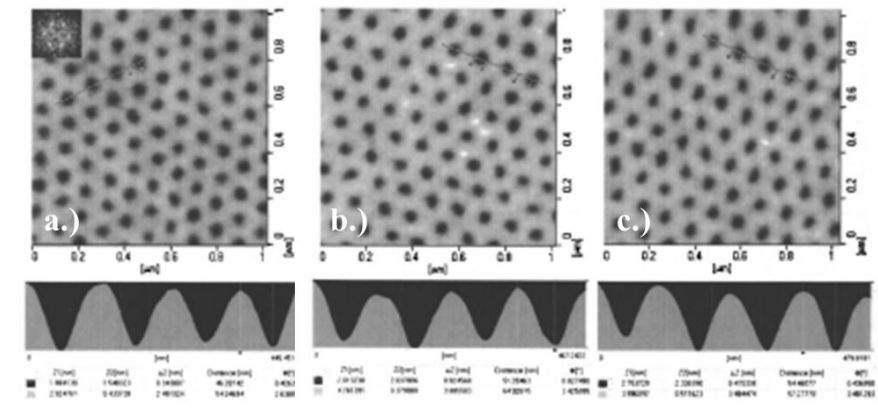

Figure 11. PS-PMMA (M_n: 263 kg/mol) with PMMA homopolymers (M_n: 15 kg/mol) where a.) is an AFM height image of a solvent annealed, pure block copolymer film (PMMA cylinders in a PS matrix), b.) contains 10 wt% PMMA, and c.) 20 wt% PMMA. The diameter and spacing of the PMMA cylinders was shown to increase with increasing PMMA homopolymers concentration (reproduced from [124]).

Additionally, the addition of homopolymers has been shown to stabilize non-equilibrium structures such as closed-packed spherical and double diamond morphologies [127] as well as promote defect-free diblock copolymer assembly on chemically nanopatterned

substrates [129]. Regardless of the application, homopolymers additions do result in changes in the morphology of a block copolymer, and the effects of the addition need to be well understood and characterized in order to properly accommodate for the effects. While block copolymer/homopolymers systems are not discussed in this dissertation, polymer-modification of nanoparticles has been shown to be an effective method for templating the particles in a block copolymer matrix as the polymer shields the nanoparticle from interaction with the block copolymer. Because the behavior of these systems is dominated by the polymer chains, the effects on the block copolymer structure would be expected to be similar to that of a homopolymer inclusion.

2.3.4 Nanoparticle Templating with Block Copolymers

Block copolymers have been widely investigated due to their self-assembly behavior and unique microphase structures for applications in templating organic [32, 131-133] and inorganic [134-139] nanoparticles. A variety of microphase morphologies can be achieved by controlling the compatibility between blocks, degree of polymerization, and volume fraction of each block [18, 140], and these structures can be used to precisely define the position and geometry of nanoparticle arrays. There are two major approaches to incorporating nanoparticles into a block copolymer matrix [141]: synthesis of the nanoparticle within a block copolymer domain [142-146] or selective incorporation into a domain [31, 32, 131, 134, 139, 147]. Selective incorporation can be achieved by modification of the nanoparticle [32, 131, 134, 139] or taking advantage of specific interactions between the nanoparticle and a domain [31, 138, 147].

Block copolymer/nanoparticle systems are particularly interesting because the microphase separation morphology can be used to direct the organization of nanoparticles within the block copolymer domains. However, using block copolymers as a template for nanoparticles is not simple as both systems simultaneously affect each other. Nanoparticles have been shown experimentally to affect both the orientation [134, 148] and morphology [149-152] of the block copolymer. This occurs because the nanoparticle acts as an obstacle to the polymer chains, forcing the chains to redirect their "path" to circumvent the nanoparticle which results in a non-ideal conformation of the polymer chain. Small nanoparticles are generally retained within a block while larger nanoparticles are forced out. Theory predicts that in an AB diblock copolymer system, large A-like nanoparticles localize to the center of A domains while smaller particles are likely to uniformly disperse [153]. This theory is supported by experimental evidence from homopolymer inclusions in block copolymer systems [124] and polymer-modified nanoparticle systems [139]. Experimentally, Kim et al investigated polystyrene-coated gold nanoparticles in a polystyrene-*b*-poly(2-vinylpyridine) (PS-P2VP) block copolymer matrix and showed the dependence of nanoparticle location within the solubilizing block on the nanoparticle size by varying the chain density on the nanoparticle (Figure 12). Smaller nanoparticles were found to locate to the interfaces, and as particle size/chain density increased, the nanoparticle transitioned from being at the interface to being evenly distributed throughout the block to locating to the center of the block at the chain ends for the largest particles investigated [139].

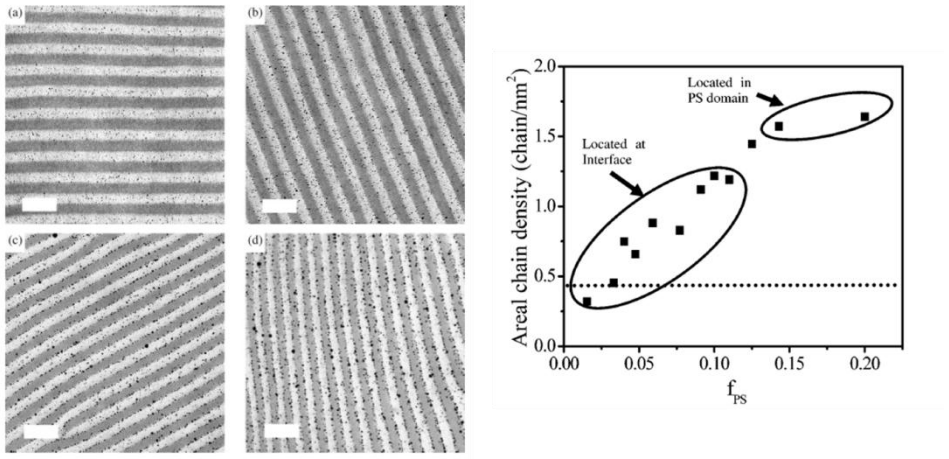

Figure 12. TEM imaging of PS-coated gold nanoparticles in a PS-P2VP block copolymer matrix with chain densities of a.) 1.64, b.) 1.45, c.) 1.22, and d.) 0.83 chains/nm^2 where higher chain densities correspond to larger nanoparticles and scale bars correspond to 100 nm. The plot on the right shows the effects of PS grafting density on the location within the diblock copolymer solubilizing block (reproduced from [139]).

The addition of nanoparticles, whether modified or not, may have additional effects on the block copolymer structure. The stretching of a polymer chain around a nanoparticle may also result in microphase morphology transitions as both theory and experiment have shown with increasing particle size. Using this knowledge, the size and chemistry of nanoparticle can be used to control the placement of a nanoparticle within a block copolymer [153]. Attaching polymer chains to the nanoparticle surface has been shown to be an effective way to compatibilize a nanoparticle for a specific block copolymer; however, addition of polymer arms to a nanoparticle can result in changes in the morphology, particularly at high loadings as noted above [93, 149]. Gold (Au) nanoparticles coated in short A-like polymer chains were shown to segregate into the center of the A-block of an AB block copolymer. The morphology remains unchanged as long as the volume fraction of PS-coated Au nanoparticles remains below a critical

concentration value. When the concentration of nanoparticle is larger than this value, a concentration gradient of nanoparticles forms through the film, and different microphase structures are observed as a function of position along the film thickness [149].

For materials such as fullerenes, where the interaction with polymers is limited and aggregation is problematic, polymer-modification is a particularly appealing method to dispersing the fullerenes in one block. Fullerenes have been incorporated into block copolymer systems with limited success [31, 147], but grafting of PS chains or even diblock copolymer chains themselves has been shown to be more effective in dispersing and aligning the fullerenes as discussed in the next section [93].

2.3.5 Block Copolymer-Fullerene Systems

Specifically related to the proposed research here, experiments have been conducted regarding fullerene nanoparticle inclusions in block copolymers [31, 93, 147]. Laiho et al investigated C_{60} fullerene inclusions in cylindrical forming poly(styrene-*b*-4-vinylpyridine) (PS-P4VP) and the effects of solution aging prior to spin coating on the morphology. The authors noted that the solution color shifted with time and attributed the shift in color to complex formation between the P4VP block and C_{60}. The visual color shift was supported by UV-visible spectroscopy measurements on solutions with aging. The effects of solution aging are also clearly seen in the morphology of block copolymer thin films. Films prepared from fresh solutions of C_{60} and PS-P4VP show a cylindrical microphase structure with P4VP cylinders in a PS matrix; the fullerenes in this case swell the PS block. However, upon aging of C_{60}/PS-P4VP solutions in xylene, a spherical morphology is noted, and the change in morphology is attributed to charge-transfer

complex formation between the C_{60} and the P4VP block (Figure 13). This morphological shift was unexpected as swelling of the P4VP block should induce a transition from cylindrical morphology to lamellar morphology. The authors attributed the shift from cylindrical morphology to spherical morphology to the effects of the complex formation [31].

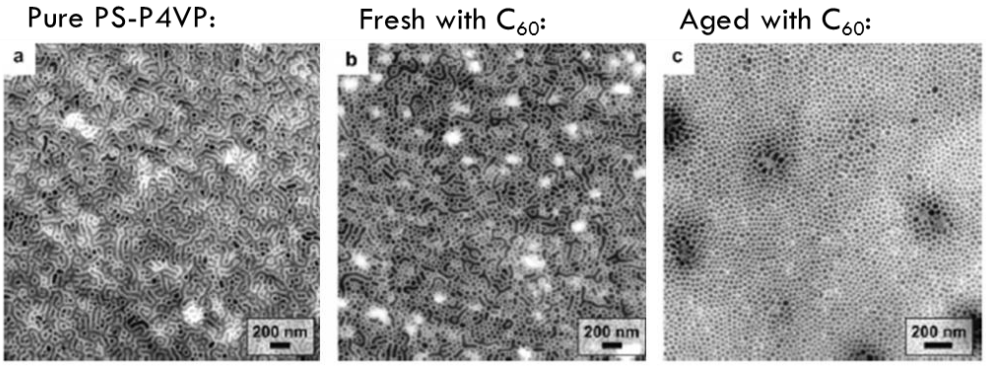

Figure 13. Thin films of a.) pure PS-P4VP, b.) PS-P4VP with C_{60} prepared from a fresh solution, and c.) PS-P4VP with C_{60} prepared from an aged solution by Laiho et al. Complex formation between C_{60} and the P4VP block was shown to induce a shift the microphase structure of the diblock copolymer (reproduced from [31]).

Fullerenes modified with PS arms have also been investigated with block copolymer systems. Mathis and coworkers synthesized fullerenes with 2, 4, and 6 PS arms and were able to achieve controlled nanoscale organization of the fullerenes using a symmetric poly(styrene-*b*-isoprene) (PS-PI) block copolymer. The addition of the PS-modified fullerenes to the block copolymer was shown to swell the lamellae with up to 40wt% of the fullerene material but not induce a phase transition (Figure 14). Interestingly, Mathis et al were also able to achieve nanoscale organization of fullerenes by directly attaching

lamellar forming PS-PI chains to the fullerene molecule. The block copolymers then self-organized into lamellae, trapping the fullerenes in the PS block [93] as shown in Figure 14. Because of the limited amount of research regarding fullerene/block copolymer systems, there is a need for continued study of the effects of fullerene addition on the phase behavior of block copolymer systems as discussed in this dissertation.

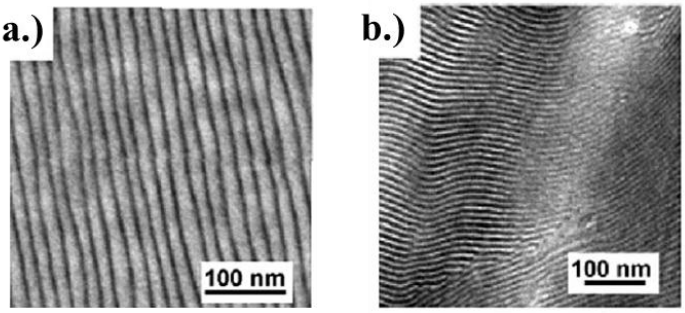

Figure 14. TEM images of thin films of a.) C_{60} modified with 6 polystyrene arms incorporated into a symmetric PS-PI diblock copolymer and b.) C_{60} modified with six symmetric PS-PI diblock copolymer chains (reproduced from [93]).

2.3.6 Techniques for Characterizing Alignment of Block Copolymer Systems

A variety of techniques are commonly used to characterize block copolymer thin films including atomic force microscopy, transmission electron microscopy, small angle and grazing incidence x-ray scattering, and x-ray and neutron reflectivity. The focus in this dissertation is primarily on the use of neutron reflectivity to characterize symmetric diblock copolymer thin films, both pure and with fullerene inclusions. Basic neutron

reflectivity approaches and techniques will be discussed here in terms of characterization of block copolymer thin films and basic analytical techniques.

Neutron reflectivity allows for a structural profile in the depth direction of thin, planar samples such as a block copolymer thin film. Layer thicknesses and surface and interfacial widths are extracted from the reflectivity measurements, and in terms of polymers, surface coverage, diffusion coefficients, and the Flory-Huggins χ-parameter can all be analyzed in addition to composition and structure data [154-156].

Neutrons behave in a wave-like manner similar to light and x-rays; therefore the reflectivity is dependent on the neutron wavelength, angle of incidence, and the chemical composition (nuclear structure) of the polymer thin film in the thickness direction. Neutron scattering lengths vary from atom to atom in terms of magnitude and sign and even among isotopes. The drastic difference in scattering length between hydrogen (^{1}H) and deuterium (^{2}H) is the best example of this, and through careful experimental setup, the contrast offered by the scattering length differences allows for extraction of detailed information from neutron reflection measurements[155, 156].

Neutron reflection (NR) is based on the elastic scattering of neutrons, where neutrons scatter without transferring energy to the material of interest. A basic NR experiments results in the measure of specular reflection as a function of the wave transfer vector Q in the thickness direction of the film. Neutron wavelength, λ, and Q are related as shown below where θ is defined as the angle of incidence [154-156]:

$$Q = \frac{4\pi}{\lambda}\sin\theta$$

Reflectivity measurements are conducted either by varying wavelength or Q depending on the neutron source where the neutron beam must be well collimated in either case. Synchrotron neutron sources use variable wavelength measurements where pulses are produced containing many different wavelengths; variable Q measurements are taken by varying the angle of incidence, θ, with a fixed wavelength source such as nuclear reactor. R(Q), or the Q-dependent reflectivity, is defined as the ratio of the intensity of the reflected beam to the incident beam [154-156]:

$$R(Q) = \frac{I_{ref}(Q)}{I_{inc}(Q)}$$

While reflectivity is well established as a measurement technique, data analysis is complicated by Fourier transforms. Analysis is typically conducted by a process of educated guess and check with proposed layered models used to calculate exact reflectivity profiles. The measured data and calculated reflectivity profiles are compared and parameters including scattering length density, roughness, and layer thickness are adjusted to improve the quality of fit as necessary. Because there are three parameters to adjust per layer, the data fitting process becomes quite tedious and time consuming [155, 156].

2.4 Langmuir and Langmuir-Blodgett Films

2.4.1 Langmuir and Langmuir-Blodgett Techniques

Langmuir monolayers first date back to Benjamin Franklin when he noticed that a drop of oil on a pond surface spread rapidly, smoothing out the pond surface on a particularly windy day. Nearly 100 years later, Lord Rayleigh proposed that the layer of oil that

spreads at the water surface is only one molecule thick, setting the stage for the study of thin films of single molecule thickness and their deposition on solid substrates. The first in-depth studies were conducted by Irwin Langmuir in the 1910s to 1920s on fatty acid, ester, and alcohol monolayers, and floating monolayers are referred to as *Langmuir films*. Transfer of monolayers and multilayers was not reported until several years later by Katherine Blodgett. The deposition and building up of mono- and multilayers is therefore known as the *Langmuir-Blodgett technique* [19].

A Langmuir film is defined as an insoluble monolayer with controllable packing floating at a liquid/gas interface. Typically materials are studied at the water/air interface for reasons described in detail below. Monolayer films form on the liquid surface as a result of self-assembly forces associated with intermolecular interactions. Because molecules typically used in this process have distinct hydrophilic ("water-loving") and hydrophobic ("water-hating") regions, they orient in a particular fashion at the interface due to their amphiphilic nature. Materials that can be used for Langmuir film formation include lipids, nanoparticles, polymers, and proteins as a few common examples [19, 157].

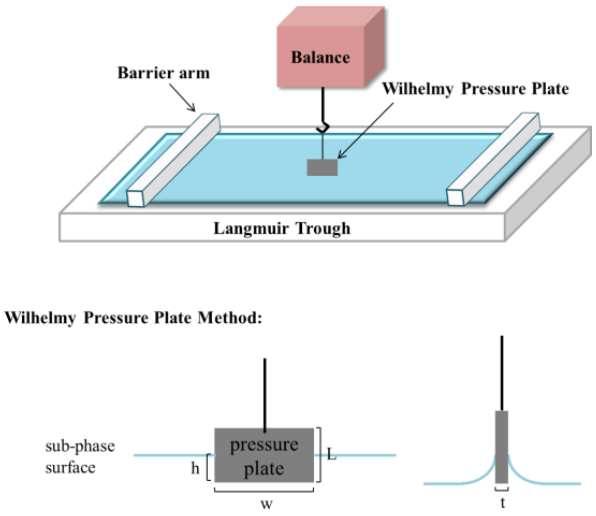

Figure 15. Langmuir trough schematic. Water is deposited on the trough (typically made of Teflon®) and barrier arms (hydrophilic material such as Delrin®) are moved to compress a monolayer on the sub-phase. Surface pressure is monitored during compression using a Wilhelmy pressure plate (typically made of platinum). The pressure plate determines the force due to surface tension on a suspended pressure plate partially immersed in the sub-phase. The force with and without the monolayer is used to determine the surface pressure.

As shown by the schematic in Figure 15, a Langmuir trough is made of a hydrophobic material such as Teflon® with a shallow well etched into the material. Water (or sub-phase of choice) is deposited in this well to form a meniscus at the air/water interface where monolayer material is then deposited. Barrier arms (either one or two), made of a hydrophilic material such as Delrin®, then compress inward towards the center of the trough, thereby compressing the monolayer material and reducing the overall surface area available to each molecule. During compression the surface pressure, Π, is monitored via the Wilhelmy plate method where a suspended, thin platinum plate is partially immersed in the water sub-phase, and the force due to surface tension is measured and converted to a surface pressure [19, 155, 157].

Langmuir monolayers can then be transferred to a solid substrate from the air/liquid interface via the Langmuir-Blodgett technique. Langmuir-Blodgett (LB) troughs have barrier arms for compression of Langmuir monolayers as well as a dipping well and dipper for deposition to substrates. First, the LB trough compresses the monolayer and measures the surface phenomena resulting from compression based largely on changes in surface pressure through a Langmuir isotherm. Isotherm measurements can typically provide information regarding the structure, area, interactions, phase transitions, compressibility, and hysteresis/recoverability of a Langmuir monolayer [19, 157].

After compression, the LB trough moves a solid substrate vertically through the liquid/gas interface, and the monolayer is transferred to the substrate (Figure 16). An alternative approach is to move the substrate horizontally to the interface through a technique known as Langmuir-Schaefer (LS) deposition which can be particularly useful for transfer of rigid monolayers (Figure 16). Multilayers can be built up by repeating the deposition process until the desired number of layers is achieved [19, 157].

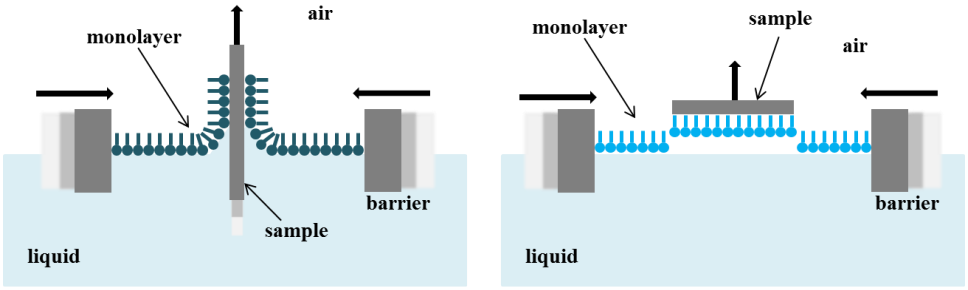

Figure 16. Schematics of the Langmuir-Blodgett (LB) and Langmuir-Schaefer (LS) monolayer deposition techniques. In both cases, a monolayer of an amphiphilic molecule (having hydrophilic and hydrophobic components) is compressed by moving barrier arms at the water/air interface. Films are transferred from the liquid surface to a solid substrate by either moving the sample vertically through (LB) or horizontally to (LS) the interface.

The unusually high surface tension, γ, of water (73 mN/m) allows for Langmuir monolayer formation at the water surface and is largely the reason why water is typically used as the liquid or sub-phase in these experiments. The high surface tension can be attributed to the strong intermolecular interactions between neighboring water molecules [19, 157, 158]; contaminants such as dirt and other debris will decrease the strength of intermolecular interactions and therefore the surface tension. For this reason, cleanliness is extremely important in Langmuir monolayer formation and LB deposition [157, 158].

Upon deposition on the water surface, the distance between molecules is large and interaction between molecules is minimal. For this reason, uncompressed monolayers at this stage are equated to 2D gas systems, and the monolayer at has little to no detectable influence on γ_{water}. As surface area available per molecule is decreased via compression of the monolayer, molecules have a repulsive interaction leading to a measureable surface pressure. Surface pressure, Π, is defined as the difference between the surface tension (γ)

in the absence of monolayer and the surface tension with monolayer deposited (γ_0). Based on this definition, the maximum possible Π for a monolayer on water is 73 mN/m but is typically much lower than this value [19] [157, 158].

The pressure-area (Π-A) isotherm, a plot of the surface pressure as a function of the area of water surface available to each molecule, is the single most important indicator of monolayer properties. The isotherm is measured while compressing a deposited film at a constant rate and monitoring Π. There are four distinct regions in a typical Π-A isotherm: gas/expanded phase, liquid-condensed phase, condensed-solid phase, and collapse region. Each of these regions (Figure 17) is associated with a distinct transition in the isotherm as well as a change in the molecular interaction and orientation [19, 157, 158].

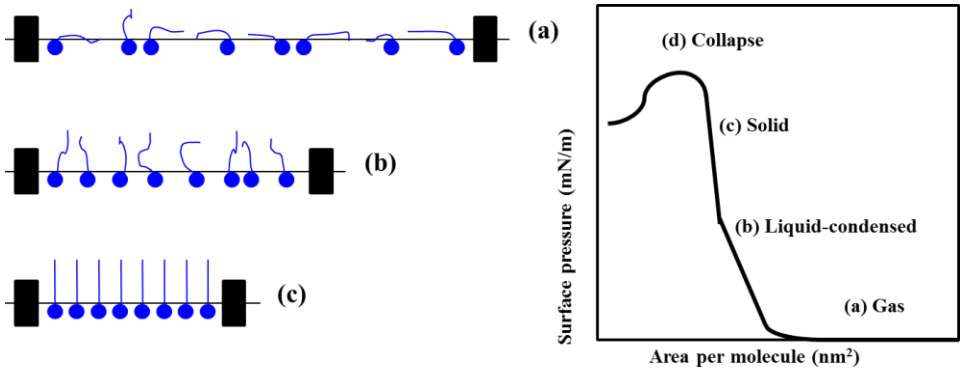

Figure 17. Ideal pressure-area isotherm with corresponding monolayer structure at different regions on the isotherm. Isotherms typically show a gas/expanded phase (a), liquid condensed phase (b), solid phase (c), and collapse point (d). Each region is ideally indicated by a sharp transition.

The gas phase as mentioned above is characterized by no discernable change in the surface pressure at deposition due to the lack of interaction between molecules on the

water sub-phase. The onset of the liquid-condensed phase is indicated by the onset of surface pressure associated with the lateral interaction of tails on the water surface followed by a linear increase in surface pressure. A sharp increase in slope indicates the onset of the solid-condensed phase where molecules are close packed and the monolayer behaves as a 2D solid. Upon extrapolation of this second linear portion of the isotherm to zero surface pressure, the x-intercept gives the area/molecule expected for a hypothetical uncompressed close-packed monolayer [19, 158]. The area/molecule is typically used to determine whether or not a successful monolayer has formed and what the structure of the monolayer on the water surface is likely to be. The final isotherm stage is associated with collapse of the monolayer and is indicated by a sharp drop in the surface pressure. At this stage it is likely that disordered multilayers form, and the collapse point is highly dependent on the film history as well as the compression rate [19] [157, 158].

Typical Langmuir monolayer materials include fatty acids [19, 159-161], aromatic compounds [162-168], heterocyclic compounds [169], dyes [170-173], and porphyrins [174-177]. An example of a classic monolayer material is stearic acid consisting of a carboxylic acid (–COOH), hydrophilic head and hydrophobic alkyl tail ($C_{17}H_{35}$–). When dissolved in a water immiscible solvent (chloroform) and deposited on a water sub-phase, the solution spreads to cover the area available, and a monolayer forms with the head-group in the water and the tail directed out [19, 157, 158].

More specifically, cyclic aromatic compounds such as benzene [162, 164] and anthracene [165-168] are of particular importance to the research in this dissertation due to the structural similarity to C_{60} fullerene. The aromatic rings are largely hydrophobic and require a hydrophilic chain attachment to spread on the water sub-phase and an alkyl

chain for stabilization of the monolayer. Pyrene derivatives and other polycyclic aromatics with greater than three rings require shorter alkyl chain lengths for stabilization as the number of rings increases [19, 163, 165].

Various techniques have been applied to incorporate non-amphiphilic materials into Langmuir monolayers including using mixed sub-phases and mixed monolayers [19, 33, 35, 38, 39, 41, 42, 45, 178-182]. In a mixed monolayer system where both materials are amphiphilic, the minor component is most likely to be evenly distributed in the major component. However, if one molecule is amphiphilic and the other is only hydrophilic or hydrophobic, the second material is relegated to either or the head or tail region depending on the respective chemistry. In the case where two molecules are present in equal quantities in a mixed system, the collapse point of the film can be used to determine the miscibility of the two materials. If the systems are immiscible, there will be two distinct collapse points, one associated with each material; if the materials are miscible, only a single collapse point will be evident at a surface pressure that is likely different from either component [19].

The transfer of a monolayer from the air/water interface to a solid substrate is known as Langmuir-Blodgett (LB) deposition. Typically LB monolayers are deposited at constant Π on films in the condensed solid phase of compression [19, 158]. Deposition of first a monolayer and then multilayers is described in Figure 18 assuming the substrate is hydrophilic (such as silicon/silicon oxide) [19, 157, 158].

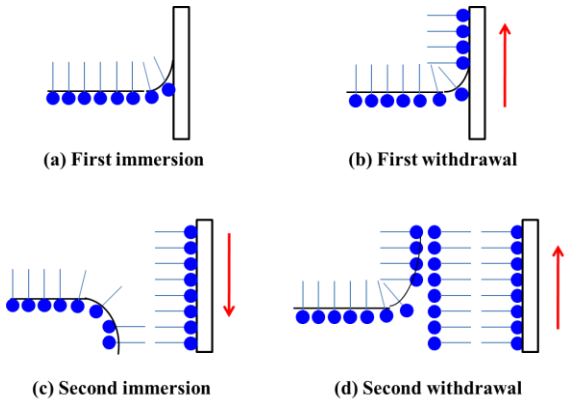

Figure 18. Langmuir-Blodgett deposition on a hydrophilic surface assuming a layer is deposited on each stroke. In the first immersion the water and monolayer creep up the substrate as shown in (a); upon the first withdrawal a monolayer is deposited on the substrate (b); subsequent motion of the substrate through the sub-phase results in additional layer deposition as depicted in (c) and (d).

This technique can be used to build up LB multilayers with repeated motion of a substrate through the sub-phase. There are three deposition types that determine the final structure of LB monolayer and multilayer films based on the monolayer material, substrate type/chemistry, sub-phase, and dipping surface pressure: Y-type, X-type, and Z-type (Figure 19). In Y-type systems, a layer is deposited on each stroke of the dipping arm or every time the substrate passes through the sub-phase. With X- and Z-type deposition a layer is only deposited on entering (down-stroke) or exiting (up stroke) the sub-phase respectively [19, 157, 158].

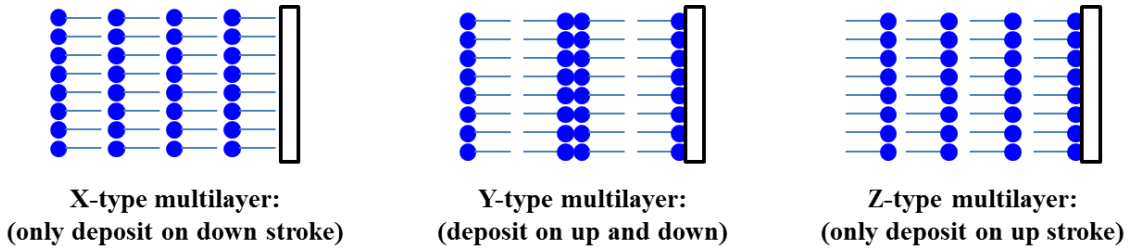

Figure 19. Types of Langmuir-Blodgett multilayer deposition: X-type deposition only occurs when the substrate is entering the sub-phase or on the down-stroke, Y-type deposition occurs on each stroke of the dipping arm (up and down), and Z-type deposition only occurs when the substrate is leaving the sub-phase on the up stroke.

It has been shown that complete drying and molecular adhesion to the substrate are both important before further treatment such as further deposition of monolayers to build up multilayer systems. Previous work on a hydrophilic substrate indicates that if a material has poor adhesion to the substrate the monolayer can simply detach from the substrate and redeposit/spread across the sub-phase on second immersion. Repeated dipping in this case leads to only a single monolayer being deposited. Monolayer detachment can also occur as a result of insufficient drying time for the first layer between depositions [19, 157].

The question as to whether or not structural reorganization can occur with multilayer dipping has been posed by a number of groups, and it has been shown that the deposition type does not always determine the final structure of a multilayer LB film. As an example, stearic acid multilayers are always Y-type regardless of whether or not an X- or Y-type deposition sequence is used; therefore, some reorganization of the multilayer clearly occurs [36, 183, 184].

The transfer ratio, defined as the ratio of the decrease in trough area to maintain Π to the substrate area, is used as an indicator of the quality of the deposition [19, 185]. A transfer ratio (TR) of one indicates good deposition with a molecular orientation on the substrate similar to the orientation at the air/water interface. There are cases where the TR is greater than one consistently; in this case, the molecules are changing orientation during transfer. Unrepeatable or inconsistent TR values are indicative of poor deposition [19, 157].

Langmuir isotherm and LB deposition studies have been widely conducted on fullerenes and fullerene derivatives as organized fullerene thin films have a wide variety of application with optical technology, glycoprotein biosensors, surface coatings [34], superconducting materials [43], and molecular electronics [40]. A review of studies conducted on fullerene-based materials [45] and the implications regarding the work in this dissertation will be discussed below.

2.4.2 Langmuir Blodgett Monolayers of Fullerenes

Previous results reported in the literature regarding LB films of unmodified C_{60} conflict regarding the successful formation of a fullerene monolayer on a pure water sub-phase [35, 37-39, 41, 42]. Obeng and coworkers have reported the formation of stable, reproducible fullerene monolayer thin films at the air/water interface [39]; however, this result has been both supported [37] and refuted [38, 42] by other groups. Langmuir isotherm studies conducted by Obeng and Bard indicated that C_{60}, an atypical material for such experiments, forms rigid monolayers that can support high surface pressures (Π) greater than 65 mN/m at low fullerene concentration on the water surface. They also

noted that bi- and multilayer formation occurs at higher fullerene concentrations and noted that these multilayers are stable at a sustained Π greater than 100 mN/m for longer than 8 hours [39]. Conversely, Williams et al determined that in all cases the area per molecule found from their measurement indicates that more than a single monolayer forms on the water surface [42]. The formation of C_{60} multilayers and not monolayers on a pure water sub-phase has been supported by other groups at high compression as well [35, 38], and is likely largely due to strong inter-fullerene interaction, the high degree of hydrophobicity of fullerenes, and their tendency to form 3D aggregate structures [33]. Transfer of pure fullerenes to solid substrates has been relatively unsuccessful due to the rigidity of fullerene mono- and multilayers [36].

However, groups have had limited success when using a sub-phase other than water such as the phenol aqueous solution used by Tomioka et al. In this case the C_{60} molecules were shown to form a homogeneous Langmuir film; it is likely this occurs because the phenol molecules promote spreading of solutions of fullerenes in aromatic solvents such as benzene. However, monolayers of fullerenes are still not formed in this case; x-ray reflection measurements indicate the film consists of approximately three molecular layers [41].

Extensive investigation has also been conducted regarding mixed systems of unmodified fullerenes and more typical monolayer molecules to determine if fullerene monolayer formation is repeatedly achievable in these systems [35, 38, 42]. Again, mixed results were seen with these techniques as far as monolayer formation. Molecules such as arachidic acid [39, 42], azacrown compounds [35], and calixarenes [178] have been investigated with fullerenes. Particular success was seen with the azacrown

compound/fullerene systems where the matrix molecule acts as a "basket" for the fullerene molecules and helps to stabilize the film [35]. While pure C_{60} monolayers have been shown to transfer poorly to substrates from pure water sub-phases [38, 42], mixed films have been shown to deposit quite successfully with high quality films up to 50 monolayers thick with arachidic acid/C_{60} systems [42].

Langmuir films of oxygen-modified "epoxy" fullerenes were also shown to form more stable films than pure fullerenes by multiple groups [33, 37]. Limited success was seen with transfer of epoxy-fullerenes to silicon substrates as the monolayer structure was highly dependent upon experimental conditions such as solvent evaporation time. Reproducibility was therefore an issue as transferred films were typically of a trapped, intermediate fullerene structure most likely dependent on the solvent evaporation conditions [33]. In general, Langmuir monolayer formation and LB deposition of pure C_{60} materials is difficult and highly dependent upon the experimental conditions, and therefore results have been highly variable regardless of incorporation technique.

The most successful approach for incorporating fullerenes into LB monolayers has been modification of the fullerene cage with hydrophilic ligands or "tails" [36, 44, 45, 47, 48, 50, 51, 54]. As noted previously, the fullerene cage readily accepts up to six electrons, allowing for the potential attachment of six ligands to the cage. These modifications to the fullerene cage allow for fullerenes that more closely resemble the typical amphiphilic nature of LB molecules. A balance between the hydrophilicity of the tails and the hydrophobic nature of the fullerene cage has been shown to be important in the repeatable formation of a monolayer [36, 44, 45, 47, 48, 50, 51, 54]. A second key factor has been the ability of the attached ligand (whether one attachment or more) to shield the

fullerenes from interaction with other fullerenes to reduce the risk of aggregation during deposition and monolayer formation [34, 36, 44, 53, 54].

Cardullo and coworkers claim the first reported success of reversible Langmuir monolayer formation at the air-water interface using C_{60}-glycodendron conjugates with either one or two attached glycodendron head-groups. Previous attempts at modification of the fullerene cage with hydrophilic ligands continued to indicate issues with 3D aggregation without induced surface pressure due to the strong fullerene-fullerene core interaction. Based on this, Cardullo et al proposed that controlling both the chemical nature and size of the hydrophilic head-group would allow for control over full monolayer formation. Results indicated that a balance in the bulkiness of the head-group is necessary where the ligand is large enough to prevent aggregation but small enough to still allow some fullerene-fullerene interaction as these same forces responsible for aggregation are also the driving forces for monolayer formation. It was determined that the carbohydrate dendrons in this case were polar enough to balance the hydrophobicity of the C_{60} core and bulky enough to prevent aggregation while still allowing for monolayer formation. Studies showed that the attachment of only one dendron still allowed for some inter-fullerene interaction prior to the application of surface pressure, indicating that the fullerene cage is not totally shielded; this interaction was determined to be ideal for monolayer formation [34].

Shielding of the fullerene core by dendritic addends has also been shown to allow for incorporation of fullerenes into well-ordered structures. Dendrimers with peripheral C_{60} subunits were shown to form stable Langmuir films at the air/water interface, and Brewster Angle Microscopy (BAM) was used to show the high quality of the film on the

water sub-phase. It should also be noted that these dendrimers were also shown to easily transfer onto solid substrates to give LB films [53].

Gao and coworkers had notable success with the synthesis and LB formation of three amphiphilic fullerenes. Two of the systems were mono-derived with a long alkyl chain terminated in either a carboxylic acid (–COOH) or amine ($–NH_2$) group. The third system they investigated had the $–NH_2$ terminated alkyl chain with 10 additional hydrophobic alkyl chains attached the C_{60} cage. All three structures are depicted in Figure 20 where a.) is the –COOH terminated system, b.) the amine $–NH_2$ terminated system, and c.) the "bushy" C_{60} structure with 10 alkyl ligands described above.

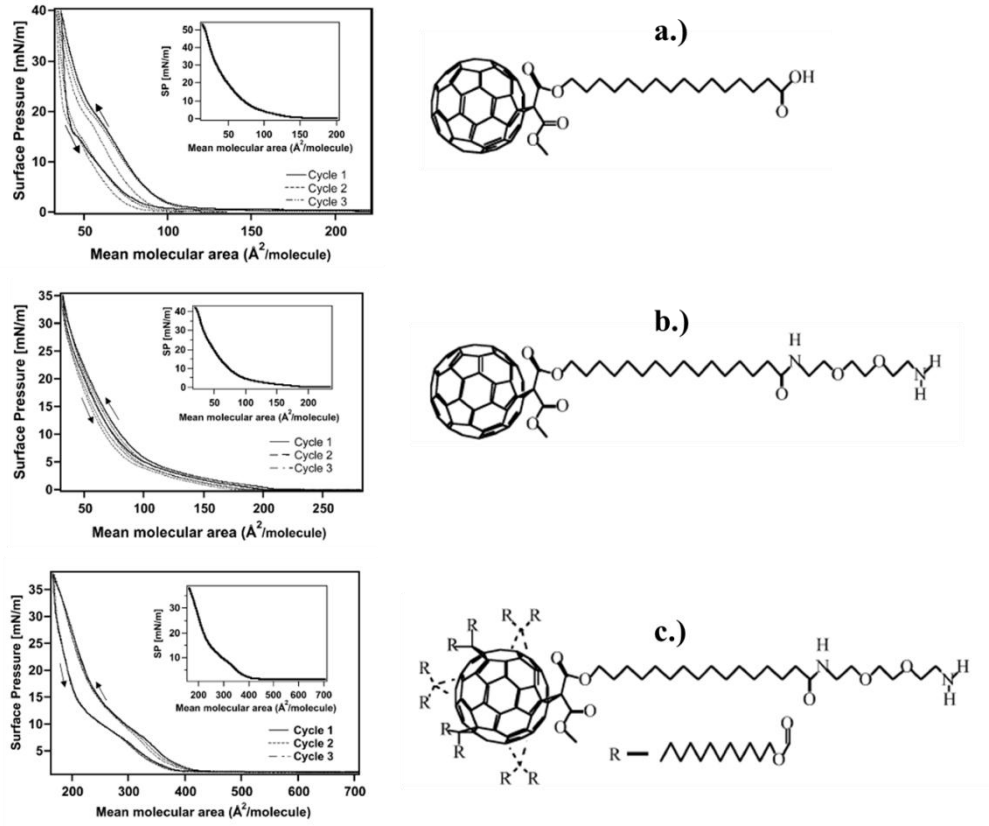

Figure 20. Compression/Expansion cycles for Langmuir isotherm studies of amphiphilic fullerenes by Gao and coworkers with single compression isotherms depicted in the inset for each corresponding structure (reproduced from [36]).

The overall outcome of these studies indicated that all three amphiphiles form a densely-packed monolayer at the air-water interface with successful transfer of both mono- and multilayer LB films to solid substrates. As far as more specific information derived from Langmuir pressure-area (Π-A) isotherm studies, the area per molecules were determined to be 98, 94, and 288 $Å^2$/molecule for –COOH terminated, $–NH_2$ terminated, and the alkyl chain-shielded C_{60} systems respectively as shown in Figure 20 [36]. The area/molecule theoretically expected for an unmodified C_{60} cage is 86.6 $Å^2$/molecule [36, 186], so the

values obtained from these studies are logical based on the structure of the amphiphilic fullerene molecules studied.

The –COOH terminated system showed a significant decrease in surface area, or a high degree of hysteresis, with subsequent compression/expansion cycles [Figure 20 a.)], indicating the gradual formation of irreversible aggregates. This suggests that the –COOH tail is not hydrophilic enough or shielding enough to limit and prevent C_{60}-C_{60} interactions. The amine terminated fullerene showed improved reversibility with only a slight decrease in the mean molecular area (MMA) after three consecutive compression/expansion cycles, indicating this monolayer is more stable and the fullerene is a better amphiphile than the –COOH terminated system [Figure 9 b.)]. The "bushy" alkyl coated fullerene with the amine tail showed interesting isotherm behavior with three distinct regions appearing [Figure 20 c.)]; these regions are indicative of increasingly close contact of alkyl chains on the C_{60} sphere and rearrangement of the molecule on the surface with increasing Π. Of the three systems studied by Gao et al, this system showed the best reversibility and stability, attributed to the bulky alkyl chain attachments on the C_{60} sphere preventing any inter-fullerene interaction [36].

Other cage modified systems include a C_{60}-azobenzene derivative synthesized by Oh-ishi et al. This system was prepared with a bulky, strongly hydrophilic, water-soluble tail consisting of an ammonium group with an azobenzene core. The azobenzene component also served as a functional group to probe the aggregation in the system as the UV-visible absorption maximum for azobenzene is highly dependent on aggregation states. Aggregation was still noted in these systems at higher concentrations of deposited material even with the strong hydrophilic group as the limiting area per molecule in the

isotherm was smaller than expected for a fullerene monolayer. However, monolayers were formed at low concentrations of deposited derivative with the hydrophilic tail dangling in the water and the C_{60} acting as a "float" to prevent the solubilization of the tail by the water sub-phase. Oh-ishi and coworkers further concluded that at lower concentrations, the hydrophilic tail actually acts to help maintain the monolayer by preventing collapse [54].

Maggini et al investigated the Langmuir film formation of compounds with a polar head group and long alkyl chains (hydrogenated and perfluorinated) that have previously been shown to form monolayers [50, 51]. The fulleropyrrolidines investigated are shown below in Figure 21, and Langmuir film thickness was investigated as a function of chain architecture, spreading solution concentration, and temperature. Results of isotherm studies indicate that monolayer formation in the case of systems (1)-(3) is highly dependent on the concentration of the spreading solution, similar to studies with unmodified C_{60}. At higher concentrations of fulleropyrrolidines (1), (2), and (3), the isotherm shifts to smaller area per molecule values than the theoretically expected value, indicating multilayers are forming in these cases. However, monolayer formation is indicated by the limiting area/molecule at the most dilute solution concentrations showing how important solution concentration can be in successful formation of fullerene monolayers [51].

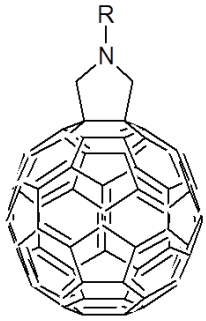

(1) R=$COCH_2$
(2) R=$CO(CH_2)_{16}CH_3$
(3) R=$CO(CH_2)_{20}CH_3$
(4) R=CH_3
(5) R=$CO(CF_2)_6CF_3$

Figure 21. Fulleropyrrolidines investigated by Maggini and coworkers for Langmuir monolayer formation. Monolayer formation for (1)-(3) was shown to be highly dependent on spreading solution concentration (similar to C60 behavior). In the absence of the carbonyl group, (4) was shown to only form multilayers regardless of solution concentration. Langmuir films of (5) were shown to be of monomolecular thickness at all solution concentrations as the rigid fluorinated chain prevents self-aggregation [50, 51].

Results from studies of amphiphilic fullerenes (1)-(3) (Figure 21) also support the conclusion that monolayer formation is dependent on the ability of the polar amide group to interact with the water sub-phase, particularly because aliphatic chain length has no apparent effect on the isotherm behavior. Self-association between molecules at higher solution concentrations can occur, or some molecules may be pushed off the water sub-phase surface. Further indication of the importance of the amide group as the hydrophilic functionality in monolayer formation and structure is provided by isotherm studies of (4). Regardless of concentration and temperature, no monolayer formation was observed by Maggini and coworkers for fullerene (4). In fact, the isotherm was similar to those seen with pure C_{60} where formation of 4-5 layers of molecules readily occurred [51].

Fulleropyrrolidine (5), with a highly rigid fluorinated chain, showed markedly different isotherm behavior than systems (1)-(4); two distinct regions separated by a plateau (less

evident at higher solution concentrations) were observed in the isotherm. Below the plateau, the area per molecule (280 $Å^2$/molecule) was found to be consistent with the total surface area occupied by a fullerene with the rigid chain. Above the plateau (at lower area/molecule), the limiting area per molecule was determined as 90 $Å^2$/molecule and was shown to be independent of the concentration of spreading solution as the isotherms nearly overlap in this region. Results indicate the formation of a monomolecular film of close-packed molecules at all solution concentrations. The difference behavior from (1)-(4) and (5) was attributed to the fluorinated chain preventing self-aggregation of the fulleropyrrolidine molecules [51]. The behavior of the fluorinated chain fulleropyrrolidine is particularly applicable to the Langmuir and Langmuir-Blodgett studies discussed in this dissertation because one of the fullerene dimer systems investigated contains a fluorinated carbon tail.

The addition of a hydrophilic linear chain to the hydrophobic C_{60} core by the addition of a short poly(ethylene glycol) (PEG) chain and the self-assembly behavior at the air/water interface was investigated by Hawker et al. PEG-modified fullerenes were shown to form Langmuir monolayers on a water sub-phase where the PEG group mediates the interaction with the water. The area per molecule determined from the Langmuir isotherm of this system was found to be 103 $Å^2$/molecule which is in good agreement with the theoretically predicted value for a close-packed monolayer of pure C_{60}. However, reversibility in the compression/expansion cycling behavior was not reported in this paper; therefore, it is unclear if the PEG attachment also prevents aggregation of the fullerene cores [48].

Amphiphilic fullerene-cholesterol derivatives have also been shown to successfully form Langmuir and Langmuir-Blodgett films. Bis-adducts (2 attachments to the fullerene cage) were prepared by Felder and coworkers with either two or four cholesterol derivatives on the cage attachments and compared to a bis-adduct system without a polar head group to determine the spreading behavior at the air/water interface. The bis-adduct without a polar head group was shown to form 3D aggregates, but the addition of the polar head group forces an attractive interaction with the sub-phase. As a result, a 2D homogeneous monolayer arrangement forms at the air/water interface for the fullerene-cholesterol derivatives with polar head groups. However, reversible Langmuir cycling was only shown to occur with the four cholesterol unit system, indicating that increasing the encapsulation of the C_{60} core is ideal for limiting the fullerene-fullerene interactions and aggregation [44].

Micellar structures have also been reported with mono- and bis-adducts of fullerenes. The molecular design was such that each adduct (whether one or two was attached the cage) contained four alkyl chains with terminal carboxylic acid groups on a C_{60} core to allow for control over the position of the fullerene cage relative to the water surface. In the case of all three systems, isotherm measurements indicate non-solid behavior, but the films were shown to be quite rigid; it was suggested that the rigidity could be attributed to either irreversible aggregation of fullerene cores or potentially the formation of spherical micelle structures at the air/water interface. Monolayers of the mono-adduct system studied by Gallani et al showed irreversible aggregation as the ligand still allowed for close contact of the fullerene cores. However, the bis-adduct systems were both shown to form spherical micellar structures at the air/water interface with a C_{60} core surrounded by

tails. Hydrogen bonding between the tails was determined to be the cause of the irreversibility of the isotherms in compression/expansion cycles [46].

Deposition of monolayers and multilayers to solid substrates was also shown to be significantly more successful with amphiphilic fullerene molecules. Tkachenko et al successfully transferred monolayers of porphyrin-fullerene dyads to a solid support and determined the deposition to be Y-type with transfer ratios (TR) between 0.9 and 1.05 [40]. Monolayers of C_{60}-azobenzene derivatives were also prepared successfully on Mica by Oh-ishi et al with uniform coverage indicate over 20 μm^2 [54]. Monolayers of a carboxylic acid fullerene were shown to have Z-type deposition on mica with the –COOH groups located at the substrate interface. AFM images of these LB monolayers indicated higher quality deposition as compared to pure C_{60} fullerene systems [52].

Multilayer transfers of the molecules studied by Gao and coworkers (discussed extensively above) were particularly interesting. In this case, the substrates were treated with octadecyltrichlorosilane (OTS) to give a freshly hydrophobic, and C_{60} attractive, surface for deposition. The –COOH and $–NH_2$ terminated alkyl chain systems described above showed transfer ratios (TR) of ~0.95 on the up-stroke and nearly 0 on the down-stroke, indicating Z-type deposition. Fullerenes were not transferred on the down-stroke in these systems (as indicated by TR of 0) because the C_{60}-C_{60} interaction was not strong enough to facilitate transfer [36]. Cardullo et al also noted no deposition on down cycles C_{60} modified with either one or two carbohydrate dendron head-groups; the authors attributed the lack a deposition to the inter-fullerene interaction being too weak to promote the attachment of second layer via head-to-head deposition [34].

Further study of amphiphilic fullerene multilayers from the –COOH and –NH2 terminated alkyl ligands systems in Figure 20 using XR and NR indicated Y-type deposition based on modeling, suggesting reorganized of the molecules occurs after deposition to give a head-to-head structure. The "bushy" fullerenes studied in this case showed Y-type deposition with the TR~1 on both up and down dipping due to the interaction of alkyl chains on the fullerene cage [36].

The fullerene-cholesterol derivatives studied by Felder et al were also successfully transferred as monolayer and multilayer LB films to hydrophilic quartz substrates. Bis-adduct fullerenes with two and four cholesterol derivatives showed Y-type multilayer transfers with transfer ratios of 1 ± 0.1, and good layer stacking was also indicated by UV-vis spectroscopy as a function of the number of layers transferred [44].

Kawai and coworkers took a particularly interesting approach to achieving LB films of fullerenes by taking advantage of the thermally reversible Diels-Alder reaction between C_{60} and an anthracene derivative. Fullerenes were functionalized with a hydrophilic side chain modified (–COOH) anthracene, and the anthracene was used to organize the C_{60} monolayer at the air/water interface. The authors hypothesized that the C_{60}-anthracene bond could then be reversed by heating and the anthracene derivative removed by careful solvent selection leaving relatively pure C_{60} multilayer films. Langmuir isotherm studies showed successful monolayer formation that is dependent on pH due to the carboxylic acid groups on the anthracene derivative. Monolayers and multilayers were successfully deposited on both hydrophilic and hydrophobic substrates. Multilayer films were heated to 70°C in a water/ethanol mixture and further study after heating indicates that the bonds between the fullerene cage and anthracene derivative are broken. Because the anthracene

derivative is soluble in the water/ethanol mixture at the elevated temperature, the majority of the unattached anthracene is removed, leaving a mostly pure C_{60} multilayer. The multilayers were not totally pure as not all the anthracene/fullerene bonds are reversed and not all the unbound anthracene derivative is removed by the water/ethanol mixture [36].

A key factor in LB multilayer deposition is allowing sufficient drying time between deposition cycles as molecules can be removed during subsequent layer additions; drying can be promoted via techniques such as drying in an N_2 gas stream. [19, 43]. During multilayer deposition, fullerene molecules have been shown to detach in varying degrees either due to weak interactions with the substrate or highly polar ligand groups as in the case of the fullerene-glycodendron conjugates studied by Cardullo et al [34]. Additionally, chemical modification of the substrate surface can promote fullerene adhesion through either covalent or non-covalent forces such as the hydrophobic octadecyltrichlorosilane substrates used by Gao and coworkers [36].

Fullerene monolayer and multilayer deposition using the LB technique, while challenging, has been shown to result in uniform monolayers with controllable molecular orientation when the C_{60} cage is modified to be more amphiphilic in nature. In particular, it is important to use hydrophilic ligands to balance the hydrophobic fullerene cage that also limit the ability of fullerenes to interact with each other through aggregation. While the fullerene dimers studied in this dissertation behave differently than fullerene monomer-based systems due to structural differences, the results of these experiments indicate that monolayers of fullerene dimers are possible when the dimer structure is properly functionalized.

2.5 Self-Assembled Monolayers and Surface-Directed Assembly

2.5.1 Introduction to Self-Assembled Monolayers

Self-assembled monolayers (SAMs) have a variety of potential applications as use as thin films or patterned templates. Thin film SAMs allow for control over surface properties such as wettability and adhesion and have found use in sensors/biosensors, nanoelectromechanical systems (NEMS), and microelectromechanical systems (MEMS). SAMs have also been used to functionalize nanostructures allowing for the further selective attachment of the structure to other molecules or SAMs. Patterened SAMs have also been used for depositing nanostructures based on differences in pattern area attractiveness to a specific molecule [187-189].

SAMs are composed of amphiphilic molecules where one end has a specific affinity for the substrate ("head group"), and the "tail group" has a terminal end with a specific functionality as well (Figure 22). SAMs are formed by chemisorption of the head group to a substrate, followed by the slow organization of the tail groups. When molecules first begin to adsorb to the surface, the organization is highly disordered; however, over time the hydrophilic head groups begin to group together at the substrate while the hydrophobic tails assemble themselves to maximize distance from the surface. Regions of close-packed molecules nucleate and grow until a monolayer is achieved. SAMs form due to adsorption of molecules to the substrate lowers the surface energy and are more stable than other monolayer types such a LB films because they are chemisorbed rather than physisorbed. Monolayer close-packing occurs due to the van der Waals interactions which further decreases the free energy of the monolayer [187-189].

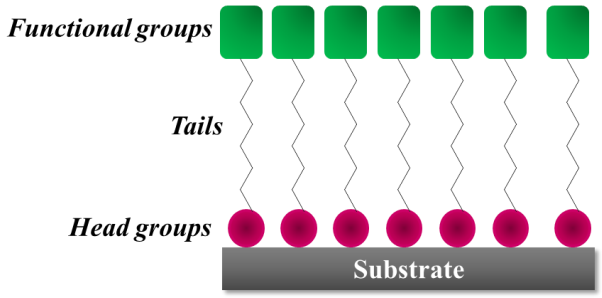

Figure 22. Schematic of a typical SAM arrangement where hydrophilic head groups chemisorb to a substrate surface and are separated by hydrophobic tails from a terminal functional group such a –COOH or –NH3.

SAM-forming molecules are typically composed of a head group, an alkyl chain, and an end functionality such –OH, $–NH_2$, or –COOH and are can formed on either planar (silicon and metals) or curved (nanoparticles) substrates. Alkanethiols are by far the most common SAM molecules investigated due to their strong interactions with noble metal substrates and semi-covalent attachment to gold surfaces. Alkanethiols are composed of a functional end group, alkyl chain, and S-H head group as shown in Figure 23. Silanes are also popular SAM materials and are deposited on nonmetallic oxide surfaces by covalent bond formation between the silane and the oxide layer on the substrate (see Figure 24 for examples) [187-189]. Silanes are particularly interesting SAMs for deposition of fullerenes as will be discussed in more detail below [20, 45, 55, 190-194].

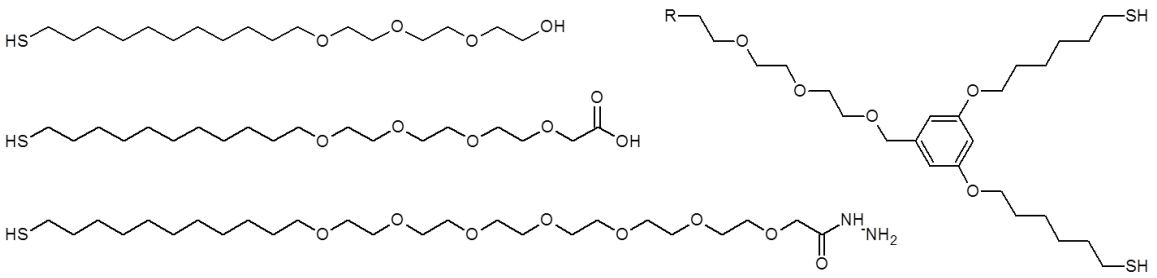

Figure 23. Representative selection of different alkanethiols used to for self-assembled monolayers as described in text. Note the various terminal functional groups.

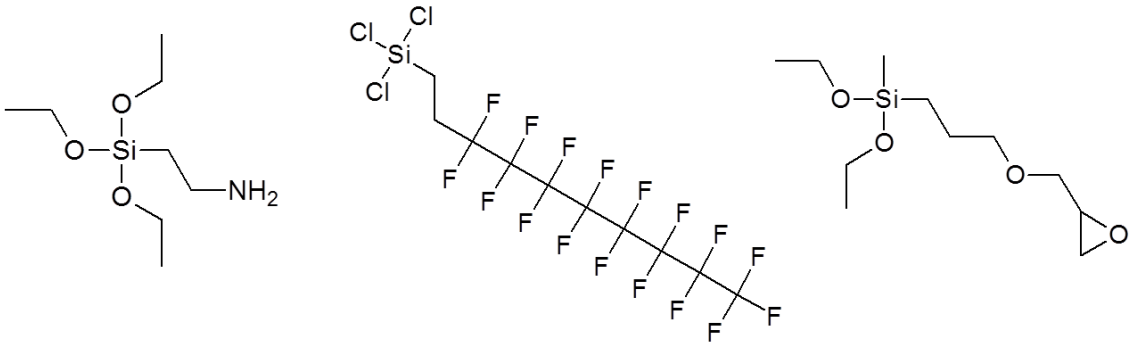

Figure 24. Silanes used in the deposition of SAMs on nonmetallic oxide surfaces (such as silicon oxide) indicating the wide range of available end group chemistry.

Preparation of SAMs can be achieved using several different methods including physical vapor deposition, electrodeposition, adsorption from solution, and adsorption from a vapor phase as examples. SAM formation kinetics in solution adsorption specifically are dependent on a number of factors such as temperature, concentration of solution, purity of adsorbate and cleanliness of substrate. Monolayer uniformity is improved by doing depositions at room temperature as the number of defects is reduced; the cleanliness of the substrate can also greatly affect defects in the SAM as any impurity will cause a

disruption in the coverage of molecules on the surface. The final SAM structure is also dependent on the chain length, adsorbate structure, and substrate structure. Specifically, the chain length largely contributes to the overall thickness and stability while adsorbate and substrate structure influence the packing properties of the monolayer [187-189].

As mentioned, self-assembled monolayers can also be patterned to arrange the SAM in a specific geometry on the substrate for various applications. There are three different approaches typically used for patterning SAMs: locally attract molecules, locally remove molecules, and modify terminal functionality. By locally attracting molecules to specific regions of the substrate, patterning is done at deposition, and the SAM is only deposited where structure is desired on the substrate. There are two general approaches to local deposition of SAMs including micro-contact printing using a pre-patterned elastomer stamp and dip-pen nanolithography using an AFM tip to transfer molecules to the substrate at a specific location. The local removal approach has the same end result as the local attract method, but patterning is done by covering an entire surface with SAM and selectively removing molecules from areas to form the pattern. This approach is typically achieved using AFM or STM tips to remove molecules or ultraviolet irradiation. The third method for patterning SAMs is to selectively modify the end functionality to make it inert or reactive to specific materials or to have different properties than the original SAM. SAMs can serve as a template for other molecules by specifically protecting/unprotecting certain regions of the SAM through the end functionality, allowing for specific attractions of molecules to a controlled region of the substrate [55, 187-189].

2.5.2 Characterization of SAMs and Functionalized Substrates

Self-assembled monolayers and functionalized substrates can be characterized using several techniques, most commonly involving wettability/contact angle measurements, infrared (IR) spectroscopy, ellipsometry, and scanning probe measurements such as AFM and STM [20, 187-189]. There are several methods for characterizing the deposition and formation of SAMs; typically, scanning probe microscopy techniques are particularly useful these applications. Scanning Tunneling Microscopy (STM) has been particularly useful for investigating the mechanisms of SAM formation and specific structural features of self-assembled monolayers. However, STM requires that the SAM be either conducting or semi-conducting and with samples where this is not the case, atomic force microscopy (AFM) can also be used to characterize the sample. AFM can provide useful information about specific SAM surface properties including the chemical nature, magnetic properties, and frictional force properties as examples [187-189].

Combining the results of these techniques yields a more complete picture of the substrate functionalization including the polarity of the outer surface, average molecular orientation, film thickness, and information regarding the packing of the adsorbates on the solid substrate respectively. Further inferences can then be made regarding the internal structure of the film and chemistry of a modified surface as well as simply determining if the surface has been successfully functionalized [188, 189].

2.5.3 Surface-directed Organization of Fullerenes

Fullerene-based monolayers have been an area of intense research for use in sensors, photovoltaics, and other nanostructured devices for advanced electronics applications.

C_{60} fullerenes have been shown to be strongly and reversibly electron accepting up to six electrons, but overcoming the aggregation tendencies and relative insolubility in common organic solvents has proved to be challenging to monolayer deposition of fullerenes through non-sublimation techniques. One approach to overcoming these issues takes advantage of the electron accepting capability by covalently modifying the fullerene cage with ligands, allowing for improved solubility and decreased aggregation tendency while retaining the majority of the fullerene properties. However, even with modification of the cage, strong van der Waals interactions continue to make aggregation a major obstacle to forming stable, ordered films at the air/solid and air/water interfaces. For this reason, the question still remains as to how to assemble C_{60} into well-defined 2-dimensional (2D) and 3-dimensional (3D) networks [20, 45]. Potential approaches include Langmuir and Langmuir-Blodgett films as discussed previously in addition to using self-assembled monolayers on solid surfaces [20, 194-197]. As mentioned briefly above for LB films of amphiphilic fullerenes by Gao and coworkers [36], substrates can be tuned to provide better interactions with fullerenes via silane chemistry, self-assembled monolayers (SAMs), and surface-directed assembly [20, 45, 55, 194].

Fullerene self-assembly into monolayers on solid substrates can be achieved through two broad, basic approaches including modifying the fullerene cage or modification of the solid substrate. There are several techniques using these approaches to achieve fullerene self-assembly on surfaces: (1) modifying the fullerene in solution with functional groups that allow for self-assembly on an unmodified solid substrate by chemisorption or physisorption (such as LB films); (2) chemically modifying substrates to have a terminal functionality that covalently binds unmodified C_{60} in solution such as using SAMs to

tether C_{60} to a solid substrate; (3) immobilizing functionalized fullerenes through covalent or non-covalent interactions with an organic layer deposited on substrate; (4) or attaching pure fullerenes to a solid substrates through non-covalent interactions with an organically-modified substrate [20, 55, 196]. There are advantages and disadvantages to each technique that will be discussed further below.

It is worth briefly noting that thermal evaporation and solution casting techniques have been used to form monomolecular pure C_{60} films on unmodified substrates. Ultrahigh vacuum (UHV) deposition and spin casting methods have been investigated on Au, Ag, GaAs, Si, Cu, Mica, KBr, and MoS_2 substrates with C_{60}, and the morphology and quality of film growth in these instances is dominated by the strength of interaction between C_{60} and a given substrate [20, 198-200]. Substrates with strong interaction with fullerenes such as Au and Ag result in chemisorption of C_{60} where the fullerenes have limited mobility and form well-defined polycrystalline monolayers. For substrates with weaker interactions with C_{60}, intermolecular interactions between fullerenes dominate and limit the C_{60}-substrate interaction. This results in the higher mobility of fullerene molecules, and crystalline film growth is dominated by large aggregates [20]. While monolayer films of fullerenes can be achieved in this way, the techniques introduced above for C_{60}-based SAM preparation are preferred for our applications as they are tunable to any substrate; limit the potential for aggregation; result in stable, reproducible monolayers through a straightforward procedure; and can be done at room temperature without requiring sublimation of fullerenes.

Various covalent attachments can be made to the fullerene cage as discussed extensively with Langmuir and LB films of amphiphilic fullerenes. Similarly, as introduced as the

first technique for C_{60}-based SAM preparation, functionalization of the C_{60} cage with appropriate groups for chemisorption of fullerenes to a solid substrate allows for the preparation of stable and homogeneous fullerene SAMs. These materials and their incorporation into monolayer films have been studied extensively over a wide-range of fullerene functionalization chemistry for covalent attachment to many different solid substrates [20]. For example, Mirkin and coworkers investigated the formation of monolayers of the fulleropyrrolidine-derived thiol in Figure 25 a.) on Au(111)/Mica substrates and determined that C_{60}-C_{60} cage interactions govern the packing of the monolayer; however, the monolayer is not formed due to aggregation or crystalline structure formation in the fullerenes [201]. Additional studies involving thiol-derivatized fullerenes have been conducted on Au(111) by Diederich and coworkers [202] as well as Fox et al [203], and these structures are also shown in Figure 25 b.) and c.) respectively. In the case of all three of these materials the terminal thiol group is responsible for the reaction with the gold substrate surface. The functional chemistry also clearly influences the packing density in addition to the fullerene-fullerene interactions as shown by Fox et al where the alkoxy-pendants on the phenyl ring close to the fullerene cage in the functional group lead to a low packing density of the molecules [20, 203].

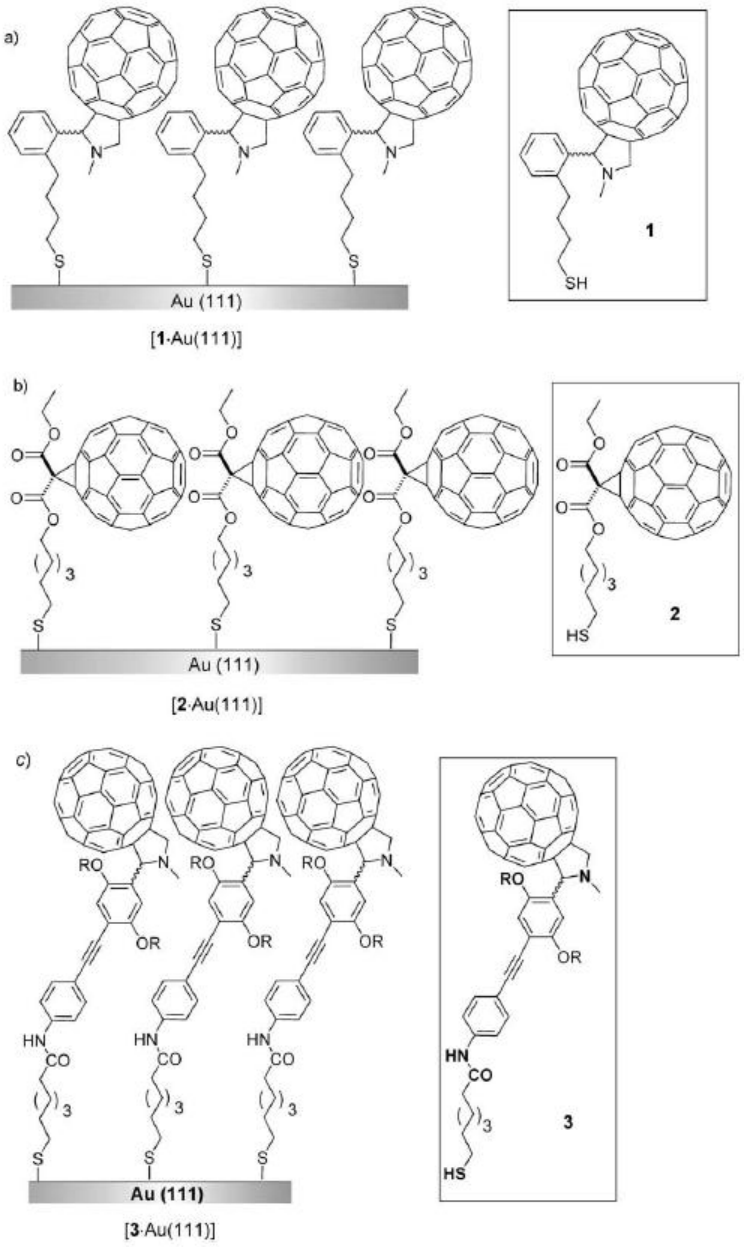

Figure 25. Examples of functionalized fullerenes for grafting to substrates. In this case the fullerenes are modified with ligands specifically designed to covalently attach to a given substrate (Au(111) in all cases shown here) (reproduced from [201-203]).

The reactivity of the fullerene cage makes the second technique of chemically modifying substrates to have terminal functionality that interacts with C_{60} particularly interesting,

especially when considering the reactions of primary and secondary amines with the carbon-carbon double bonds (C=C) in C_{60} that fuse the six-membered rings [196] [45, 55, 194]. A wide-range of other reaction chemistries are possible [20, 190, 191, 195], but amine reactions are most interesting and applicable to the research in this dissertation. Monolayers of pristine fullerenes on SAM modified substrates have been achieved through interactions with OsO_4 [195], terminal amino groups [45, 55, 194], and terminal azido functionalities [190, 191].

Several groups have investigated covalently tethering fullerenes to a substrate surface via SAM patterning [20, 45, 55, 190, 191, 194-196]. For example, Chupa et al bound C_{60} to a silicon oxide surface by taking advantage of SAM end-functionalization chemistry and the complex formation between OsO_4 and pyridyl groups and covalent bond formation between OsO_4 and C_{60} (Figure 26). The tethering of C_{60} involves three major steps: attachment of a pyridyl-terminated alkylsiloxane monolayer to a silicon oxide surface; reaction of the SAM with OsO_4 to form a coordination complex; and finally treatment with C_{60} fullerenes [195].

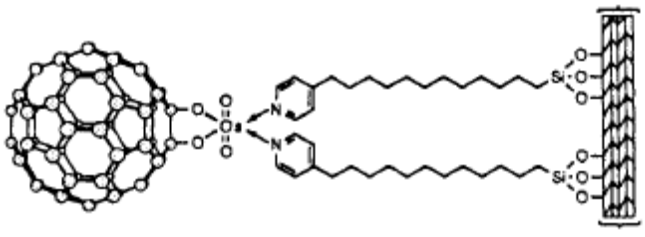

Figure 26. Covalently tethered fullerenes to silicon oxide surface via covalent bond formation between C_{60} and OsO_4 (reproduced from [195]).

As briefly discussed, C_{60} reacts quite readily with primary and secondary amines [20, 45, 55, 196], making amine terminated SAMs particularly useful for covalently attaching C_{60} to a substrate. Chen and coworkers showed the successful assembly of fullerenes onto $(MeO)_3Si(CH_2)_3NH_2$-modified oxide surfaces [196]. The attachment of the C_{60} cage to the amino-silane SAM, where the preparation of amino-silane SAMs has been well documented [192, 193], would then allow for the build-up of multilayers by further modifying the covalently bound fullerene cages with amines [196].

The third technique combines modification of the cage with surface functionalization to either covalently or non-covalently immobilize the fullerenes on a solid substrate [197, 204, 205]. Cecchet et al showed that monolayers of water-soluble C_{60} mono- and bis-adducts with hydrophilic chains linked to the cage by a pyrollidine ring can be attached to carboxylic acid, –COOH, terminated thiol SAMs on gold. XPS measurements indicated the formation of a covalent bond between the SAM and modified C_{60} via amide bond formation (Figure 27). However, the reaction between $–NH_2$ terminated fullerene adducts and the –COOH terminated thiol SAM requires an activator for the reaction to proceed [197]. Other reactions such as the reaction between aldehydes and terminal $–NH_2$ groups proceed in solution without additional activators or catalysts [55]. Therefore, a fullerene with this aldehyde chemistry could readily attach to an amine-terminated substrate in solution as will be discussed further through the experiments and results reported in this dissertation.

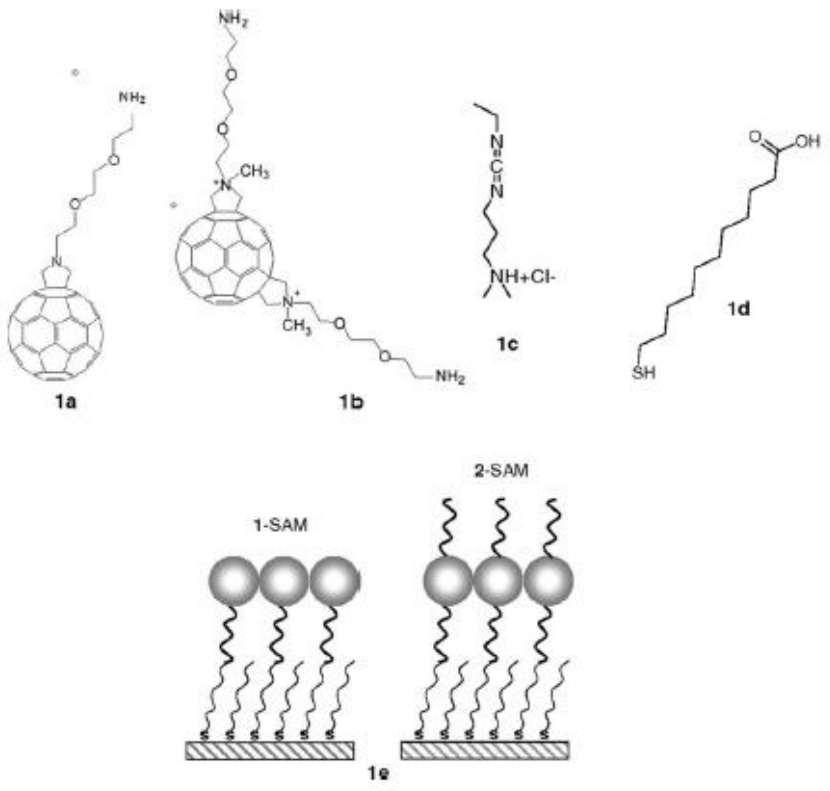

Figure 27. Schematics of the fullerene systems (1a and 1b) investigated by Cecchet et al for monolayer formation on an acid terminated self-assembled monolayer of 1d. The molecule shown as 1c is the activator for the reaction between the fullerenes and the –COOH groups on the monolayer. 1e shows a pictorial representation of monolayers of 1a and 1b covalently attached to the SAM (reproduced from [197]).

The fourth and final approach to depositing fullerene monolayers is through the non-covalent interaction of pristine fullerenes with the terminal end group of a self-assembled monolayer [20, 28, 206-212]. Examples include studies by Shinkai et al where C_{60}-calix[3]arene complexes were deposited on Au(111) surfaces with an anionic coating as shown in Figure 28 [206, 207]. Beton and Champness also used this approach by depositing fullerenes onto a 2D, pre-patterned honeycomb network monolayer with empty spaces where the fullerene cages cluster [208, 209]. It should be noted that this approach does result in the partial destruction of the π-delocalization on the fullerene

cage [20] which may negatively impact fullerene properties required for certain applications.

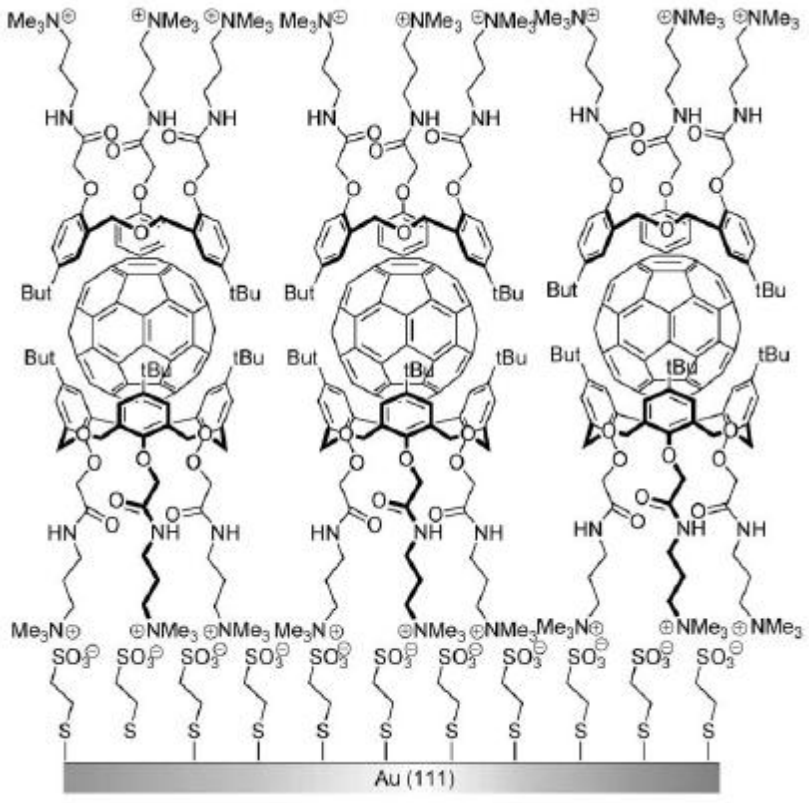

Figure 28. C_{60}-containing thin films using the assembly of C60-calix[3]arene complexes (1:2) on a charged gold surface (reproduced from [206, 207]).

Using SAMs as templates for alignment of fullerenes is largely successful due to the simplicity of the procedure, ease of reproducibility, and wide-range of surfaces available through modification of terminal group chemistry. The two approaches discussed here include taking advantage of the interaction between SAM terminal chemistry and functional groups on the fullerene cage and using the reaction between fullerene cages

with terminal amino groups. These end groups allow for grafting and can serve as the starting point for building complex molecular structures for applications such as molecular electronic devices [197]. This dissertation will address attachment of a C_{60} mono-adduct with an aldehyde terminal group and various fullerene dimer systems to functionalized surfaces as well as their endohedral counterparts.

CHAPTER III: UNDERSTANDING POLYMER-FULLERENE INTERACTIONS

3.1 Overview

In order to use a block copolymer matrix to develop ordered arrays of fullerenes, it was first necessary to understand how polymers interact with C_{60} and what polymer structures and functional groups allow for improved miscibility. Our main motivation for studying polymer-fullerene interactions stems from previous results regarding block copolymer-fullerene systems conducted by Waller et al [147]. In these studies, a mixture of low molecular weight cylindrical-forming polystyrene-*b*-poly(dimethylsiloxane) (PS-PDMS) block copolymer was investigated with C_{60} where the fullerenes are highly immiscible with the PDMS and show limited miscibility with the PS block. For this reason, C_{60} fully segregates into the PS minor phase and would be expected to align along the PS cylinders with annealing [147, 213].

As shown by Figure 29, the PS cylinders in PDMS matrix show alignment parallel to the substrate, but the degree of alignment decreases with an increase in C_{60} concentration, particularly when greater than 3 wt% C_{60} is incorporated relative to the PS block. The microphase structure is disrupted by the clustering of C_{60} molecules due to strong intermolecular fullerene interactions as well as the limited miscibility of C_{60} with PS of ~1 wt% [147, 213].

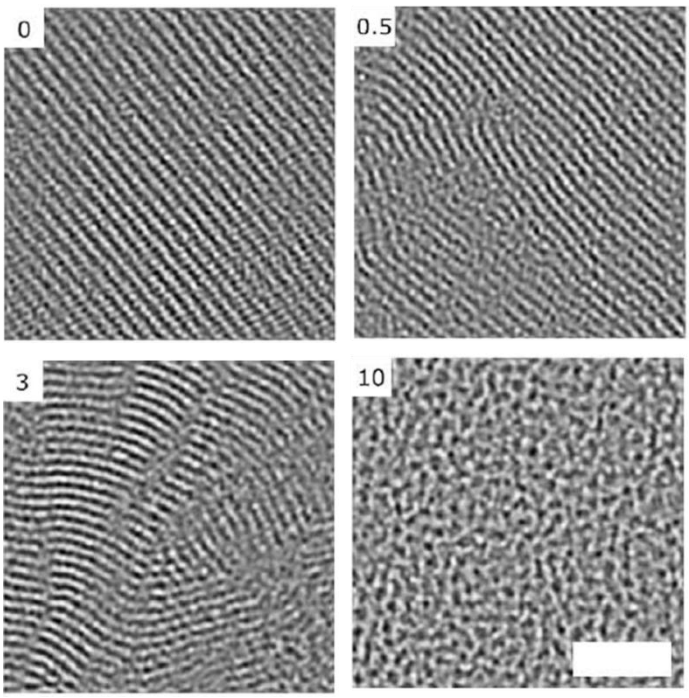

Figure 29. Cylinder-forming PS-PDMS diblock copolymer TEM images with increasing fullerene concentration. The amount of fullerene in the system is given by the number in the upper left corner in terms of wt% of C_{60} relative to the PS (minor) phase. The scale bar shown in the 10 wt% image corresponds to 100 nm (reproduced from [147]).

In order to incorporate larger quantities of fullerenes into a block copolymer system, we investigated various polymers to ascertain which materials show better miscibility with C_{60} than that seen with PS and also why these materials show improved or worse behavior with fullerenes. A secondary approach to finding a more miscible system than PS involves better dispersion of C_{60} in a PS-based block copolymer by grafting PS chains to the C_{60} cage to act as a shield to prevent aggregation and solubilize the fullerene in larger quantities with PS [32, 93, 95].

The first series of experiments introduced and discussed below were used to characterize the strength of interaction between C_{60} and conjugated polymers. The family of

conjugated polymers investigated, poly(*para*-phenylene ethynylene), are fluorescent and when the polymer forms a charge-transfer complex, this fluorescence can be quenched. The magnitude of the decrease in fluorescence intensity is used to quantify the strength of the complex formed. In our case, we have used C_{60} to quench the polymer fluorescence, and the interactions were shown to be at least an order of magnitude stronger with conjugated polymers than other C_{60}-polymer systems studied previously [31, 90-92].

Studies of C_{60} with a series of aromatic vinyl polymers are also discussed in terms of the characterization of dispersion of fullerenes using wide angle x-ray scattering (WAXS). The polymers studied were selected in order to have a systematic study of how an increasing number of phenylic moieties influence C_{60} miscibility. Polystyrene, poly(2-vinylnaphthalene), and poly(9-vinylphenanthrene), having one, two, and three phenyl rings respectively, were blended with C_{60}, and WAXS measurements on solid-state blends indicate there is a non-linear increase in the miscibility with increasing aromaticity. Density functional theory (DFT) simulations and interaction geometry studies are included for comparison to experimental results [213].

Lastly, a brief study of the characterization of polystyrene-modified C_{60} (C_{60}PS) and their behavior in a PS matrix as determined by WAXS measurements is examined. In this case, fullerene solubility was found to be drastically enhanced for C_{60}PS in PS versus pristine C_{60} systems. Polystyrene-modified fullerenes will be further discussed in terms of their behavior in a PS-based block copolymer system in Chapter IV.

3.2 Fluorescence Quenching of Poly(para-phenylene ethynylene) systems by C_{60}

As discussed previously, fullerenes have been relatively limited in their use thus far due to their low solubility in common organic solvents [58, 59, 61-63, 68, 95]. However, C_{60} fullerenes can accept up to six electrons and readily form charge-transfer (CT) complexes with a variety of materials including small molecules [84-89] and polymers [31, 90-92]. The strength of CT complexes formed between C_{60} and several small molecules has been determined by the association constant, K, using Benesi-Hildebrand theory [84-89, 96]. The complex strength between C_{60} and small molecules tend to be weak compared to complex formation with larger molecules such as polymers, but electron donating and aromatic molecules both have been shown to form stronger CT complexes than other molecules. For example, benzene [87], phenanthrene, and pyrene [89] have association constants, K, of 0.18 ± 0.04, 0.37 ± 0.07, and 1.1 ± 0.2 M^{-1} respectively in order of increasing aromaticity (one, three, and four phenylic rings). The structures for these systems are provided in Figure 30 for comparison purposes.

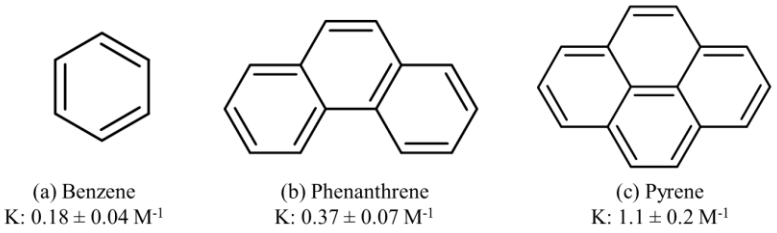

Figure 30. Examples of C_{60} complex formation with small molecules and the strengths associated with these complexes. Note the increase in CT complex strength with increasing number of phenyl rings and therefore increased aromaticity and potential for π-π interactions [87, 89].

Complexes between C_{60} and short cyclic polymers have been shown to be three to four orders of magnitude larger than C_{60}/small molecule complexes as discussed by Yamaguchi and coworkers [92] depending on the system (see Figure 31). Theory and experiment both suggest that C_{60} interacts more strongly with molecules possessing electron donating groups, atoms that are much larger than carbon such as chlorine, and aromatic systems due to increased potential for π-π interactions [58, 59, 61, 84, 88, 89].

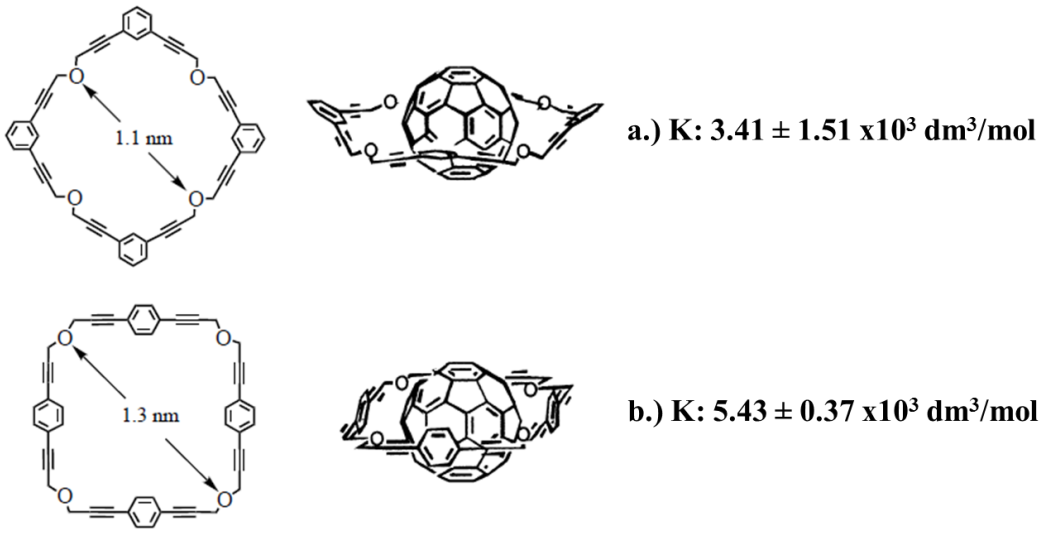

Figure 31. Cyclic polymers studied for complex formation with C_{60} by Yamaguchi et al where the strength of complexes formed determined by the association constant, K, was found to be on the order of 10^3 dm^3/mol, several orders of magnitude larger than that seen with small molecules (reproduced from reference [92]).

Interactions between poly(*para*-phenylene ethynylene)s (PPE) (Figure 32) and C_{60} are particularly interesting due to the high degree of conjugation and delocalization of π-electrons in the polymer backbone [214-218]. As the interaction between C_{60} and PPEs is

expected to be strong, it is expected that fullerenes will be highly miscible with these highly conjugated materials due to the potential for π-π interactions in both systems.

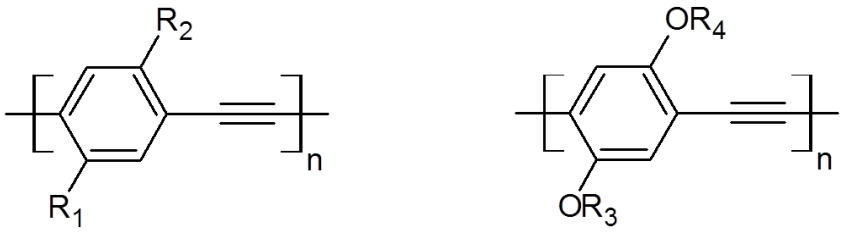

Figure 32. Example PPE structures where side R-groups are used to solubilize the PPE but also allow for the potential for tuning interactions with molecules such as fullerenes. With the benzene ring and carbon-carbon triple bond in the polymer backbone, there is a high degree of conjugation of π-electron delocalization.

The strength of interaction between C_{60} and PPE can be determined using fluorescence spectroscopy and Stern-Volmer (SV) theory. PPEs in dilute solution show a short fluorescent lifetime that does not change with the addition of a fluorescence quencher. There are two potential mechanisms for fluorescence quenching: static and dynamic. Static quenching occurs as a result of complex formation between a fluorescent molecule or fluorophore and a fluorescence quencher. The resulting complex is not fluorescent leading to a decrease in the overall measured intensity as there is less free fluorophore in the system. Dynamic quenching is also called collisional quenching because the fluorophore is quenched by a collision with a quencher through random molecular motion [214]. Fluorescence lifetime measurements are typically used to distinguish between mechanisms as the fluorescence lifetime remains unchanged with the addition of quencher in static quenching but changes with added quencher in dynamic quenching as this is a time dependent process [214, 219]. The magnitude of the SV constant, K_{sv}, as

well as absorbance spectra can also be used to distinguish between static and dynamic quenching mechanisms [219]. Both mechanisms are always present, but PPEs are dominated by a static quenching mechanism [214]. Where static quenching is dominant, a binding or association constant between the fluorophore and quencher can be extracted using SV theory [214, 219-223].

Experimentally, we have investigated the fluorescence quenching behavior of the PPEs shown in Figure 33 with C_{60}. Molecular weight effects were examined using several different molecular weights of **PPE(1)**, and the effects of different side groups on the association constant were probed by comparison of all four PPE structures. Electron donating capability of the side groups, specifically with **PPE(2)**, **PPE(3),** and **PPE(4)**, was of particular interest in terms of the effect on the strength of interaction between C_{60} and a given PPE. Paraquat (PQ^{+2}) measurements were undertaken with **PPE(1)** as well for comparison to previous work with PPE quenching by PQ^{+2} [218, 224].

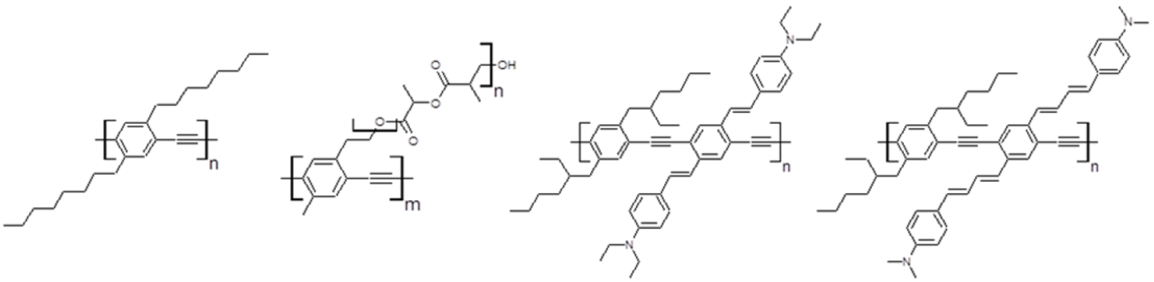

PPE(1) **PPE(2)** **PPE(3)** **PPE(4)**

Figure 33. PPE structures investigated for interactions with C_{60} fullerenes. All four structures were compared for side group effects on the strength of interaction. PPE(1) was also studied with C_{60} at 3 different molecular weights to determine the molecular weight effects on the interaction with C_{60} [217, 218].

3.2.1 Materials and Methods

Materials

The PPE polymers investigated were synthesized at Georgia Tech by the Bunz group (Figure 33). The number of repeat units and M_n values for **PPE(1)** and **PPE(2)** are given below in Table 2. The molecular weights of polymers **PPE(3)** and **PPE(4)** are unknown due to difficulties associated with GPC measurements; however, both polymer chain lengths are of a high enough molecular weight that the polymers exhibit fluorescent behavior in solution. For this reason, the concentrations used are in terms of monomer concentration.

Table 2. Molecular weight information for PPE chains used in fluorescence quenching experiments with C_{60} where number of repeat units (n, m) corresponds to Figure 33.

Polymer Structure	***Number of repeat units***	***M_n (kg/mol)***
PPE(1)	n=7	2.6
	n=136	44.4
	n=226	73.3
PPE(2)	m=50, n=16	123.3

The C_{60} fullerenes used in these experiments were of 99.5% purity and used as received from VWR International. HPLC grade toluene was purchased and used as received from Fisher Scientific for solution preparation. A brief study was conducted with paraquat

(PQ^{+2}) quenching of **PPE(1)** for method verification. PQ^{+2} was obtained from Sigma Aldrich and used as received.

Experimental Setup

All fluorescence quenching measurements were conducted using a Photon Technology International (PTI) QuantaMaster fluorescence spectrometer and rectangular quartz cuvette. Fluorescence quenching measurements were taken at an excitation wavelength of 396nm using dilute solutions of each PPE at five different starting concentrations in toluene. The solution concentrations in terms of monomer units that were used are given below in Table 3. All concentrations experimentally investigated were in the region where fluorescence intensity is directly proportional to fluorophore concentration.

Table 3. Concentration of monomer units in solution for all PPE structures experimentally studied for fullerene interactions.

PPE structure		***Concentration of Monomer (M)***				
PPE(1)	n=7	7.91×10^{-7}	1.32×10^{-6}	2.89×10^{-6}	4.20×10^{-6}	7.08×10^{-6}
	n=136	1.23×10^{-6}	2.45×10^{-6}	4.96×10^{-6}	7.30×10^{-6}	1.23×10^{-5}
	n=226	2.02×10^{-6}	4.04×10^{-6}	8.04×10^{-6}	1.21×10^{-5}	2.02×10^{-5}
PPE(2)		2.47×10^{-7}	4.93×10^{-7}	9.90×10^{-7}	1.48×10^{-6}	2.47×10^{-6}
PPE(3)		8.52×10^{-7}	1.71×10^{-6}	3.40×10^{-6}	5.11×10^{-6}	8.51×10^{-6}
PPE(4)		8.50×10^{-7}	1.70×10^{-6}	3.39×10^{-6}	5.10×10^{-6}	8.50×10^{-6}

In all cases the fluorescence intensity of the PPE solution in the absence of quencher was measured first. To each dilute PPE solution, incremental amounts of C_{60} in toluene were then added, the mixed solution agitated, and a measurement taken after each addition. The resulting data was then analyzed based on monomer concentration using the non-linear Stern-Volmer equation described below.

For paraquat quenching measurements of **PPE(1)** with n=226, toluene solutions were prepared at two concentrations of PPE, and the method described above for C_{60}/PPE systems was applied. PQ^{+2} concentrations ranged from $1.29x10^{-5}$ M to $6.12x10^{-4}$ mol/L with the incremental additions of paraquat to the PPE solution in the measurement cuvette. Figure 34 shows the molecular structure of PQ^{+2} as well as the PPE used in these studies. Based on previous studies with similar materials [224], it was expected that the quenching would result in linear Stern-Volmer plots [214, 219, 222]. However, because the PQ^{+2} measurements were used as a verification of our non-linear method of data analysis, we used both the non-linear Stern-Volmer approach derived below as well as the traditional linear approach to analyze the paraquat data.

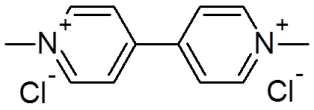

Figure 34. Chemical structures for paraquat (PQ^{+2}) (left) and PPE(1), n=226 investigated for fluorescence quenching where the PPE is the fluorophore and PQ^{+2} is the quencher.

3.2.2 Explanation of Data Analysis: Stern-Volmer Approach

The Stern-Volmer (SV) equation relative to static quenching is derived by considering the complex formation between fluorophore, F, and quencher, Q, as a reversible chemical reaction with association constant, K. The SV constant, K_{sv}, contains both static and dynamic components, but where static quenching is dominant, the K_{sv} can be assumed to be equal to the association constant, K, between the fluorophore and quencher [214, 219, 222]. The fluorescence intensity is assumed to be proportional to the fluorophore concentration and the initial fluorophore concentration, $[F]_0$, is equal to the sum of the concentrations of free fluorophore, [F], and non-fluorescent complex, [FQ]. This results in the linear form of the static quenching Stern-Volmer equation as shown by **Equation 1** where I_0 is defined as the fluorescence intensity in the absence of quencher, [Q] is the quencher concentration at any given time, and I is the fluorescence intensity at [Q] [214, 219, 221, 222].

$$\frac{I_0}{I} = 1 + K[Q] \qquad \textbf{Equation 1}$$

The Stern-Volmer or association constant is determined by plotting normalized intensity versus quencher concentration. The slope of this typically linear plot is equal to K. The initial quencher concentration, $[Q]_0$, is inherently assumed to be much larger than $[F]_0$ such that $[Q]_0$ equals the free quencher concentration, [Q], in the system at any given time. The plot is linear if either quenching mechanism is dominant [214, 219, 221, 222]. However, deviations from linearity may occur for a variety of reasons [219-221, 223]. Deviations from linearity can occur as a result of both static and dynamic mechanisms being active in the quenching process, resulting in upward curvature of the Stern-Volmer

plot [219, 221]. Positive deviation may also occur as a result of a large degree of quenching at large quencher concentrations [219, 221, 223]. In this case, results indicate false static quenching due to what is known as a "sphere of action" where the quencher is near the fluorophore at excitation resulting in no fluorescence intensity from these molecules. However, in sphere of action quenching no ground state complex is formed [219, 221].

To distinguish between static and dynamic mechanisms occurring simultaneously, it is necessary to apply the plotting method described by both Geddes and Lakowicz [219, 221]. Because the assumption that the initial quencher concentration, $[Q]_0$, is equivalent to the quencher concentration at any time, [Q], results in the linearity of the original Stern-Volmer equation, we have instead derived and used a non-linear form of the Stern-Volmer equation that does not use this assumption. As with the original Stern-Volmer equation derivation, complex formation was considered as a reversible chemical reaction with an equilibrium constant, K. From this consideration it can be shown:

$$[FQ] = K[F][Q] \qquad \textbf{Equation 2}$$

$$[F] = [F]_0 - [FQ] \qquad \textbf{Equation 3}$$

$$[Q] = [Q]_0 - [FQ] \qquad \textbf{Equation 4}$$

By combining **Equations 2-4**, the fluorescence quenching behavior is described in terms of the initial quencher and fluorophore concentrations, both known quantities, as shown in **Equation 5**.

$$[FQ] = K([F]_0 - [FQ])([Q]_0 - [FQ]) \qquad \textbf{Equation 5}$$

$$[FQ]^2 - \left(\frac{1}{K} + [F]_0 + [Q]_0\right)[FQ] + [F]_0[Q]_0 = 0 \qquad \textbf{Equation 6}$$

Solving **Equation 6** for [FQ] results in **Equation 7** where the concentration of complex, [FQ], is equal to difference between the initial fluorophore concentration and the free fluorophore concentration at any given time. The concentration of fluorophore is assumed to be proportional to fluorescence intensity as in the original SV equation, leading to **Equation 8**. It is necessary to relate the fluorophore concentration to the fluorescence intensity using a proportionality constant, c, where c is equal to I_0 divided by $[F]_0$ as measured experimentally. **Equation 8** was used to fit the data acquired from fluorescence quenching experiments and extract a value for the association constant, K.

$$[FQ] = \frac{1}{2}\left(\frac{1}{K} + [F]_0 + [Q]_0 - \sqrt{\left(\frac{1}{K} + [F]_0 + [Q]_0\right)^2 - 4[F]_0[Q]_0}\right) \qquad \textbf{Equation 7}$$

$$I = I_0 - \frac{c}{2}\left(\frac{1}{K} + [F]_0 + [Q]_0 - \sqrt{\left(\frac{1}{K} + [F]_0 + [Q]_0\right)^2 - 4[F]_0[Q]_0}\right) \qquad \textbf{Equation 8}$$

3.2.3 Discussion of Fluorescence Quenching Results

Paraquat Quenching and Method Verification

The experimental method and analytical techniques for non-linear Stern-Volmer applications were verified using paraquat quenching of polymer **PPE(1)** (n=226). The results were found to be in agreement with work previously conducted on paraquat and similar PPE systems by Zhou and Swager [225, 226]. An example of the quenching of **PPE(1)** by PQ^{+2} is shown by the decrease in fluorescence intensity with increasing paraquat (quencher) concentration in Figure 35, where the arrow indicates the direction of increasing quencher concentration.

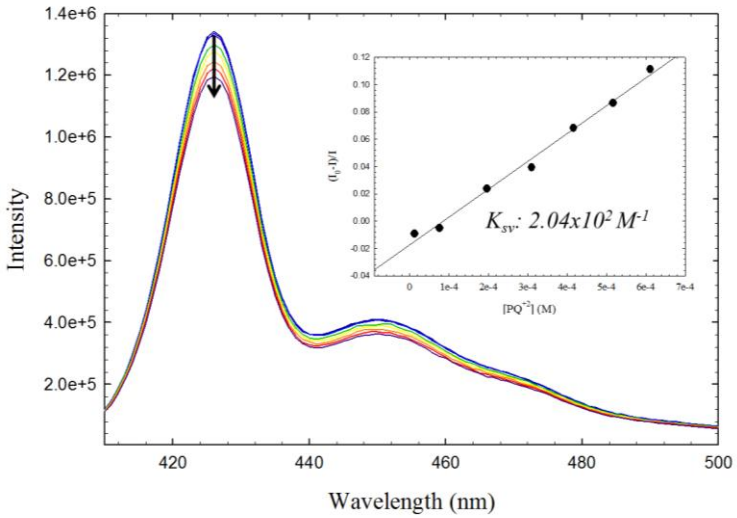

Figure 35. Fluorescence quenching of PPE(1) (n=226) by PQ^{+2} where the downward arrow indicates the direction if increasing paraquat concentration as well as the peak location where intensity data was used for the SV plot shown in the inset. The data fit using the non-linear SV equation is shown by the solid line on the inset plot. K_{sv} was determined to be 2.04x10^2 M^{-1} at both concentrations of PPE solution investigated with paraquat.

SV plots for the fluorescence quenching of **PPE(1)** by paraquat are also shown in Figure 35, where the data was fit and the Stern-Volmer constant extracted using the non-linear approach described above by **Equation 8**. While this approach uses an equation that is non-linear in nature and the SV plots for PPE quenching by PQ^{+2} are linear in nature, the data is well described by the fit, and the extracted Stern-Volmer constant values from the fit are consistent with values determined using the traditional linear SV approach. Comparing the non-linear and linear SV equation results, we determined the non-linear model to be valid for extracting information regarding the association constant for complex formation from non-linear C_{60}/PPE SV plots as discussed further below.

The data modeling as well as experimental method was further verified by comparison to literature of paraquat quenching of similar PPE structures. For both PPE polymer structures investigated by Zhou and Swager with paraquat (Figure 36) the value determined for K_{sv} using the linear SV approach was found to be comparable with the results determined using our non-linear approach. K_{sv} was determined to be 5.74×10^2 M^{-1} and 6.11×10^2 M^{-1} for the polymer on the left in Figure 36 with molecular weights (M_n) of 2.688×10^5 g/mol and 1.5×10^6 g/mol respectively. For the polymer on the right with molecular weight of 1.34×10^5 g/mol, K_{sv} was calculated as 9.04×10^2 M^{-1} using the linear SV equation by Zhou et al [224]. Because PPEs used by Zhou and Swager are structurally similar but not identical to the polymer used in our experiment, we cannot make a direct comparison of K_{sv} values. Additionally differences in the overall value may result from molecular weight effects as our polymer was several orders of magnitude smaller than the systems reported in the literature. However, the order of magnitude for the association/SV constant is the same at 10^2, as would be expected for similar materials.

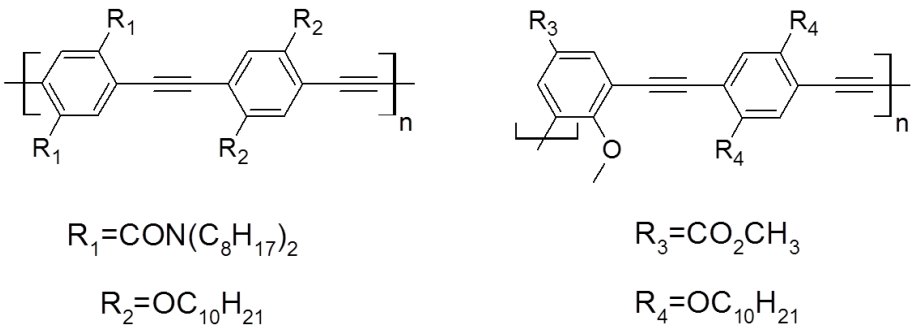

Figure 36. PPE structures investigated by Zhou and Swager with paraquat using fluorescence quenching experiments to determine the value for the association constant or SV constant for complex formation. For the PPE on the left, K_{sv} was found to be $5.74x10^2$ M^{-1} at M_n: $2.688x10^5$ g/mol and $6.11x10^2$ M^{-1} at M_n: $1.5x10^6$ g/mol. For the PPE on the right, K_{sv} was found to be $9.04x10^2$ M^{-1} for M_n: $1.34x10^5$ g/mol [224].These values are comparable to our values obtained for paraquat with the PPE(1) structure at M_n: $73.3x10^3$ g/mol.

Fluorescence Quenching of PPEs by C_{60} Fullerenes

The addition of C_{60} fullerenes to PPE solutions results in the quenching of PPE fluorescence as shown by Figure 37 for experiments with **PPE(1)** and **PPE(2)**. Similar quenching behavior was observed for all PPE structures investigated with C_{60}. A decrease in PPE fluorescence intensity results due to a decreased quantity of free PPE fluorophore in solution. We attribute the decrease in fluorescence intensity with increasing C_{60} concentration to strong interactions between the C_{60} and PPE chains. The strength of this interaction was quantified using the non-linear Stern-Volmer equation described above. It is relevant to qualitatively compare the degree of fluorescence quenching of **PPE(1)** by C_{60} to the quenching by paraquat shown in Figure 35; the fluorescence intensity decrease is significantly larger for C_{60} added to **PPE(1)** than that seen for paraquat at comparable quencher concentrations. We can infer from this qualitative analysis of the degree of

quenching that the interaction between PPEs and C_{60} is much stronger than that for paraquat with PPE.

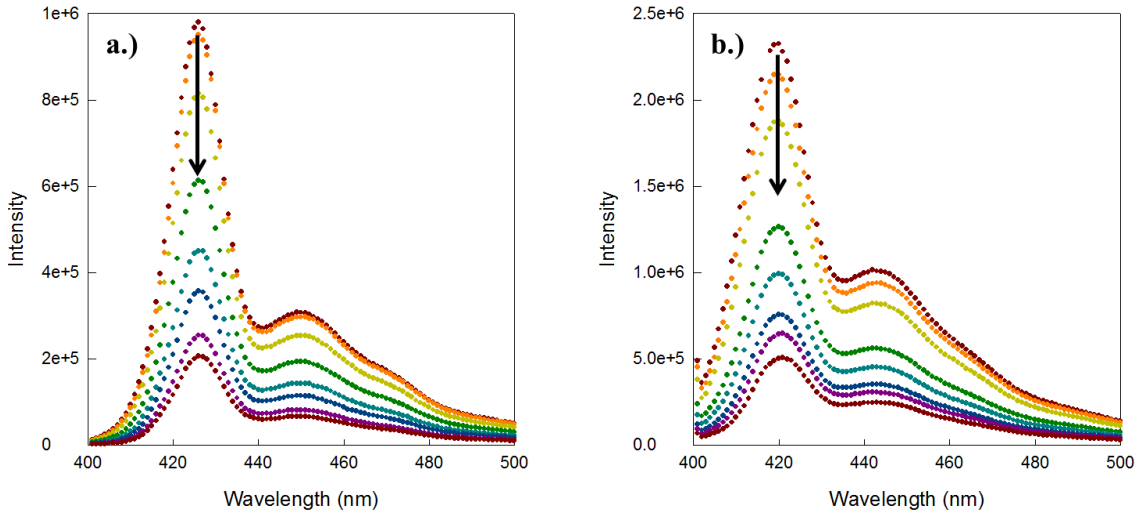

Figure 37. Fluorescence quenching of PPE by C_{60} where fluorescence intensity measurements are taken after each addition of C_{60} to a.) PPE(1) (n=226) at a monomer concentration of $2.02x10^{-6}$ M and b.) PPE(2) at monomer concentration of $2.47x10^{-7}$ M. The arrows in the figure indicate the direction increasing C_{60} concentration as well as the peak where fluorescence intensity values were taken for Stern-Volmer analysis (at 425.95 nm).

Figure 38 shows the typical Stern-Volmer plots at all concentrations of **PPE(1)** (n=226) and **PPE(2)** measured. The resulting plots are non-linear with upward curvature that cannot be accurately fitted using the linear Stern-Volmer equation. While not shown here, the behavior was similar for all four PPE structures. As expected, there is little deviation in the traditional Stern-Volmer plot based on different starting concentrations; K_{sv} should be independent of the starting concentration of PPE in solution for a given PPE structure as long as fluorescence intensity increases with increasing concentration.

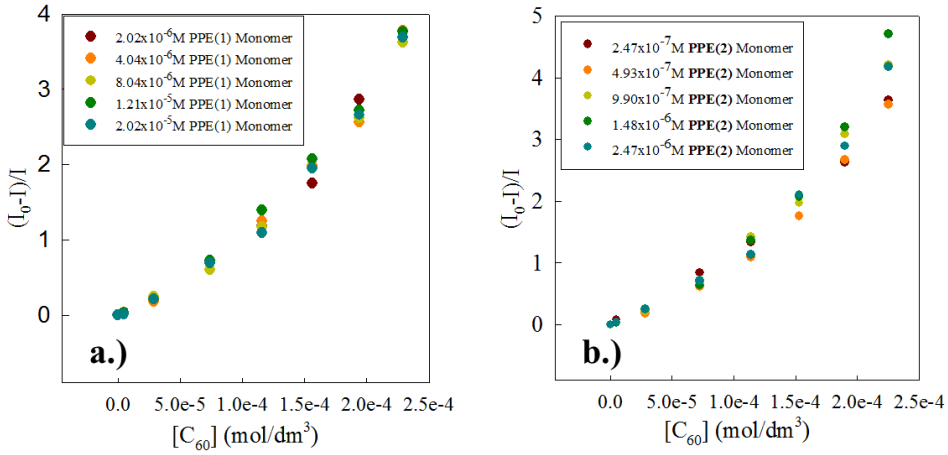

Figure 38. Traditional SV plots for a.) PPE(1) and b.) PPE(2) at all concentrations of PPE measured. The plots show the deviation from linearity in the quenching behavior resulting in an upward curvature of the plots.

The data was modeled using **Equation 8** with the plot and non-linear fit for **PPE(1)** (n=226) shown in Figure 39 at the highest starting concentration used. From this plot, we are able to extract a value for K_{sv}.

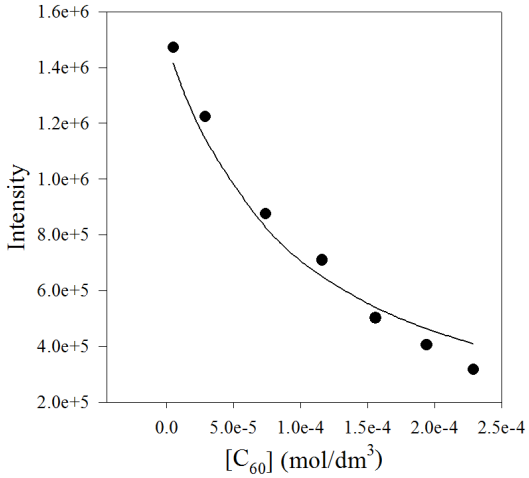

Figure 39. Non-linear SV plot for PPE(1) (n=226) at 2.02x10^{-5} M of monomer in toluene with increasing C_{60} concentration. The fit is represented by the solid line and intensity values were all extracted at a wavelength of 425.95 nm (corresponding to the larger peak on fluorescence data in Figure 37.

The values of the Stern-Volmer constant for C_{60} quenching of the four PPE structures at the specified molecular weight are given in Table 4. It is important to note that all the values are determined assuming a 1:1 interaction between PPE monomer and C_{60} fullerene. The values obtained indicate that PPE and C_{60} have a strong interaction which may be expected due to the degree of conjugation in the PPE backbone.

Table 4. K_{sv} values using the non-linear SV equation as derived above for each of the four PPE structures investigated. Repeat units are designated for PPE(1) as different molecular weights were investigated to determine the effect of number of polymer repeats on K_{sv}.

PPE Structure		***K_{sv} (dm^3/mol)***
PPE(1)	7 repeats	9380 ± 670
	136 repeats	8910 ± 610
	226 repeats	11,680 ± 1140
PPE(2)		11,970 ± 1420
PPE(3)		10,930 ± 1900
PPE(4)		11,510 ± 1230

We initially investigated PPEs with different side group chemistry to determine the effect of electron donating capability in the side group on the strength of interaction between C_{60} and the specified PPE. The electron donating ability of the side group was of particular interest because C_{60} interactions have been shown to be stronger for molecules with electron donating groups [58, 59, 61, 84, 88, 89]. We expected that polymers **PPE(2)**, **PPE(3)**, and **PPE(4)** would all have stronger interactions than **PPE(1)** with C_{60}

due to the possibility of electron donation. However, experimental results and K_{sv} values show no significant difference in the interaction strength among the PPEs with different polymer side groups. These results indicate that the interactions between C_{60} and PPEs are dominated by the polymer backbone, and the side group plays very little role in determining the interaction strength.

Molecular weight effects on the strength of interaction were also examined using three different molecular weights of **PPE(1)**. The number of repeat units for each of these systems is given in Table 2. The relationship between number of repeat units and K_{sv} is shown in Figure 40. Stern-Volmer constant values can be found in Table 4 for each of the molecular weights investigated. We observe that the K_{sv} value remains constant within the error for both 7 and 136 repeat unit polymer chains. However, an increase in K_{sv} is noted between 136 and 226 repeat units for **PPE(1)**. An increase in K_{sv} at longer chain lengths was not anticipated based on previous results in the literature.

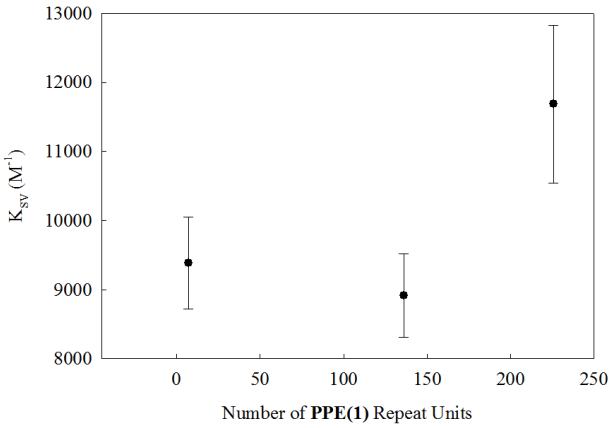

Figure 40. Fluorescence quenching measurements of PPE(1) at different molecular weights where n=7, 136, and 226. SV constant values were determined using the non-linear fit and are given in Table 4.

Previous studies on PPE fluorescence quenching and the effects of molecular weight were conducted by both Zhou et al with PPE/paraquat systems [218] and Zhao et al with conjugated PPE-based polyelectrolytes and monovalent cation quenchers [217]. For conjugated polyelectrolyte PPEs, systems with 7, 13, 35, 49, and 108 repeat units were studied and a three-fold increase in K_{sv} was noted between 7 repeat units and 35 repeat units while a negligible change was noted between 35 and 49 repeat units. For the 108 repeat unit system, a decrease in K_{sv} was attributed to the increased aggregation tendencies for PPE chains at higher molecular weight, making the quenching process a combination of self-quenching and static quenching by a monovalent cation. Based on these results, it was concluded that molecular weight effects saturate at approximately 40 repeat units (or ~80 phenylene ethynylene units). Further interpretation of these results by Zhao and coworkers led to the conclusions that a single exciton can sample a chain length of ~40 nm within its lifetime [217]. Similarly, for natural PPEs (uncharged) quenched by paraquat, Zhou and Swager determined that K_{sv} increased with chain length at molecular weights less than 65 kDa, and only a small increase in K_{sv} was observed for PPEs of higher molecular weights [218].

We, however, do not see this behavior for our PPEs when quenched by C_{60} as noted above and shown in Figure 40. Instead of observing an increase in K_{sv} with increasing molecular weight, we see constant values at lower molecular weight systems, followed by an increase at much high molecular weights. A number of factors may contribute to this behavior including the nature of the interaction between the PPE and the C_{60}. C_{60} is a much larger molecule than the quenchers investigated previously with PPEs. For this reason it is likely that an individual C_{60} molecule quenches more than one repeat unit at

the same time. Particularly, the increase in K_{sv} noted for **PPE(1)** at n=226 may be related to this as at longer chain lengths more fullerenes can interact and quench the polymer which is experimentally observed by a larger decrease in fluorescence intensity and stronger interaction between the C_{60} and the PPE. Similarly, at smaller chain lengths, the number of fullerenes quenching the fluorescence may not be drastically different enough to be evident in the K_{sv} value extracted or the level of fluorescence quenching observed.

Overall, the results of these experiments indicate that fullerenes interact strongly with conjugated polymers such as PPE. Assuming a dominant static quenching mechanism, we can equate the Stern-Volmer constant, K_{sv}, to the association constant, K, for complex formation. Using K, we can gauge the strength of interaction between C_{60} and PPE and compare to previous work done with small molecules and cyclic polymers. When comparing to small molecules, our association constant values are up to six orders of magnitude larger as typical values of K for small molecule-C_{60} complexes are on the order of 10^{-1} M^{-1} [84-89], and our values for C_{60}-PPE interaction at longer chain lengths are 10^5 M^{-1}. In comparison to short cyclic polymers, C_{60}-PPE complex association constants are an order of magnitude larger than those determined by Yamaguchi and coworkers [92]. Polymers show enhanced K_{sv} values in comparison to small molecules and this can be attributed to the molecular weight effects discussed above where there is a large degree of enhancement due to longer average diffusion lengths and increased mobility of excitons for larger molecules. For an isolated polymer in solution, if the diffusion length is greater than the polymer length, then an increase in molecular weight will produce a further increase in K_{sv} (or binding constant in the case of static quenching) [218]; for this reason, larger polymers such as the PPEs discussed here, show increased

interaction strength with fullerenes when compared to small molecules and even oligomers.

3.2.4 Conclusions, Implications, and Future Work

In summary, our studies on PPE interactions with C_{60} have shown that the interaction can be characterized as strong, being at least one order of magnitude larger than previously reported polymer-fullerene complexes. The interaction itself is largely dominated by the conjugated backbone of the polymer, where any side group chemistry has little to no effect on how strongly the C_{60} binds to the PPE; π-π interactions between the fullerene cage and the polymer backbone are likely in this case as inferred from the strength of interaction. The strength of interaction was shown to be influenced by the molecular weight of the polymer, although the trend was not as expected. At higher molecular weights the Stern-Volmer constant, K_{sv}, was found to increase while remaining nearly constant for the smaller polymers studied; this was in fact the opposite of the expected behavior based on previous studies of PPE with other quenchers. We have attributed this difference to the size of the quencher molecule, which in our case at 1 nm is much larger than quenchers used in other studies. Overall, we have concluded that conjugation and the potential for π-π interaction drastically improves fullerene interactions with polymers, and we further extrapolate that stronger interactions will lead to improved C_{60} dispersion when compared to a polystyrene system.

Further study of these materials would allow for better understanding of the stoichiometry of the interactions as far as how many fullerenes interact per chain. This would provide a more accurate assessment of the interaction strength as the method we

have used inherently assumes a 1:1 interaction. As with previous studies [217], the amplification factor (AF) can be used as an assessment of the number of repeats that are effectively quenched by one quencher molecule. The AF is defined as the ratio between the K_{sv} for the polymer to the K_{sv} for a monomer in the presence of the same quencher, assuming the association constant for complex formation is equivalent for monomer and the polymer. While PPE monomers are not fluorescent, it is likely that the Stern-Volmer constant would not vary significantly from that of a PPE trimer which is weakly fluorescent. Therefore, the AF for PPE-C_{60} interactions should be determined by taking the ration of $K_{sv,polymer}$ to $K_{sv,trimer}$. Additionally, preparation of solid state blends of C_{60} in PPE and subsequent characterization of the dispersion using WAXS (similar to studies described below) would provide clearer insight into whether or not CT complex strength can be directly linked to fullerene miscibility.

3.3 Role of Molecular Orientation and π-π Interactions in Polymer-Fullerene Miscibility

Only limited investigation has been conducted regarding polymer-fullerene systems and further research is required to fully characterize the nature and forces responsible for these interactions. Understanding polymer/fullerene behavior is useful for a wide range of potential applications including nanoparticle templating and photovoltaic applications. While results of small molecule-C_{60} studies have some implications regarding polymer-C_{60} systems, the size of polymer structures and placement of interacting functional groups is likely to influence the magnitude of the interaction. The nature of the miscibility between C_{60} fullerene and a series of phenylic vinyl polymers has been

investigated using wide-angle x-ray scattering (WAXS) measurements and comparison to density functional theory (DFT) simulations.

3.3.1 Materials, Methods, and Techniques

Materials

HPLC grade toluene and ACS grade methanol were purchased from VWR International as solvent and non-solvent respectively for polymer/fullerene blend preparation. C_{60} fullerene (purity 99.5+%) was used as received from VWR International. Polystyrene (PS) with M_n of 100,000 g/mol, PDI = 1.1, was used as a base system for investigation of aromaticity effects on C_{60} dispersion limits. Poly(2-vinylnaphthalene) (M_n = 45,000 g/mol, PDI = 1.6) and poly(9-vinylphenanthrene) (M_n = 6800 g/mol, PDI = 1.13) were purchased from Polymer Source, Inc. Polymer structures are shown below in Figure 41.

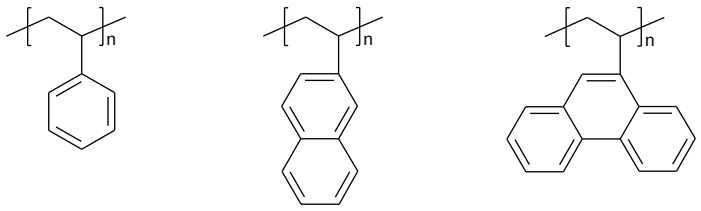

Figure 41. Polymer structures investigated experimentally with C_{60} for effects of increased aromaticity on dispersion in a polymer matrix: (a) polystyrene (PS), (b) poly(2-vinylnaphthalene) (P2VN), and (c) poly(9-vinylphenanthrene) (P9VPh).

Two additional PS molecular weights (M_n = 41,400 g/mol, PDI = 1.02; M_n = 6240 g/mol, PDI = 1.04) were investigated for molecular weight effects. Both PS systems were

purchased from Polymer Standards Service-USA, Inc. The molecular weights selected in this instance were directly comparable to those of the poly(2-vinylnaphthalene) (P2VN) and poly(9-vinylphenanthrene) (P9VPh). All polymer materials were used as received.

Polymer/Fullerene Blend Preparation

Polymer and C_{60} were dissolved separately in toluene and sonicated for 30 minutes. The C_{60} solutions were then added to those of the polymer to give various compositions. The polymer-fullerene solutions were then sonicated for an additional 30 minutes before precipitation into cold, stirred methanol. The solid precipitate was then vacuum filtered and dried prior to WAXS measurements. Pure polymers were treated in the same way for comparison to polymer-fullerene blends. PS samples were measured as prepared and after annealing for 24 hours above T_g (100-120°C depending on molecular weight) in a vacuum oven; P2VN and P9VPh samples were annealed at 200°C, also above T_g. No differences were noted in the WAXS results before and after thermal treatment.

Wide Angle X-ray Scattering Setup and Measurement

Wide angle X-ray scattering (WAXS) was conducted using a Rigaku Micro Max 002 X-ray generator operating a CuK_α source at 45 kV and 0.66 mA and a R-axis VI++ detector. Polymer-fullerene blends were pressed into films using elevated temperature, and scattering from these samples was collected for 5 min. Data was corrected for film thickness prior to processing. Brittleness of some samples prevented film formation, particularly in the case of higher loadings C_{60} in P9VPh. In these cases powder samples were measured using glass capillary tubes with 1 mm diameter and wall thickness of 0.01 mm were used as purchased from Hamilton Research. Scattering was collected for 1 hour

for powder samples, and scattering from empty capillary and air was collected for equal time to correct for background. AreaMax software was used for background subtraction and integration. It is important to note that both film and capillary measurements were conducted for PS systems, and no difference was observed in the WAXS patterns or dispersion limit.

3.3.2 Wide Angle X-ray Scattering Data Analysis

The vinyl polymers investigated for miscibility are amorphous polymers where WAXS measurements are characterized by broad peaks in the 1D WAXS patterns, shown in Figure 42 (a)-(c). C_{60}, however, is highly crystalline, and the 1D WAXS pattern of pure fullerene in Figure 42 (d) shows the sharp peaks characteristic of diffraction from crystalline materials. The observation of these characteristic Bragg peaks in the WAXS patterns as a function of increasing concentration of C_{60} was used to define the upper limit of solubility of the fullerene in that particular polymer. This method is insensitive to the initial onset of clustering of the C_{60} molecules from initially fully dispersed fullerenes to the point where two or more C_{60} molecules cluster together. Determination of the aggregation number at the experimentally derived solubility limit was attempted using AFM measurements, but is below the resolution limit of the instrument. Assuming the aggregates are near the polymer matrix surface, we estimate that the resolution limit for detecting fullerene aggregates using AFM is approximately a 5 nm aggregate diameter. Using this figure as an upper limit, this would mean aggregates are forming which contain up to 100 C_{60} atoms.

3.3.3 Density Functional Theory Simulations

All-electron DFT calculations were conducted by our collaborators (B. Sumpter) at the Center for Nanophase Material Science at Oak Ridge National Lab (Oak Ridge, TN) to provide insight as to the nature of the interaction between C_{60} and oligomers (5 repeat units) related to the vinyl aromatic polymers investigated experimentally: polystyrene, poly(2-vinylnaphthalene), and poly(9-vinylphenanthrene). The results are reported here for comparison to WAXS experimental results on polymer-fullerene interactions and help to provide full understanding of the interactions responsible for improvements in dispersion of C_{60} [213].

Calculations were performed using NWChem [227] with the local density (LDA) and generalized gradient approximation (GGA). The atom centered, contracted Gaussian basis set, 6-31G* [228], was used during the calculation of self-consistent solution. The initial geometries for the different C_{60}-polymer systems were obtained by optimizing the geometry of the C_{60}-oligomers using molecular mechanics and dynamics (Materials Studio 5.0, Accelrys). In this study, the DFT-D approach was also used, specifically the B97-D method as described by Vazquez-Mayagoitia et al [229] to validate the relative strength and trends of the intermolecular interactions as computed from DFT-LDA. Finally, the relative amount of charge transfer that occurs at the nanoscale interface was estimated from the difference between a simple Mulliken population analysis of the C_{60}-oligomer and that for C_{60} and the oligomers. This is a very crude estimation of the charge transfer.

3.3.4 Discussion of Wide Angle X-ray Scattering Results

To determine the effect of increased aromaticity on the solubility of C_{60}, a homologous series of vinyl polymers (PS, P2VN and P9VPh) has been investigated experimentally using WAXS measurements [147, 213]. All the polymers are fully amorphous as shown by their WAXS patterns in Figure 42 a.)-c.). By comparison aggregates of C_{60} are highly crystalline with a characteristic WAXS pattern of pure fullerene as shown in Figure 42 d.), and crystalline peaks due to C_{60} are relatively simple to distinguish from the amorphous polymer scattering. The 1D WAXS patterns for each series of the three polymer blends with varying C_{60} content are shown in Figure 42 a.)-c.). At zero or very low concentrations of C_{60} in each polymer, the WAXS patterns from the polymers show the typical amorphous scattering attributed to the polymer matrix. At higher loadings of C_{60} above the solubility limit, the three strongest peaks in the WAXS pattern of pure C_{60}, Figure 42 (d), are clearly evident at 2θ = 10.8, 17.8 and 20.9°.

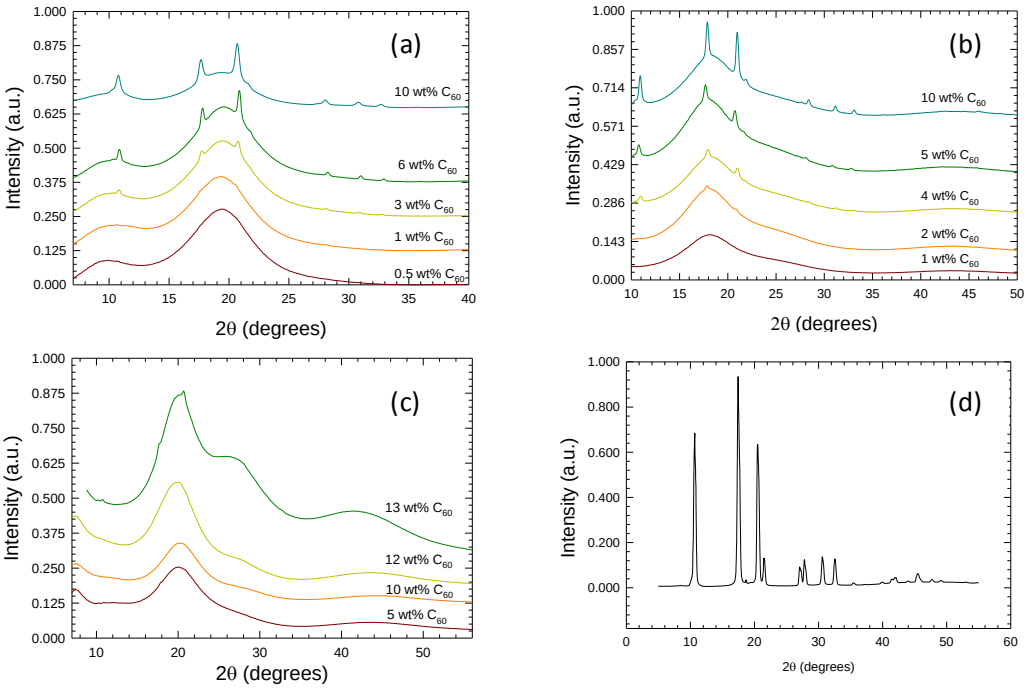

Figure 42. 1D WAXS patterns of blends of (a) PS_{100}, (b) P2VN, (c) P9VPh with C_{60}, and (d) pure C_{60}. The miscibility limit for each polymer system is determined by the appearance of fullerene crystalline peaks as seen at 1, 2, and 12 wt% for PS, P2VN, and P9VPh respectively. The data in figures (a-c) have been scaled and translated vertically for clarity.

In all of the 1D WAXS patterns, the sharp crystalline diffraction peaks are due to C_{60} fullerene aggregates, while the broad amorphous peaks are due to the polymers. Based on the presence of these peaks in the WAXS patterns, we have shown a miscibility limit of between 0.5-1 wt% C_{60} in PS (M_n = 100 kg/mol) using WAXS as shown in Figure 42 [147]. The upper limit of 1 wt% is indicated by the observation of weak C_{60} diffraction peaks in the WAXS data. The dispersion limit increases to 1-2 wt% C_{60} in the case of C_{60}-P2VN blends and to 12-13 wt% for P9VPh blends.

The increase in the miscibility with increasing aromaticity can be anticipated based on published solvent-fullerene solubility data. However, the magnitude of the increase between P2VN and P9VPh with the addition of one additional phenyl ring is unexpected. It could be suspected that the low molecular weight the P9VPh in comparison to both the PS and P2VN systems investigated could explain this result. Therefore, additional measurements were made using PS with molecular weights similar to those of the P2VN and P9VPh used in order to determine if this was a factor in the degree of increased miscibility seen with the C_{60}-P9VPh system.

The results of WAXS measurements with PS_6 (M_n=6240 g/mol) and PS_{41} (M_n=41,400 g/mol) are shown in Figure 43. As indicated by the 1D WAXS patterns of both systems, the miscibility limit of C_{60} is between 1 and 2 wt%. This value is slightly higher than that seen for PS with a M_n of 100,000 g/mol (PS_{100}) and comparable to that of the P2VN-C_{60} system investigated. The marginal increase in miscibility is clearly due to the effects of lower molecular weight in both systems. However, these results also show that molecular weight effects are not responsible for the magnitude of the miscibility increase seen with C_{60}-P9VPh blends.

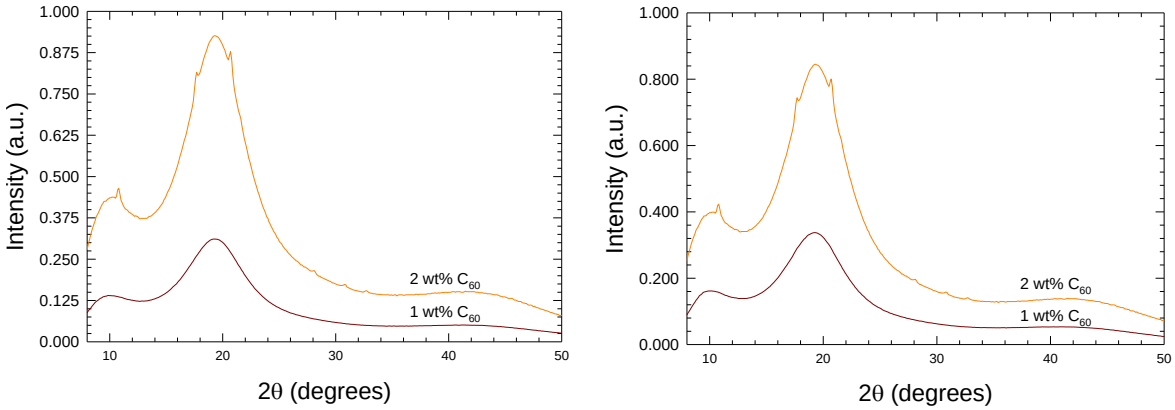

Figure 43. 1D WAXS patterns of PS_6 (left) and PS_{41} (right) with 1 and 2 wt% C_{60}. Data are scaled and vertically translated for clarity. As indicated by the appearance of crystalline peaks associated with C_{60}, the miscibility limit for both systems is between 1 and 2 wt%.

3.3.5 Comparison of Experimental and Simulation Results

All-electron quantum Density Functional Theory (DFT) calculations were used to provide additional insight into the extent of molecular interaction between oligomer units and C_{60}. Table 5 shows the DFT calculation results for binding energy and electrons donated for each oligomer-C_{60} system [213]. The results indicate that the binding energy increases with increasing aromaticity, and that the increase is non-linear. This is entirely consistent with the observed experimentally determined solubility limits for corresponding polymer systems with C_{60} as shown in Figure 44. However, based on the simulation results this is not due to an increase in electrons donated as there is no consistent change in this from system to system.

Table 5. DFT results for C_{60}-oligomer interactions [213].

Oligomer Structure	*Binding Energy (eV)*	*Electrons Donated*
PS	0.24	0.16
P2VN	0.31	0.10
P9VPh	0.43	0.12

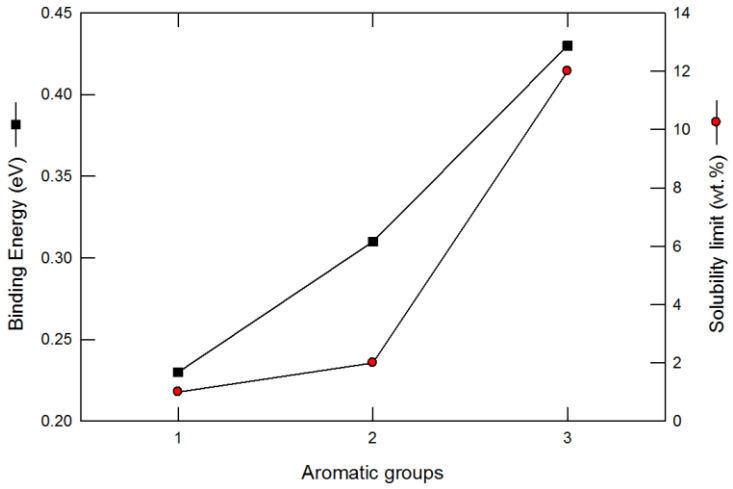

Figure 44. Comparison of miscibility limit of C_{60} with polymers with binding energy calculated for C_{60}-oligomer systems as a function of number of aromatic groups.

Comparing the simulation results of binding energy to the miscibility limits observed experimentally with increasing number of phenyl rings in the vinyl side group, the experimental results agree well with the trend seen in the simulations. Both binding energy and miscibility limit increase with increasing aromaticity as shown in Figure 44. The molecular origin of this increased interaction strength induced by the phenyl group is however, not clear. Increased π-π interactions with the C_{60} cage would be expected for

these phenyl groups. This would be promoted most strongly if the phenyl groups were oriented parallel to the tangent of the C_{60}. Another favorable orientation would be if the phenyl groups are perpendicular with the C_{60} tangent, i.e., a T-junction configuration [230].

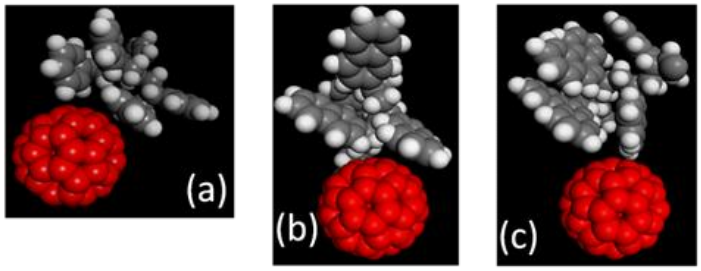

Figure 45. Optimized conformation of oligomer-C_{60} systems of (a) PS, (b) P2VN, and (c) P9VPh [213].

Detailed analysis of the simulation results is limited by the structure of the DFT where the simulation space size is based on five polymer repeat units. Therefore a more in-depth analysis of the geometric conformation for the DFT models was done [213]. As can be seen from the molecular images in Figure 45 in each case the lowest energy conformation has the phenylic groups closest to the C_{60} with the backbone further away. This implies the phenyl groups are largely responsible for the interaction with the fullerene and not the polymer backbone. The angles between the plane of each of the phenylic side groups and the tangent of the C_{60} (ie φ) as defined in Figure 46 was calculated and are reported in Table 6 [213]. As shown, there are very few phenylic groups that are in an optimal interaction geometry with respect to the C_{60}, nor is there any difference in the number of the two strongest interacting conformational orientations in the three oligomers, as shown

by the average value of φ of 43 ± 27°, 42 ± 16° and 49 ± 24°, for PS, P2VN and P9VPh, respectively. This behavior differs from the interactions observed in aromatic small molecules, where molecular reorientation of the small molecules is possible to enable strong π-π and T-junction interactions [231, 232]. In the polymers, these orientations are not possible due to the connectivity with the backbone, which significantly restricts the available conformations for the vinyl interacting groups relative to the fullerene.

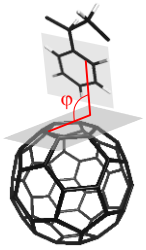

Figure 46. Definition of angle, φ , between the plane of a PS phenylic group and tangent of C_{60} [213].

These results are also consistent with the minimum distance of the closest carbon atom of the phenylic groups and the fullerene (d_{min}), where the values for the three different polymers are the same within statistics, with average values of d_{min} = 2.6 ± 0.6Å, 2.6 ± 0.6Å and 2.4 ± 0.4Å, for PS, P2VN and P9VPh, respectively. Wide angle neutron scattering (WANS) studies correspond well to the DFT results, showing a clear peak corresponding to C-C distances (*d*) of 2.44Å [213]. It is also clear that as anticipated from the DFT calculations made on a very limited molecular size, the interactions between the polymers and fullerene are non-specific (attributed to Van der Waals interactions, etc). The strength of the interaction therefore relies on the number of interactions rather than

strong π-π interactions that are seen in small molecules such as naphthalenes, calixarenes, and corannulene [233].

Table 6. Minimum distance between C_{60} and nearest carbon in phenyl ring (d_{min}) and the angle between planes, φ, (defined in Figure 46) determined from DFT optimized geometry calculations [213].

Oligomer	Phenyl Number	d_{min} (Å)	φ (°)
PS	1	2.88	42.0
	2	1.79	9.5
	3	3.32	60.6
	4	2.72	70.2
	5	2.08	61.2
P2VN	1	3.38	45.3
	2	2.50	26.0
	3	2.99	68.2
	4	2.11	31.8
	5	1.83	39.6
P9VPh	1	2.33	71.1
	2	2.21	54.6
	3	1.92	3.2
	4	3.06	59.9
	5	2.52	26.7

Given that the interaction geometries for these three polymers are on average the same, it suggests that the increase binding energy is due to the increase of bonding interactions associated with the increase in sp^2 carbons between PS and P9VPh. The step increase between P2VN and P9VPh, we believe is due to the configuration of the three phenyl groups in the vinyl phenanthrene, which is approximately conformal with the curvature of the C_{60} (Figure 47).

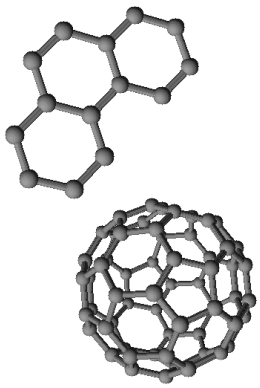

Figure 47. Schematic showing how the three phenyl rings on the vinyl group of P9VPh conform to the curvature of the C_{60} cage.

These orientations are very different than that for a similar diameter carbon nanotube, which would have the same local curvature, but due to the availability of a 1D periodic axis along the nanotube, could support face-down orientations [234]. We also mention that in general the interaction energies between spatially small monomers and C_{60} tend to be larger than those for single-walled carbon nanotubes when the orientation of the monomers are the same in part due to the presence of pentagons in the sp^2 network of C_{60}.

3.3.6 Conclusions, Implications, and Future Work

Using wide angle x-ray scattering (WAXS) we have shown that solubility of fullerene C_{60} increases with increasing aromaticity in a homologous series of vinyl polymers. The solubility increase is however non-linear with the number of aromatic groups in the polymer vinyl group, from ~ 1 wt% for PS (one aromatic ring) to 12 wt% in P9VPh (3 aromatic rings). DFT simulation results from studies conducted in collaboration with

CNMS at ORNL were found to correlate well with our experimental data, showing a non-linear increase in binding energy between oligomers of C_{60} [213].

Analysis of the energetically favored conformations shows that all the intermolecular interactions result from the oligomeric phenyl side groups with the C_{60} cage. The extent of these intermolecular interactions are dictated by the polymeric backbone, which although it does not play a direct role in the intermolecular interactions, does hinder the ability of the phenylic side groups to arrange themselves into planar π-π stacking or T-junction conformations. The DFT calculations show that the increase in binding energy, observed experimentally as an increase in solubility limit, is due to the increasing number of molecular interactions between the phenylic moieties and the C_{60} [213]. The non-linearity of this increase is believed to be due to the slight curvature associated with the configuration of phenyl groups in the phenanthrene side groups.

In terms of the overall research goal of this dissertation, the results of these studies indicate that we can disperse more C_{60} in a P9VPh-based block copolymer than seen previously with PS-based block copolymers. Furthermore, these results suggest that having a functional group that can conform to the curvature of the C_{60} cage is more important than optimizing π-π interactions in a polymer system; this is due to the restrictive nature of the polymer backbone in terms of vinyl group mobility. However, fullerene addition to a P9VPh block copolymer may still result in complications with phase behavior and other consequences associated with swelling one block with respect to another. With this in mind, P9VPh containing block copolymers should be synthesized and studied for their behavior with C_{60}.

Also future studies using WAXS to characterize dispersion of C_{60} in a polymer matrix where the vinyl group is an anthracene unit such as poly(1-vinylanthracene) (P1VA) should be conducted in a similar fashion to those described here. Anthracene is similar in structure to phenanthrene, having three fused benzene rings, but instead of being curved as in phenanthrene, the phenyl rings are arranged linearly. Comparisons of C_{60} miscibility in P1VA to the polymers studied here would provide additional support to our conclusions attributing the non-linear increase in miscibility observed between P2VN and P9VPh to the curvature of the vinyl side group of P9VPh. The linear nature of the anthracene rings should result in a more linear increase in miscibility when P1VA is compared to PS and P2VN systems.

Lastly, these studies regarding polymer-fullerene interactions have wider implications than just block copolymer templating. Polymer-fullerene systems have been an area of intense study for the development of organic photovoltaics. Typically in these systems, [6,6]-phenyl-C_{61}-butyric acid methyl ester (PCBM), a fullerene derivative, is used due to improved solubility of PCBM (shown in Figure 48) relative to C_{60}.

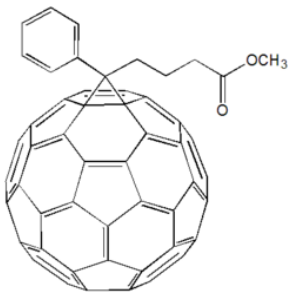

Figure 48. Chemical structure of PCBM, a fullerene derivative that shows improved solubility due to the functionalization of the cage. PCBM has found use in a variety of photovoltaic applications.

In terms of photovoltaic applications, further study would be warranted to determine if PCBM behaves similarly to C_{60} with a non-linear increase in miscibility associated with the ability of the vinyl side functionality to conform to the fullerene cage or if the cage functionalization limits this interaction in some way.

3.4 Polymer Modification of C_{60} and Miscibility in a Polymer Matrix

Understanding how fullerenes interact with various polymer functional groups and determining structures that allow for improved miscibility relative to a reference system of polystyrene is one approach we have used in selecting a block copolymer system for preparing ordered arrays of fullerenes. However, because the goal is to selectively incorporate and disperse the fullerenes into one block only, and dispersion of pure C_{60} has been shown to be limited in a polymer matrix, a secondary approach is to modify the C_{60} cage with covalently linked polymer attachment or "arms."

Polymer-modification of nanoparticles including fullerenes has been shown to be an effective means for aligning both organic and inorganic nanoparticles [32, 131, 134, 139] using a block copolymer matrix. The grafting of PS chains to the fullerene cage has been shown to be particularly successful in dispersing fullerenes in a PS matrix [95] and PS-PI symmetric block copolymers [32]. With this approach there are a variety of variables that can be manipulated to optimize the conditions for achieving ordered arrays of PS-modified fullerenes in a PS-based block copolymer matrix including polymer chain length. Reducing the chain length and number of attachments to a minimum required to maintain miscibility and dispersion would greatly increase the overall quantity of

fullerenes in a system as both the polymer arms and polymer matrix will "dilute" the amount of C_{60} in an aligned system.

Prior to incorporating PS-modified fullerenes ($C_{60}PS_6$) (synthesized by collaborators in the Beckham group at Georgia Tech) into a block copolymer matrix, we first demonstrated our ability to disperse $C_{60}PS_6$ in a pure PS matrix using the WAXS techniques described in section 3.3.1. Further discussion of results regarding $C_{60}PS_6$ stars of different sizes and the characterization of alignment in a symmetric block copolymer system using neutron reflectivity (NR) can be found in Chapter IV.

3.4.1 Materials and Methods

Materials

HPLC grade toluene and ACS grade methanol was purchased and used as received from VWR International. Polystyrene (M_n=100 kg/mol, PDI=1.1) was used as received for polymer blends with PS-modified fullerenes (synthesis briefly described below).

Synthesis of PS-modified Fullerene Stars

Star polymers composed of C_{60} cores and six polystyrene (PS) arms ($C_{60}PS_6$) were synthesized by our collaborators at Georgia Tech in the Beckham research lab (M. Kincer and M. Kempf) through addition of living PS anions to C_{60} using a procedure modified from Mathis *et al* as described below [235]. A more detailed explanation of the synthesis can be found in CHAPTER IV. Specifically for the WAXS studies of $C_{60}PS_6$-PS blends discussed in this chapter, the PS molecular weight per arm was determined to be 2000 g/mol to give a total star molecular weight (M_n) of 12,720 g/mol.

Differential Scanning Calorimetry Studies

A series of fullerene-core stars were also synthesized with different molecular weights of PS arms (2.2 kg/mol and 6.6 kg/mol) for neutron reflectivity studies discussed in Chapter IV and were thermally characterized using a TA Instruments Q200 Differential Scanning Calorimeter (DSC). Using PS standards of varying molecular weight as received from Polymer Standards Service-USA, Inc (M_n: 2.62, 6.24, 41.4, 109 kg/mol), a series of DSC studies were conducted to compare the glass transition temperature, T_g, of PS standards and PS-modified fullerene stars as a function of molecular weight.

Polymer- $C_{60}PS_6$ *Blend Preparation*

The preparation procedure for $C_{60}PS_6$ blends is the same as that used for WAXS studies of pristine C_{60}-polymer systems. PS and $C_{60}PS_6$ were separately dissolved in toluene, sonicated for 30 minutes, then combined to give blends with 10, 20, and 50 wt% $C_{60}PS_6$ relative to the PS in solution. Polymer- $C_{60}PS_6$ solutions were further sonicated for 30 minutes to fully mix before precipitation into cold, stirred methanol (non-solvent). The solid precipitate was then vacuum filtered and dried before measurements using wide angle x-ray scattering. WAXS measurements were conducted using the same setup and method described previously. Blends were measured as prepared and after annealing at 100 °C. No difference was noted in measurements before and after annealing.

3.4.2 Characterization of Polystyrene Functionalized C_{60}-Polymer Blends

DSC Studies

The T_g values measured for the PS standards are shown below in Table 7 with the corresponding molecular weights of the polystyrene used. As expected the T_g increases with increasing molecular weight for PS, depicted more clearly in Figure 49 where the T_g is shown in increase before leveling off at higher molecular weights.

Table 7. Glass transition temperatures (T_g) measured using DSC for polystyrene standards of varying molecular weight.

PS Standard M_n (g/mol)	***T_g (°C)***
2620	85.0
6240	98.9
41,400	110.1
109,000	107.0

The fullerene stars were then measured and compared to the reference plot prepared for T_g (°C) based on molecular weight of the PS standards (Figure 49, black circles). The glass transition temperatures determined for the two PS-modified fullerenes investigated using DSC with PS arm molecular weights of 2.2 and 6.6 kg/mol are provided in Table 8. These values are then plotted in Figure 49 against the molecular weight of the individual PS arms (red triangles) and also against the molecular weight of the entire PS-modified fullerenes (green squares) for comparison.

Table 8. T_g as measured using DSC for fullerene-core PS stars of two different molecular weights.

PS Arm M_n (kg/mol)	***T_g (°C)***
2.2 (total M_n: 13 kg/mol)	94.1
6.6 (total M_n: 38 kg/mol)	78.0

As shown in Figure 49, the T_g of the fullerene stars when plotted against the molecular weight of the individual polystyrene arms fall on the reference plot for T_g as a function of pure PS molecular weight. Based on these results, we have concluded that the PS-modified fullerenes behave like polystyrene chains of a molecular weight equivalent to the individual PS arms. This behavior has implications in terms of miscibility of the stars in a PS matrix but is also important to understanding the behavior and effects these stars will have on the morphology and phase behavior of a block copolymer system as discussed in Chapter IV.

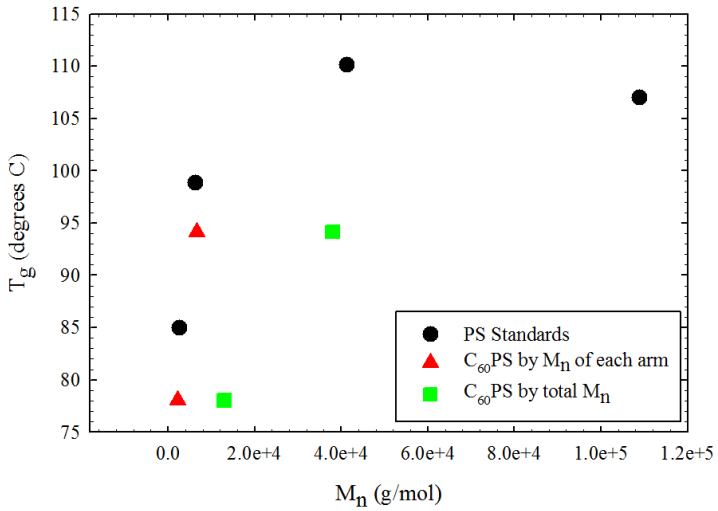

Figure 49. Glass transition temperatures measured using DSC for PS standards of varying molecular weight (black circles) and PS-modified fullerene stars plotted based on PS arm molecular weight (red triangles) and total star molecular weight (green square). T_g values can be found in Tables 7 and 8 for PS standards and fullerene stars respectively.

WAXS Studies of $C_{60}PS_6$-Polystyrene Blends

As with pristine fullerene-polymer blends discussed previously, WAXS was used to characterize our ability to disperse PS-modified fullerenes in a polystyrene matrix. Blends of 10, 20 and 50 wt% fullerene stars were prepared using fullerene stars with 2000 g/mol molecular weight PS arms. The WAXS data are shown in Figure 50.

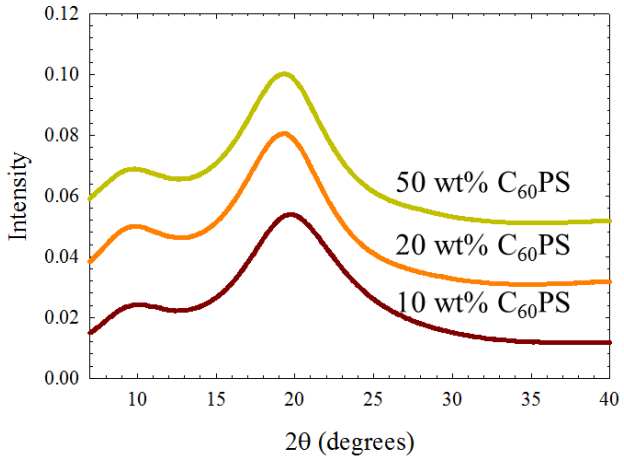

Figure 50. Wide angle x-ray scattering results for $C_{60}PS_6$-PS blends. Broad peaks associated with polymer scattering are evident, but even up to 50 wt% $C_{60}PS_6$ incorporated, no peaks associated with fullerene aggregation are noted.

The WAXS results indicate that we are able to fully disperse PS-modified fullerene in a PS matrix up to 50 wt%, and the PS arms provide enough shielding to prevent fullerene aggregation in the blends. These results further suggest that we can incorporate large concentrations of fullerene stars into a polystyrene-based block copolymer system.

There are drawbacks to using polymer-modified fullerenes to disperse the fullerenes in a polymer matrix, largely due to the fact that modification of the fullerene cage was shown to result in the loss of the endohedral element in the case of $N@C_{60}$. Also, the number of fullerenes that can be incorporated is diluted by the presence of the polymer arms. As an example, in a system with six 2000 g/mol PS arms attached the fullerene cage, only 6 wt% of the pure material (prior to incorporation into a PS matrix) is actually C_{60}. Furthermore, the quantity of C_{60} is further diminished with the addition of the star to a

polymer matrix; however, the quantity of fullerenes incorporated using this technique is still larger than that achievable with pure C_{60} in a polystyrene matrix (<1 wt%) [147].

3.4.3 Conclusions, Implications, and Future Work

PS-modified fullerenes show essentially unlimited miscibility in a PS matrix. WAXS studies $C_{60}PS_6$-PS blends do not shown any crystalline peaks associated with C_{60} aggregation and resemble the WAXS patterns collected for pure, amorphous PS samples. Additional study of these fullerenes in a symmetric polystyrene-*b*-poly(methylmethacrylate) diblock copolymer will be discussed in Chapter IV. Thermal analysis results indicate that the T_g properties of PS-modified fullerenes behave like PS homopolymers of a molecular weight equivalent to that of an individual PS arm. Further experiments on these systems would be interesting, particularly with regard to systems having fewer than 6 PS arms and PS chains of lower molecular weight. Achieving dispersion while making minimal modification to the fullerene cage would allow for an overall increase in the quantity of fullerene added to a block copolymer matrix.

3.5 Polymer-Fullerene Interactions: Overall Conclusions

Studies regarding polymer interactions with fullerenes have led us to a clearer understanding of the structural factors in a polymer that enhance miscibility with C_{60}. As described, improving miscibility relative to a comparison system of polystyrene is necessary to achieving dispersion of fullerenes in a block copolymer matrix and further alignment driven by the microphase separation structure. We have determined that conjugation, aromaticity, and molecular conformation all play important roles in fullerene interactions with polymers. The relative importance of each contribution depends on the

system being studied. For fluorescent conjugated polymers such as the PPEs discussed here, the conjugation in the polymer backbone drives the interaction with the fullerene, and results in a formation of strong charge-transfer complexes. However, the polymer backbone in the case of the vinyl polymers (PS, P2VN, and P9VPh) limits the ability of the aromatic functional groups to orient and maximize interaction with the C_{60} cage. Instead, in these cases, miscibility is enhanced by the ability of the P9VPh phenanthrene moiety to conform to the curvature of the fullerene sphere. These factors are key to selecting an appropriate block copolymer system for the alignment of pristine fullerenes.

Lastly, we have shown that an additional approach to incorporating fullerenes into a polymer matrix is to modify the fullerene cage with polymer arms. The functionalization is straight forward due to the high reactivity of C_{60}. PS-modified fullerenes in a PS matrix were shown to be well dispersed and were further studied with polystyrene-based block copolymer systems using neutron reflectivity.

CHAPTER IV: BLOCK COPOLYMER-FULLERENE SYSTEMS

4.1 Overview

We have investigated the effects of nanoparticle size on the phase behavior of a symmetric dPS-PMMA diblock copolymer as well as the location and layer formation of the nanoparticle within the diblock copolymer matrix. In this case, the nanoparticle consists of a C_{60} fullerene core with six covalently attached PS chains ($C_{60}PS_6$). Nanoparticle size was controlled by varying the molecular weight of the grafted PS arms. Two different PS arm lengths were synthesized, 2.2 kg/mol (C_{60}PS2) and 6.6 kg/mol (C_{60}PS6). These molecules were incorporated into a dPS-PMMA (15-b-15 kg/mol) diblock copolymer on both clean silicon (PMMA selective) and a PS brush layer grafted to silicon substrates (PS selective). The structures of the assembly were investigated using neutron reflectivity (NR). Film thickness was also varied by controlling block copolymer concentration in solution for pure dPS-PMMA systems on both clean silicon and PS-modified silicon substrates.

While the goal of NR studies was to examine the layer formation in the thickness direction of the film through specular reflectivity, off-specular reflectivity was also detected, indicating some lateral structure to the film as well as structure if the thickness direction. The majority of this chapter is focused on the quantitative analysis of specular results and the structure of block copolymer and block copolymer-nanoparticle films in the thickness direction. However, off-specular results are mentioned as they provide some relevant insight into the overall structure of the thin films, particularly in terms of

the effects of nanoparticle addition on the block copolymer structure. All off-specular data analysis presented here is qualitative and used primarily to support specular results.

4.2 Materials and Methods for Neutron Reflectivity Studies

4.2.1 Materials

With the exception of toluene and styrene, all solvents and reagents were purchased from Sigma-Aldrich and used without further purification: C_{60} (99% purity), *sec*-butyl lithium (1.4 M in toluene), di-butylmagnesium. All polymers were obtained from Polymer Source and used as received. Symmetric poly(deuterated styrene-*b*-methylmethacrylate) (dPS-PMMA) had a reported M_n of 15 kg/mol for each block and PDI of 1.09. ω-Hydroxy-terminated polystyrene was characterized by a reported M_n of 50 kg/mol and PDI of 1.06. HPLC-grade toluene was distilled from sodium benzophenone prior to use. Styrene was purified using a two-step method: (1) calcium hydride (CaH_2) was added (20 mg CaH_2/mL styrene) under argon in a Schlenk flask and held for 12 hours, and (2) styrene was vacuum-distilled into another Schlenk flask containing di-butylmagnesium and then stirred for an additional 12 hours. After purification, the styrene was then vacuum-distilled into a Schlenk tube for polymerization.

4.2.2 Hard-core Polystyrene Star Synthesis

Star polymers composed of C_{60} cores and six polystyrene (PS) arms ($C_{60}PS_6$) were synthesized by addition of living PS anions to C_{60} using a procedure modified from Mathis and coworkers by M. Kincer in the Beckham research lab at Georgia Tech [235]. Star polymers were synthesized with arm molecular weights of either 2.2 kg/mol or 6.6

kg/mol. For the 2.2 kg/mol arms, 3.47 mL of 1.4 M *sec*-butyllithium (*sec*-BuLi) was added to a solution of 9.72 g styrene in about 50 mL freshly distilled toluene contained in a Schlenk flask. Upon addition of the initiator, the solution turned orange which is consistent with the presence of living styryl carbanions. Targeted PS molecular weights were achieved by controlling the stoichiometric addition of initiator to monomer. For the 6.6 kg/mol PS arms, 0.63 mL of 1.4 M *sec*-BuLi was added to a solution of 5.53 g styrene in about 50 mL freshly distilled toluene. After 10 hours, a small amount of the living PS was removed from the Schlenk tube for molecular weight analysis by GPC. To form the stars, the living PS was added (10 moles PS/mole C_{60}) to a solution of 50 mg of C_{60} in approximately 100 mL freshly distilled toluene and stirred for 2 hours. The color of the C_{60} solution changed from purple to brown upon addition of the PS. Deactivation of the anionic charge on the fullerene cage was achieved by addition of methanol. Precipitation of the fullerene stars was induced by further addition of methanol allowing for isolation by filtration. Purification of the fullerene stars was achieved by fractionation using THF as solvent and methanol as non-solvent. The yield of the fullerene stars after isolation and purification was 90%.

Molecular weights of the fullerene stars were determined using gel permeation chromatography (GPC) employing polystyrene standards. The GPC was conducted in toluene on a Waters 2410 Separations Module equipped with Waters Styragel HR 4, 3, and 1 columns and a Waters 410 differential refractive index detector. Molecular weights were confirmed to be 2.2 kg/mol (C_{60}PS2) or 6.6 kg/mol (C_{60}PS6) per arm, with an average of six PS arms grafted to each fullerene cage in both cases.

4.2.3 Thin Film Preparation on Silicon Substrates

Thin films of varying thickness of pure block copolymer were prepared by dissolving dPS-PMMA in toluene to give 4, 6, and 8 wt% solutions followed by spin coating at 2500 rpm for 30 seconds on piranha-cleaned silicon (70% H_2SO_4, 30% H_2O_2 by volume at 100°C for 30 minutes followed by rinse with distilled water). Pure block copolymer thin films were annealed at 175°C for 19 hours. Block copolymer/$C_{60}PS_6$ thin films were prepared under the same spin coating conditions. Using 4 wt% polymer solutions, dPS-PMMA and $C_{60}PS_6$ were mixed and co-dissolved in toluene with increasing amounts of fullerene ranging from 1 wt% to 44 wt% relative to the dPS block. Films were prepared for both C_{60}PS2 and C_{60}PS6 fullerenes and after spin coating on clean silicon wafers were annealed at 175°C for 12 to 24 hours.

4.2.4 Polymer Brush Functionalized Substrate Preparation

Measurements were also conducted on thin films spin coated on an end-grafted PS brush layer on silicon, prepared by methods detailed previously in the literature [7, 236-238]. The brush layer was prepared by spin-coating ω-hydroxy terminated polystyrene in toluene (1 wt%) at 1000 rpm for 30 seconds on piranha-cleaned silicon. The films were then annealed at 150°C, above the PS glass transition temperature (T_g) of 105°C, under vacuum for 48 hours to allow the terminal hydroxy groups to react with the native oxide layer on the silicon. After annealing, samples were rinsed and sonicated three times with toluene to remove any un-reacted polymer. Solutions of pure dPS-PMMA (4, 6, and 8 wt%) and dPS-PMMA/$C_{60}PS_6$ (4 wt% polymer in solution) in toluene were then spin

coated at 2500 rpm for 30 seconds on top of the grafted PS brush layer and annealed at 175°C for 24 hours.

4.3 Neutron Reflectivity Studies: Measurement Techniques and Data Analysis

Neutron reflectivity measurements were conducted on the variable wavelength Liquid Reflectometer 4B at the Spallation Neutron Source at Oak Ridge National Lab (Oak Ridge, Tennessee). The reflectometer set up used at Oak Ridge National Lab (ORNL) is shown below in Figure 51. All samples were measured as prepared and after annealing. The chemically modified substrates were also measured prior to spin coating of dPS-PMMA thin films. Given the wavelength range of $2.5 < \lambda < 6$ Å for this reflectometer, we measured reflectivity at multiple incident angles (θ = 0.15°, 0.25°, 0.35°, 0.449°, 0.65°, 0.849°, 1.60°, and 2.8°) to provide data over an extended Q-range. The resolution ($\delta Q/Q$) of the instrument determined by fitting the reflectivity data from D_2O standard was found to be 0.078.

Figure 51. Liquid Reflectometer, Beamline 4B at the Spallation Neutron Source, Oak Ridge National Lab in Oak Ridge, TN. All neutron reflectivity measurements were conducted using this set up.

The ideal coherent scattering length densities (SLDs) of dPS, PMMA, PS, silicon oxide (SiO*x*), and Si (substrate) used were 6.41×10^{-6}, 1.07×10^{-6}, 1.41×10^{-6}, 3.20×10^{-6}, and 2.07×10^{-6}, respectively, in units of $Å^{-2}$. All relevant values for maximum SLD are provided below in Table 9. The neutron reflectivity curves were fit using statistical error minimization techniques until the agreement between the calculated reflectivity and the experimental reflectivity data was suitable. The resulting scattering length density profiles, SLD versus thickness, *z*, were then used to determine the structure of thin films in the thickness direction to assess the formation and location of a fullerene layer within the deuterated PS block of the block copolymer.

Table 9. Neutron Reflectivity ideal scattering length densities (SLD) for relevant compounds.

Compound	*SLD ($Å^{-2}$)*
Polystyrene (PS)	$1.41x10^{-6}$
Deuterated Polystyrene (dPS)	$6.41x10^{-6}$
C_{60} fullerene	$5.73x10^{-6}$
Poly(methylmethacrylate)	$1.07x10^{-6}$
Silicon oxide	$3.76x10^{-6}$
Silicon	$2.07x10^{-6}$

The materials used for NR studies were selected specifically to allow us to be able to determine the location of fullerene stars through changes in the SLD at different fullerene star loadings. In this case, the PS-arms attached to the fullerene cage were hydrogenated, where PS has a SLD of $1.41x10^{-6}$ $Å^{-2}$, vastly different from that of deuterated PS ($6.41x10^{-6}$ $Å^{-2}$). Although the fullerene cage itself has a relatively high SLD, calculated to be $3.33x10^{-6}$ $Å^{-2}$, the behavior of the fullerene stars is dominated by the six grafted polymer chains. Because of the differences in the SLD between deuterated PS (dPS) and the fullerene stars, the contrast offered by the NR measurements allows the location of the fullerene stars to be easily determined from data modeling as the SLD of the dPS block would be reduced due to the presence of hydrogenated $C_{60}PS_6$. The SLD of the PMMA block should remain unchanged due to the addition of PS-modified fullerene stars to the thin films.

4.4 Neutron Reflectivity Studies of Pure Block Copolymer Thin Films

Pure block copolymer thin films of symmetric dPS-PMMA have been studied extensively using NR techniques. We conducted a series of experiments on pure dPS-PMMA thin films on silicon and PS brush layers for comparison purposes, both to previous literature as well as block copolymer-nanoparticle systems discussed below. Three different factors were manipulated including film thickness (via solution concentration), annealing temperature, and substrate specificity. At all film thicknesses investigated, lamellae were found to be aligned parallel to the substrate, and repeat spacing was determined to be consistent with previous literature. For dPS-PMMA films on silicon, PMMA was found to wet the silicon substrate while dPS was located at the air interface as was also expected. Similarly, dPS wets the PS brush layer on modified substrates and also locates to the air interface.

4.4.1 Pure Symmetric dPS-PMMA Thin Films on Silicon

Qualitative analysis of pure block copolymer films indicates that after annealing thin films of dPS-PMMA of different thickness at 175°C, lamellae aligned parallel to the silicon substrate as indicated by the appearance of Bragg peaks in the reflectivity profile. Figure 52 a.) shows the NR profile of a dPS-PMMA thin film prepared from a 4wt% solution annealed at 135°C for 24 hours while Figure 52 b.) shows the reflectivity from dPS-PMMA films prepared from 2-8 wt% solutions after annealing. Bragg peaks are clearly evident in the NR profiles of samples annealed at 175°C but are not present in the one annealed at 135°C. In Figure 52 b.), particularly for 2 and 4wt% films, Kiessig

fringes are clearly evident where the spacing from minima to minima (or maxima to maxima) provides direct information about the overall film thickness, *d*.

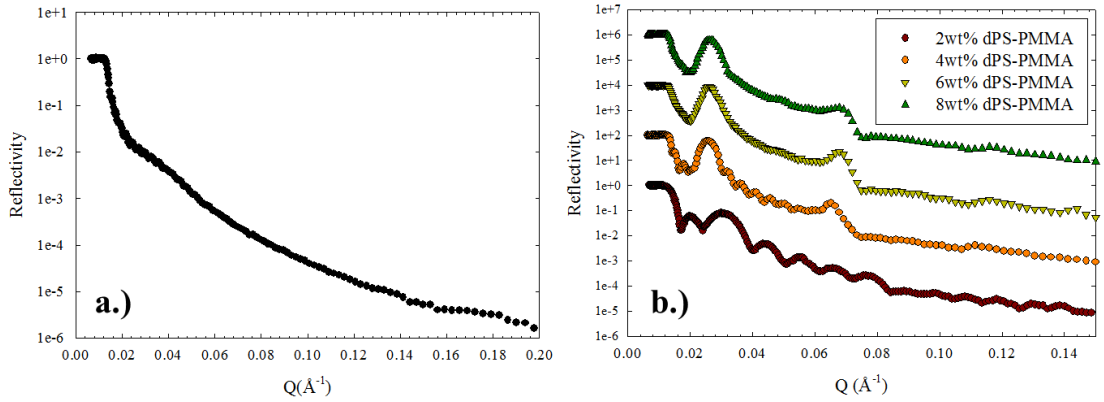

Figure 52. Neutron reflectivity of pure dPS-PMMA annealed at a.) 135°C for 24 hours (4 wt% polymer solution) and b.) 175°C for 24 hours from four different polymer solution concentrations (2, 4, 6, and 8 wt% in toluene). Reflectivity values in b.) are scaled to allow for comparison. Note the absence of Bragg peaks in the reflectivity data of the film in a.) annealed at 135°C.

Fitting of the reflectivity data using a layered model further supports lamellar structure formation parallel to the silicon substrate in the case of pure dPS-PMMA films. Figure 53 shows the results and corresponding model for a pure dPS-PMMA film prepared from a 4 wt% polymer solution. The scattering length density (SLD) profile determined from the model is given as an inset in the reflectivity profile. As expected based on extensive previous research with PS-PMMA systems [239, 240], PMMA wets the unmodified silicon substrate, and the dPS is located at the air/polymer interface. The lamellar repeat spacing was determined to be 287 Å with four repeats with an $L_0/2$ layer of dPS and PMMA at the air/polymer interface and polymer/substrate interface respectively. The

SLD (N_b) values, layer thicknesses (d), and roughness (σ) values used for the model shown in Figure 53 are provided in Table 10. The information extracted from data modeling is consistent with NR measurements conducted using this block copolymer previously by other research groups [154, 239, 240].

Table 10. Modeling parameters used for 4 wt% dPS-PMMA on clean silicon corresponding to the results shown in Figure 53.

Layer	*N_b (Å^{-2})*	*Max N_b (Å^{-2})*	*d (Å)*	*σ (Å)*
dPS	5.97×10^{-6}	6.41×10^{-6}	154	55
PMMA	1.00×10^{-6}	1.07×10^{-6}	133	55

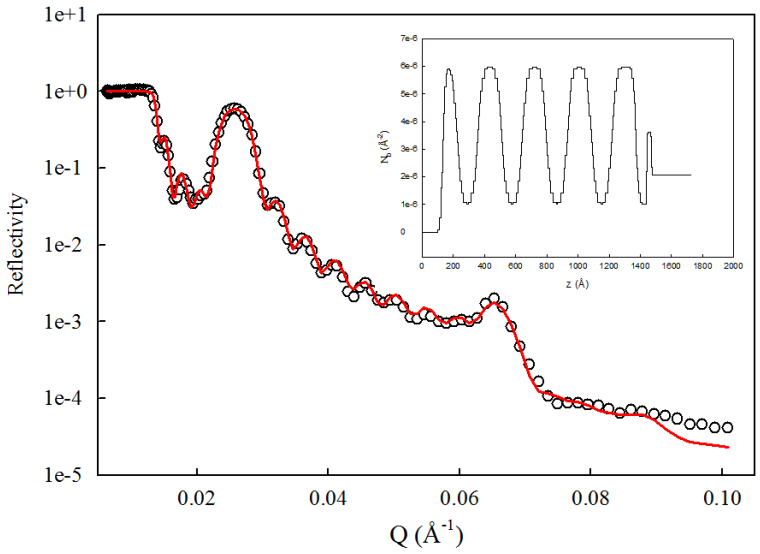

Figure 53. Reflectivity profile for a pure dPS-PMMA thin film prepared on clean silicon from 4 wt% polymer solution and annealed at 175°C with the corresponding data modeling (red solid line). The SLD profile is shown in the inset. Total film thickess, d, was determined to be 13.08 nm with 4 repeats and lamellar spacing, L_0, of 287 Å. Layers of $L_0/2$ of dPS and PMMA were present at the polymer/air and polymer/silicon oxide interfaces respectively.

4.4.2 Pure Symmetric dPS-PMMA Thin Films on PS Brush Layer

Block copolymer were similarly studied using neutron reflectivity on silicon substrates modified with a PS brush as shown by Figure 54. The modification of the silicon substrate with a PS layer makes the substrate PS-selective. The results of pure dPS-PMMA films prepared on a PS brush indicate that dPS layers of $L_0/2$ thickness are located at both the polymer/substrate and polymer/air interfaces. A reflectivity profile of a PS brush is shown in Figure 55 with the SLD profile from modeling provided in the inset. All PS brush layers were measured using NR prior to the addition of a block copolymer thin film, and modeling results indicate that all PS brush layers ranged in thickness from 40 to 45 nm.

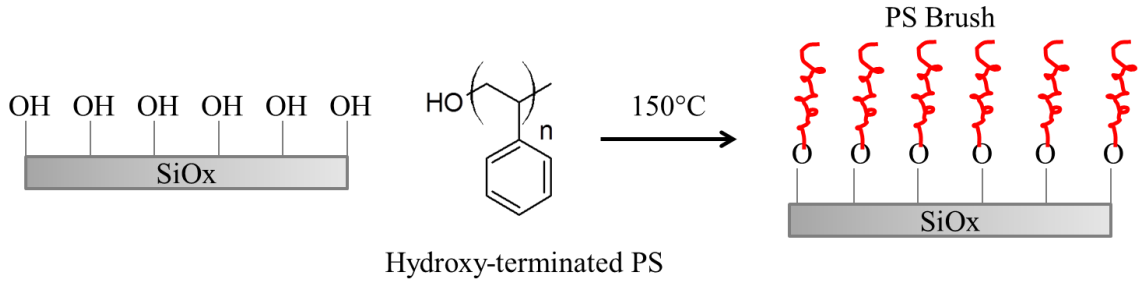

Figure 54. Schematic indicating the structure of PS brush layer on a silicon substrate prior to the addition of a block copolymer thin film. The addition of a dPS-PMMA thin film results in a layer of dPS in contact with the PS brush after annealing.

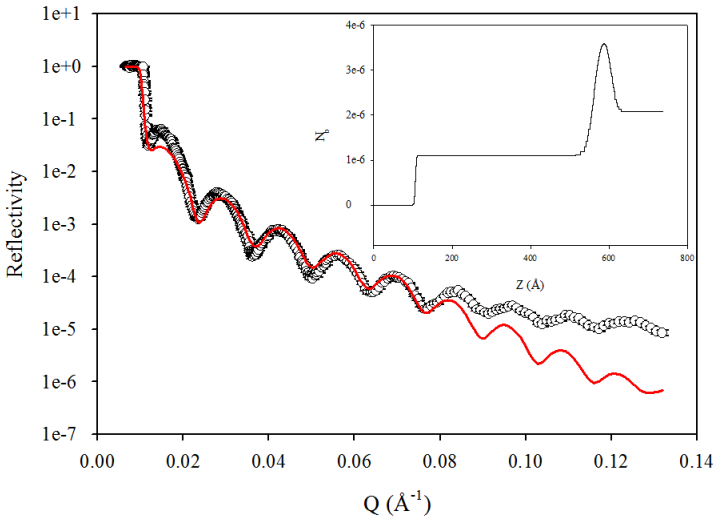

Figure 55. NR profile of pure PS brush end grafted to a silicon substrate prior to deposition of a thin block copolymer film. Modeling (solid red line) gives a film thickness in this case of 455 Å. In general, PS brush thicknesses ranged from 40 to 45 nm.

Analysis of reflectivity profiles for dPS-PMMA films spin coated from 4, 6, and 8 wt% polymer solutions on a PS brush (Figure 56) indicates that lamellae form parallel to the substrate in all cases as shown by the Bragg peaks clearly visible in the reflectivity profiles. Off-specular scattering was noted to be more intense in the case of samples on PS brush in general as compared to the clean silicon samples, but followed a similar trend with increasing intensity with star concentration before disappearing at the highest loadings (44 wt%) of star. The increased intensity of off-specular scattering of thin films on the PS brush is likely due to the added waviness at the PS brush interface.

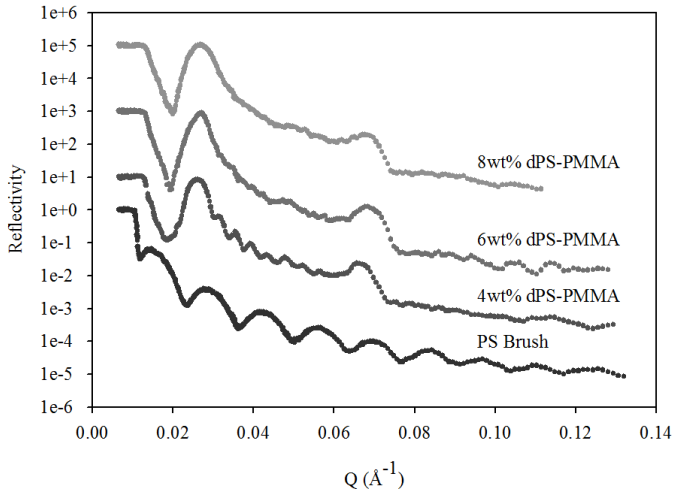

Figure 56. Reflectivity profiles for dPS-PMMA thin films spin coated from 4, 6, and 8 wt% toluene solutions on PS brush-modified silicon substrates. The films were annealed at 175°C prior to NR measurements. NR of a pure PS brush layer is included for comparison. Reflectivity values are scaled for comparison purposes.

Modeling for pure block copolymer thin films on the PS brush indicates that a lamellar structure with repeat spacing, L, of 280Å forms after annealing. The main difference from pure dPS-PMMA films on clean silicon is at the polymer/substrate interface where a dPS layer wets the PS brush as well as localizing to the air interface. The results of data fitting for a pure 4 wt% dPS-PMMA thin film on a PS brush are given in Figure 57. Layer thicknesses, roughnesses, and SLD values were comparable to those used for fitting films on silicon. The lamellar structure remained the same for 6 and 8 wt% films, with the only change in the model being the number of layers and overall film thickness.

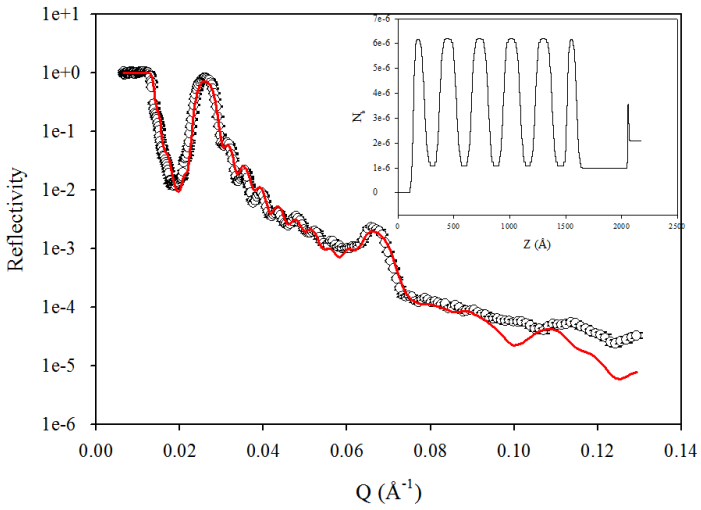

Figure 57. Reflectivity profile with the data fit given as the solid red line for a 4 wt% dPS-PMMA thin film on a PS brush-modified silicon substrate. The SLD profile used for modeling is given in the inset. Results of modeling indicate a dPS layer of $L_0/2$ thickness forms at both the air and substrate interfaces and the lamellar repeat spacing is 280 Å.

4.5 Neutron Reflectivity Studies of Block Copolymer- $C_{60}PS_6$ Thin Films

Symmetric diblock copolymers were combined with polymer-modified fullerenes and studied using neutron reflectivity to determine the conditions required to form a layer of fullerene stars. We examined the effects of nanoparticle size and concentration on the threshold for layer formation as well as effects on the overall structure of the block copolymer thin film. Thin films of dPS-PMMA co-dissolved with polystyrene-modified fullerenes were prepared on both silicon and PS-brush substrates. We found that as in the case of pure block copolymer thin films, lamellae are formed parallel to the substrate after thermal annealing in the case of nanocomposite films. NR results also show that a layer of fullerene stars does form in the PS block for both sizes of nanoparticle; however, the required concentration where this occurs is lower for a larger star. We also note that

at the highest concentrations investigated (44 wt%), the lamellar structure is disrupted by the attempt to accommodate the nanoparticle in the structure.

4.5.1 Block Copolymer/Nanoparticle Thin Films on Silicon

As mentioned previously, two different sizes of nanoparticles were investigated with symmetric dPS-PMMA. Hydrogenated-PS arms were grafted to C_{60} fullerene cages as described in section 4.2.2; due to the natural contrast offered by differences in the scattering length density of hydrogen and deuterium in NR, the hydrogenated nanoparticle location could be determined from the reflectivity data fit as it was assumed that PS-coated fullerenes would fully segregate into the PS block based on previous work with $C_{60}PS_6$/block copolymer systems by Mathis and coworkers [131].

Comparing the NR profiles of the smaller (C_{60}PS2) and larger (C_{60}PS6) nanoparticle systems on silicon, we see the development of a third Bragg peak at lower nanoparticle concentration for the larger particles. The reflectivity profiles for both systems as a function of nanoparticle concentration are given in Figure 58. Both sets of samples were prepared from 4 wt% polymer solutions with the appropriate nanoparticle inclusion concentration. Figure 58 a.) shows that a new structural peak becomes clear at 33 wt% for the smaller particle versus 17 wt% for the larger star as shown in Figure 58 b.). Shifts in the Bragg peaks in both systems to smaller Q ($Å^{-1}$) indicates a change in the lamellar repeat spacing with the addition of $C_{60}PS_6$. Further examination of Figure 58 indicates that the lamellar structure is disrupted by the addition of $C_{60}PS_6$ to the block copolymer system at 44 wt% in both systems as the Bragg peaks become indistinguishable at this nanoparticle concentration in the NR profile.

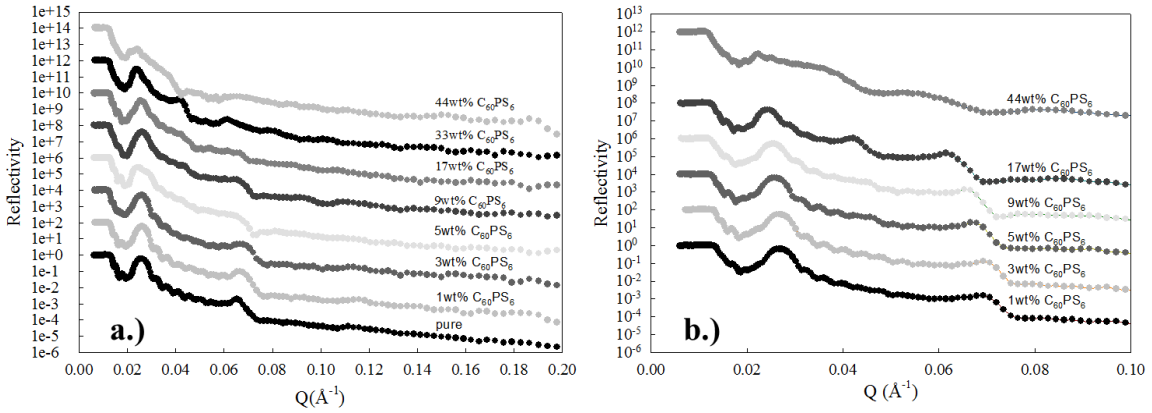

Figure 58. Reflectivity profiles for dPS-PMMA films prepared from 4 wt% polymer solutions on clean silicon substrates. Concentration $C_{60}PS_6$ was varied with respect to the dPS block for a.) $C_{60}PS2$ and b.) $C_{60}PS6$ from 1 wt% to 44 wt%. Reflectivity profiles are scaled here in order to be shown on the same plot for comparison.

Quantitative analysis of the reflectivity profiles overall indicates a reduction in the scattering length density (SLD) of the dPS block with increasing concentration of $C_{60}PS_6$. This supports the assumption that the nanoparticles preferentially locate in the dPS block. At lower fullerene concentrations for both size stars the reflectivity profiles can be fit by using a model of dPS and PMMA layers where the dPS SLD is reduced with increasing concentration of stars. Based on the physical size of the system and previous work on block copolymer/homopolymer [124, 126-128, 240-243] and block copolymer/nanoparticle [31, 32, 139, 244-252] systems, it is most likely that the nanoparticles are located near the chain ends or the center of the dPS block. However, at lower concentrations, less than 33 wt% for $C_{60}PS2$ or 17 wt% for $C_{60}PS6$, formation of a separate $C_{60}PS_6$ layer is not evident from the data fitting. This is most likely because the nanoparticles are at a concentration where interaction with other particles is at a

minimum. Therefore, there is a threshold for layer formation that shows dependence on both the size and concentration of the nanoparticle.

Example data fits for 3 wt% C_{60}PS2 and C_{60}PS6 are shown in Figure 59 and Figure 60 respectively with the SLD profiles given in the inset of each plot. As shown by the SLD profiles, the fullerene stars appear to be evenly distributed among the layers as the SLD is reduced comparably for each layer of dPS within one film and domain repeat spacing is consistent throughout each film thickness. An increase in roughness is also seen with addition of $C_{60}PS_6$ to the dPS-PMMA system that is likely due to distortion of dPS chains to accommodate the nanoparticle within the domain.

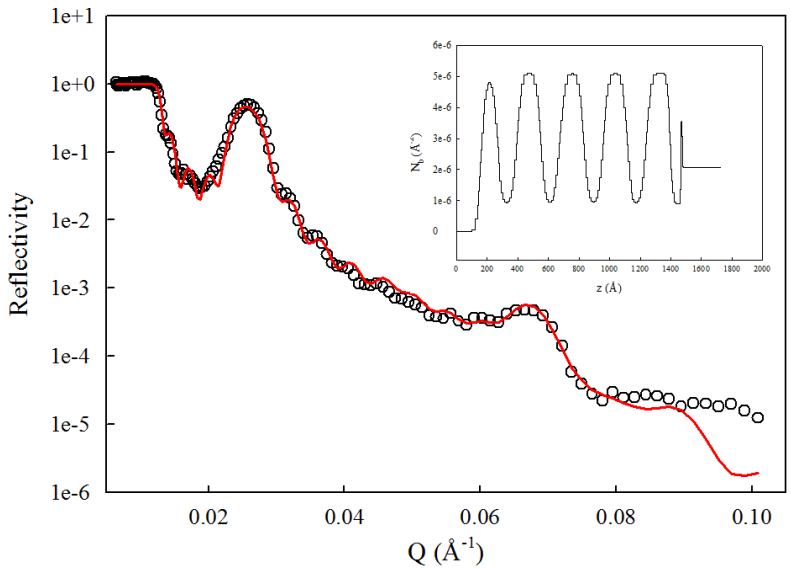

Figure 59. NR profile with model data fit determined using the SLD profile in the inset for 3 wt% C_{60}PS2 fullerene stars. At lower concentrations of fullerene stars, modeling indicates that the stars are located in the dPS block but do not form a distinct layer of fullerenes. The location of fullerenes within the dPS block was shown by the decrease in SLD for dPS due to more hydrogenated material within the layer as well as swelling of the block associated with the additional PS material.

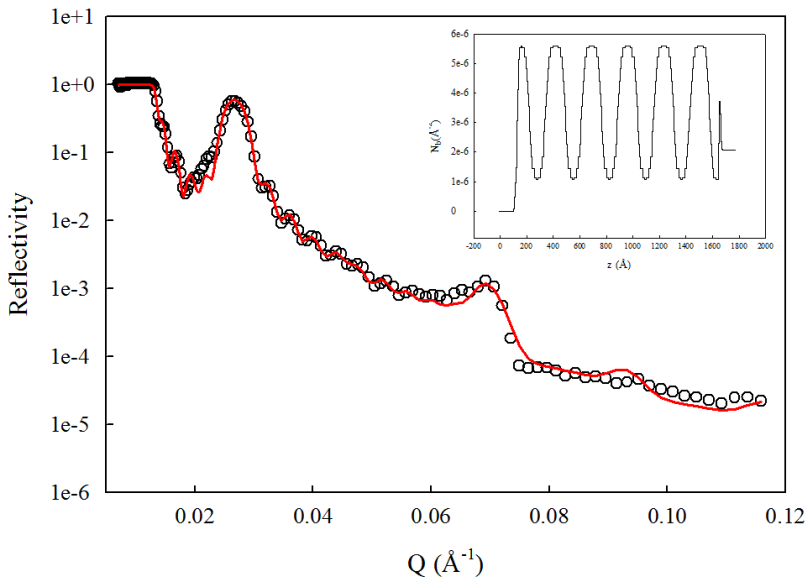

Figure 60. NR Profile with model data fit determined using the SLD profile in the inset for 3 wt% C_{60}PS6 fullerene stars. Modeling results in this case are similar to those for the smaller stars shown in Figure 59 with the main difference being a larger decrease in the SLD for the larger star.

This distortion likely causes some waviness at the interfaces between the dPS and PMMA blocks as illustrated in Figure 62 and increases in frequency at higher star concentrations. As the concentration of $C_{60}PS_6$ stars increases in the dPS block, there is also some swelling of the dPS block similar to that seen with homopolymer/block copolymer systems [124, 126-128, 240-243]. Additionally, the inclusion of the larger star results in a larger drop in the SLD of the dPS layer for a comparable concentration of the small (2.2 kg/mol) star. A comparison of the SLD profiles for a pure dPS-PMMA thin film versus thin films with 1 and 3 wt % C_{60}PS2 is provided in Figure 61. The swelling of the dPS block, roughness increase, and decreased SLD are all evident in this case.

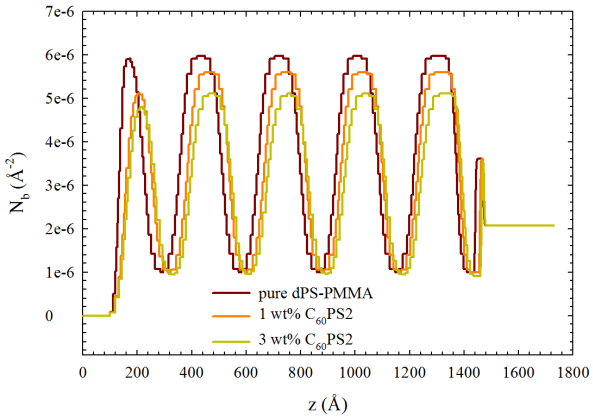

Figure 61. SLD profiles for models of pure dPS-PMMA thin films and thin films with 1 and 3 wt% C_{60}PS2 included. The SLD density of the dPS block decreases, indicating that fullerenes are solubilized in this block. Furthermore, the dPS block swells and the interfacial roughness increases, also consistent with incorporation of the nanoparticles.

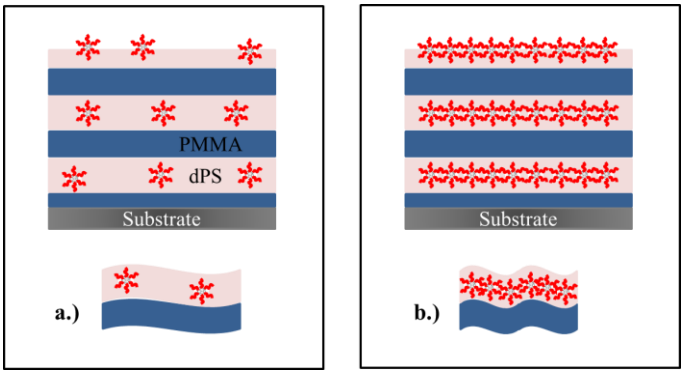

Figure 62. Schematic describing the structure of block copolymer- $C_{60}PS_6$ thin films at a.) lower star concentration (less than 17 wt% for large stars and 33wt% for small stars) and b.) high concentrations (17 and 33 wt% for large and small stars investigated respectively). As described, waviness develops at the interface to allow the dPS block to accommodate the addition of the nanoparticles. This waviness results in an increased roughness at the interface as well as off-specular scattering at length scales corresponding to the Bragg peaks in the specular reflectivity.

Modeling the new structural peak that develops at 17 wt% for C_{60}PS6 and 33 wt% for C_{60}PS2 proved to be more complicated than using the layered dPS/PMMA model with decreased SLD of the dPS block that was used for lower wt% of fullerene star in each case. While this approach was attempted, the model proved to only describe the data when the interfacial roughness was skewed, specifically when the interface at the top of a dPS layer was much rougher than the lower interface. Physically this scenario is not feasible, so the data was fit using a model that assumes dPS and PMMA layers with a $C_{60}PS_6$ layer in the center of the dPS domain. This model also describes the development of a new peak at the same location and is physically a much more likely scenario. Figure 63 shows the data fit assuming C_{60}PS6 layer formation at 17 wt% with the SLD profile describing the model in Figure 64.

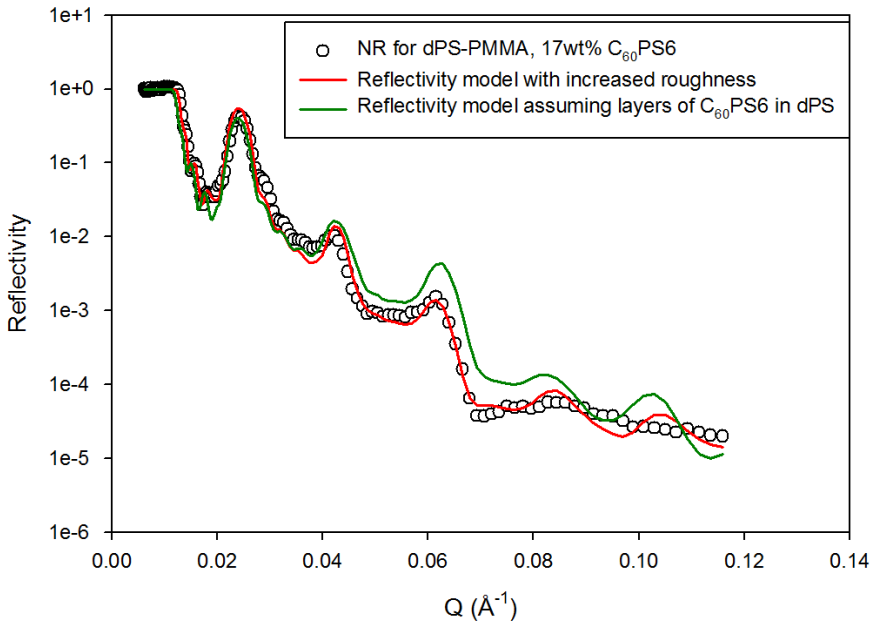

Figure 63. Reflectivity profile with modeling for 17 wt% C_{60}PS6. Two different potential models are shown with the solid red line determined from a fit assuming a large disparity in roughness between the top and bottom interfaces of a block of dPS and the solid green line assuming layers of C_{60}PS6 at the center of each dPS block.

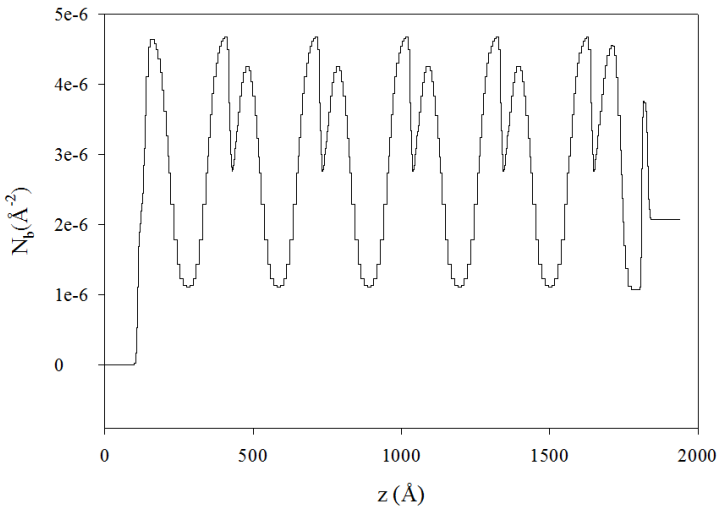

Figure 64. SLD profile for model fit shown in green for 17 wt% C_{60}PS6 in dPS-PMMA on silicon in Figure 63. The dips in SLD at the peaks (dPS layer) are due to the formation of layers of fullerene stars that have a lower SLD than deuterated PS.

It should also be noted here that off-specular reflectivity occurs weakly in the pure block copolymer system on silicon and increases in intensity with increasing $C_{60}PS_6$ concentration before dropping off in intensity again and disappearing at the highest star concentrations. The off-specular scattering may be related to waviness at the interface (Figure 62), particularly as it occurs at the same Q as the Bragg peaks and is therefore associated with structure of the same length scale as the domain repeat distance. The waviness increases in frequency with increasing star concentration as the fullerenes are packing laterally closer to one another, supported by an increase in off-specular reflectivity intensity. The off-specular scattering decreases at higher fullerene concentrations as the fullerenes are tightly packed to form a distinct layer within each dPS block and the interfaces are therefore smoother. At the highest fullerene concentrations, off-specular reflectivity is not present due to the fact that the lamellar block copolymer structure is disrupted by the presence of the fullerene stars and distinct

interfaces no longer exist. Off-specular reflectivity is only mentioned here in support of the interpretation of specular reflectivity results.

4.5.2 Block Copolymer/Nanoparticle Thin Films on PS Brush Layer

Block copolymer/$C_{60}PS_6$ systems were also studied with both fullerene star sizes incorporated into thin films on a PS brush layer grafted to a solid substrate. NR profiles for 4 wt% dPS-PMMA films with C_{60}PS2 and C_{60}PS6 are shown below in Figure 65 and Figure 66 respectively. For each system three concentrations of $C_{60}PS_6$ were used including 5, 17, and 44 wt%. Reflectivity values are scaled in order to compare related profiles on the same graph. Modeling of these systems proved to be different when compared to films prepared on unmodified silicon in that no $C_{60}PS_6$ layer formation was noted. There is a third peak in the reflectivity profiles of both sets of samples at all concentrations of fullerene stars; however, unlike previous samples, this third peak is due to the PS brush layer and not associated with fullerene star layer formation.

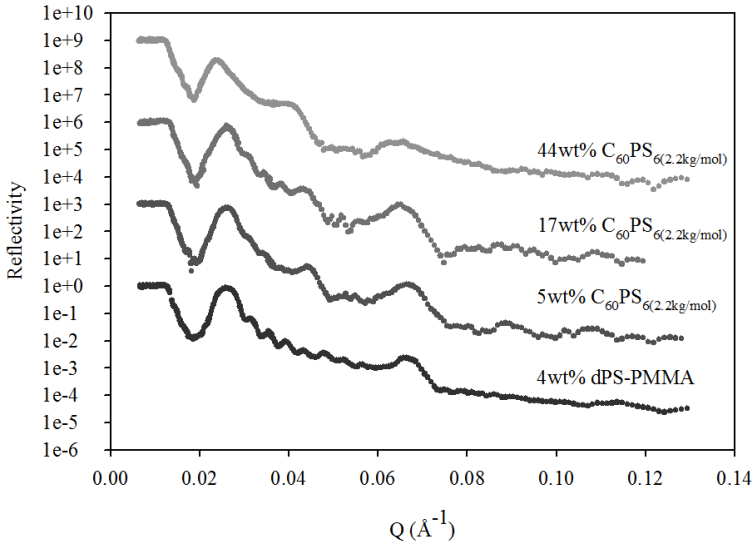

Figure 65. NR results for C_{60}PS2 (noted as $C_{60}PS_{6(2.2kg/mol)}$)on PS brush for 5, 17, and 44wt% small fullerene star with respect to dPS in the system. As indicated by the Bragg peaks clearly evident in the NR profiles, lamellae form parallel to the substrate after annealing at 175°C for 24 hours.

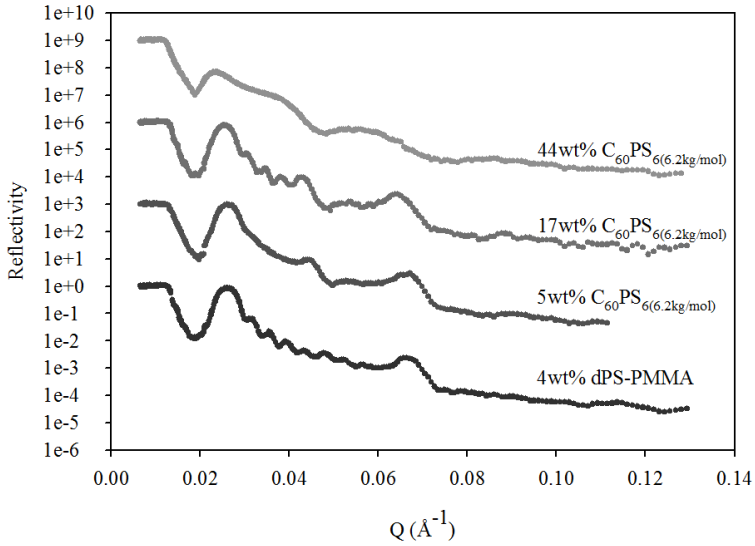

Figure 66. NR results for the C_{60}PS6 (noted as $C_{60}PS_{6(6.2kg/mol)}$) on PS brush at 5, 17, and 44 wt% large fullerene star relative to dPS in the system.

Data fits for 5 and 17 wt% of both fullerene systems (Figure 67 and Figure 68) indicate that the dPS SLD decreases and thickness increases with increasing fullerene concentration, but no clear distinct layer is formed. It is evident that the stars are located within the dPS block based on the swelling and decreased SLD due to the hydrogenated nature of the modified fullerenes as shown by the SLD profiles in Figure 67 and Figure 68. The effects of fullerene star inclusions on the thickness, roughness, and scattering length density shown in Figure 69.

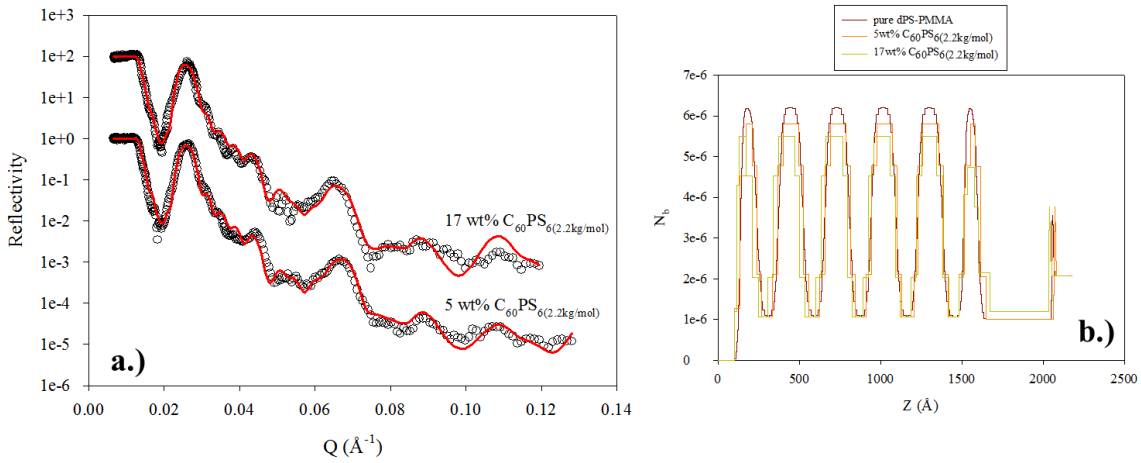

Figure 67. a.) NR results for dPS-PMMA with 5 and 17 wt% of fullerene star, C_{60}PS2, on a PS brush with modeling results (solid red line) as determined from the SLD profiles shown in b.) Modeling indicates that the fullerene stars are located within the dPS blocks as expected but no distinct layer formation of stars is seen with these films. The location of the fullerenes within the dPS block is clear based on the decreased SLD and increasing thickness of dPS lamellae with increasing star concentration as shown in b.).

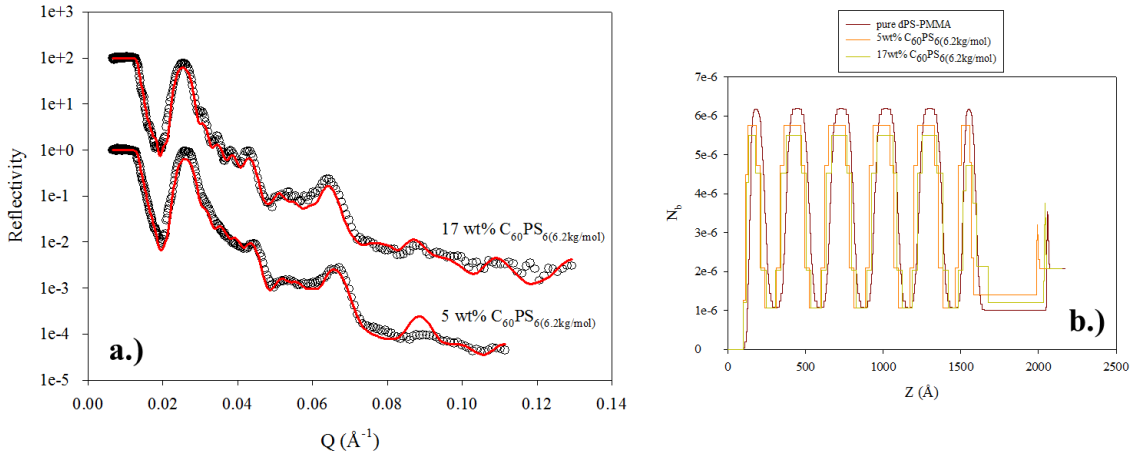

Figure 68. a.) NR results for dPS-PMMA with 5 and 17 wt% of fullerene star, C_{60}PS6, on a PS brush with modeling results (solid lines) as determined from the SLD profiles shown in b.). Modeling results are similar to those for the smaller star in terms of location of the fullerene star within the lamellar block copolymer thin film structure. In the case of the large star, distinct layer formation was not noted in the samples measured on the PS brush.

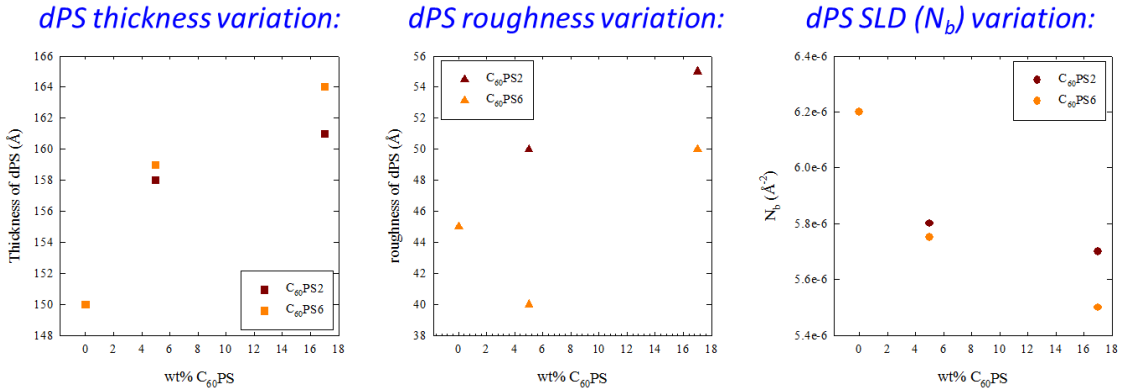

Figure 69. Effects of fullerene star addition on solubilizing block thickness, roughness, and scattering length density in dPS-PMMA thin films on a PS brush layer. Red symbols correlate to the C_{60}PS2 system and orange to the C_{60}PS6 system.

However, modeling of the NR results for thin films with fullerene stars on a PS brush do not indicate the formation of clearly defined layers of fullerenes within the dPS block at the concentrations studied. This may be due to the fact that fewer stars are located within

each dPS layer for the comparable concentration of fullerenes on a clean silicon substrate. It is likely there are fewer stars per dPS layer due to the PS brush layer where some fullerenes are also likely located. Because the number of layers is small, the quantity of fullerenes located in the PS brush layer could be significant. The detection of fullerenes within the PS brush is not as simple as the stars and PS brush layer are both hydrogenated materials with similar SLD values. It is likely that the fullerene stars do form a layer at a concentration between 17 and 44 wt% as there is no physical reason why this should not occur.

The NR results for 44 wt% of both stars in PS brush systems were not able to be fit as the lamellar structure is largely disrupted by the higher concentration of fullerene stars as shown by the raw reflectivity data in Figure 65 and Figure 66. The off-specular scattering also disappears at these concentrations, most likely due to the lack of clearly defined, and therefore wavy, interfaces that we believe are responsible for the off-specular scattering.

4.6 Conclusions and Future Work: Block Copolymer/Fullerene Systems

Our studies on block copolymer/fullerene systems have shown that we can confine fullerenes that are modified with polystyrene chains of varying molecular weight in a symmetric block copolymer system. In fact, we can achieve distinct layers of fullerenes located at the center of a dPS lamellae as shown by neutron reflectivity. The formation of these layers is dependent on both size and concentration of nanoparticle but does occur in both cases investigated. Substrate modification with a PS-brush has also been shown to affect the concentration at which layers of fullerenes are achieved, most likely because

PS-modified fullerenes not only locate in the PS block of the diblock copolymer but also segregate to the PS brush layer.

In addition to the results in terms of the layer structure in the film thickness direction obtained from specular reflectivity results, a combination of the increased roughness with increasing fullerene concentration with off-specular scattering has led us to the conclusion that a wave-like structure forms at the PS/PMMA interface due to the accommodation of the fullerene within the PS block. This waviness at the interface may be similar in nature to the "chevron" morphology associated with buckling in aligned thin films of lamellar block copolymers [253, 254], or a more likely scenario is that the waviness is associated with the transition from lamellar morphology to cylindrical PS microdomains due to swelling of the PS block. The off-specular scattering occurs at the same Q position as the Bragg peaks associated with lamellar stacking in specular scattering, and therefore the off-specular can be associated with lateral order on the same length scale as the lamellar repeat spacing. At this time, only qualitative analysis of off-specular reflectivity has been performed, and better understanding can be achieved by analyzing the off-specular scattering quantitatively. This, however, is not as straight forward as modeling specular reflectivity and will require further effort in the future.

Another area for future research involves using PS-modified fullerenes with fewer grafted arms to determine the effects of less shielding on the incorporation of the nanoparticle into the block copolymer matrix. Additionally, using a block copolymer with a larger molecular weight would allow for studies to be conducted on the effects of size of the nanoparticle on the location within the solubilizing block (interfaces, center, or dispersed). In our case, the low molecular weight limited our ability to study this as the

fullerenes were in general at least on the order of, if not larger than, the solubilizing dPS block. Further study would also be warranted on the alignment of these materials using solvent annealing instead of thermal annealing, particularly when considering applications such as quantum computing with endohedral fullerenes where materials are unstable at higher temperatures. Lastly, insertion of PS-modified fullerenes into cylinder-forming block copolymer systems would be of interest for future studies to determine if long, linear chains of fullerenes can be achieved by alignment along the cylindrical long axis.

CHAPTER V: LANGMUIR AND LANGMUIR-BLODGETT FILMS OF AMPHIPHILIC FULLERENE DIMERS

5.1 Overview

Fullerenes are notoriously poor materials for Langmuir and Langmuir-Blodgett films due to the highly hydrophobic nature of the fullerene cage [35, 37-39, 41, 42]. A variety of approaches have been investigated to form stable monolayers of pristine fullerenes at the air/water interface including using matrix molecules to mediate the fullerene-water interaction and adding a chemical agent to the water sub-phase to promote fullerene spreading. However, the majority of success regarding fullerene monolayer formation using the Langmuir approach has been through modifying the fullerene cage to be more amphiphilic with ligands to mediate the interaction between the water sub-phase while also dictating the interaction between neighboring fullerenes.

Fullerene monomer systems have been studied extensively through direct modification of the fullerene cage with anywhere from one to six adducts, and the behavior of a variety of modified fullerene monomers is relatively well characterized at the air/water interface. We, however, are interested in fullerene dimer materials, which are likely to have different behavior at the air/water interface. Typically dimers are synthesized with ligands on the bridging unit between cages in order to improve solubility of the dimers with common organic solvents. We have taken advantage of these modifications to tailor our dimer systems to be more ideal Langmuir materials by addition of either two hydrophilic poly(ethylene glycol) (PEG) ligands or one PEG ligand and one hydrophobic ligand on the dimer bridge.

Discussed in this chapter below are first the Langmuir isotherm studies using a series of these fullerene dimers in order to determine if monolayer formation was possible with these materials, and then to ascertain the structure of the film. Second, Langmuir-Blodgett monolayer transfer was studied on silicon substrates for the dimers, and films were characterized for their thickness, uniformity, and surface chemistry. Combining the data from LB monolayers and Langmuir isotherms we were able to determine that we can tune the relative angle of the fullerene dimer long-axis with respect to the substrate through simple variations in the ligand chemistry. Lastly, we studied multilayer transfer on both clean and chemically-modified silicon substrates. Multilayer transfer on clean silicon proved to be challenging, but repeatable success of multilayer transfer was shown on chemically-modified silicon substrates.

5.2 Materials: Amphiphilic Fullerene Dimers

A series of amphiphilic fullerene dimers were synthesized by our collaborators at the Quantum Information Processing Interdisciplinary Research Collaboration at Oxford University. These dimers were structurally designed specifically for use as Langmuir and Langmuir-Blodgett (LB) materials where the extremely hydrophobic nature of the fullerene cage is balanced by the addition of at least one hydrophilic ligand. In the case of all dimer materials investigated, the hydrophilic tail was a short poly(ethylene glycol) (PEG) chain, and the bridge between C_{60} cages also remained unchanged; dimer systems were divided into two categories: those with two hydrophilic "tails" and those with one hydrophilic tail and one hydrophobic tail. The systems investigated for Langmuir and LB film formation are described in detail below.

5.2.1 Modified-Fullerene Monomer

A hydrophilic-modified fullerene monomer with a short PEG chain that is structurally similar to the amphiphilic dimers is shown in Figure 70.

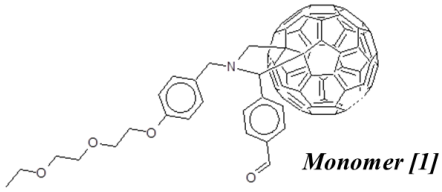

Figure 70. PEG-modified fullerene monomer unit investigated for Langmuir film formation. The hydrophilic PEG ligand serves to balance the hydrophobic nature of the fullerene cage, creating an amphiphilic system potentially capable of producing stable Langmuir films.

This C_{60}-monomer based material was investigated for its Langmuir and LB film formation capabilities as a comparison point for fullerene dimer systems. The monomer is synthesized using a Prato 2+3 cycloaddition reaction at a 1:1 stoichiometry of C_{60} to the amino acid of choice. The reaction is allowed to proceed at ~120°C for 2 minutes before precipitation, purification, and drying of the resulting material. The dimers discussed below are synthesized from this monomer unit.

5.2.2 Fullerene Dimer Systems with Two Hydrophilic Ligands

The first amphiphilic fullerene dimer system investigated using the Langmuir approach is shown below in Figure 71 where the bridge unit between C_{60} cages is functionalized with two PEG oligomers. Symmetric dimers such as this are synthesized in a one-step Prato 2+3 cycloaddition reaction. In order to prepare the dimer the fullerenes are mixed in solution with the amino acid in a 1:2 ratio and proceeds for approximately 5 minutes.

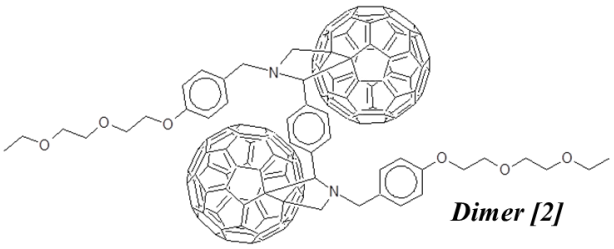

Figure 71. C_{60} dimer system investigated using Langmuir/LB approaches with two hydrophilic PEG oligomers attached to the bridge linking the two fullerene cages.

This dimer was investigated for both Langmuir film formation and Langmuir-Blodgett deposition on a solid substrate. It was expected that the PEG oligomers in this case would balance the hydrophobicity of the fullerene cages and would mediate the interaction between the dimer and the water surface, allowing for Langmuir film formation. It was further anticipated that the PEG units would also provide suitable interaction with the native oxide layer of silicon substrates to allow for monolayer and multilayer transfer of LB films.

5.2.3 Fullerene Dimer Systems with One Hydrophilic and One Hydrophobic Ligand

In addition to the doubly hydrophilic ligand dimer discussed above (dimer ***[2]***), we also conducted experiments with dimers with one hydrophilic PEG chain and one hydrophobic chain of variable chemistry attached to the bridging unit as shown in Figure 72. Asymmetric dimers are synthesized as described, except the reaction is a two-step reaction with two different amino acids.

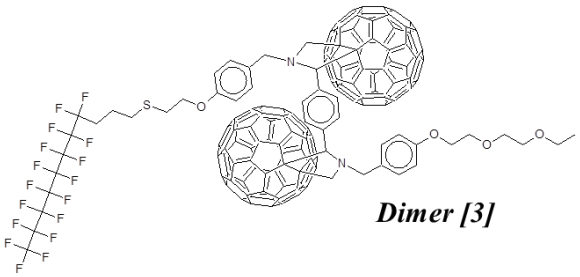

Dimer [3]

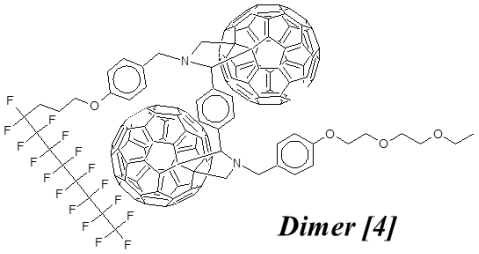

Dimer [4]

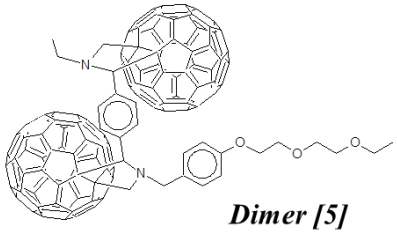

Dimer [5]

Figure 72. Fullerene dimer systems with one hydrophilic PEG chain and one hydrophobic chain of variable chemistry investigated for monolayer formation at the air/water interface and subsequent transfer to solid substrates.

Dimers ***[3]*** and ***[4]*** are structurally similar, with the only difference being the presence of a sulfur group in the middle of the hydrocarbon tail connecting the phenyl ring to the fluorinated chain in dimer ***[3]*** and not ***[4]***, and dimer ***[4]*** having one less carbon atom in this hydrocarbon tail. In both of these dimer system, the hydrophobic ligand consists of a fluorinated carbon tail ($–C_8F_{17}$). Dimer ***[5]***, however, contains a different hydrophobic tail chemistry with just a short, two carbon tail ($–C_2H_5$) serving as the ligand in this case. These materials were investigated using Langmuir isotherm studies and LB film deposition, and results for each of these dimers were compared to each other as well as the doubly hydrophilic dimer system and monomer unit described above.

5.3 Langmuir Isotherm Studies

5.3.1 Materials and Methods

Materials

HPLC grade toluene was purchased from VWR International and used as received for fullerene solution preparation. Nanopure water with resistivity of 18 MΩ cm was used as the sub-phase for all studies. All fullerene materials investigated are shown above in Figure 70, Figure 71, and Figure 72 and were synthesized by our collaborators.

Langmuir Isotherm Studies

Pressure-Area (Π-A) isotherm studies were performed using a KSV Instruments LTD solid PTFE Minitrough with an effective film area of 364 mm x 75 mm and two moving barrier arms. Surface pressure was monitored using a platinum Wilhelmy plate with a resolution of 4 μN/m. The KSV Minitrough was enclosed to minimize the effects of dust

and other atmospheric impurities on the measurements. Nanopure water (18 MΩ cm) was used as obtained from a Barnstead Nanopure Water system as the sub-phase for all isotherm studies. The Langmuir trough was thoroughly cleaned by repeated chloroform and toluene rinses followed by deposition of three Nanopure water sub-phases prior to depositing fullerene material. This process was conducted before each deposition to ensure reproducibility and cleanliness of experiments. The Langmuir trough and experimental set up used for all isotherm studies is shown below in Figure 73.

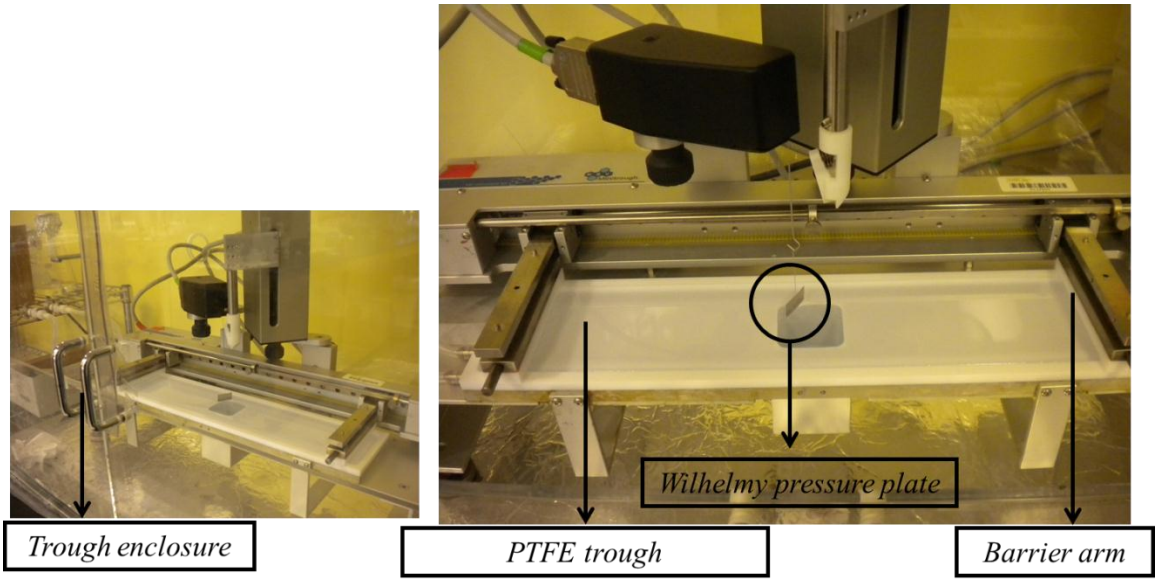

Figure 73. Langmuir-Blodgett trough used for fullerene dimer studies. As shown in the picture on the left, the trough was enclosed to limit atmospheric impurities settling on the water and substrate surface. The image on the right shows the PTFE trough with a deposited Nanopure water sub-phase, pressure plate, and two moving barrier arms.

Solutions of 0.2 mg/ml dimer in toluene were prepared for each of the fullerene systems described above. Monolayers were spread from fresh toluene solutions on a Nanopure

water sub-phase at room temperature. Solution deposition quantities ranged from 70 µL to 200 µL, depending on the molecular weight of each dimer system; the material quantities deposited were determined such that the mean molecular area (MMA) prior to compression was below where the onset of surface pressure was experimentally observed. After allowing 35 minutes for toluene evaporation to occur, compression was started at a rate of 2 mm/min, and surface pressure, Π, was monitored to obtain the Π-A isotherms. Compression was halted prior to the barrier arms colliding with the pressure plate as no monolayer collapse was evident in the isotherms for any of the materials investigated under the conditions described above.

Isotherm cycling experiments with three compression/expansion cycles were also conducted to determine the recoverability of the gas phase. In these experiments, the barrier arms compress the material on the film surface by moving towards one another, and the expansion cycle is achieved by reversing this barrier arm motion, allowing the material to redistribute back across the larger available surface area. Recoverability is useful in determining whether the molecules separate as compression is released; separation of molecules indicates that monolayer formation is not attributed to irreversible aggregation of molecules.

A series of isotherm experiments was also conducted with dimer ***[4]*** in order to determine the effects on compression rate on the isotherm obtained and determine the best rate for compression. Compression rates used ranged from 2 mm/min to 10 mm/min. The setup described above was also used for these studies.

5.3.2 Analysis of Langmuir Isotherms

Langmuir isotherms provide useful information pertaining to monolayer formation, molecular orientation, and packing density for molecules at the air/water interface. Solutions of known concentrations and specified volume are deposited on the water sub-phase. Combining this input with the molecular weight of the deposited molecule and the available trough area based on barrier arm position, the area per molecule is calculated and monitored throughout the compression cycle. Based on what is known about the pressure-area isotherm shape, we can determine if the molecules are isolated, beginning to laterally interact, or are close-packed by monitoring the surface pressure, Π. Based on the area per molecule extracted at a given surface pressure, we can infer information about both monolayer formation and in our case, molecular orientation. The theoretical value for a close-packed monolayer of fullerenes has been determined to be 86.6 $Å^2$ [36, 186], and the empirical value, 96 $Å^2$ [39]. If the area per molecule is determined to be smaller than these values, we can conclude that a multilayer rather than a monolayer is forming at the water surface. Similarly, due to the asymmetry of our dimer structures, values that are on the order of the expected values or larger also give us insight into the orientation of the dimer long-axis and how many fullerenes, of the two possible with a dimer, are located at the air/water interface. Results and conclusions regarding Langmuir isotherm studies are reported and discussed in detail below.

5.3.3 Results and Discussion of Langmuir Isotherm Studies

Isotherms serve as a measure of the surface pressure as a function of the area occupied by each molecule on the sub-phase and can provide information about a system such as

molecular orientation as well as the point of monolayer collapse [19]. Pressure-Area (Π-A) isotherms were obtained for monomer ***[1]*** and dimers ***[2]-[5]***. The isotherms recorded for monomer ***[1]*** and each dimer system are shown in Figure 74 and Figure 75 respectively. Molecular structures are included as insets in each isotherm for clarity.

.

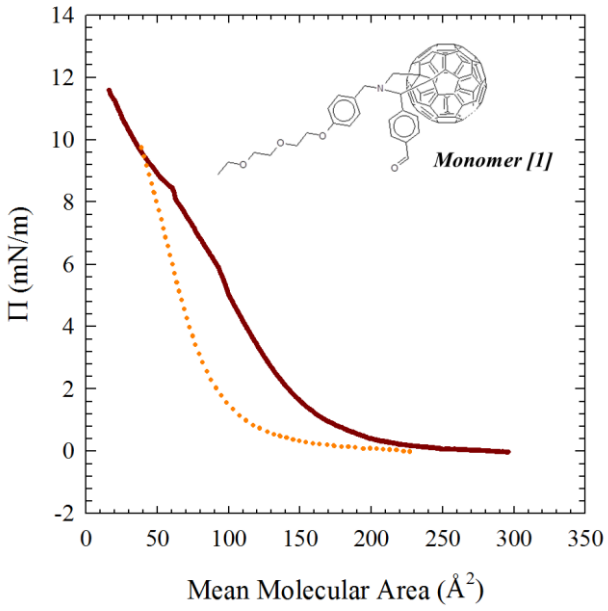

Figure 74. Monomer [1] Π-A isotherms taken from two different depositions under identical conditions. Note the lack of reproducibility in isotherm measurements and monolayer formation (orange versus red).

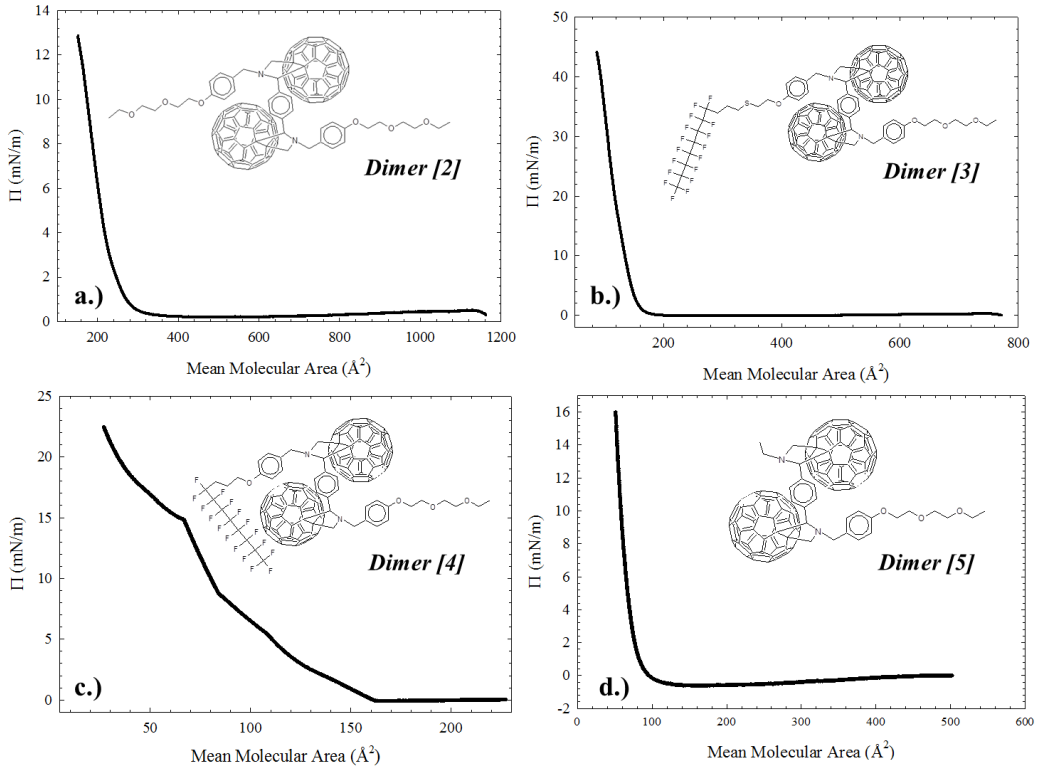

Figure 75. Π-A isotherms for Langmuir film studies on dimers [2]-[5]. The maximum surface pressure achieved prior to pausing compression is different for each dimer for the same deposition quantities, solution concentration, and compression rate. The area per molecule extracted from the condensed solid phase also differs for each system as shown in Table 11.

It is important to note that monolayer collapse, indicated by a sudden decrease in Π, was not observed in any case prior to stopping compression due to the physical limitations of the LB trough barrier arms. All isotherms are depicted on the same plot in Figure 76 for comparison purposes. The starting MMA differs for the all systems due to differences in molecular weight and solution deposition quantities, but as noted previously, the surface pressure was essentially zero when compression was started.

By extrapolating the linear portion of the isotherm associated with the onset of the condensed phase to Π of 0 mN/m, we can determine the area per molecule that would

theoretically occur naturally in an uncompressed close-packed layer. This region of the isotherm is indicated by a sharp increase in slope. In our case this area per molecule, or mean molecular area (MMA), provides insight as to the orientation of the long-axis of the dimer with respect to the water sub-phase. Table 11 below gives the results for the area per molecule determine from isotherms for each material investigated. The differences in area per molecule are also apparent when qualitatively comparing the isotherms for each system as shown in Figure 76; the MMA at the onset of surface pressure as well as the maximum surface pressure achieved before compression was stopped also differ from system to system.

Table 11. Area per molecule information as determined from Langmuir isotherm studies. The theoretically expected value for pure C_{60} is 86.6 $Å^2$ [39] and experimentally determined to be 96 $Å^2$ [36, 186].

Dimer	*Area per molecule ($Å^2$)*
[2]	240
[3]	145
[4]	100
[5]	90
Monomer [1]	70/90

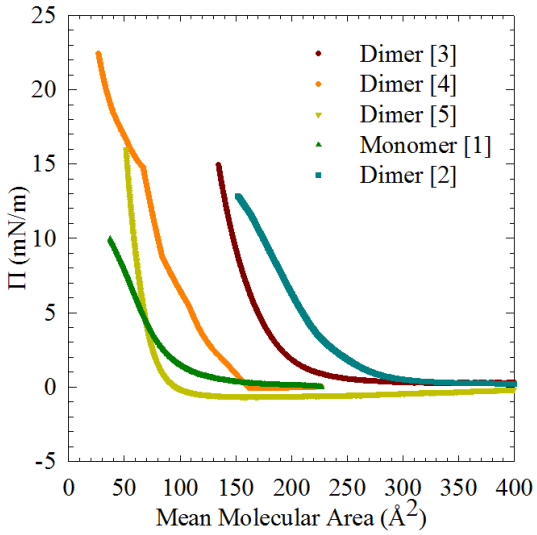

Figure 76. Isotherms for all fullerene systems studied for comparison purposes. Qualitatively, it is apparent from the isotherms that the onset of surface pressure and mean molecular area are different in each case.

As shown by Figure 74, pressure-area isotherms for monomer ***[1]*** are not repeatable under the same experimental conditions. The mean molecular areas extracted from both isotherms are ~70 $Å^2$ and ~90 $Å^2$ for red and orange curves in Figure 74 respectively. These results are similar to those achieved with pristine C_{60} where reproducibility of monolayer formation was proven to be difficult. While an MMA of 90 $Å^2$ would be consistent with the theoretically expected value for the area/molecule of C_{60} (86.6 $Å^2$), this value could not be confirmed through repeated experimentation. Instead, values consistent with the red isotherm in Figure 74 were obtained with area per molecule values on the order of 70 $Å^2$. These values indicate the formation of a multilayer instead of a monolayer due to aggregation of molecules of monomer ***[1]***, similar to multilayer formation noted by Williams et al [42] and others for unmodified C_{60} [38]. The hydrophilic PEG ligand on the fullerene cage of monomer ***[1]*** is likely not shielding

enough to prevent aggregation and may not be long enough to create the necessary hydrophilic/hydrophobic balance for repeatable monolayer formation at the air/water interface. However, dimer monolayer formation was shown to be both successful and highly reproducible as discussed below, at least in part due to the increased comparative rigidity of the perfluorinated tail playing an active role in preventing self-aggregation similar to results reported by Maggini et al [50, 51].

In the case of dimer ***[2]***, the extrapolated MMA is ~240 $Å^2$. Previous work by Obeng and coworkers has shown that the C_{60} monomer area per molecule is around 96 $Å^2$ [39] and the theoretically expected value of 86.6 $Å^2$ [36, 186]; from this we conclude results that the long axis of the dimer system with two hydrophilic PEG oligomers is oriented parallel to the water sub-phase. Due to the hydrophobic nature of the fullerene cage and hydrophilic nature of the tails, we further conclude that both hydrophilic tails are pointed into the sub-phase while the fullerene cage rests at the surface to minimize interaction with water. These interactions are responsible for the alignment of the dimer ***[2]*** parallel to the sub-phase, and the orientation is depicted in the illustration in Figure 77.

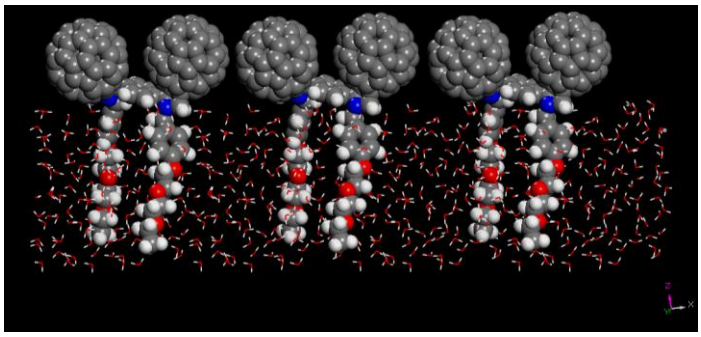

Figure 77. Illustration of fullerene dimers with two hydrophilic PEG oligomers on the bridge linker between C_{60} cages at the air/water interface; dimer [2] aligns parallel to a hydrophilic surface with the hydrophilic tails directed into the water and the hydrophobic fullerenes minimizing contact with the sub-phase.

The onset of surface pressure for ***[3]*** is noted at MMA of approximately 220 $Å^2$ and continues to increase until the limits of the barrier arms are reached at a surface pressure and MMA of 15 mN/m and 145 $Å^2$ respectively. The quantity of solution deposited in this case was 70 µL. Under these conditions monolayer collapse was not noted within the measurement limits. The MMA extrapolated from the linear portion of the isotherm at 15 mN/m to zero pressure gives a mean area per molecule of 145 $Å^2$ as noted above. This value is greater than the theoretically predicted value for a single C_{60} cage of 86.6 $Å^2$/molecule [186, 255] but not double this predicted value that would be the minimum expected if the dimer long-axis were parallel to the water sub-phase. If the dimer were oriented perpendicular to the water surface, we would expect a MMA similar to that of the C_{60} cage. Therefore, we determined the orientation of the dimer ***[3]*** was somewhere between 0° and 90°.

As shown by the simple modeling in Figure 78, we attribute this area per molecule to the dimer long-axis being oriented at an angle to the water sub-phase surface. Based on this area per molecule information from the isotherm and the ***[3]*** monolayer deposition film

thicknesses discussed below, we have calculated this angle to be ~47°. As shown in the model snapshot (Figure 78), the hydrophilic tail interacts with the water while the hydrophobic tail is arranged to minimize contact with the sub-phase. This is true for the amphiphilic dimer systems ***[3]-[5]*** but with a variation in tilt angle. The tilt angle is likely due to a combination of minimizing both hydrophobic tail and fullerene cage contact with the water surface while maintaining PEG oligomer interaction with the sub-phase.

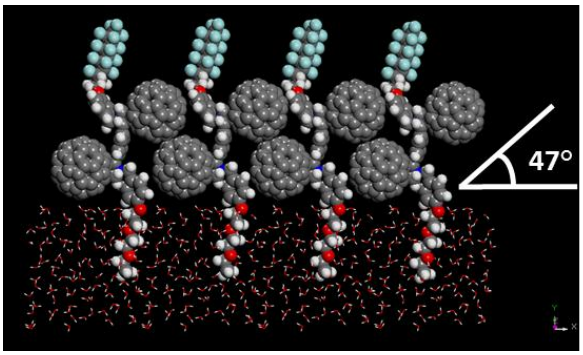

Figure 78. Illustration of dimer [3] on a water sub-phase, indicating the dimer is oriented at an angle between parallel and perpendicular to the sub-phase. This angle was determined to be ~47° and is in agreement with the area per molecule extraction as well as deposited monolayer thicknesses discussed later in the chapter.

Using ***[3]***, we also conducted experiments to determine the reproducibility of the isotherm by taking multiple isotherm measurements on freshly deposited material and comparing the results. Figure 79 shows the results of four different isotherm measurements on this dimer taken on films prepared under the same conditions of solution concentration and compression rate. As shown, the isotherms are reproducible,

having a similar shape and giving similar MMA values for the onset of the condensed phase.

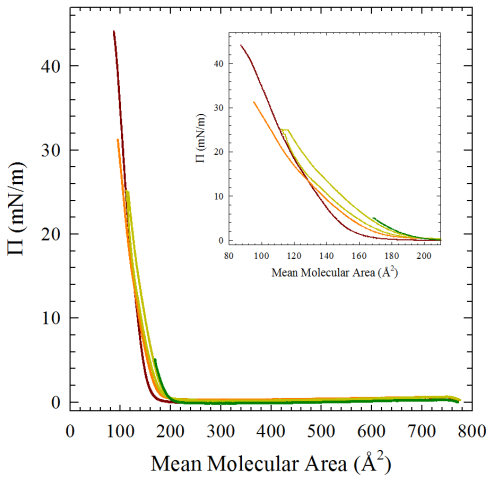

Figure 79. Π-A isotherms for dimer [3] monolayers on a water sub-phase. Each isotherm is taken from freshly deposited films of 70 µL of 0.2 mg/ml solutions of [3] in toluene to determine the reproducibility of the isotherm and monolayer formation.

The isotherm for the dimer ***[4]*** shows that surface pressure begins to increase, indicating the start of the liquid-expanded (LE) phase, at an MMA of approximately 160 Å^2. Unlike the isotherms for the other two dimer systems, the transitions among phases are clearly evident in the ***[4]*** isotherm obtained in Figure 75 (200 µL deposited on Nanopure water subphase). However, there are more steps than would ordinarily be expect in a Langmuir isotherm which traditionally shows the change from a gas-like phase to the LE phase to a condensed solid (CS) phase. The isotherm for ***[4]*** shows five distinct regions, starting with the gas phase leading to the LE transition. The LE phase exists from the beginning

of surface pressure to 3 mN/m where a transition to a third region from 3 mN/m to 8 mN/m is evident. It is likely that this third region is still part of the traditional liquid-like phase and may be attributed to increased interaction of the hydrophobic or hydrophilic tails with each other. The fourth region begins at 8 mN/m and continues to 15mN/m, and we have associated this with the beginning of the CS phase where the dimer long-axis is tilted with respect to the water surface and dimer molecules are close-packed. As compression is continued, a further transition is noted giving rise to a fifth region from 15 mN/m to 23 mN/m that we attribute to the dimers changing their packing structure to become more perpendicular to the water to accommodate the significantly decreased sub-phase surface area available and minimize energy. Figure 80 gives a visual depiction of the likely monolayer structure in each distinct region (I to V) of the ***[4]*** isotherm [157].

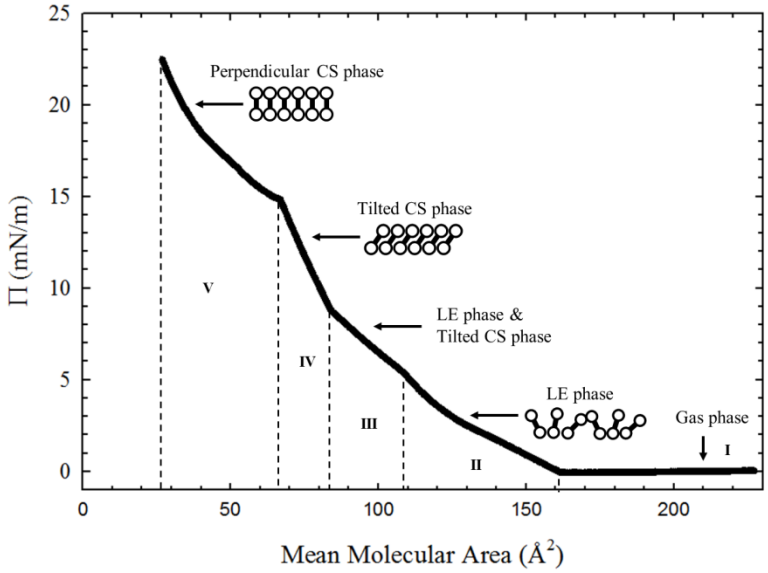

Figure 80. Dimer [4] isotherm showing transitions between five different distinct regions (labeled I to V on isotherm). The monolayer structures for each region are given as insets. Two intermediate phases are noted in addition to the typical gas, liquid expanded, and condensed solid phases.

It is important to note that again monolayer collapse was not evident with dimer ***[4]*** as compression was physically stopped at 23 mN/m to prevent a collision of the barrier arms with the pressure plate. The area per molecule from the extrapolation of the linear slope of the last region of the ***[4]*** isotherm (15 mN/m to 23 mN/m) to zero pressure was determined to be approximately 100 $Å^2$. The ***[4]*** mean area per molecule is similar to experimentally determined values for pristine C_{60} and smaller than that for dimer ***[3]***. This supports the notion that the ***[4]*** dimers are oriented more perpendicular to the water sub-phase than the ***[3]*** as each dimer occupies less area on the water surface, particularly at higher compression where surface pressure is between 15 mN/m and 23 mN/m. The difference in the hydrophobic side chain chemistry between ***[3]*** and ***[4]*** is minimal, but we have shown here that this slight manipulation has a clear and definitive influence on the dimer orientation on a water sub-phase.

The effect of compression rate on the Π-A isotherm was investigated with ***[4]*** using compression rates ranging from 2 to 10 mm/min. For these experiments, 200 µL of 0.2 mg/ml solution were deposited on a water subphase, and films were compressed at 2, 5, and 10 mm/min. Results are given in Figure 81, with the most noticeable effect of compression rate on the isotherm being the ability to distinguish between different phases at low compression rates. At 2 mm/min transitions are clearly identifiable in the isotherm as discussed in more detail while this is lost at higher compression rates. This is likely due to the increased ability of the fullerenes to arrange themselves at the slower compression rate as there more time available for molecular rearrangement. There are no significant differences noted in the onset of pressure and mean area per molecule determined from the isotherms.

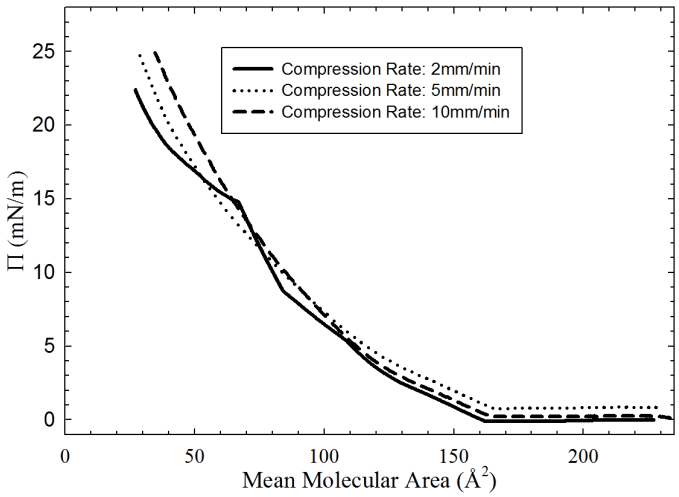

Figure 81. Pressure-area isotherm for the dimer [4] system at different compression rates. Experiments were conducted to determine what effect, if any, compression rate would have on the isotherm and fullerene monolayer behavior.

Finally, the ***[5]*** isotherm also shown in Figure 75 shows behavior that is different from both of the systems discussed previously. Surface pressure onset is seen at an MMA of approximately 100 $Å^2$ for ***[5]*** with a sharp increase from 0 mN/m to 15 mN/m in surface pressure. Extrapolation of the linear slope to zero surface pressure gives an average area per molecule of approximately 90 $Å^2$, on par with that theoretically predicted for a monolayer of pure C_{60}. Because the area occupied per molecule is nearly equal that expected for C_{60}, the likely monolayer structure is such that dimer ***[5]*** is nearly perpendicular to the water sub-phase when close packed such that only one fullerene cage of the dimer is occupying space on the surface.

When comparing the results of isotherms for dimers ***[3]-[5]***, the question then arises as to why dimer ***[5]*** appears to arrange more perpendicularly with respect to the sub-phase. The major difference between dimers ***[3]*** and ***[4]*** versus dimer ***[5]*** is in the chemistry and

resulting flexibility of the hydrophobic ligand. The perfluorinated tail on dimers ***[3]*** and ***[4]*** is significantly more rigid than the short hydrocarbon tail on ***[5]***. The most likely explanation for the difference in orientation is that the rigidity of the $-C_8F_{17}$ tail prevents dimers ***[3]*** and ***[4]*** from being aligned vertically in a monolayer film. Once the hydrophobic fluorinated tails begin to interact, they "lock" and limit the orientation of the dimer with further monolayer compression to an angle less than 90° with respect to the sub-phase. Conversely, the short hydrocarbon is not likely to interact in any significant way with neighboring tails to prevent the perpendicular alignment seen with ***[5]*** due to both the short length and flexibility of the ligand.

Recoverability studies were conducted using dimers ***[2]-[4]*** by completing one compression/expansion cycle on ***[3]*** and three compression/expansion cycles on ***[2]*** and ***[4]*** and analyzing the resulting isotherms. The recoverability of the monolayer is determined by measuring the hysteresis or difference between the compression isotherm and the expansion isotherm. Multiple cycles were completed for dimers ***[2]*** and ***[4]*** to determine if there is any shift to smaller mean molecular area with repeated cycling, also a measure of recoverability as well as stability of the monolayer formed at the air/water interface. In the ideal case, the compression isotherm and expansion isotherms would fall along the same path if monolayer formation is reversible with nearly no hysteresis, and with subsequent compression/expansion cycles, there would be no significant shift in the isotherm to smaller area/molecule.

For cycling experiments on dimer ***[2]*** the barrier arms were compressed until the surface pressure reached 5 mN/m, and the film was then allowed to expand back to 0 mN/m surface pressure before compression was applied again. All three compression/expansion

curves are plotted in Figure 82 with the red, orange, yellow curves corresponding to the first, second, and third cycles respectively. The inset in Figure 82 provides a close-up of the area of interest, where there is measureable surface pressure in the system, and the hysteresis and isotherm shift to smaller mean molecular area (MMA) are more evident in this plot. Specifically, for each compression/expansion cycle the curve at lower and higher MMA are the compression and expansion curves respectively. The flat regions at the top of each cycling curve are due to the experimental setup where the target surface pressure is held steady before the barrier arms are moved to allow for monolayer expansion. The results show that there is approximately 10 $Å^2$ difference between compression and expansion curves for each cycle, and the MMA shifts to a smaller value by 20 $Å^2$ between cycle 1 (red) and cycle 3 (yellow). In the case of each individual cycle, compression and expansion curves result in the same MMA extracted from the upper portion of the isotherm curve, and the degree of hysteresis between curves is minimal. The shift from higher MMA to lower MMA with each repeated cycle is also minimal, indicating that the dimer ***[2]*** monolayer is stable, and dimer ***[2]*** shows behavior typical of amphiphilic molecules.

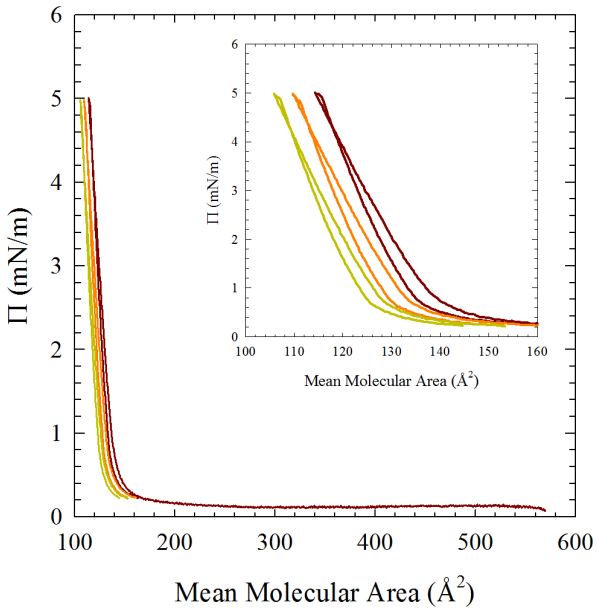

Figure 82. Isotherm cycling experiment results for dimer [2] with two PEG ligands. The entire isotherm is shown with the region of interest shown in the inset. The hysteresis per cycle is ~10 Å^2, and there is a shift of approximately 20 Å^2 from the beginning of cycle 1 (red) to the end of cycle 3 (yellow).

The hysteresis in the case of ***[3]*** was determined to be small at ~10 Å^2, indicating that the molecules separate when compression is removed, and the gas phase is recoverable (Figure 83). This degree of hysteresis is also consistent with both dimers ***[2]*** and ***[4]*** also investigated for their compression/expansion behavior. As with dimer ***[2]***, the flat region at the top of the curve, visible in the inset in Figure 83, results from holding the target pressure for a specified amount of time prior to beginning expansion. The red arrows in the inset indicate the direction of the barrier arms with the upward arrow indicating compression and the down arrow showing expansion. Similar to dimer ***[2]*** studies, the degree of hysteresis between compression and expansion in dimer ***[3]*** isotherm cycling

experiments is approximately 10 Å^2, which indicates that the monolayer formation is reversible and not associated with fullerene aggregation.

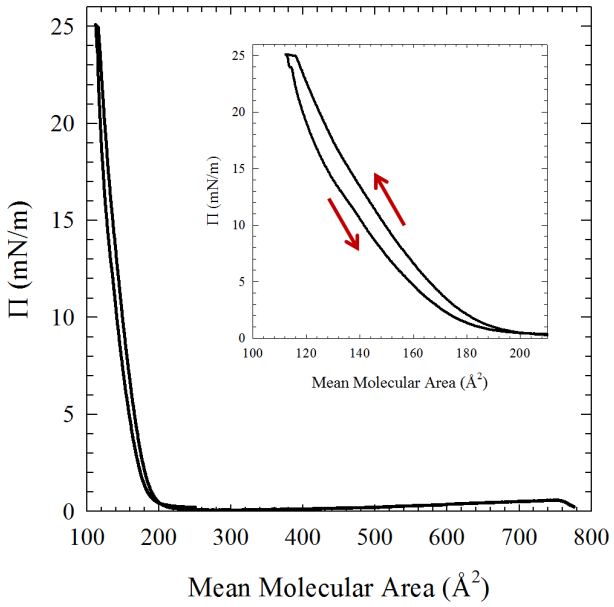

Figure 83. Isotherm cycling experiment with for dimer [3]. One compression/expansion cycle was completed with a target maximum pressure of 25 mN/m. The hysteresis was determined to be ~10 Å^2 between compression and decompression curves (see inset).

Three consecutive compression/expansion cycles conducted on dimer ***[4]*** resulted in similar behavior with reversible monolayer formation and small amount of hysteresis (Figure 84). As with dimer ***[2]***, cycling was conducted by compressing the monolayer to 5 mN/m surface pressure, holding this target surface pressure, and then allowing expansion to occur back to approximately 0 mN/m before beginning the next compression cycle. The hysteresis per cycle (inset, Figure 84) was determined to be

approximately 4 Å^2; furthermore, the isotherm was found to shift to smaller MMA by ~16 Å^2 between cycle 1 (red) and cycle 3 (yellow). These results indicate that the monolayer formation is reversible, and the monolayer formed is stable in the case of dimer ***[4]***.

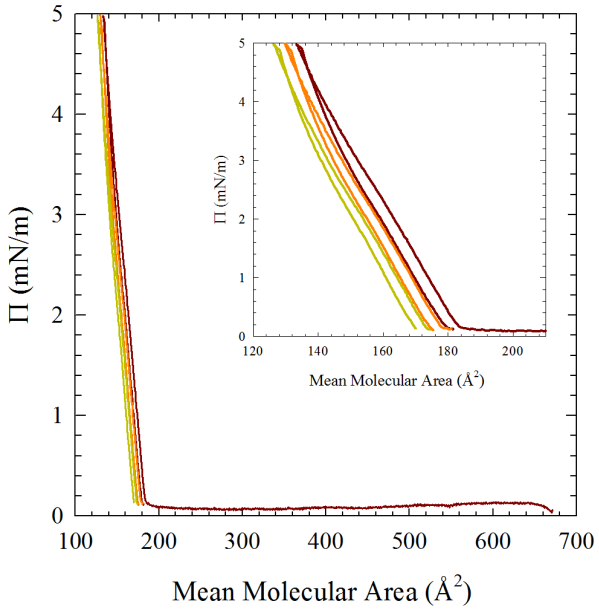

Figure 84. Three consecutive Langmuir isotherm compression/expansion cycles for dimer [4] where the target surface pressure was set at 5 mN/m. The hysteresis per cycle was determined to be 4 Å^2 and a total shift to smaller MMA from cycle 1 (red) to cycle 3 (yellow) was determined to be 16 Å^2.

The results shown here for fullerene dimer monolayer reversibility are comparable to those seen by Gao and coworkers for amphiphilic fullerene systems shown in Figure 20 in Chapter II (page 51). The monolayers in the case of Gao et al were determined to be reversible and stable with hysteresis and isotherm shifts comparable to and even larger

than the dimer systems we have investigated [36]. Because the gas phase was shown to be recoverable in the case of all three dimer systems we investigated, the monolayer formation is likely not due to the permanent aggregation of fullerene molecules. We can therefore conclude that the hydrophilic ligand attachment provides sufficient shielding to prevent fullerene aggregation while still allowing for the fullerene interaction required for monolayer formation and providing sufficient hydrophilic contributions to also allow monolayer formation at the air/water interface.

5.3.4 Conclusions: Langmuir Isotherm Studies

Langmuir isotherm studies provided us with a number of useful insights regarding the monolayers of fullerene monomer ***[1]*** and dimers ***[2]-[5]***. The results of the isotherm studies show first, that the monomer materials studied here does not form a repeatable monolayer at the air/water interface. However, all four fullerene dimers investigated were shown to form a monolayer on the water surface. Monolayer formation was also repeatable and reversible for the dimer systems studied. Furthermore, Langmuir isotherm experiments indicated that the orientation of the fullerene dimer long-axis varies depending on the ligand chemistry. Taking into consideration the results of isotherm studies, Langmuir-Blodgett monolayer transfers to solid substrates are discussed below for the four dimer systems, and results of characterization of transferred films, particularly thickness measurements, are compared to the isotherm studies discussed above.

5.4 Langmuir-Blodgett Film Deposition on Silicon

Amphiphilic fullerene dimers were investigated for their Langmuir-Blodgett (LB) film behavior under a variety of different conditions on solid silicon substrates. In particular, the effects of surface pressure at transfer on the monolayer film obtained were of interest as well as the effects of the dimer chemistry on the orientation of the fullerene dimer in a transferred film. Monolayers were characterized using atomic force microscopy (AFM) for surface coverage and film quality, ellipsometry to determine monolayer thickness, and contact angle measurements to ascertain the surface chemistry based on hydrophilicity. Successful transfer of monolayers was shown for all four fullerene dimers shown in Figure 71 and Figure 72 as discussed in detail in this section.

5.4.1 Materials and Methods

Monolayers were deposited using the Langmuir-Blodgett trough described previously, having a 70 mm deep, square (37 mm x 37 mm) dipping well at the center of the trough (Figure 85). As in Langmuir isotherm studies, surface pressure was monitored using the Wilhelmy plate-method during compression. Langmuir-Blodgett film deposition studies were only conducted on dimers ***[2]-[5]***, but not on monomer ***[1]*** shown in Figure 70, as the isotherm studies indicate the monomer does not form stable and repeatable Langmuir monolayers at the air/water interface as discussed above.

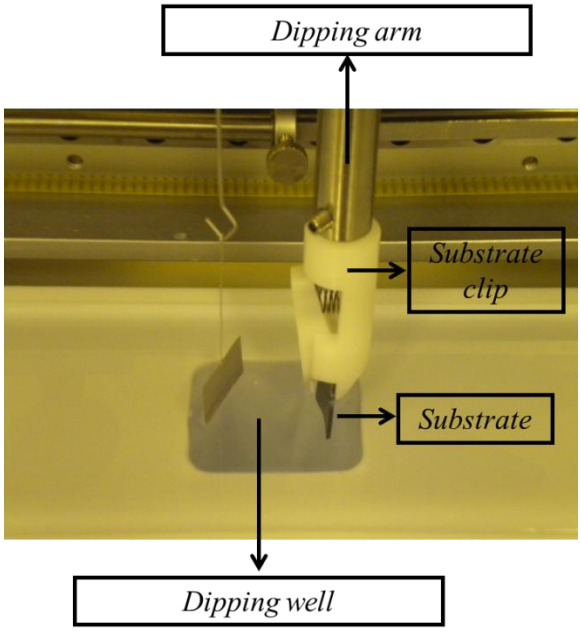

Figure 85. Langmuir-Blodgett film transfer setup using the trough described in the previous section and shown in Figure 73. As shown in the image, the substrate begins submerged in the dipping well, and the monolayer is deposited with the dipping arm moves upward.

Piranha-cleaned silicon wafers (3:1 H_2SO_4:30% H_2O_2 for 1 hour followed by rinse with Nanopure water) were used as substrates for monolayer transfer to a freshly prepared hydrophilic surface. Prior to depositing fullerene dimer solution on the sub-phase, the substrate was fully submerged in the dipping well. The dimensions (length, width, and thickness) of each substrate were measured using a micrometer in order to determine the transfer ratio (TR) as accurately as possible, where the TR is defined as the decrease in trough area to maintain constant surface pressure divided by the substrate area. Silicon oxide layer thickness on each piranha-cleaned silicon wafer was also determined using the ellipsometry setup described below immediately prior to monolayer deposition. For monolayer deposition, the number of layers deposited was set at "1", where a single layer of material was deposited on the up-stroke of the dipping arm (Figure 85). For multilayer

films, the desired number of layers was set prior to deposition, and the drying time allowed between layers was varied to determine optimal conditions.

As with isotherm studies, 0.2 mg/ml dimer in toluene solution was deposited on a Nanopure water sub-phase, allowing 35 minutes for toluene evaporation before film compression at 2 mm/min. Target surface pressure was set and maintained throughout the deposition process, ranging from 5 to 20 mN/m for each dimer structure. Monolayer deposition was initiated once the target dipping pressure was reached and transfer occurred on the upstroke of the dipping arm, moved vertically out of the dipping well at 2 mm/min. A series of experiments was conducted to determine the effects of this dipping arm speed on the quality of film transfer and will be discussed briefly below. Surface pressure and TR were monitored throughout the dipping process, and Π-A isotherms were collected for each deposited monolayer. Monolayers were allowed to dry for 24 hours prior to thickness measurements using ellipsometry and AFM studies described below.

5.4.2 Characterization Techniques for Langmuir-Blodgett Films

Monolayer thickness measurements were conducted using a Woollam M2000U multiangle spectroscopic ellipsometer with measurements at three different angles: 65º, 70º and 75º. Thicknesses were determined using the Cauchy model over the range of wavelengths, λ, of 250 nm to 1000 nm. Silicon oxide layer thicknesses were measured and determined prior to monolayer transfer to the silicon wafer using the SiO_2 model, with typical oxide layer thicknesses of approximately 2 nm or less.

Atomic force microscopy (AFM) imaging was used to characterize the uniformity of the monolayer deposition on the substrate. AFM images at different magnifications were taken using a Veeco MultiMode microscope with a Nanoscope IIIa controller. A light tapping regime was used in accordance with established procedures [256-258]. Aluminum backed triangle silicon cantilevers (MikroMasch) with a nominal spring constant of 40 N/m were used for all measurements. AFM measurements were also performed using a Pacific Nanotechnology AFM with an Agilent U3120A Mounted Close Contact Silicon Probe with spring constant of 40 N/m, resonance frequency of 300 kHz, and tip radius of 10 nm.

Water contact angle measurements were also conducted on monolayer films to further support results in terms of orientation of dimers in monolayer films obtained from isotherm studies and ellipsometry thickness measurements. CA measurements were conducted using a KSV CAM 101 Contact Angle and Surface Tension Meter with a FireWire camera with 50 mm optics and 40 mm extension tube and LED-based red background lighting.

Contact angle measurements were taken using a water contact angle on three separate locations on the film surface using fresh Nanopure water to form the droplet. Images of the droplet were collected at each location after allowing the drop to equilibrate for 30 seconds, and the droplet curve was fitted, resulting in a separate contact angle for each side of the droplet. The value reported as a CA measurement result is an average of the CA at each of these three locations on the surface. Lower CA results indicate a more hydrophilic surface where the CA for a clean silicon wafer has been shown to be <10° [259]. Similarly, expected contact angles can be determined from previous research for

certain surface functionalities. Studies on self-assembled monolayers of perfluorodecyltricholorosilane (FDTS) result in contact angles of anywhere from 109.6° [259] to 119° [260]; these values are relevant to fullerene dimers with fluorinated carbon tails as FDTS has $–C_8F_{17}$ end group chemistry, and we would expect similar values if the fluorinated tail were located at the air interface of monolayers of dimers ***[3]*** and ***[4]***. Similarly, we can expect a value of around 65° for films where the fullerene cage is located at the air interface [261] or CA of 25° ± 2° for films where PEG oligomers are located at the air/film interface [262].

5.4.3 Langmuir-Blodgett Monolayer Deposition on Silicon

Monolayers of dimers ***[2]-[5]*** were transferred from the water surface to clean silicon wafers at target dipping pressures shown in Table 12. The native oxide layer on the silicon gives a hydrophilic surface on the substrate, so the dimer behavior was expected to be similar to that on water. After transfer of the monolayer, the films were characterized using ellipsometry, AFM, and contact angle measurements as described in detail above. As mentioned, monomer ***[1]*** was not transferred to a solid substrate because Langmuir isotherm studies indicated the formation of a multilayer film with irreversible aggregation at the air/water interface and behavior was difficult to reproduce.

Table 12. Monolayer thicknesses for LB films of amphiphilic fullerene dimers as determined by ellipsometry at various target dipping surface pressures (Π). Dimer structures can be found in Figure 71 and Figure 72.

Dimer	*Target Π (mN/m)*	*Monolayer Thickness (nm)*
[2]	5	1.142
[3]	5	1.757
	10	2.048
	15	2.31
	20	2.45
[4]	5	1.81
	10	1.93
[5]	10	2.57
	15	3.06

As shown in Figure 86 for all hydrophilic/hydrophobic tail dimers (***[3]-[5]***), the thickness of the monolayer increases with increasing dipping pressure. This is to be expected as the molecules are more tightly packed at higher surface pressures; all comparisons among these dimer systems for monolayer thickness are for monolayers that were transferred at the same target Π for consistency.

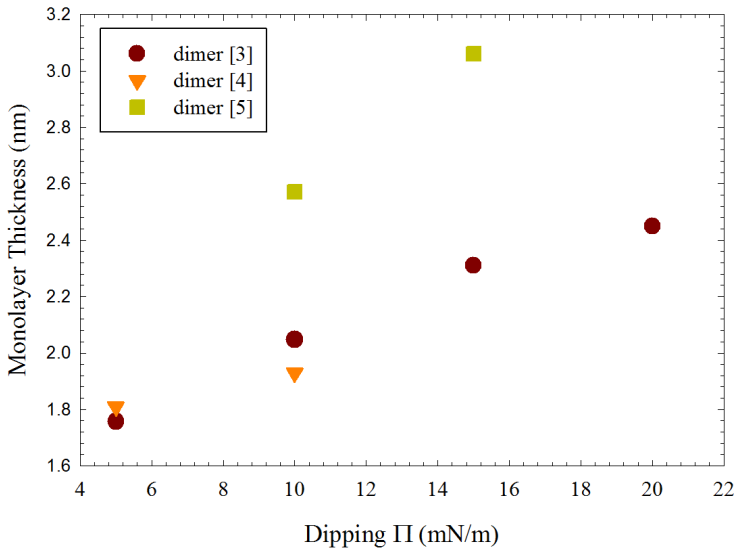

Figure 86. Monolayer thickness as a function of target dipping pressure for dimers [3]-[5] transferred to solid silicon substrates using the LB technique.

Thicknesses obtained from ellipsometry are consistent with molecular orientation information determined from the Π-A isotherms and MMA extrapolation and are provided in Table 12 for monolayers of ***[2]*** transferred to solid substrates. The C_{60} cage is approximately 1 nm in diameter, and the ellipsometry measurements for a monolayer of ***[2]*** indicate that the monolayer thickness is consistent with the diameter of a fullerene monomer. This supports the conclusion from the isotherm measurement that the long-axis of dimer ***[2]*** is parallel to the silicon substrate as depicted in Figure 77 as this would result in a monolayer with a thickness similar to the size of the C_{60} cage. AFM results for dimer ***[2]*** are given in Figure 87. Most noticeable in these images is that the coverage of the dimer ***[2]*** monolayer is highly uniform, particularly when compared to dimers ***[3]-[5]*** discussed below. The high degree of coverage is likely due to the stronger attraction of

dimer ***[2]*** to the silicon oxide layer on the substrate surface with two hydrophilic tails interacting with the substrate versus one for other dimer systems.

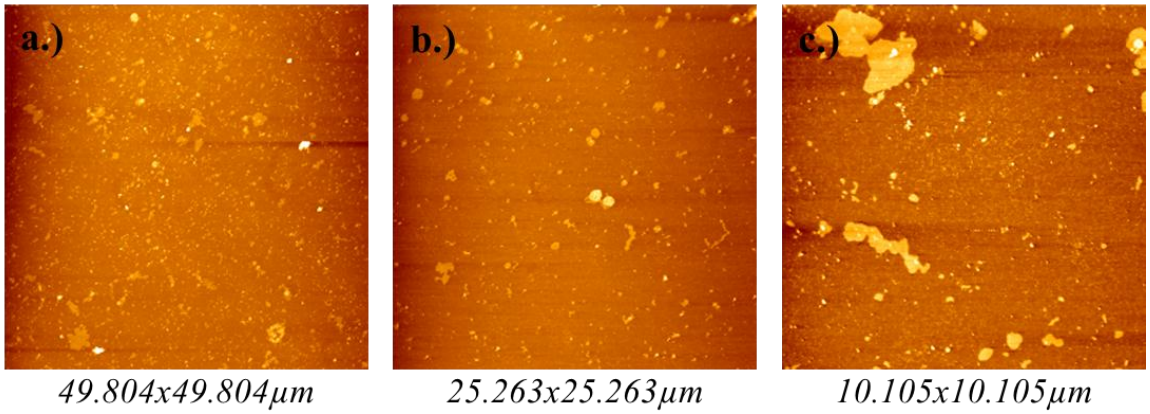

Figure 87. AFM images obtained for a monolayer of dimer [2], transferred to solid silicon substrates at 5 mN/m target dipping pressure at scan sizes of a.) 49.804x49.804 μm, b.) 25.263x25.263 μm, and c.) 10.105x10.105 μm. Monolayer thickness was determined to be 1.142 nm by ellipsometry.

Ellipsometry on monolayers of ***[3]*** also supports the isotherm and illustrated structure; the thicknesses measured (Table 12), combined with the size of the dimer molecule, support the assertion that the long-axis of the dimer is at an angle of approximately 47° to the substrate. Figure 88 shows the AFM height scan results for a monolayer of dimer ***[3]*** transferred at a target Π of 15 mN/m. These images are consistent with images taken across the sample. While AFM imaging shows holes in the transferred monolayers and debris on the monolayer surface, overall the coverage of the monolayer on the substrate is uniform over several microns. The darkest regions are due to holes in the monolayer where the substrate is exposed while brighter spots are likely from dust and other

contaminants on the water surface and in the surrounding atmosphere during monolayer transfer. AFM image analysis of height scans for the monolayer shown in Figure 88 also gives a monolayer thickness of 2.5 nm, in agreement with both isotherm and ellipsometry measurements as well as modeling results. Thickness from ellipsometry for this sample was determined to be 2.31 nm. There is some apparent alignment of material into parallel chains in certain regions across the dimer ***[3]*** sample transferred at 15 mN/m, particularly visible in Figure 88 c.) which was found in several locations on the film surface as well as across multiple samples.

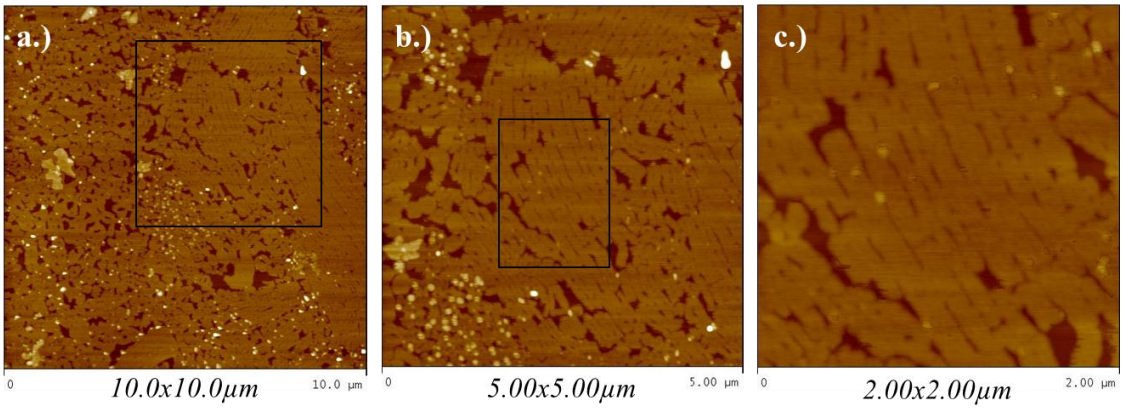

Figure 88. AFM imaging of a dimer [3] monolayer transferred to silicon at 15 mN/m at scan sizes: a.) 10.0x10.0 µm, b.) 5.00x5.00 µm, and c.) 2.00x2.00 µm. The block boxes in a.) and b.) indicate the area that was zoomed in on for the following smaller scan size.

The effects of the surface pressure at monolayer transfer can be seen by comparing the AFM images of a monolayer of dimer ***[3]*** transferred at 15 mN/m to images of a monolayer of the same material dipped at 5 and 10 mN/m (Figure 89 and Figure 90 respectively). The AFM height scan, shown in Figure 91 for the 10.0x10.0 µm scan of the

monolayer prepared at 5 mN/m, shows a monolayer height of 1.713nm which is consistent with the ellipsometry measurements on the same sample (1.757 nm, Table 12). Comparing the AFM images for dimer ***[3]*** the coverage is more uniform at higher dipping pressures, and the dimers appear to align at 15 mN/m, alignment that is not visible in AFM images of monolayers transferred at 5 and 10 mN/m.

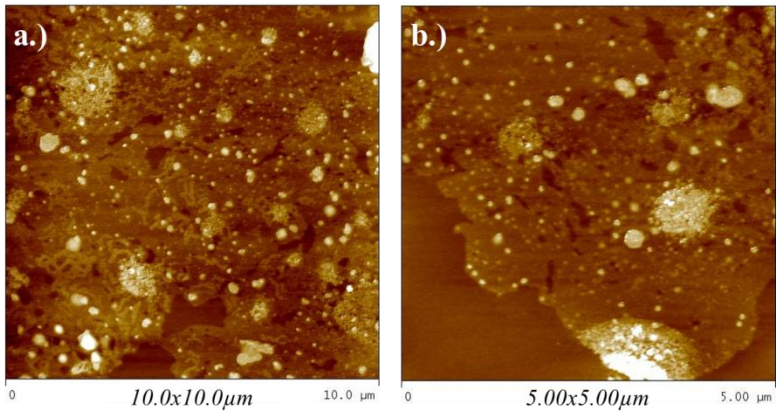

Figure 89. AFM images of a dimer [3] monolayer transferred at 5 mN/m onto silicon from a water sub-phase. Scan sizes are a.) 10.0x10.0 μm and b.) 5.00x5.00 μm.

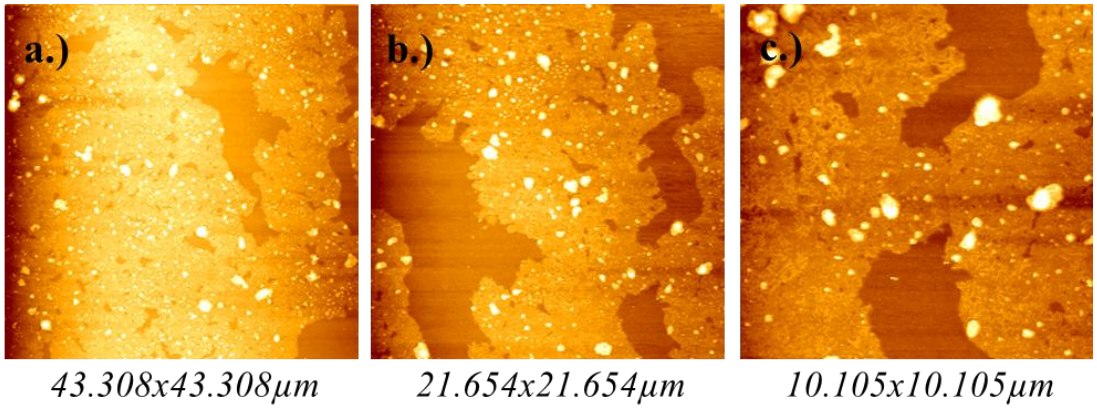

Figure 90. AFM images of a dimer [3] monolayer transferred at 10 mN/m onto a silicon substrate where scan sizes are a.) 43.308x43.308 µm, b.) 21.654x21.654 µm, and c.) 10.105x10.105 µm.

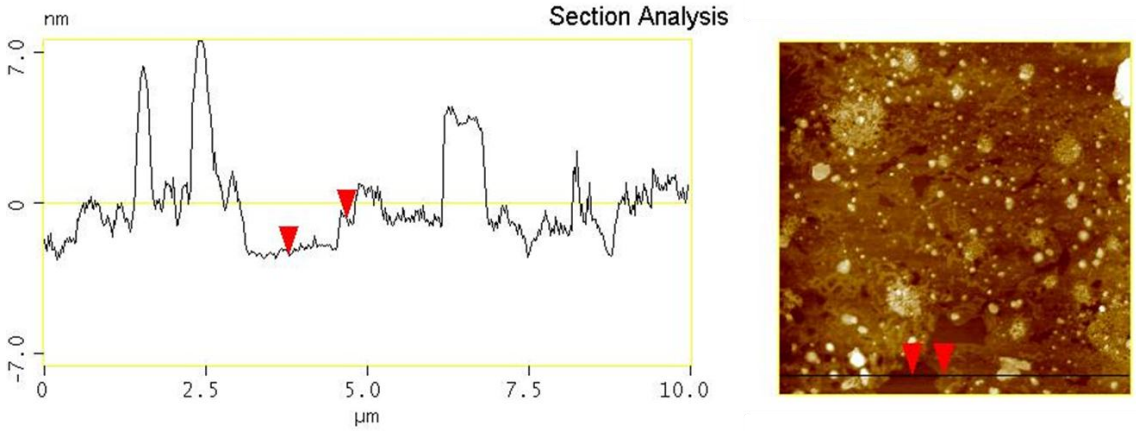

Figure 91. AFM height scan section analysis on a monolayer of dimer [3] deposited at 5 mN/m. The red triangles on the Section Analysis graph correspond to the red triangles on the 10.0x10.0 µm AFM image on the right. The difference in height was determined to be 1.713 nm, agreeing well with ellipsometry measurements on this sample.

The thickness measurements determined from ellipsometry support the information derived from the mean area per molecule and Π-A isotherms in terms of the orientation of the fullerene dimer ***[4]***. Comparing the thickness of monolayers of ***[3]*** to ***[4]***, the dimer ***[4]*** films are thinner than ***[3]*** at comparable dipping pressure which would appear to conflict with the MMA results showing that dimer ***[4]*** is more perpendicular. However, this is most likely due to the shorter hydrophobic side chain on ***[4]*** (see Figure 73) as the thicknesses are within an angstrom of each other for similar experiments. Despite this we still conclude that the evidence supports our assertion that dimer ***[4]*** is more upright than dimer ***[3]*** with respect to the water or substrate surface. AFM height images of a dimer ***[4]*** monolayer transferred at 10 mN/m are shown in Figure 92. As the in the case of dimer ***[3]***, the surface coverage is relatively uniform across the sample with some holes in the monolayer. Dimer ***[4]*** monolayers transferred at 10 mN/m are comparable to those of the similarly structured dimer ***[3]*** monolayer transferred at 10 mN/m in Figure 90. Higher transfer pressures (15 mN/m or more) are required to achieve aligned dimer structures such as those for dimer ***[3]*** at 15 mN/m (Figure 88).

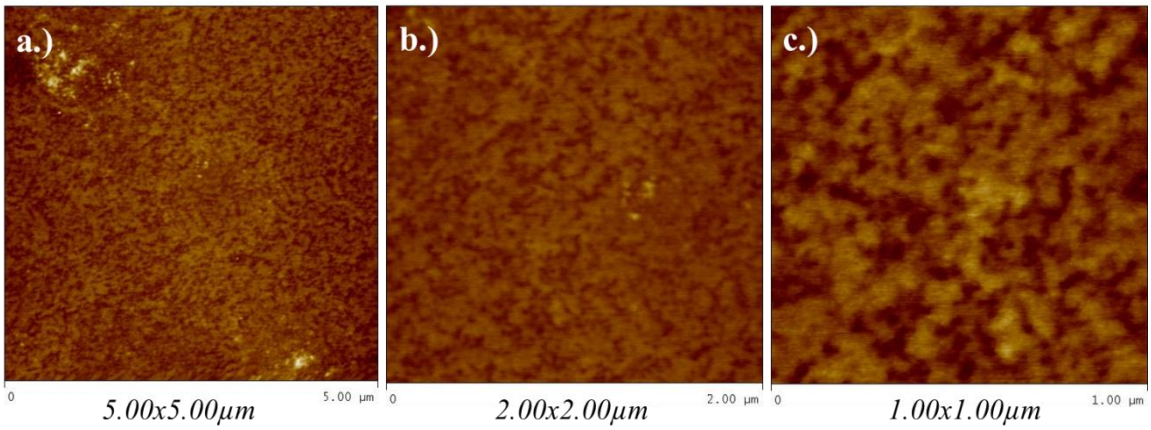

Figure 92. AFM images of a dimer [4] monolayer on silicon deposited at a surface pressure of 10 mN/m with scan size of a.) 5.00x5.00µm, b.) 2.00x2.00µm, and c.) 1.00x1.00µm. Thickness of this monolayer was determined to be 1.84 nm from ellipsometry.

Monolayers of dimer ***[5]*** were also successfully transferred to silicon substrates at several dipping pressures. Overall, these films were found to be thicker at comparable dipping pressures than either ***[3]*** or ***[4]*** with thicknesses of 2.57 nm at 10 mN/m transfer pressure and 3.06 nm at 15 mN/m, and the isotherm area per molecule information supports the transfer results where both independently indicate the dimers are nearly perpendicular to the substrate surface. AFM height scans of a monolayer of ***[5]*** transferred at 15 mN/m are shown below in Figure 93 with a corresponding AFM height section analysis in Figure 94. AFM height section analysis determined from the height difference in the film between the locations marked with red arrows in Figure 94, results in a monolayer thickness of 3.978 nm, in agreement with ellipsometry measurements on the same film.

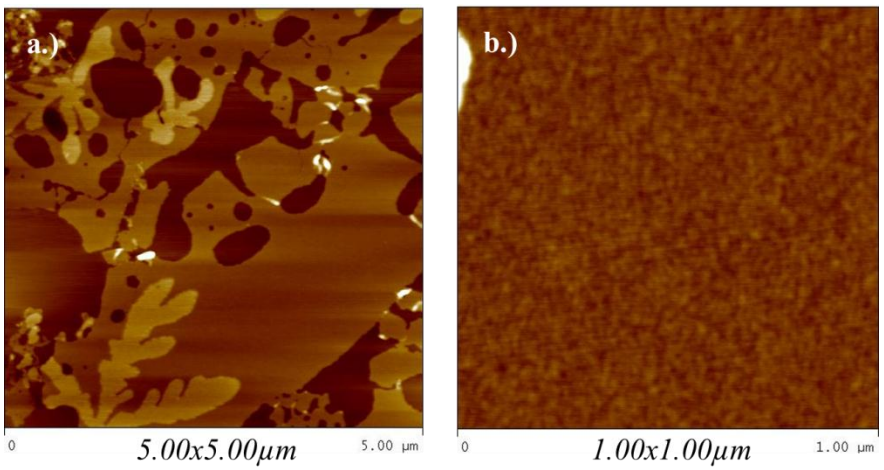

Figure 93. AFM height scans of a monolayer of dimer [5] transferred at 15 mN/m with scan sizes of a.) 5.00x5.00µm and b.) 1.00x1.00µm. In a.) darker regions are holes in the film where the underlying silicon substrate can be seen and brighter regions are deposited fullerene dimer. b.) is a smaller scan of a region where dimer was deposited uniformly.

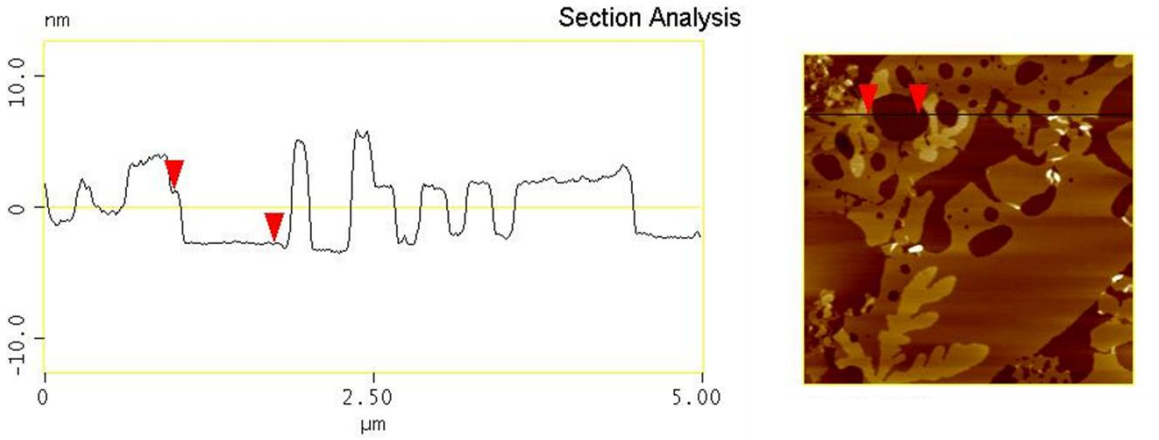

Figure 94. AFM height scan analysis of a monolayer of [5] transferred at 15 mN/m. The difference in heights between the two locations on the film marked by red arrows in the figure was determined to be 3.978 nm which is comparable to an ellipsometry measurement result of 3.06 nm on the same film.

As evident in the AFM images in Figure 93 of monolayers of ***[5]***, particularly in the 5.00x5.00µm scan, the surface coverage is not as uniform as the other dimer systems studied. There are large holes in the monolayer film, some of which are at least a micron in one direction; poor monolayer surface coverage would be detrimental to depositing clean, multilayer films of these materials. Additionally, large, fractal-like structures are observed as the brightest spots in the larger height scan image. These structures are most likely to be fullerene aggregates forming a second layer on top of the deposited monolayer. Again, AFM height scan analysis, Figure 95, supports this conclusion where the height difference was determined to be 7.625 nm, consistent with two layers of dimer [5] present at these locations on the substrate.

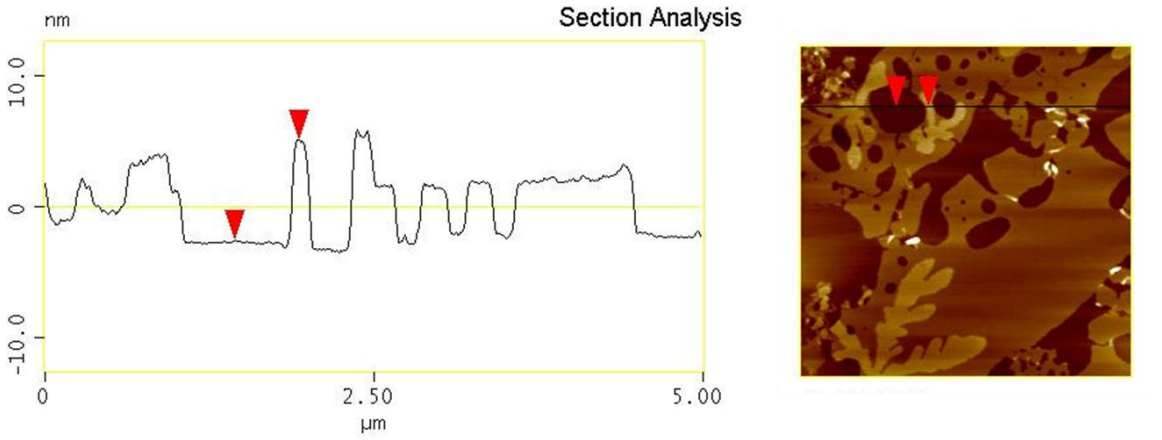

Figure 95. AFM height scan analysis on a monolayer of dimer [5]. In this case, the markers were placed at a region exposing the substrate and atop one of the fractal structures on the monolayer surface. The height difference in this case was found to be 7.625 nm.

However, as shown in the 1.00x1.00μm scans, the regions of the substrate that are covered uniformly by a monolayer of dimer ***[5]*** show very high quality packing. A possible explanation for the gaps in the surface coverage, particularly when compared to ***[3]*** and ***[4]***, is the shorter length, lack of rigidity, and weaker inter-chain interactions of the hydrophobic ligand in the case of ***[5]***. The limited interaction between hydrophobic ligands on dimer ***[5]*** results in a monolayer with less uniform coverage due to the in ability of weaker intermolecular interactions to hold the monolayer together during transfer. This is particularly true in the case of dimer ***[5]***, but also relevant to other dimer systems studied, enhancing the interaction between the substrate and one of the dimer ligands or the fullerene cage through surface functionalization may allow for more uniform and repeatable surface coverage of LB monolayers.

Water contact angle measurements were also conducted on monolayers of dimers [3]-[5] deposited on silicon. The average CA determined from three separate measurements for each of the dimers characterized is provided in Table 13 below. Representative camera images analyzed for contact angle measurements are also shown in Figure 96 for each dimer system.

Table 13. Contact angle measurements for LB monolayers of dimers [3]-[5].

Material	*Target Π (mN/m)*	*Monolayer Thickness (nm)*	*Transfer Ratio*	*Contact Angle (°)*
Clean silicon	n/a	n/a	n/a	<5
Dimer [3]	15	2.31	0.912	86 ± 2
Dimer [4]	5	1.81	1.606	73 ± 6
Dimer [5]	50	n/a	n/a	85 ± 2

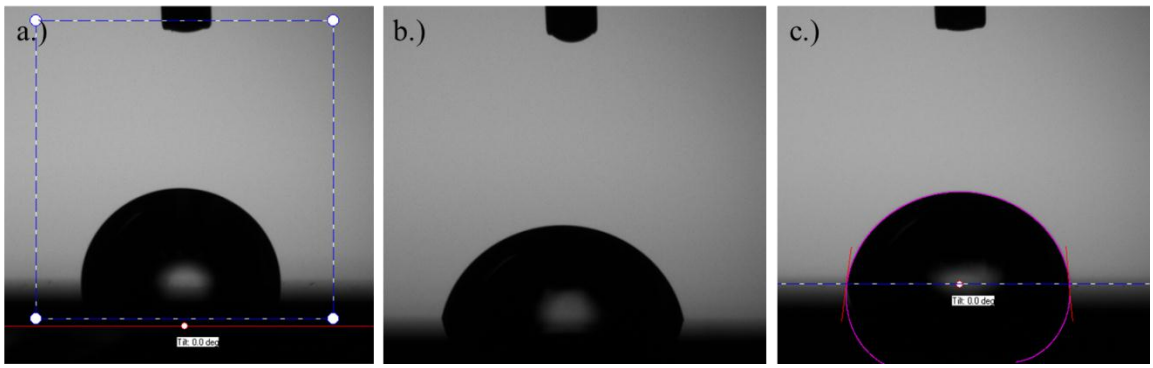

Figure 96. Water contact angle measurements on monolayers of a.) dimer [3], b.) dimer [4], and c.) dimer [5]. Contact angles were determined to be 86.31 ± 2.09°, 72.94 ± 6.08°, and 85.31 ± 2.42° respectively for each of the three systems.

Based on the difference in contact angle between clean silicon and the monolayer systems, it is clear that a monolayer has been transferred to the silicon substrates. Furthermore, the larger contact angles indicate a more hydrophobic surface that can be attributed to the presence of either fullerenes or hydrophobic ligands at the surface. The

expected contact angles for fullerenes indicate that if pure fullerene material was present at the surface, the contact angle would be ~65° [261], and in the case that a fluorinated tail, such as that on ***[3]*** and ***[4]***, were located at the surface, the contact angle would be approximately 109° or higher [259, 260]. Similarly, if the hydrophilic PEG ligands were located at the surface, the contact angle would be much smaller, ~25° [262] or slightly larger due to the likelihood that fullerenes are not fully shielded by the chains and some may be present at the surface.

Our CA measurements of between ~73° and 86° indicate that a combination of hydrophobic tails and fullerene cages are located at the surface. It is clearly evident that the hydrophilic tails are directed toward the silicon surface with CA values much larger than 25° clearly indicating a hydrophobic surface. The dimer ***[4]*** monolayer CA reported here is lower than both dimers ***[3]*** and ***[5]*** which have comparable values; dimer ***[4]*** likely has a contact angle more similar to that of C_{60} because the transfer pressure on this monolayer was lower, so the hydrophobic tails are not as tightly packed and more fullerene material is exposed at the surface. Combining isotherm data and monolayer thickness, AFM, and contact angle measurements, we can conclude that the amphiphilic fullerene dimers studied here orient depending on their ligand chemistry and transfer as uniform monolayers to silicon substrates with hydrophilic tails directed towards the substrate surface.

5.4.4 Langmuir-Blodgett Multilayer Deposition on Silicon

Multilayer deposition proved to be more difficult than monolayer transfer to silicon substrates with fullerene dimers ***[2]-[5]***. Several factors can influence multilayer transfer

including drying time between layer addition, substrate-molecule interaction, and molecular interaction between molecules in transferred layers. In our experiments we varied first the drying time and then the substrate-fullerene interaction as discussed below in order to determine the best approach to achieving the multilayer deposition that would be required for sufficient spins to be incorporated for ESR measurements.

In particular, drying time between the transfers of individual layers was shown to be highly important for amphiphilic fullerene dimers. Based on ellipsometry studies and transfer ratio data from multilayer deposition studies, the initial monolayer deposited washes off the substrate surface with subsequent layer additions, resulting ultimately in one layer being present on the substrate at the conclusion of an odd number of dipping cycles. Table 14 below provides examples of the transfer ratio data obtained from several different multilayer transfer attempts using dimer ***[3]*** as well as the thickness of the final film after deposition was complete. A transfer ratio (TR) of ~1 on the first layer indicates that a uniform monolayer has been deposited; however, negative values for TR on second pass of the substrate through the monolayer surface indicate that the monolayer is being removed from the substrate surface. In all cases, the thickness of the transferred film is consistent with the approximate thickness for a dimer ***[3]*** monolayer. Where the thickness was found to be slightly larger than that of a monolayer, the slight increase in thickness is most likely due to an increased roughness of the film surface as fullerenes are deposited and washed off the substrate repeatedly.

Table 14. Transfer ratio values for multilayers of dimer [3] transferred to a solid silicon substrate (in all cases the number of layers to transfer was set to 3).

Dimer	Transfer Π (mN/m)	Drying Time (s)	Transfer Ratio (by layer)	Film thickness (nm)
[3]	15	0	(1) 1.202 (2) -1.035 (3) 1.448	3.37
[3]	15	1200	n/a	2.54
[3]	15	3600	(1) 0.953 (2) -0.661 (3) 1.102	3.12

The initial monolayer was allowed to dry for anywhere from no drying time to 1 hour before the wafer was re-submerged in the water sub-phase for subsequent layer addition. However, even at drying times of an hour between layers, the initial layer was found to redeposit across the sub-phase when the substrate re-entered the water, and another monolayer, of lower quality, was found to deposit on the substrate surface based on ellipsometry measurements. This occurs either because the fullerene PEG ligand interaction with the native oxide layer on the silicon substrate surface is weaker than the pull to other fullerene molecules on the water surface and/or the initially deposited layer has enough residual water to pull the fullerenes back to the water surface on re-contacting with the sub-phase. It should be noted that the TR value was less negative for a drying

time of an hour when compared to values for the sample that was allowed no drying time, which may be an indicator that multilayer transfer is possible with sufficient drying time.

Successful deposition of a second layer was achieved with dimer ***[3]***, however, after allowing the initial monolayer to dry for 20 consecutive days prior. The initial monolayer corresponds to that shown in the previous section in Figure 88 and had a film thickness of 2.31 nm based on ellipsometry. With the addition of the second layer (AFM imaging in Figure 97 and Figure 98), the total film thickness was determined to be 5.38 nm using ellipsometry. AFM height scan analysis, shown in Figure 99 and Figure 100, corresponds well with ellipsometry measurements with a thickness of 2.417 nm for the initial monolayer and bilayer thickness of 6.215 nm. The respective transfer ratios for each layer were 0.912 and 1.350 for the first and second layer, also supporting the idea that second layer has been deposited.

As shown by the AFM images in Figure 97 and Figure 98, the surface coverage of the second layer is as uniform as the monolayer coverage. The initial monolayer is visible through gaps in the second layer deposition, but the gaps are less than 500 nm in size and no larger than those noted for monolayer transfer of dimer ***[3]***. The brightest regions in the 20.00x20.00µm and 10.00x10.00µm scans are large dust particles that would be detrimental to the build-up of any further multilayer structure in those regions. Also, as is the case typically with LB multilayer films, the quality of the film degrades with an increasing number of layers. Therefore, the quality of each new layer is important to maintaining the best layer coverage achievable with further deposition.

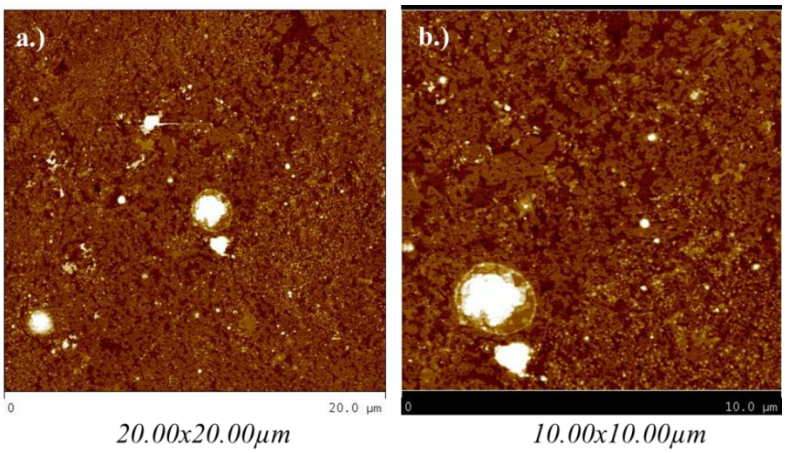

Figure 97. AFM height images of a bilayer of dimer [3] with scan sizes a.) 20.00x20.00µm and b.) 10.00x10.00µm. The second layer in this case was deposited after allowing the first monolayer to dry for 20 days.

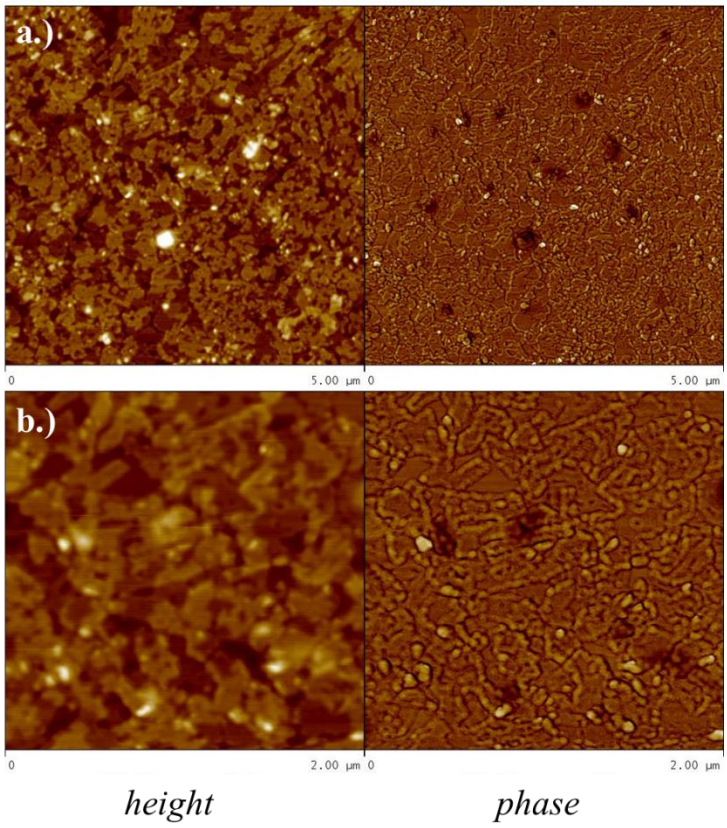

Figure 98. AFM height (left) and phase (right) images of a dimer [3] bilayer with scan size a.) 5.00x5.00µm and b.) 2.00x2.00µm. Images here correspond to the larger scan size height images in Figure 97.

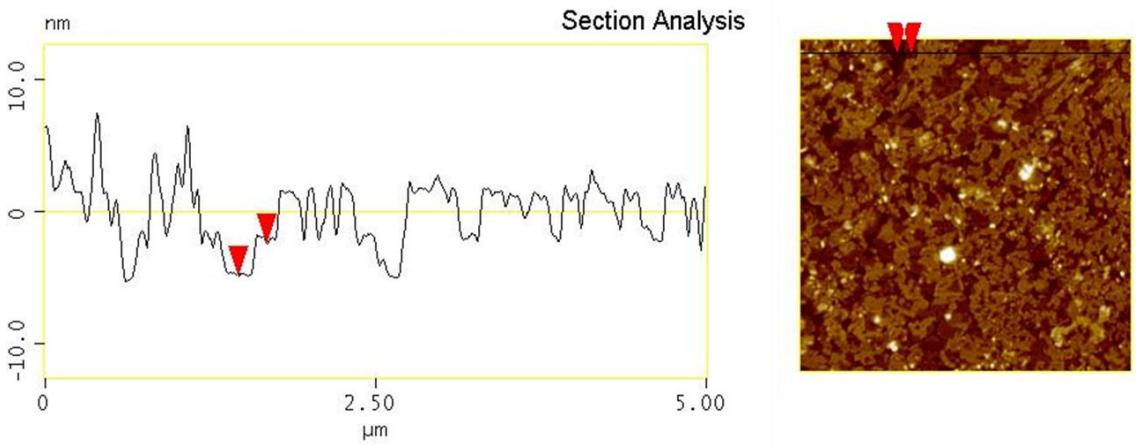

Figure 99. AFM height section analysis for a dimer [3] bilayer. The red arrows in this case are located on the first monolayer (left) and the second layer surface (right). The difference in height was determined to be 2.417 nm, consistent with a monolayer thickness in this case of 2.31 nm determined from ellipsometry.

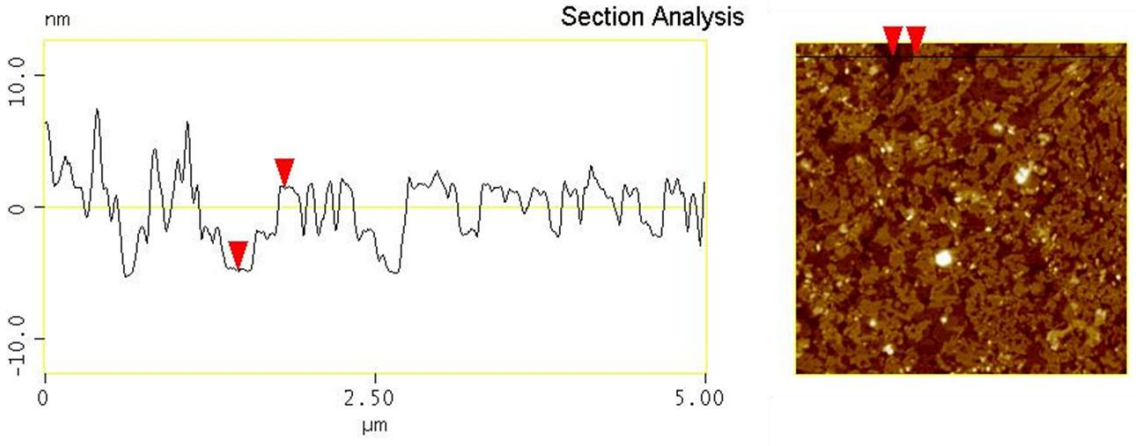

Figure 100. AFM height section analysis for a dimer [3] bilayer. The red arrows in this case are located on the underlying silicon substrate (left) and the second layer surface (right). The difference in height was determined to be 6.215 nm, consistent with a bilayer of dimer [3] and ellipsometry determined thickness of 5.38 nm.

We were able to show that multilayer deposition of the amphiphilic fullerene dimer is achievable if sufficient drying time is allowed between layer depositions. A minimum drying time was not determined and further study is required to find the optimal multilayer deposition conditions, but a drying period of 20 days is not practical or viable. With this in mind, we conducted further studies regarding multilayer deposition with amphiphilic fullerenes on chemically functionalized substrates. Substrates were modified to have greater potential interaction with the fullerene dimers, and results of these studies are discussed below.

5.4.5 Conclusions: Langmuir-Blodgett Films on Silicon

We have successfully shown the transfer of monolayers of fullerene dimers bearing either two PEG ligands or one PEG ligand and one perfluorinated carbon tail to solid silicon substrates. To our knowledge, this is the first report of LB films of fullerene dimer materials to date. Additionally, results of the transfer of LB monolayers of all four dimers support the Langmuir isotherm studies discussed previously. Ellipsometry and AFM height scan analysis both indicate that the fullerene dimer orientation can be manipulated by varying the side chain chemistry, allowing for some control over the final fullerene structure in the transferred film. Also, contact angle measurements indicate that the hydrophilic PEG ligand in all cases is directed towards the silicon substrate surface while hydrophobic tails are located at the air interface. Multilayer transfer to silicon substrates was determined to be possible if sufficient drying time is allowed between the deposition of individual monolayers. However, manipulating the substrate surface chemistry may

decrease the amount of drying time required or eliminate the need for drying entirely as discussed in the next section.

5.5 Langmuir-Blodgett Deposition on Silane-Functionalized Silicon

5. 5. 1 Materials and Methods

Toluene, ethanol, acetic acid, and 3-aminopropyltriethoxysilane were all purchased from Sigma Aldrich and used as received. Nanopure water was obtained from a Barnstead Nanopure water system (18.2 MΩ cm resistivity). All silicon wafers were piranha-cleaned using standard procedures and stored in Nanopure water prior to use. In this case, dimer ***[5]*** was solely investigated with the amine-functionalized substrates.

Amino-silane molecules were chemically grafted to silicon substrates using a well-publicized, straightforward procedure. The amino-silane of choice, 3-aminopropyltriethoxysilane (3-APTES), was selected due to the known interaction between primary amines and the fullerene cage [20, 55, 190, 191, 196, 263, 264]. The structure of 3-APTES is provided in Figure 101. The amino-silane chemically attaches to the silicon substrate through reaction between the three $–OCH_2CH_3$ groups and the native oxide layer on the silicon substrate.

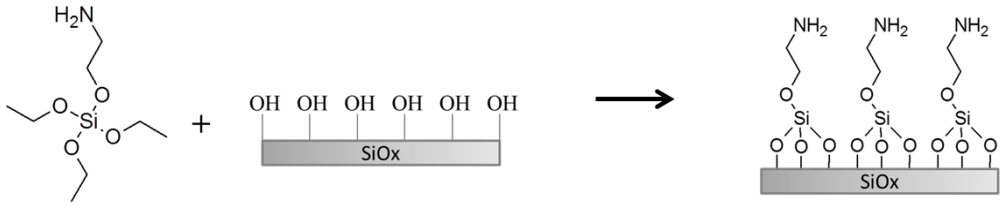

Figure 101. 3-APTES (far left) reacts with the native –OH groups at the silicon oxide surface, resulting in covalent attachment of an amine-terminated monolayer on a silicon substrate [265, 266].

In order to graft 3-APTES to silicon substrates, 18.8 mL of ethanol was combined with 1 mL of Nanopure water and well mixed. To this solution, 0.2 mL of 3-APTES was added, and a piranha-cleaned silicon wafer (3:1 H_2SO_4:30% H_2O_2 for 1 hour followed by rinse with Nanopure water and stored in Nanopure water) was allowed to soak for 1 minute. After soaking the silicon substrate in this solution for 1 minute, 2-3 drops of acetic acid were added to the solution. The acetic acid is used to reduce the pH and increase the reactivity of the silane with the silicon substrate. The silicon susbstrate was then allowed to soak for 1 hour at room temperature before being rinsed thoroughly with Nanopure water and dried in a nitrogen stream. Functionalized surfaces were characterized using AFM, ellipsometry, and contact angle measurements as described previously in Chapter V. In all cases the native oxide layer thickness was determined using ellipsometry prior to surface functionalization.

5.5.2 Characterization Techniques for Langmuir-Blodgett Films

LB films transferred to amine-functionalized substrates were characterized in the same manner as previously LB monolayers and multilayers. AFM and ellipsometry measurements were all conducted on prepared LB films, and the results are reported

below. As mentioned, thicknesses and contact angle measurements of both the native oxide and grafted 3-APTES layers were taken prior to transfer of fullerenes from the air/water interface to the solid substrate. The amino-silane layer thickness was determined to be between 0.9 and 1.29 nm in all cases, and the native oxide layer was on the order of 2 nm for all surfaces. The clean silicon substrate contact angle was determined to be <5° as expected, and the 3-APTES CA was determined to 46 ± 3° (Figure 102); this value is within the expected range for amino-silane functionalization of substrates where values have been previously determined to be between 40° and 63° [267].

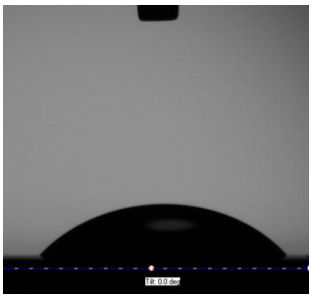

Figure 102. Example of a contact angle camera capture used for determining the water CA of a 3-APTES monolayer on silicon determined to be 46.30 ± 3.02°, within the expected range for typical amino-silane functionalized substrates.

Representative AFM height images of the 3-APTES layer on silicon are provided in Figure 103. As shown by the height scans, the coverage of the 3-APTES layer is uniform in nature which is important to achieving uniform LB monolayer coverage as well as maintaining film quality in multilayer depositions.

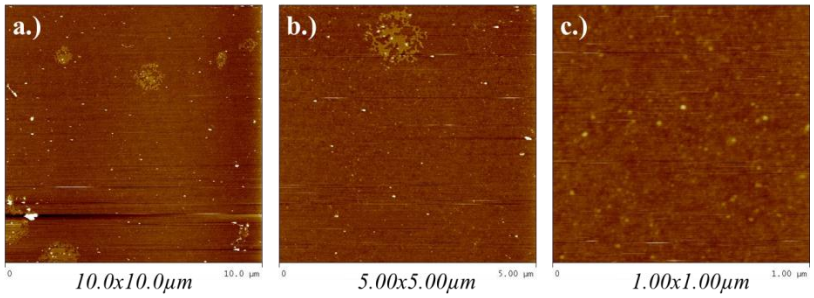

Figure 103. AFM height scans of a 3-APTES monolayer on a silicon substrate at scan sizes of a.) 10.0x10.0μm, b.) 5.00x5.00μm, and c.) 1.00x1.00μm.

5.5.3 Langmuir-Blodgett Deposition on Silane-Functionalized Substrates

Monolayers and multilayers of dimer ***[5]*** were shown to transfer successfully from the air/water interface to 3-APTES modified silicon substrates using the same method described previously for layer transfer as schematically depicted in Figure 104. Our main interest in functionalizing the substrate surface was to improve the transfer of multilayers by reducing the drying time between layer depositions by increasing the strength of interaction between fullerenes and the substrate.

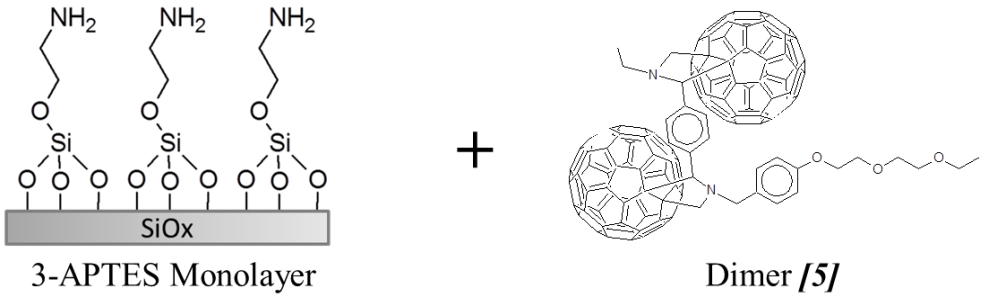

Figure 104. In LB studies of fullerene dimers on 3-APTES, dimer [5] was transferred as both a monolayer and multilayer to a 3-APTES modified silicon substrate.

With multilayer transfers, the number of layers was set to be three and the target surface pressure to 20 mN/m. A waiting time of 1200 seconds (20 minutes) was set between transfer of the first layer and the second passing of the substrate through the sub-phase surface. No delay was set between the second and third layer transfers.

Multilayer transfer under these conditions was shown to be successful. Of particular note was the transfer ratio of the second layer of 0.530, indicating the initial monolayer remains on the substrate surface with subsequent dipping cycles. However, a transfer ration of between 0 and 1 does not indicate full layer transfer. The transfer ratio for the third layer of 1.260, indicates that a full layer was transferred in this case. The thickness of the transferred multilayer was found to be 6.17 nm. Based on monolayer thicknesses achieved with dimer ***[5]***, this would be consistent with the two layers of dimer with z-type transfer. Z-type transfer occurs when a layer is transferred from the water surface only on the upstroke of the dipping arm.

Fullerenes are known to react with primary amines [20, 55, 190, 191, 196, 263, 264], and the most likely reason that multilayer transfer is successful on a 3-APTES modified substrate is due to a covalent reaction between the fullerene cage and the terminal amine groups. While this is advantageous in allowing us to build up multilayers, there is a disadvantage to this when considering an endohedral fullerene system. The covalent attachment to the cage does cause distortion to the cage structure and may result in instability or "escape" of an endohedral element.

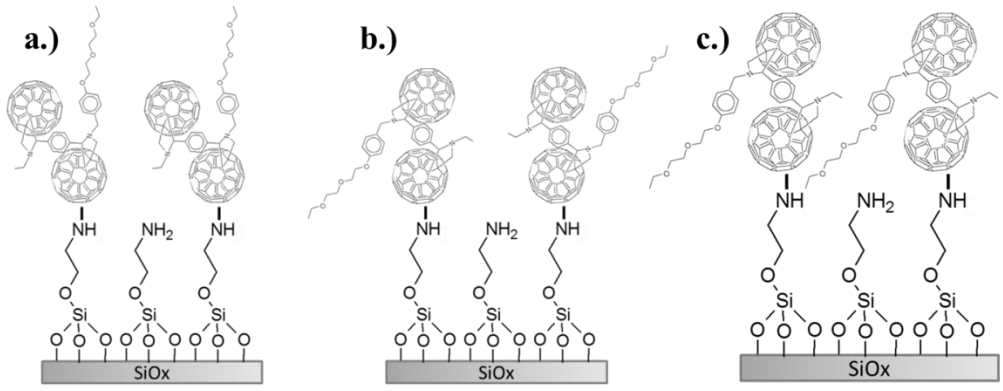

Figure 105. Possible schematics for the orientation of fullerene dimer [5] during reaction with a 3-APTES monolayer.

Because the dimer used here, ***[5]***, is asymmetrically modified, the exact reaction scheme is unclear. Possible orientations for the dimer reaction with the amino-silane are shown in Figure 105. With the Langmuir-Blodgett method and the orientation of the dimer with respect to the air/water interface, it seems most probable that the majority of transfer would occur in a fashion similar to c.) in Figure 105 with the hydrophilic tail directed

downwards. However, the other two scenarios presented are both also possible as there is the potential for rearrangement during monolayer transfer.

5.5.4 Conclusions: Langmuir-Blodgett Films on Silane-Functionalized Silicon

We have successfully shown the transfer of fullerene dimer monolayers and multilayers to amino-silane functionalized silicon substrates using the Langmuir-Blodgett technique via z-type transfer from the water surface. By using a chemically-modified substrate, we have decreased the drying time required to be more reasonable for transferring many layers. However, the layer quality will decrease with each additional layer, particularly if material (although less than a monolayer) is being deposited on the down-stroke as indicated by the transfer ratio data. Additionally, covalent bonding between the C_{60} cage and the $–NH_2$ group on the functional monolayer is not ideal as discussed, but there are a wide-range of available terminal chemistries for silane molecules including perfluorinated carbon tails and tacky epoxysilanes. Also, other surface modifications that involve non-covalent interactions such as grafting of poly(ethylene gycol) (PEG) chains to the surface may also be of use in this situation. Suggestions for future work will be discussed in further detail below. The successful transfer of fullerene dimer multilayers to an amino-silane surface shown here, however, is an important first step to achieving ordered layers of fullerenes over a large area.

5.6 Future Work

The results we have presented thus far for amphiphilic fullerene dimers in Langmuir and Langmuir-Blodgett films shows that this technique has a great deal of promise for creating aligned arrays of fullerenes. There are several avenues of pursuit for future work in this area including further characterization of films and transfer of multilayers of dimers ***[2]-[4]***; using different surface chemistries as well as different substrates; investigating additional fullerene dimer functional chemistries; making improvements in film quality and identifying ideal transfer conditions; and building up multilayers of ten or more deposited fullerene dimer monolayers.

First, while we have characterized the surfaces of transferred LB films on solid substrates in detail using contact angle and AFM measurements and thickness information using ellipsometry, we have not given intense study to the internal structure of multilayer films. We know from transfer ratio data as well as thickness studies on multilayer films that transfer seems to occur in a z-type manner with deposition only on the up-stroke of the dipping arm. However, as shown by Gao and coworkers [36], rearrangements of the film can occur after deposition, so the final structure of the multilayer may not actually be z-type in nature. For this reason, reflectivity studies, both x-ray and neutron, would be warranted to characterize in more detail the internal structure of multilayer films. The orientation of dimers and the quality of the layered structure are both important factors in determining if we can achieve the degree of alignment necessary for endohedral fullerene measurements using LB techniques.

Also, while successful multilayer transfer to $–NH_2$ terminated surfaces was shown, there were a number of issues associated with these films, particularly due to the covalent interaction that occurs between the C_{60} cage and the functionalized surface. There are a number of ways to address this issue, including using different surface functional chemistry. There are a variety of ways to chemically modified substrates, but some specific examples that would be potentially most useful for us are silanes with a perfluorinated, $–C_8F_{17}$, terminal group such as that studied by Luscombe et al [268] or "tacky" epoxysilanes [265, 266]. Both of these systems would promote non-covalent interaction with the functional monolayer. We know from our research on fullerene dimers with perfluorinated carbon tail ligands that the perfluorinated groups are extremely rigid and lock-in with each other; therefore, functionalizing substrates with a $–C_8F_{17}$ terminated silane is likely to interact strongly enough with dimers ***[3]*** and ***[4]*** to allow for multilayer transfer. However, studies regarding this are required as using a hydrophobic surface may have different implications regarding transfer. Additionally, epoxysilanes have been used as a tacky monolayer to stick polymers to a substrate and may prove useful for multilayer formation of amphiphilic fullerene dimers also through non-covalent interaction between the fullerenes and silane monolayer. Surface modification using polymer brushes, specifically poly(ethylene glycol) (see Appendix D), may also prove useful to transferring multilayers from the air/water interface to solid substrates. PEG- functionalized or "PEGylated" substrates have the potential to be useful for all four dimer systems studied here as they all contain at least one hydrophilic PEG ligand on the dimer bridge. However, it is unknown if the strength of interaction between a PEG brush layer and the dimers is sufficient to allow for multilayer transfer.

There is also the possibility of taking advantage of the covalent interaction between 3-APTES monolayers and fullerene cages by using a buffer layer of pristine C_{60} monomer grafted to a 3-APTES layer [55] and then using the LB technique to transfer dimers to this substrate. The interaction between C_{60} cages and the dimer fullerenes may be sufficient to allow for multilayer transfer, particularly due to the strong tendency for fullerenes to form irreversible aggregates. Preliminary studies indicate that this would be a sufficient method to forming multilayers, but further studies are required to identify ideal experimental conditions and repeatability as well characterize these films to ascertain the internal structure and arrangement of fullerenes. It may also be possible to use an amphiphilic fullerene dimer with a functional group such a terminal aldehyde known to interact with primary amines [55] similar to that on monomer ***[1]*** or even use a silane functionalized dimer to directly react the monolayer material with the silicon substrate.

Another problem in transferring multilayers onto amine-terminated monolayers is that while a full monolayer is not deposited on the down-stroke, the transfer ratio indicates that some material is being moved from the water surface to the substrate. This can result in non-uniformity and reduced quality with each additional layer transferred. It may be that adjusting the experimental conditions and drying time (20 minutes was the only time used) may improve this behavior, and therefore different scenarios need to be investigated by systematically adjusting variables. Another possible approach, although tedious, would be to clean the trough between layer transfers and essentially treat each layer addition as the transfer of a single monolayer.

Lastly, we need to investigate the quality of multilayers of ten or more layers as thus far we have only looked at bi- and tri-layer systems. It is well known that film quality typically degrades with each layer addition using the Langmuir-Blodgett approach for a variety of reasons but largely due to dust and other impurities or irregularities in a transferred layer. We have calculated that in the case of a low purity endohedral system (10^{-4} fill ratio where 1 in 10^4 molecules is filled) anywhere from 50 to 100 layers would be required. In a higher purity fill system (10^{-2} or better), fewer layers are necessary, on the order of 10 rather than 100. In either case, we need to find a way to maintain quality with multiple layer additions. One possible approach is to investigate different substrates such as mica or glass (which can be chemically functionalized similar to silicon) where a layer is transferred to each side of the substrate with each deposition. Similarly, double-sided polished silicon would also In this way, only 5 layers would technically need to be transferred in order to achieve a sample with the necessary 10 layers required in a high purity system.

5.7 Overall Conclusions: Langmuir-Blodgett Films of Amphiphilic Fullerene Dimers

In conclusion, we have shown that Langmuir and Langmuir-Blodgett films of amphiphilic fullerene dimers are viable approaches to achieving long-range ordered arrays, despite the difficulties associated with forming Langmuir films with fullerene monomer materials. Results indicate that the orientation of the dimer long-axis can be manipulated by controlling the functional ligand chemistry on the dimer bridge. This means that the dimer orientation can be tuned to the specific use whether the requirement

is for dimers aligned parallel to the substrate, perpendicular to the substrate, or at any angle in-between. Successful transfer of multilayers was also achieved on both clean silicon and chemically modified silicon substrates. Both Langmuir film formation at the air/water interface and the transfer of monolayers and multilayers shown here are the first reported to our knowledge for these novel amphiphilic fullerene dimer materials. Further investigation is required to determine the full potential of this approach and these materials to develop ordered arrays of fullerene dimers for quantum computing applications.

CHAPTER VI: SURFACE-DIRECTED ASSEMBLY OF FULLERENE MONOLAYERS

6.1 Overview

Chemically patterned substrates that take advantage of fullerene interaction, either covalent or non-covalent, with the functional surface chemistry may simplify the process of achieving ordered fullerene-based monolayer on a solid substrate. While chemically-modified substrates can be used in conjunction with the LB approach as discussed in Chapter V, fullerene materials can also simply be solution cast onto functionalized substrates; after allowing the solvent to dry and rinsing away any non-surface-bound material, a self-assembled fullerene monolayer can be achieved. The possibilities with this approach are endless as functional monolayers on a solid substrate can be patterned, either physically or chemically, to specifically direct molecules to desired locations on the substrate. In this chapter, we will discuss initial studies of fullerene dimers and a functionalized fullerene monomer on 3-aminopropyltriethoxysilane (3-APTES) functionalized silicon and mica substrates. Also discussed in this chapter are the initial electron spin resonance (ESR) studies on a high purity endohedral fullerene monomer system prepared in this way. While only single monolayers can be deposited on each substrate surface, several substrates can be stacked to create a multilayer system.

6.2 Materials and Methods

6.2.1 Materials

Materials for silicon functionalization are described in Section 5.5.1. Mica substrates were freshly cleaved and soaked in Nanopure water immediately prior to use.

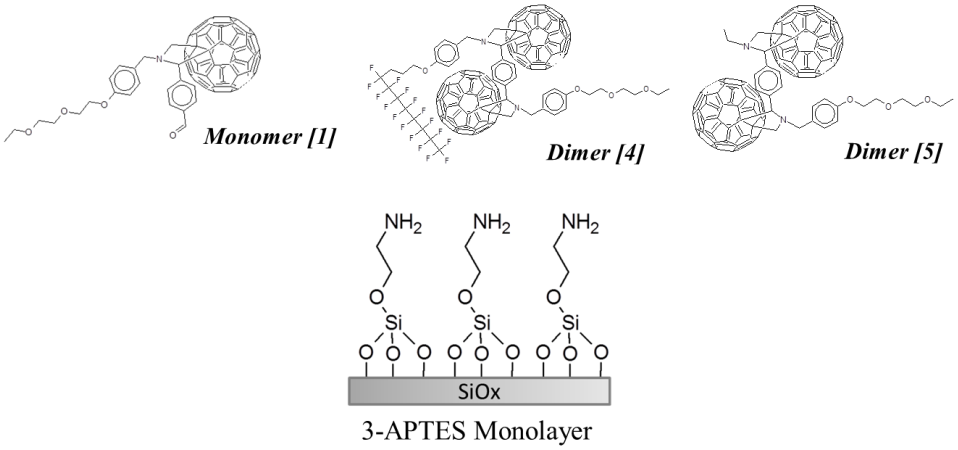

Figure 106. Functionalized fullerene monomer and two dimer systems investigated with a 3-APTES monolayer grafted to silicon and mica substrates for fullerene monomer formation via covalent attachment to a chemically functionalized substrate.

The surface assembly of modified fullerene monomer ***[1]*** and dimers ***[4]*** and ***[5]*** on substrates modified with 3-APTES monolayers was investigated (Figure 105). High purity ^{14}N-filled ***[1]*** was used for ESR studies.

6.2.2 Amino-silane Functionalization of Silicon Substrates

Amino-silane molecules were chemically grafted to silicon substrates using the procedure described in section 5.5.1. An amino-silane (3-APTES) was chosen for the known interaction between primary amines and the fullerene cage [20, 55, 190, 191, 196, 263, 264] as well as the reaction between primary amines and aldehydes such as the aldehyde group on the monomer ***[1]*** cage. As described in Chapter V, 18.8 mL of ethanol, 1 mL of water, and 0.2 mL of 3-APTES were combined thoroughly and a clean silicon wafer was deposited in the solution. After allowing the wafer to soak for 1 minute, two drops of

acetic acid were added to the solution to reduce the pH and increase reactivity. In the case of monomer ***[1]***, the acetic acid proved to be particularly important to promoting the reaction between the terminal aldehyde on the monomer and the $–NH_2$ groups on the substrate surface. The substrate was then soaked for 1 hour at room temperature before being rinsed thoroughly with Nanopure water and dried in a nitrogen stream. Functionalized surfaces were characterized using AFM, ellipsometry, and contact angle measurements as described previously in Chapter V.

6.2.3 Amino-silane Functionalization of Mica Substrates

The grafting of 3-APTES to a silicon substrate occurs through reaction of the 3-APTES head-group with the SiO_2 layer formed on piranha-cleaned silicon. However, mica has no native oxide layer, and furthermore, mica has a high negative surface charge density in solution which could react with protonated amine groups of an amino-silane. The structure and chemical composition of mica is shown below in Figure 107. For both of these reasons, covalent attachment of 3-APTES is more complicated on mica but still achievable [269]. Mica is particularly advantageous for our purposes due to our ability to cleave very thin sheets of mica which are flexible and allow for the potential to manually stack deposited fullerene monolayers to increase the quantity of spin-active material available in an electron spin resonance (ESR) tube for measurement of endohedral systems. This stacking is not possible with standard silicon wafers as the inner diameter of the ESR tube is ~2.5 mm, making the insertion of just one silicon wafer piece a challenge, much less a stack of multiple silicon wafers.

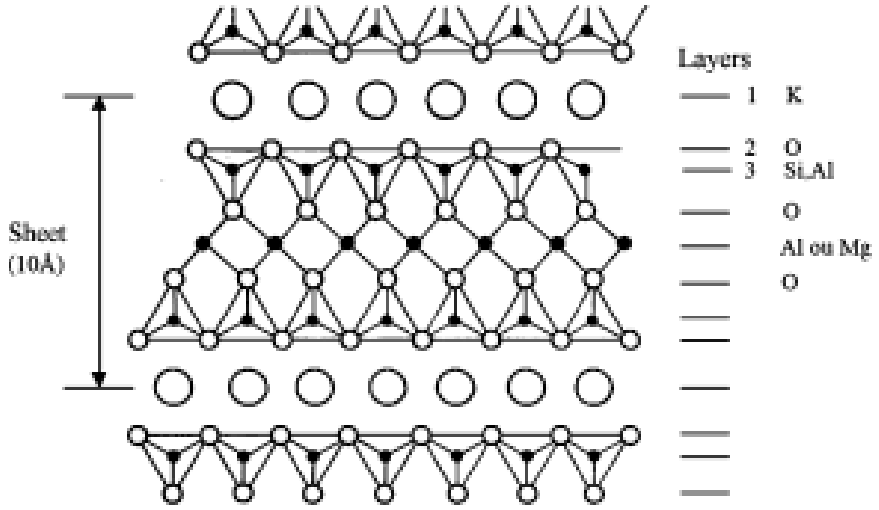

Figure 107. Mica ($KAl_2Si_3AlO_{10}(OH)_2$) layer structure as reported by Mourougou-Candoni et al where cleavage occurs along the potassium (K) layer, producing a new surface with half the potassium ions (reproduced from [269]).

To address the first issue with 3-APTES functionalization of mica surfaces, freshly-cleaved mica was hydrated to create –OH groups on the surface. Mourougou-Candoni and Thibaudau showed that without hydrating the mica surface, no amino-silane layer was attached, but after hydration, covalent attachment of the amino-silane, N-(2-aminoethyl)-3-aminopropyltrimethoxysilane (AAPS) [267, 269]. The hydration step simply involves soaking freshly cleaved mica wafers in Nanopure water for 30 minutes, which is a standard procedure for hydrating mica surfaces [269]. Following hydration of mica substrates, functionalization of the surface was completed using a method similar to that for silicon wafers. A solution of 18.8 mL ethanol, 1 mL Nanopure water, and 0.2 mL 3-APTES was prepared, and the mica substrates were added and allowed to react for 1 hour. Unlike silicon substrate functionalization, no acetic acid was used in the standard preparation of mica samples because higher solution pH allows for the preferential reaction of silane groups with the –OH terminated mica surfaces; at lower pH, protonated

terminal amine groups also react with the mica surface due to the high negative surface charge density. In the presence of acetic acid, the surface chemistry of grafted amino-silane is variable, where some regions are amine terminated and other regions are terminated with the reactive silane groups [269]. All surfaces were characterized before and after grafting of 3-APTES using contact angle measurements prior to the deposition of fullerene materials.

6.2.4 Deposition of Fullerenes on Modified Substrates

Monomer ***[1]*** and fullerene dimers ***[4]*** and ***[5]*** were all investigated for their monolayer formation on chemically functionalized substrates. Monomer ***[1]*** films were prepared by solution casting 0.2 mg/ml solution of ***[1]*** in toluene on 3-APTES substrates (both mica and silicon). The toluene was allowed to evaporate for ~30 minutes, and then the samples were rinsed with toluene to remove any unreacted monomer. For samples prepared on functionalized silicon substrates, ellipsometry and contact angle measurements were conducted on the clean silicon, 3-APTES surface, and monomer ***[1]*** treated substrates to characterize thickness and surface chemistry of the films. For samples prepared on mica, only contact angle measurements and AFM studies were conducted.

Dimers ***[4]*** and ***[5]*** were deposited on 3-APTES films in a similar fashion. Solutions of 0.2 mg/ml dimer in toluene were solution cast on modified silicon substrates, and the toluene was allowed to evaporate for approximately 30 minutes. Films were then rinsed with toluene and dried under nitrogen. Film thickness and contact angle measurements were conducted as above. Film thicknesses in the case of dimers deposited on 3-APTES were compared to monolayer thickness from LB transferred films.

6.2.5 Endohedral Fullerene Studies on Chemically-Modified Substrates

Our collaborators with QIPIRC at Oxford University provided us with high purity endohedral monomer ***[1]***. The fill ratio was 1% ^{14}N or 1 out of every 100 fullerenes is filled. Due to the difficulty in the preparation methods, only 50 µg of this material (^{14}N@***[1]***) was received. An electron spin resonance (ESR) measurement was conducted on a highly dilute solution of ^{14}N@***[1]*** to verify spin activity prior to deposition on $-NH_2$ terminated mica substrates using the technique described above; the resulting ESR spectra is shown below in Figure 108. As shown, even at a dilution that results essentially in a colorless solution (whereas solutions at 0.2 mg/ml in toluene are known to be a rust color), the spin activity is still evident from ESR measurements.

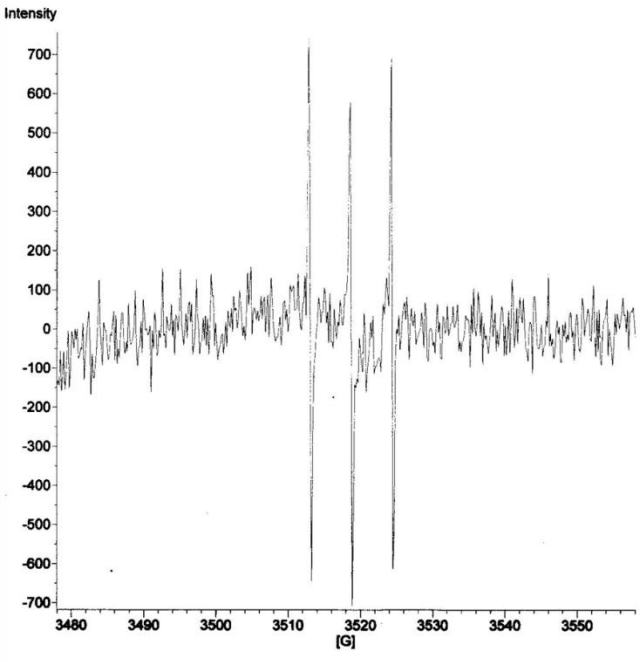

Figure 108. ESR spectrum for high purity ^{14}N@[1] in solution as received from our collaborators.

Based on the purity of ***^{14}N@[1]***, it was determined that a monolayer on a substrate with dimensions 2 mm x 5 mm would be at the lower limit of 10^{12} for detection using ESR. With this in mind, mica substrates were cut and prepared specifically for this purpose to be 2 mm x 25 mm, and 3-APTES was attached to these substrates using the approach described above. A 0.2 mg/ml solution of ***^{14}N@[1]*** in toluene was prepared and cast onto 3-APTES mica substrates. After allowing toluene to evaporate, the films were rinsed and inserted in an ESR tube for measurement. The thinness of mica sheets allowed us to insert 6-7 ***^{14}N@[1]*** covered mica strips into a single ESR tube in attempt to increase the overall quantity of spin available for ESR measurements. ESR measurements were then conducted on these films to determine if the endohedral spin was detectable. Due to the light and heat-sensitivity of ***^{14}N@[1]*** and other endohedral systems, the above processes involving endohedral material were conducted in the dark at room temperature, and all solutions were maintained and stored in the dark at room temperature as well.

6.3 Characterization of Functionalized Substrates

Contact angle measurements on piranha-cleaned silicon and freshly cleaved mica were both determined to be <5° as expected based on literature. Literature values for the contact angle are < 5°, 20° ± 3°, and 40°-63° for freshly cleaved mica, –OH terminated mica, and typical amino-silane SAMs respectively [267, 269]. The contact angle of hydrated mica (–OH terminated) was determined to be consistent with previous results using this technique [269]. Water CA values of 46 ± 3° and 46 ± 14° were measured on functionalized silicon and mica substrates respectively. The average values for both substrates are comparable to previous results [267]. Note that the error on the CA value on mica is large; this can be attributed to non-uniform coverage of the mica surface with

terminal amine groups due to either reaction between the amine-terminal group and the mica surface [269] or roughness of the underlying mica surface due to terracing. Images of the water droplet used for contact angle analysis for hydrated mica and silanized mica and silicon are provided in Figure 109. AFM images and ellipsometry measurements are provided in Chapter V for silicon substrates.

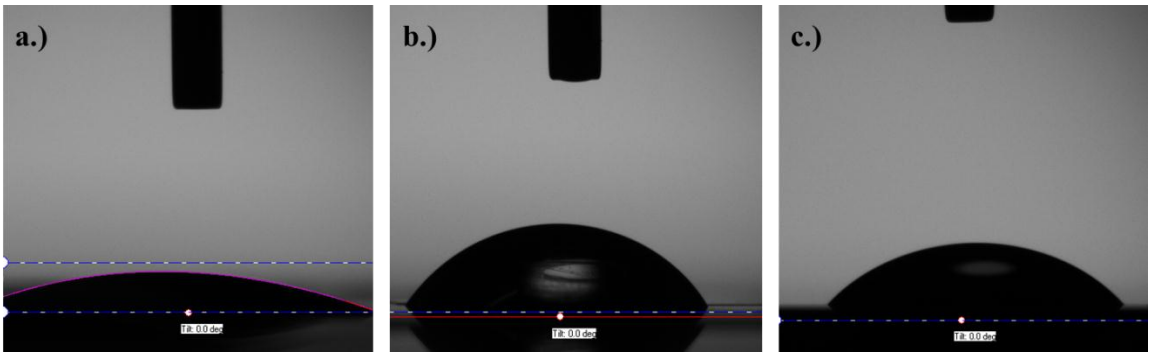

Figure 109. Contact angle camera images used for measurements for a.) hydrated mica surface (19 ± 3°), b.) 3-APTES on mica (46 ± 14°) and c.) 3-APTES on silicon (46 ± 3°).

6.4 Fullerene Monolayers on Functionalized Substrates

Monomer ***[1]*** was deposited on 3-APTES modified silicon, and AFM images from the resulting film after rinsing away any unreacted material are shown in Figure 110. As indicated by the AFM images, fractal structures associated with fullerene physisorbed on the underlying monolayer of ***[1]*** on 3-APTES are visible and widespread. However, smaller scan sizes indicate that the underlying monolayer is uniform, and the underlying structure is particularly evident in the 500x500 nm AFM scan.

The thickness of the deposited monolayer of ***[1]*** was determined to be 2.41 nm using ellipsometry when acetic acid was used in the preparation of the 3-APTES layer. This thickness suggests that more than a monolayer remains attached to the substrate surface after rinsing because the thickness of this monolayer would be expected to be on the order of the fullerene diamater, ~1 nm. The presence of more than a monolayer of ***[1]*** is supported by the AFM imaging in Figure 110.

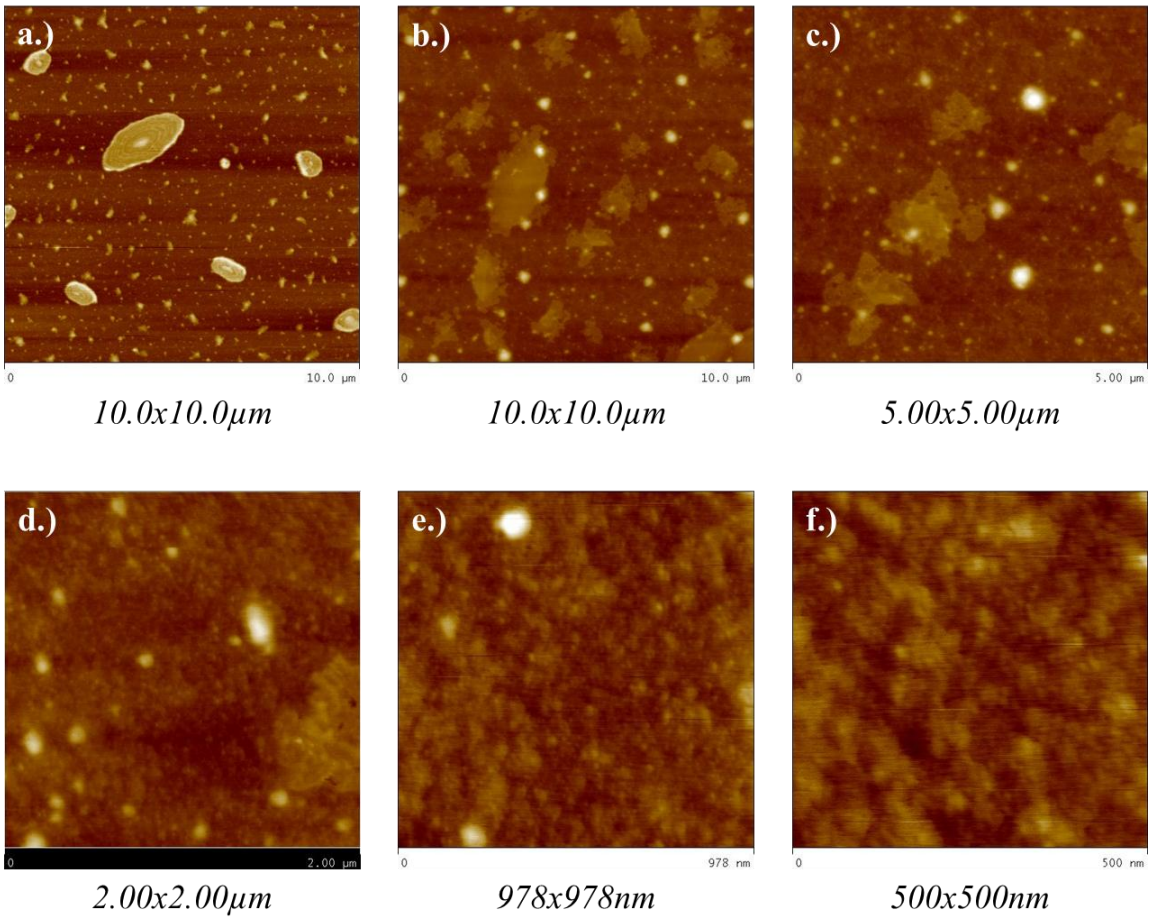

Figure 110. AFM images of monomer [1] on a 3-APTES monolayer at scan sizes of a.) and b.) 10.0x10.0μm, c.) 5.00x5.00μm, d.) 2.00x2.00μm, e.) 978x978nm, and f.) 500x500nm.

In the case of ***[1]***, the contact angle was determined to be 74 ± 5° on silicon (with acetic acid) and 68 ± 5° on mica (without acetic acid). CA values are consistent with a fullerene cage being located at the surface (Figure 111). Monomer ***[1]*** was the only fullerene material investigated on mica because ***[1]*** was the only material we obtained with a large enough fill ratio to perform ESR experiments. The thickness and CA measurements in combination with the AFM images support the conclusion that monomer ***[1]*** remains attached to the $–NH_2$ functional group on the substrate after rinsing. When the 3-APTES layer is deposited on silicon without using acetic acid followed by solution casting of monomer ***[1]*** and toluene rinse, the film thickness in addition to the functional layer was determined to be 0.31 nm, which is less than the thickness of one C_{60} molecule. This result suggests that the majority of monomer ***[1]*** is removed during the toluene rinse, indicating that the monomer does not covalently attach to the 3-APTES layer in the absence of acetic acid.

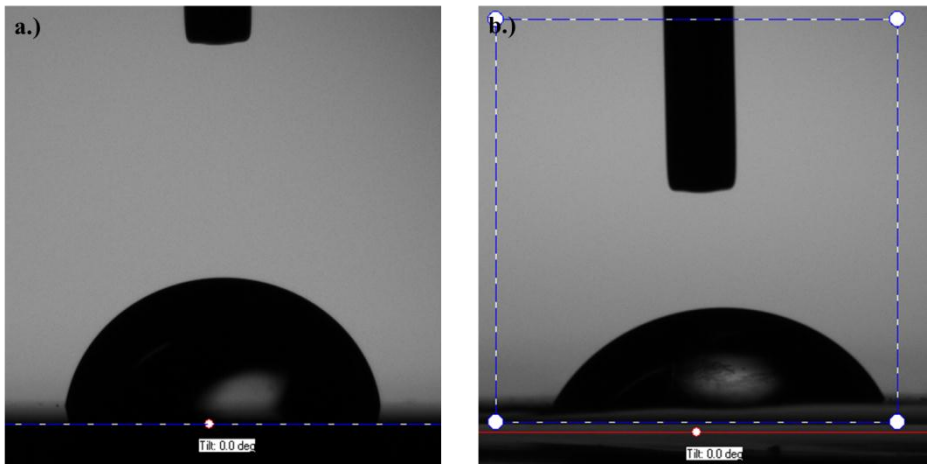

Figure 111. Contact angle image captures for monomer [1] a.) on silicon (with acetic acid) and b.) mica (without acetic acid).

This supports our conclusions regarding the reaction being dominated by covalent bonding formation between the terminal aldehyde and the primary amine group. This reaction is well known [55] and results in the formation of an imide bond (N=C) and the loss of water. Because monomer ***[1]*** only attaches to the 3-APTES layer when acetic acid is used to promote interaction between 3-APTES and silicon, it is likely that the reaction occurring is the formation of an imide bond. Therefore, the covalent attachment of monomer ***[1]*** to the 3-APTES layer is likely to be due to residual acetic acid in the layer promoting the imide bond formation over reaction of the fullerene cage with the primary cage as discussed in Chapter V.

The resulting structure of this film is more ideal than other fullerene systems we investigated with 3-APTES because the covalent attachment is with the modifying ligand rather than the fullerene cage, limiting any further distortion of the fullerene cage. Further investigation revealed that upon rinsing with a 50/50 (v/v) water/ethanol solution, known to break imide bonds, removed the attached layer of monomer ***[1]***. For this reason, high purity endohedral monomer ***[1]*** monolayers were prepared on mica as discussed above. A single monolayer was calculated to be sufficient to achieving an ESR measurement; however, in order to improve the potential quality of signal, we stacked several mica sheets in one ESR tube to manually create multilayers and increase the quantity of spin-active material available. However, as shown by the ESR measurements in Figure 112 and Figure 113, there is no indication of spin-active material on the measured samples. This may be due to insufficient amounts of fullerenes deposited or the loss of the endohedral element; ESR measurements on the endohedral washings collected after deposition, however, still showed measureable signal attributed to ^{14}N.

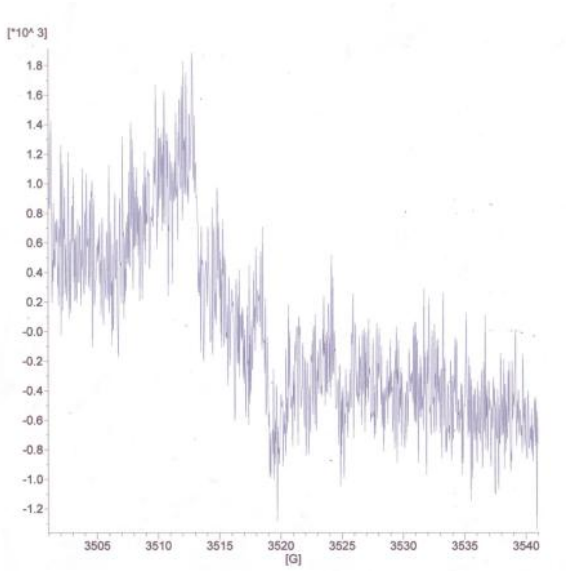

Figure 112. ESR spectrum of high purity endohedral monomer [1] deposited on 3-APTES modified mica (6 samples).

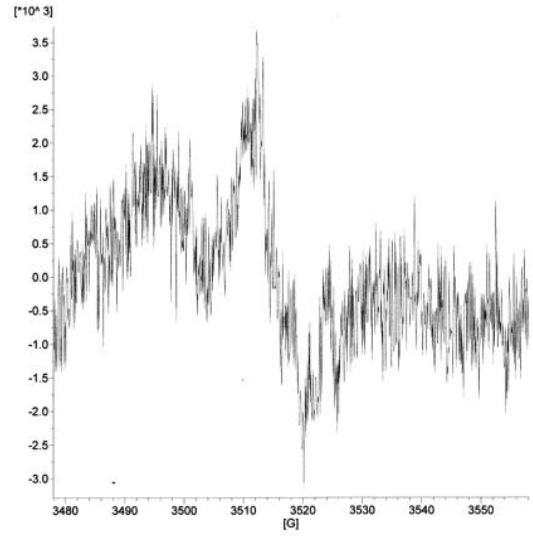

Figure 113. ESR spectrum of high purity endohedral monomer [1] deposited on 3-APTES modified mica (7 samples).

AFM images of dimer ***[4]*** solution cast from a 0.2 mg/ml solution in toluene onto 3-APTES modified silicon are provided in Figure 114. Ellipsometry measurements found the thickness of the layer of ***[4]*** deposited was 1.32 nm, and this measurement is consistent with a monolayer of fullerene material deposited. The contact angle measurements resulted in a value of 84 ± 2°, also consistent with CA values determined from LB transferred monolayers. As indicated by the AFM imaging of dimer ***[4]*** on 3-APTES, the coverage is highly uniform over a large sample area. The images provided are consistent with images taken at multiple locations on the sample surface. While the fullerene dimer structure appears to prevent the physisorption of a second fullerene layer on the covalently attached monolayer, the covalent attachment to the 3-APTES layer is like to occur via reaction of a C_{60} cage with $–NH_2$, causing further distortion to the cage symmetry.

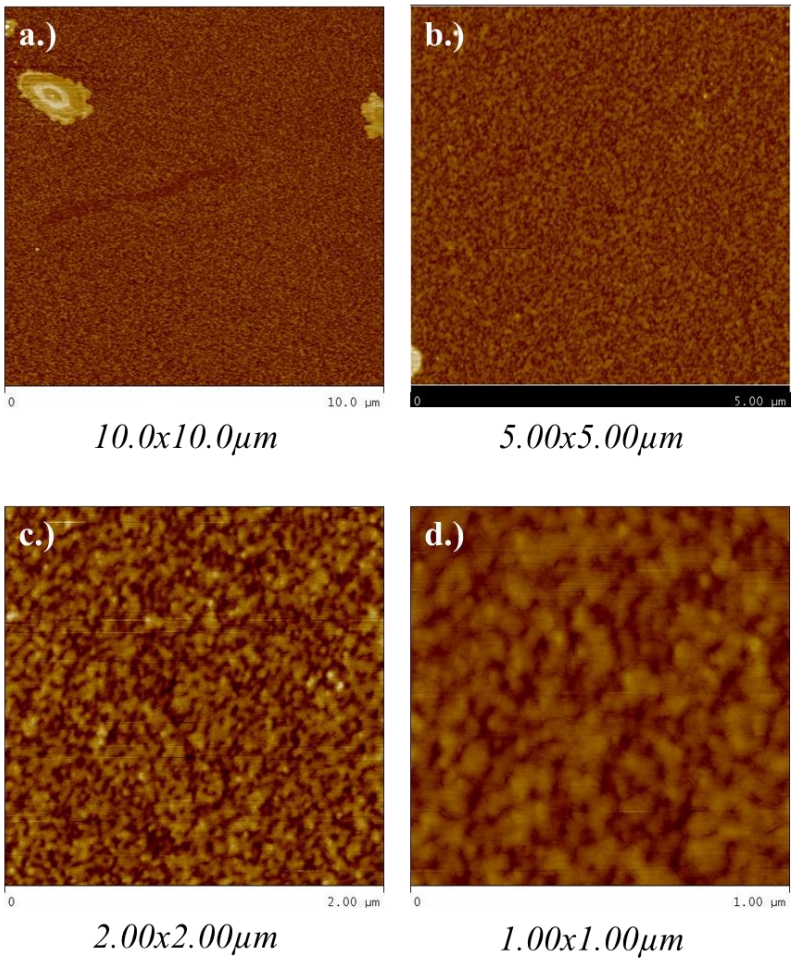

Figure 114. AFM height images of dimer [4] deposited on 3-APTES modified silicon at scan sizes of a.) 10.0x10.0µm, b.) 5.00x5.00µm, c.) 2.00x2.00µm, and d.) 1.00x1.00µm.

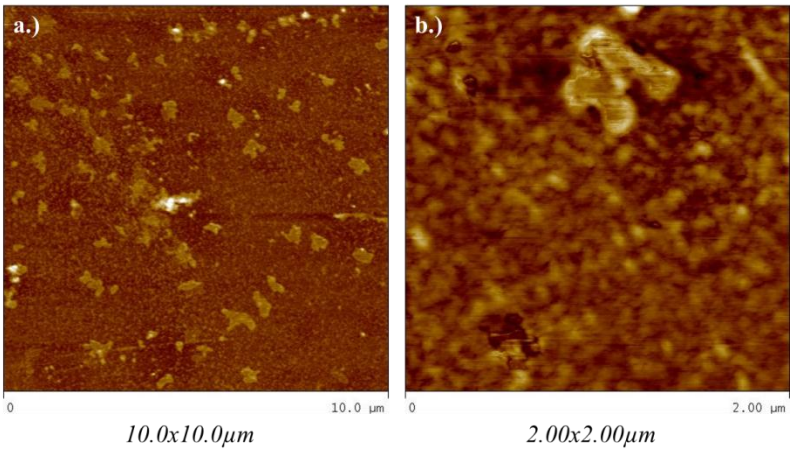

Figure 115. AFM height images of a dimer [5] monolayer deposited on 3-APTES modified silicon at scan sizes of a.) 10.0x10.0µm and b.) 2.00x2.00µm.

Finally, dimer ***[5]*** was deposited on 3-APTES modified silicon using the same procedure. The film thickness after rinsing determined by ellipsometry was 3.12 nm, and as the case with dimer ***[4]***, this thickness is consistent with monolayer thicknesses measured on LB films of 2.57 nm (10 mN/m) and 3.06 nm (15 mN/m). The thickness obtained in this case suggests that the dimers are oriented perpendicularly as expected at higher LB transfer surface pressures. AFM imaging for this film is shown in Figure 115, and in fact, the coverage is more uniform using this method than on films transferred using the LB approach from a water sub-phase. However, also similar to dimer ***[4]***, the covalent attachment between the dimer and the $–NH_2$ group is most likely to occur via the fullerene cage, which may be problematic in the case of endohedral fullerene systems.

6.5 Conclusions and Future Work

The studies presented here are preliminary in nature, but the initial results indicate that this method provides uniform coverage of monolayers of fullerene dimers and a modified fullerene monomer through covalent reaction with a terminal amine group. AFM, ellipsometry, and contact angle results all support the deposition of fullerene material on the 3-APTES surface by solution casting after thorough rinsing with toluene. In the case of dimer systems, the covalent reaction occurs with the cage, which is not ideal for our purposes. However, the monomer contains an aldehyde functional unit that reacts with the $–NH_2$ modified surface to form an imide bond. A reaction such as this, where covalent attachment to the substrate is achieved through an avenue other than with the fullerene cage, shows a great deal of potential for using this method to achieve ordered arrays of fullerenes. Monolayer deposition of a high purity endohedral monomer resulted in inconclusive ESR measurements.

Recommendations for future work include using fullerene dimers having terminal aldehyde chemistry in order to obtain covalently attached dimers via imide bond formation rather than hydroamination of the fullerene cage by a primary amine. Also, further experiments should be conducted using substrates that are patterned by specifically grafting 3-APTES to certain regions or protecting certain regions from fullerene interaction in order to create patterns of fullerenes. If the pattern can be prepared with small enough dimensions, it may be possible to achieve nanowires of fullerenes that are a single fullerene cage in width. This approach has the potential to be powerful in terms of our ability to manipulate the structure and spacing of a fullerene monolayer.

In terms of endohedral fullerene systems, this approach is only valid for high purity materials where a monolayer would contain sufficient numbers of spin (10^{12}). Mica substrates allow some flexibility with this, as more than one mica substrate can be inserted into an ESR tube for measurement. Because the coverage of 3-APTES is non-uniform on mica, the deposited endohedral monomer monolayer is also non-uniform and the surface coverage of each prepared substrate is not maximized. In order to successfully conduct ESR experiments, the quality of the 3-APTES layer must first be improved. Additionally, taking advantage of the capability to functionalize both sides of single mica substrate would allow for the amount of spin material in an ESR tube to be doubled using the same number of samples (6-7) which would increase the spin quantity by an order of magnitude if ideal coverage is achieved.

Using surface modification to direct assembly shows immense potential for controlled organization of fullerenes. Thus far we have shown the technique to result in high quality

monolayer films on silicon of modified fullerene dimers and monomers. Additionally, the flexibility offered by this technique in terms of patterning as well as the ability to combine this approach with other alignment strategies such as the LB method discussed in Chapter V, opens up a wide-range of potential avenues to developing ordered arrays of fullerenes for specific applications. While, ESR measurements using endohedral fullerene systems have not proven successful thus far, improvements in functionalization on mica surfaces will allow for increased potential in this area.

CHAPTER VII: ANALYSIS OF ALIGNMENT STRATEGIES

The goal of this research at the outset was to combine the self-assembly behavior of block copolymers with endohedral fullerenes to create functional nanomaterials. The initial approach was to selectively incorporate fullerenes into the minor phase of a diblock or triblock copolymer having a cylindrical morphology. The cylindrical microphase was required to be small enough to force alignment of a fullerene dimer long-axis along the long-axis of the cylinder. Achieving microphase separation dimensions on this scale (approximately 1 nm) is challenging on its own, but the limited miscibility of fullerenes further complicates the process. There were two major considerations for this strategy: incorporating a sufficient quantity of fullerenes that if the systems were endohedral, there would be the necessary 10^{12} spins required for ESR measurement and secondly, alignment of the microphase structure using non-thermal techniques such as solvent annealing.

Block copolymer alignment proved to be challenging using pure fullerenes in a block copolymer with polystyrene as the solubilizing unit. The miscibility limit of <1 wt% of C_{60} in PS means aggregates form at higher loadings, which in turn disrupt the alignment and microphase separation in the block copolymer. We did show better dispersion can be achieved in vinyl polymers when the vinyl functional group is capable of conforming to the shape of the C_{60} cage as with poly(9-vinylphenantherene). However, further study is required to determine if this improved miscibility translates to better segregation in a block copolymer system at higher loadings of C_{60} using a P9VPh-containing block copolymer compared to that seen previously with PS. Furthermore, even the incorporation of 12 wt% of fullerenes in a P9VPh block is not likely to result in sufficient

spin quantity for ESR measurements in films that are one microphase cylinder diameter in thickness, a requirement for aligning the cylinders by shearing the thin film surface. The advantage of using a block copolymer system with improved miscibility of fullerenes as compared to PS is that more fullerene can be incorporated without complications associated with modifying the fullerene cage to be more soluble such as local distortion at the attachment sites of the spherical cage shape.

Functionalization of the fullerene cage with polystyrene chains is advantageous in the fact that essentially unlimited miscibility is achieved with a PS block so long as any swelling effects are compensated for and well characterized. At higher additions of a PS-modified fullerene it is possible that due to selectively swelling one block with respect to another may induce a morphological shift, so to achieve a final cylindrical morphology, it may be necessary to use a sphere-forming block copolymer to compensate. We have shown localization of fullerenes modified with six PS arms in a lamellae-forming PS-PMMA diblock copolymer with thermal annealing in this dissertation, and at concentrations of fullerenes up to 44 wt% relative to the PS, the lamellar morphology is retained based on neutron reflectivity results. In the case of these lamellar diblock copolymers the fullerenes are likely only aligned in one plane, in a layer at the chain ends or center of the PS block. Therefore it is still necessary to investigate these fullerene stars with systems that can provide alignment in more than one plane such as that potentially offered by cylindrical-forming block copolymers. Also, our results show that if the domain dimension is appropriately small relative to the fullerene size, then a single layer of fullerenes can be achieved in a block copolymer; we can further extrapolate that if the nanoparticle is large enough to segregate to the chain ends in a cylindrical system, then

we could achieve linear arrays of fullerenes along the cylinder long-axis. We did note distortion or "waviness" using neutron reflectivity at the PS/PMMA interface associated with accommodating the fullerene stars, and while this does not appear to affect the formation of a fullerene layer in a lamellar system, it is unclear what may occur to a cylindrical structure in a similar situation when solubilizing these nanoparticles.

Additionally, we have only studied systems that have been thermally annealed. The low molecular weight of the PS-PMMA system used (15-*b*-15 kg/mol) that resulted in the segregation of the fullerenes to the chain ends, also proved to be difficult to align using solvent annealing (see Appendix A). While PS-PMMA morphology has been shown to be controllable based on solvent selection in annealing studies, these studies were conducted on higher molecular weight (> 100 kg/mol) block copolymers; the low molecular weight results in dewetting of the film rather than alignment using solvent annealing. Further investigation would be required to achieve alignment of these systems using solvent annealing to determine what size fullerene star would be required to result in similar alignment behavior in a higher molecular weight block copolymer.

A major practical issue associated with using polymer modification of the fullerene case to disperse in a block copolymer matrix is the dilution of the total available quantity of fullerene in the system. Even in the case of pristine fullerenes, the quantity of fullerenes in the system is diluted by the polymer matrix; this concentration is then further decreased with the addition of polymer arms to the cage. For example, in the 13 kg/mol, six-arm fullerene star we investigated, only 6 wt% of the pure material is actually C_{60}, so when 33 wt% of this material relative to PS in the system is incorporated, the amount of fullerene is approximately 3 wt% in the PS block; this is lower than the potential loadings

of pristine C_{60} in a P9VPh block (12 wt%). However, the amount of fullerene in the system using polymer modification is still an improvement when compared to how much pure C_{60} can be loaded without noticeable aggregation in a PS domain (<1 wt%). It would be possible to increase the amount of fullerene by either reducing the PS molecular weight or reducing how many PS chains are attached. Of course, these adjustments may have implications in terms of solubilization of the fullerene star by the PS block; for example, one-armed stars are significantly more likely to show the aggregation associated with inter-fullerene interactions. Reduction in the overall particle size may also mean the block copolymer size needs adjustment to maintain fullerene location to the center of the PS block, requiring further investigation of these materials.

More ideal alignment strategies would allow for self-assembly of pure fullerene materials without the use a matrix molecule; approaches such as Langmuir monolayer formation at the air/water interface and surface-directed assembly show more promise in terms of our ability to create aligned samples for the desired purpose, although self-assembly of pristine fullerenes using the Langmuir approach is historically difficult due to aggregation tendencies and the highly hydrophobic nature of the fullerene cage. However, we have shown that with simple modification to the bridge chemistry on fullerene dimers, we can achieve well-ordered films at the air/water interface that can subsequently be transferred with uniform surface coverage reproducibly to solid substrates. Furthermore, these films once transferred to a solid substrate require no further alignment treatment. Additionally, adjusting the chemical modification of the bridge between cages in a dimer system allows us the control to manipulate the orientation of the dimer in a film. We have shown that we can achieve film geometries

with dimers that are anywhere from parallel to perpendicular to the water/hydrophilic substrate surface. This level of control has the potential to be very powerful for applications relating to quantum computing where one cage encapsulates ^{14}N and the other ^{15}N. Our ability to control the orientation of the dimer could in theory allow us to also control the position of specific endohedral electronic spins (i.e., all ^{15}N located at the substrate interface and all ^{14}N at the air interface), although this requires further investigation.

In spite of the alignment of the dimer long-axis, the in-plane packing of fullerenes in monolayers prepared via Langmuir-Blodgett deposition is difficult to characterize. Surface coverage is fairly uniform in transferred monolayers; however, the position of one fullerene cage relative to another and particularly in the case of endohedral systems, one spin relative to another, is difficult to control with this method. There is an optimal interaction distance for ESR spin measurements, and it is probable that the lateral packing in LB monolayers is closer than is ideal. Substrate surface patterning may allow for better control of spacing deposited fullerene dimer material in LB films where surface functionalities attract the fullerenes to specified substrate locations and other regions are protected. It may also be possible to achieve linear arrays of fullerenes by patterning such that fullerenes transferred from the air/water interface to a substrate can only attach to pre-patterned linear structures on the surface, either by specifically functionalizing those locations or protecting the rest of the surface from fullerene interaction.

Additional difficulties associated with LB films include the sensitivity of film quality to dust and other atmospheric debris, and the implications this has on building up multilayers. Regardless of dust and other impurities, film quality also typically degrades

as more and more layers are added. This problem can be circumvented by using endohedral fullerene systems of a high enough purity that only one layer of dimer material is required. Because the dimer films are not diluted in any significant way by a matrix molecule (the solubilizing ligands are negligible), enough fullerene material can be packed into a single layer to obtain an ESR signal if the fill ratio is high enough, ~1%. With this in mind, the issues associated with LB films are not insurmountable, and Langmuir-Blodgett monolayers are a viable option to obtaining ordered arrays of endohedral fullerene dimers.

Similar to LB films, monolayers of fullerene-based materials can be formed on chemically functionalized substrates by either covalent or non-covalent interaction. We have shown that an aldehyde-modified fullerene monolayer as well as fullerene dimers can be aligned through covalent attachment to an amine-terminated substrate, although by different mechanisms. The aldehyde-functionalized monomer fullerene has a more ideal interaction with the amine group as the amine reacts with the aldehyde functional group rather than the fullerene cage. As is the case with the dimer systems investigated, the covalent attachment of $–NH_2$ to the actual fullerene cage results in distortion of the cage which can cause an endohedral atom, if present, to escape the cage. A potentially more ideal interaction for the fullerene dimer systems investigated is through non-covalent attachment to a poly(ethylene glycol) (PEG) modified substrate (Appendix D). Because the fullerene dimers all possess a short PEG ligand, the PEG surface will allow for strong interaction without covalent attachment of the fullerene cage. In the monomer and dimers investigated, the coverage of the surface is highly uniform, more so than even the LB films, and the sample preparation process is easy and adaptable to multiple substrates;

monolayer films in these systems would also contain enough spin for ESR measurements if the endohedral fullerenes are of high purity. In terms of the alignment strategies discussed in this dissertation, LB monolayers as well as surface-directed monolayer assembly, or even the combination of the two approaches, are the most promising in terms of obtaining necessary alignment for ordered arrays of fullerenes in amount sufficient to be measured in ESR.

APPENDIX A: ALIGNMENT OF BLOCK COPOLYMER THIN FILMS USING SOLVENT ANNEALING

As discussed extensively in the dissertation text, large linear arrays of spins are required to realize quantum computing applications; in the case of block copolymer/fullerene systems, this requires long range order of the block copolymer as a template for ordering endohedral fullerenes. Due to the thermal instability of endohedral fullerenes, however, standard thermal annealing treatment to order the block copolymer microphase structure could not be implanted. We conducted a series of studies regarding solvent annealing with pure block copolymer thin films as well as block copolymer thin films with fullerenes. Within the confines of these studies, we also investigated the use of topographic substrates and soft molding, both in conjunction with solvent annealing.

The triblock copolymer selected for these studies, poly(styrene)-*b*-poly(butadiene)-*b*-poly(styrene) (SBS), was chosen due to previous investigation regarding solvent annealing on these systems [270]. A cylindrical morphology SBS with molecular weight by block of 39-30-39 kg/mol was spin-coated from a toluene solution on both mica and piranha-cleaned silicon for solvent annealing in cyclohexanone vapor. Cyclohexanone is a solvent for both PS and PB and has been shown to order pure SBS thin films previously by solvent annealing under similar conditions [270]. The experimental setup used for the solvent annealing process is shown in Figure 116. The spin coated sample is placed in a desiccator on a rack above a pot of solvent and then sealed off to create a solvent vapor environment. The sample remains in the desiccator for a specified period of time before removal and imaging using AFM.

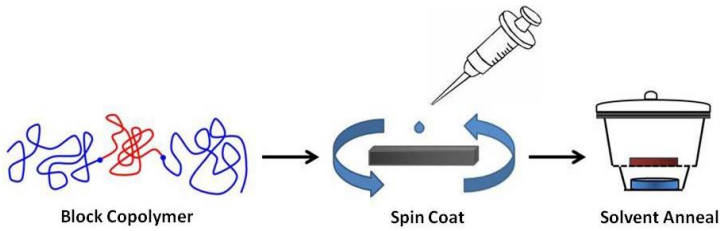

Figure 116. Schematic representation of solvent annealing of block copolymer thin films. Block copolymer solutions are spin coated onto a substrate before being placed in a desiccator for solvent annealing for a specified amount of time.

A series of SBS thin films on mica and silicon were examined using several different solvent anneal times to monitor changes in the alignment and structure with time and the effects of different substrates. Results on mica and silicon were similar, indicating the order achieved is independent of the substrate as expected based on previous solvent annealing studies [107-114]. AFM imaging indicates hexagonally-packed cylinders of PB form perpendicular to the surface after 24 hours of annealing in cyclohexanone and further annealing for 30 hours leads to PB cylinders aligned parallel to the surface on silicon. A sample AFM image of SBS as spin coated on is provided in Figure 117 for comparison purpose before and after solvent annealing. The AFM height and phase images in Figure 118 show the alignment of PB cylinders perpendicular to the silicon surface at different scan sizes after 24 hours of solvent annealing in cyclohexanone vapors.

Figure 117. AFM phase image (1.444 µm x 1.444 µm) of a pure SBS thin film as spin coated from a 4 wt% toluene solution.

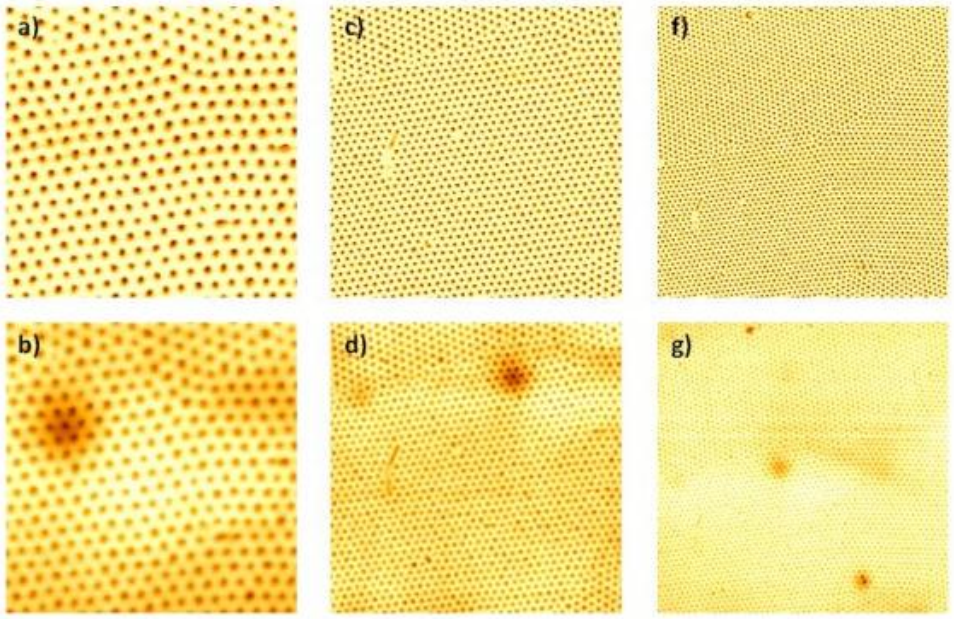

Figure 118. AFM images of SBS (4 wt% in toluene) spin coated on clean silicon wafers (2500 rpm, 30 seconds) after 24 hour solvent anneal in cyclohexanone: a-b) Phase and height images respectively with scan size of 0.722 µm x 0.722 µm, c-d) Phase and height images respectively with scan size of 1.444 µm x 1.444 µm, e-f) Phase and height images respectively with scan size of 2.165 µm x 2.165 µm. After 24 hours of solvent annealing in cyclohexanone, PB cylinders are well ordered perpendicular to the silicon substrate.

SBS thin films were also investigated on topographic substrates of patterned silicon with several different pattern dimensions (trench width, trench depth, and pitch). Topographic substrates have been shown to guide alignment along the trench walls with thermal annealing (refs), so films prepared on similarly patterned silicon substrates were studied for the alignment quality with solvent annealing. Thin films were spin coated on the patterned silicon substrate and imaged as spin coated using AFM. Patterned silicon with trench depth, width, and pitch of 300 nm, 260 nm, and 600 nm respectively and 280 nm, 158 nm, and 300 nm respectively were investigated. The silicon patterning is evident in AFM conducted on clean patterned wafers; however, once the SBS is spin coated onto the patterned silicon, the pattern is no longer clearly visible using AFM on the substrate having the smaller trench width and pitch. This may result because the polymer solution is not drawn down into the trench. Using what we know of SBS thin films and ordering on flat silicon substrates, we then solvent annealed the prepared thin films in cyclohexanone for 24 hours, and AFM images of the as spin coated and annealed films are shown in Figure 119 and Figure 120 respectively for the two different patterns used. Figure 120 shows that our systems of SBS on patterned silicon are not as well ordered compared to flat substrates after solvent annealing.

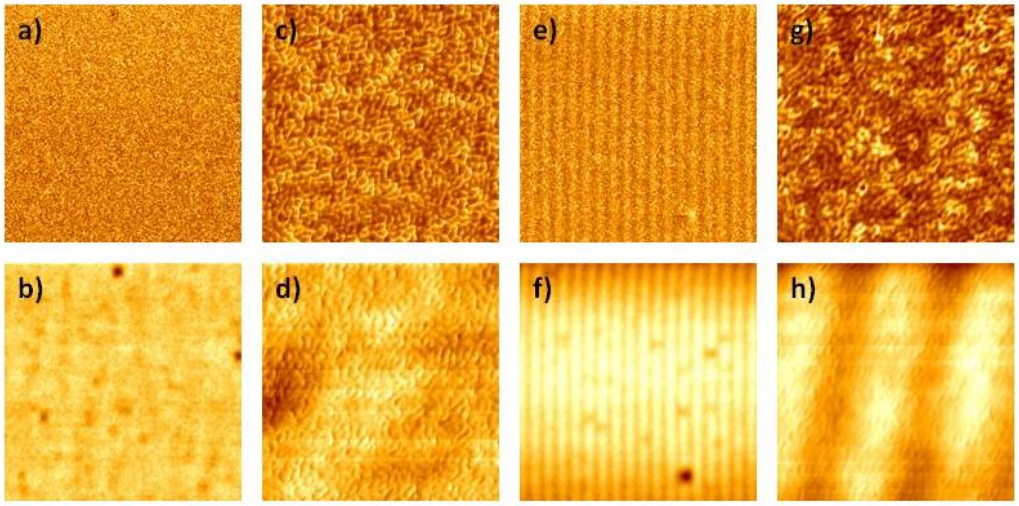

Figure 119. AFM images of SBS (4 wt% in toluene) as spin coated on clean, patterned silicon substrates with the top row of phase images and bottom row of height images: a-d) AFM images of SBS on patterned silicon with depth: 280 nm, width: 158 nm, and pitch: 300 nm with scan size of a,b) 10.105 µm x 10.105 µm and c,d) 1.444 µm x 1.444 µm; e-h) AFM images of SBS on patterned silicon with depth:300 nm, width: 260 nm, and pitch: 600 nm with scan size of e,f) 10.105 µm x 10.105 µm and g,h) 1.444 µm x 1.444 µm.

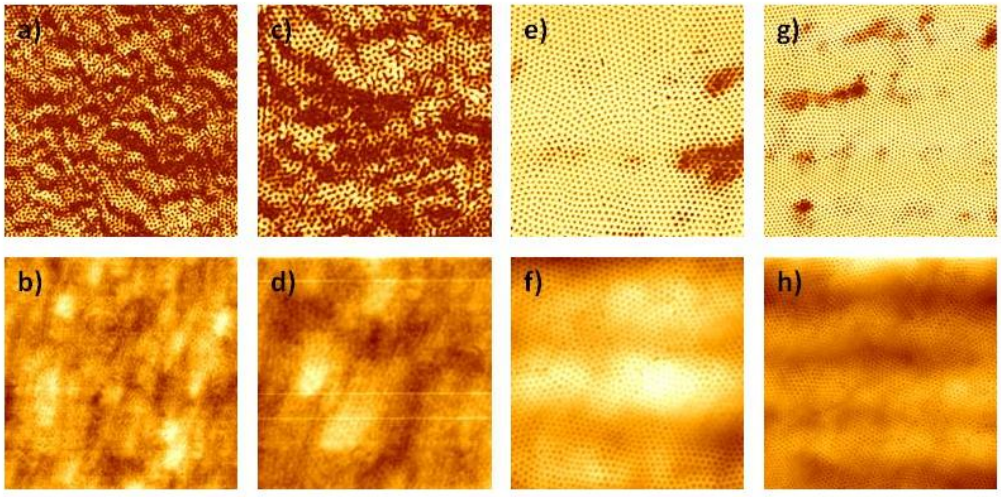

Figure 120. AFM images of SBS (4 wt% in toluene) after 24 hr solvent anneal in cyclohexanone on patterned silicon substrates with the top row of phase images and bottom row of height images: a-d) AFM images of SBS on patterned silicon with depth: 280 nm, width: 158 nm, and pitch: 300 nm with scan size of a,b) 10.105 µm x 10.105 µm and c,d) 1.444 µm x 1.444 µm; e-h) AFM images of SBS on patterned silicon with depth: 300 nm, width=260 nm, and pitch: 600 nm with scan size of e,f) 10.105 µm x 10.105 µm and g,h) 1.444 µm x 1.444 µm.

In a method similar to topographic alignment, block copolymer systems have also been previously aligned using a pre-patterned elastomer stamp pressed onto the surface of a thermally annealed thin film prepared on a flat substrate [120]; we used a similar technique with SBS thin films and solvent annealing to determine if this was a feasible approach to alignment without thermal treatment. A soft PDMS mold was prepared to conduct experiments using the soft molding technique with solvent annealing for ordering block copolymer thin films. The patterned PDMS mold was prepared using a patterned silicon substrate with a depth of 265 nm, width of 200 nm, and pitch of 500 nm. Previous work using this technique used a holographic grating to prepare the patterned PDMS mold [120]. The thin film was placed in solvent vapor for 24 hours prior to the mold being pressed to the thin film surface as it was shown this step was important to pattern transfer to the film from the mold. AFM imaging (Figure 121) of the thin film after this process indicates that the pattern is transferred to the thin, indicated by the grooves seen in the height image in Figure 121. However, alignment of the block copolymer with respect to the grooves does not occur. It may be that further experiment is required to optimize the methods and conditions for using soft molding in conjunction with solvent annealing to in order to align cylindrical morphology block copolymer thin films. In theory, solvent annealing should work essentially like thermally annealing for soft molding alignment; therefore, it is likely the groove dimensions were too small and the morphology of cylinders perpendicular to the substrate hampered the alignment process. It is also possible that traces of the PDMS stamp remain on the thin film surface to the presence of cyclohexanone droplets on the sample surface.

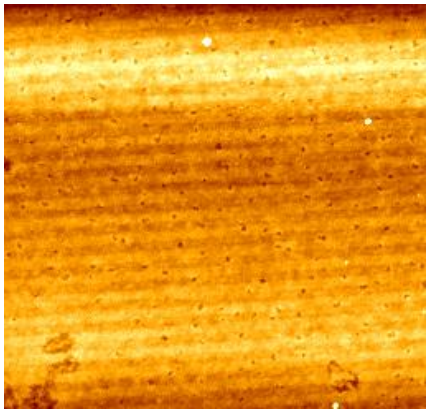

Figure 121. AFM height image (10.105 µm x 10.105 µm) of SBS (4 wt% in toluene) after 24 hour solvent anneal in cyclohexanone and soft mold alignment.

Solvent annealing studies were also conducted on SBS thin films containing pristine C_{60}. Thin films were prepared from 2 wt% SBS in toluene solution on freshly cleaved mica. Fullerene concentrations included 0.5, 1, 3, and 6 wt% C_{60} relative to the PS blocks of the SBS block copolymer used (39-30-39 kg/mol). Figure 122 shows the thin films as spin coated at each fullerene concentration. From the AFM images of SBS-C_{60} thin films, we do not see any change in the phase behavior as spin coated on freshly cleaved mica. However, swelling of the PS blocks (brighter structures in AFM images) does occur with increasing weight percent of fullerene in the system which indicates that at least some of the C_{60} is segregating into the PS blocks. After solvent annealing in cyclohexanone vapors for 24 hours the pure block copolymer maintains the cylindrical microphase (Figure 123); however, the PS blocks are swollen significantly by the solvent annealing process. Solvent annealing has little effect on thin films of SBS with C_{60}. The films maintain the worm-like pattern seen in the as spin coated films with a cylindrical morphology. However, with increasing fullerene concentration, the AFM images indicate the appearance of clumps on the film surface after solvent annealing, particularly at 6

wt% C_{60} relative to the PS blocks. The clumps that develop on the surface may be clusters of fullerenes that are forced out of the block copolymer during the solvent annealing process. The case may be that the presence of fullerene materials in the block copolymer hampers the mobility of the polymer chains such that alignment is more difficult or takes more time. Further study is required to better understand the behavior of block copolymer/C_{60} thin films during solvent annealing.

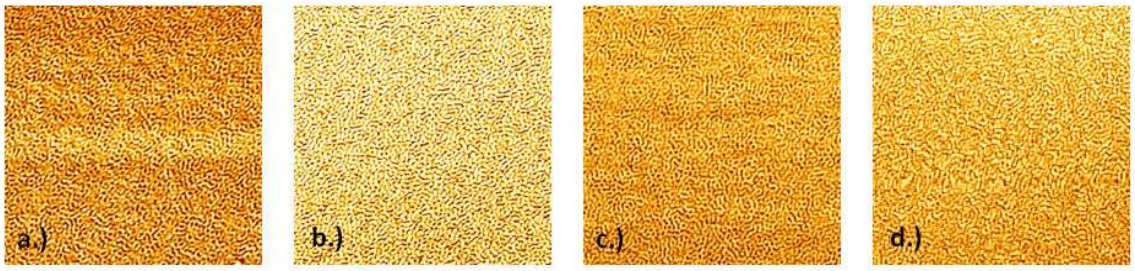

Figure 122. AFM phase images (2.165 µm x 2.165 µm) of SBS/C_{60} thin films with a) 0.5 wt% C_{60}, b.) 1 wt% C_{60}, c) 3 wt% C_{60}, and d) 6 wt% C_{60} as spin coated.

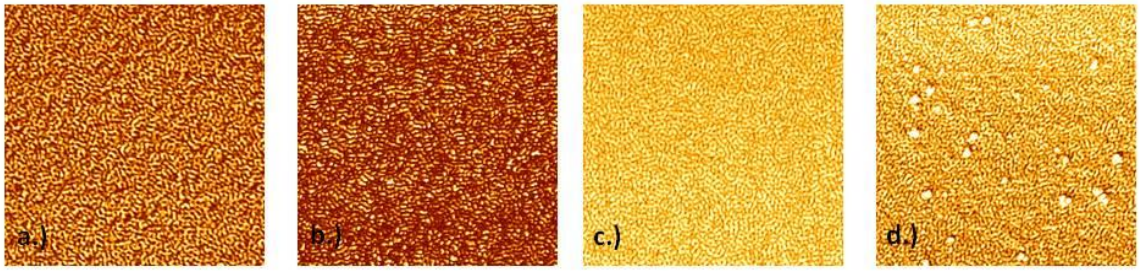

Figure 123. AFM phase images (2.165 µm x 2.165 µm) of SBS/C_{60} thin films after 24 hour solvent anneal in cyclohexanone vapors with a) 0.5 wt% C_{60}, b.) 1 wt% C_{60}, c) 3 wt% C_{60}, and d) 6 wt% C_{60} from 2 wt% polymer solutions in toluene.

A brief study was also conducted with PS-modified fullerenes, C_{60}PS, in SBS thin films using AFM. These same fullerene stars, with six covalently grated polystyrene arms, were investigated with a symmetric diblock copolymer using neutron reflectivity as discussed in Chapter IV. It was expected that the addition of PS arms to the fullerene cage would force the C_{60} to occupy the PS block of the copolymer. Figure 124 shows an AFM phase image of an SBS thin film with 1 wt% C_{60}PS as a function of the PS block. Compared to both the pure SBS thin films and thin films with C_{60}, the styrene block is significantly more swollen with the addition of the C_{60}PS as we expected due to the increase in the relative amount of polystyrene. At 1 wt% C_{60}PS the increased PS content does not appear to force a phase shift as the cylindrical morphology is maintained.

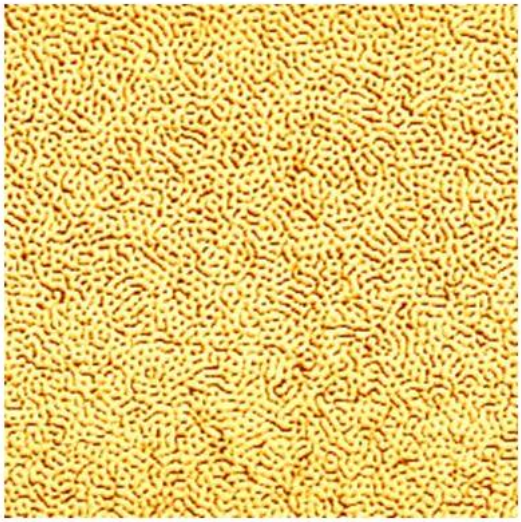

Figure 124. AFM phase image (2.165 µm x 2.165 µm) of an SBS thin film (2 wt%) with 1 wt% C_{60}PS as spin coated.

Solvent annealing can be applied in a number of different ways, either alone or in conjunction with other techniques such as patterned substrates or soft molding, to achieve ordered microphase structures. The structure and orientation can be further controlled by taking advantage of solvent selectivity and specifically swelling either one or all blocks. We have shown that cylinder-forming SBS films annealed in cyclohexanone vapor for 24 hours results in hexagonally-packed PB cylinders oriented perpendicularly to the substrate for both mica and silicon. This supports the proposed mechanism of ordering via solvent annealing starting at the film surface and propagating downward rather being substrate-driven. Furthermore, we have shown that the same type and quality of alignment observed in pure SBS films with solvent annealing are not achieved when C_{60} is included in the thin film. The incorporation of C_{60} does results in swelling of the PS blocks indicating C_{60}, at least at lower concentrations, is located in the PS block. At higher fullerene concentrations clumps appear on the film surface as indicated by AFM studies, and it is probable that these clumps are fullerene aggregates that have been forced out of the block copolymer due to their size. Further study would be required to verify this. Finally, we also showed the incorporation of PS-modified fullerenes into an SBS thin film. These materials were further investigated with symmetric PS-PMMA as discussed in Chapter IV. In general, further study is required to determine if solvent annealing is an effective method to achieving alignment of block copolymer-fullerene nanocomposite thin films.

APPENDIX B: FLUORESCENCE QUENCHING OF LINEAR AND CYCLIC POLYSTYRENE BY C_{60}

Similar to studies conducted with PPE and C_{60} for fluorescence quenching discussed in Chapter III, we also conducted a series of studies on the fluorescence quenching of polystyrene by C_{60}. Cyclic and linear PS have been shown by Gan and coworkers to be weakly fluorescence with cyclic PS showing enhanced fluorescence compared to a similar size linear PS [271].

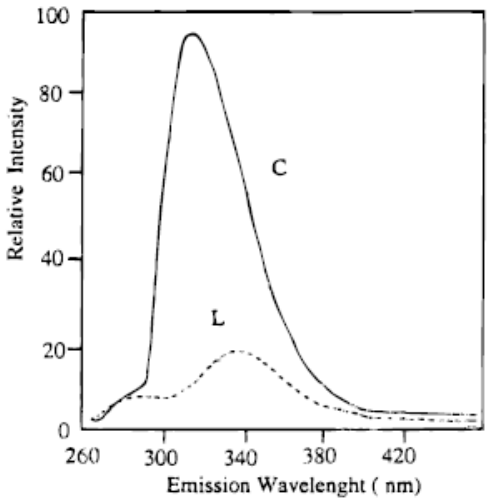

Figure 125. Fluorescence spectrum obtained for cyclic (solid line, labeled 'C') and linear (dashed line, labeled 'L') PS reported by Gan et al [271].

As shown by Figure 126 below, our initial experiments conducted on cyclic PS (M_n: 2963 g/mol) and linear PS (M_n: 3256 g/mol) show similar behavior, although slightly different fluorescence spectra when compared to Gan et al (Figure 125) [271]. In both cases an excitation wavelength of 253 nm was used.

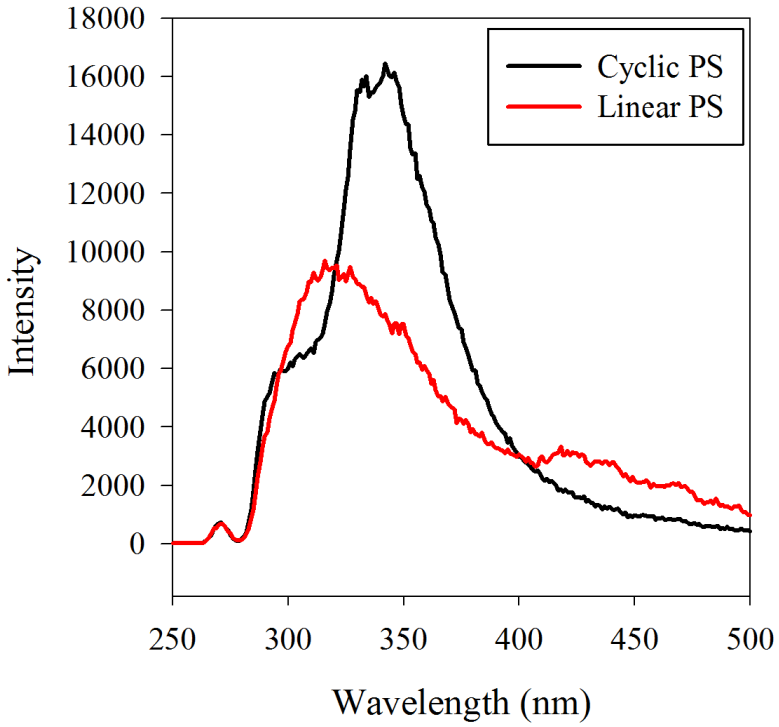

Figure 126. Fluorescence intensity measurements for cyclic PS (M_n: 2963 g/mol) and linear PS (M_n: 3256 g/mol), measured using an excitation wavelength of 253 nm. The small speak at 250 nm and 300 nm is associated with this excitation wavelength.

In terms of the cyclic PS we obtained a similar spectrum with a weaker intensity shoulder at 290 nm (comparable to 280 nm reported by Gan et al [271]) followed by a broad, more intense peak at 340 nm (compared to 334 nm [271]). However, the linear PS spectrum differs from that shown previously. In our case, an initial peak of higher intensity is observed at 320 nm followed by a weaker shoulder at 420 nm. When compared to the linear specture in Figure 125 [271], we see this is essentially the opposite of the expected behavior in terms of intensity, and the peak locations are shifted to higher wavelength in

our measurements. Gan et al report that the first peak is associated with monomer fluorescence and the second peak is associated with excimer fluorescence [271] where excimers are dimerized units of the polymer that occur in the excited state. This is important when studying fluorescence quenching by C_{60} discussed below. However, this behavior is only noted in the case of pure linear PS fluorescence; in the case of quencher, the fluorescence spectra more closely resemble that previously measured.

C60 in toluene was added to cyclic and linear PS solutions (in toluene) in incremental quantities resulting in fullerene concentrations ranging from 4.75×10^{-6} M C_{60} to 2.81×10^{-5} M C_{60}, and fluorescence intensity measurements were made after each addition. The results were then analyzed using the traditional Stern-Volmer approach introduced and described in detail in Chapter III [214, 219, 221, 222]. Stern-Volmer constants (K_{sv}) and association constants for complex formation (K) were extracted from this analysis and used to provide insight as to the strength of interaction between C_{60} and PS.

The addition of C_{60} does quench the fluorescence of both cyclic and linear PS as shown in Figure 127 and Figure 128 respectively. The spectrum in red is for the pure PS in both cases, and the purple spectra correspond to the highest C_{60} quantities and therefore exhibit the lowest fluorescence intensities. With increasing fullerene concentration for both systems, both peaks in the spectra decrease in intensity and also become more clearly defined (Figure 127). Importantly, in the cyclic PS studies, the first peak switches from being lower in intensity with respect to the second peak to being more intense than the second peak. As mentioned, this second peak is associated with excimer fluorescence and may reduce in intensity when compared to the pure cyclic PS measurements because of the presence of fullerene limits the excimer formation in the excited state due to

binding; less dimerized polymer units present in solution would results in a lower fluorescence intensity attributed to this material. It may also be possible that the fluorescence intensity associated with excimers decreases overall and with respect to the monomer fluorescence peak because the C_{60} quenches the dimer units more efficiently than the monomers. As mentioned, the first monomer peak also reduces in fluorescence intensity with increasing fullerene concentration for cyclic PS, attributed to collisional and binding interactions with C_{60} molecules in solution. This peak was used for subsequent Stern-Volmer analysis.

In the case of linear PS quenching by C_{60}, we observe similar behavior. When comparing to the pure linear PS spectrum, however, the first peak remains at higher intensity relative to the second excimer peak. Both peaks become more distinguishable at higher fullerene concentrations, and the excimer peak becomes relatively weaker when compared to the monomer peak as in the case of cyclic PS quenching. Again, this may result due to either reduced dimer formation in the excited state or more efficient quenching of the dimerized linear polymer.

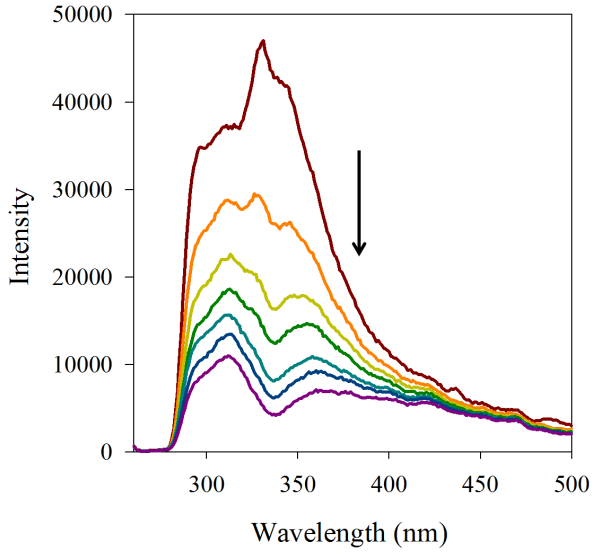

Figure 127. Fluorescence quenching of cyclic PS (M_n: 2936 g/mol) by C_{60}. The arrow indicates the direction increasing C_{60} concentration (up to $2.81x10^{-5}$ M). Pure cyclic PS measurements are provided by the red plot for comparison purposes.

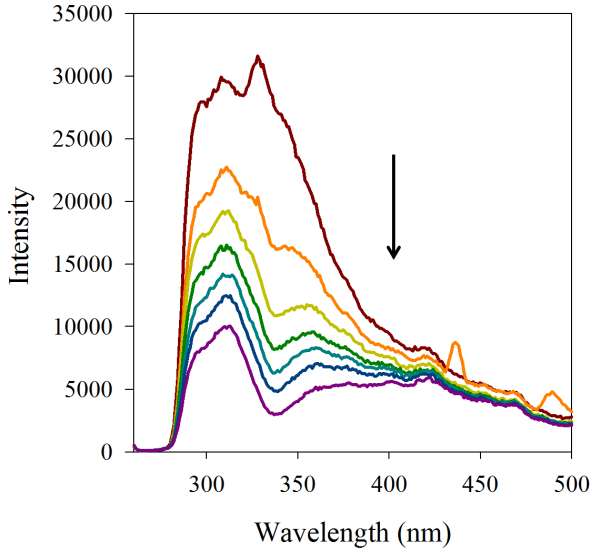

Figure 128. Fluorescence quenching of linear PS (M_n: 3256 g/mol) by C_{60}. The arrow indicates the direction increasing fullerene concentration up to $2.81x10^{-5}$ M C_{60}. The pure linear PS spectrum is provided by the red plot for comparison purposes.

Stern-Volmer analysis for cyclic PS quenching by C_{60} is shown in Figure 129 and Figure 130; Intensity values were taken at a wavelength of 310.95 nm for all concentrations of fullerene. The Stern-Volmer plot (Figure 129) shows mostly linear behavior with a slight upward curvature and K_{sv} (including static and dynamic quenching components) of 8.39 x 10^4 M^{-1} as determined from the slope. The upward curvature in the Stern-Volmer plot can likely be attributed to both static and dynamic quenching being present in the system [219, 221]. Because static quenching occurs by complex formation between fluorophore (cyclic PS) and quencher (C_{60}), the static Stern-Volmer constant component is equivalent to the association complex between cyclic PS and C_{60}. Using the plotting method provided by Acquavella et al [222], the binding constant, K, is given by the negative slope of the linear plot shown in Figure 130. The association constant was determined to be 5.92 x 10^3 M^{-1} for cyclic PS with C_{60}.

Similarly, Stern-Volmer analysis of linear PS quenching by C_{60} results in the determination of a binding constant. The Stern-Volmer plot is relatively linear with some upward curvature, as shown by Figure 131, and K_{sv} was found to be 6.63 x 10^4 M^{-1} for linear PS, smaller than that determined for cyclic PS with C_{60}. Furthermore, the association or binding constant, K, between linear PS and C_{60} was determined as 5.11 x 10^3 M^{-1} from the inverse slope of the linear plot in Figure 132.

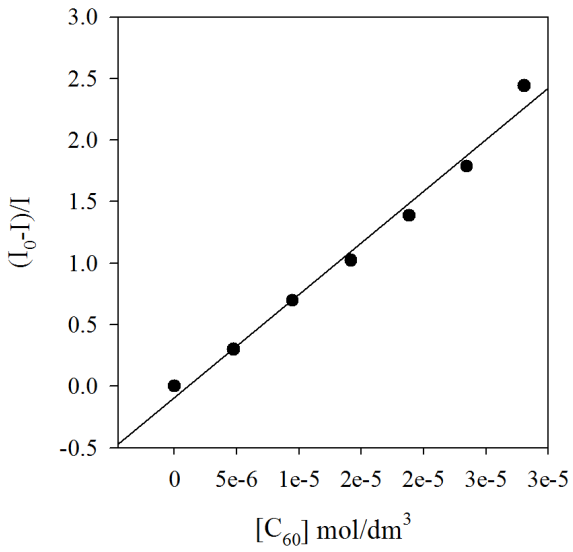

Figure 129. Stern-Volmer plot for cyclic PS fluorescence quenching by C_{60}. The slope in this case was determined to be 8.39 x 10^4 M^{-1}, equivalent to the Stern-Volmer constant, K_{sv}, containing both static (complex formation) and dynamic (collisional) quenching components.

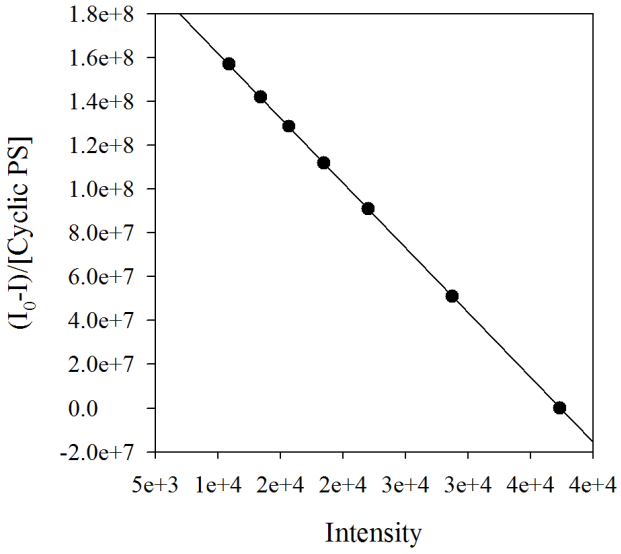

Figure 130. Determination of association constant from fluorescence quenching experiments for cyclic PS and fullerenes. The association constant for complex formation, determined as the negative of the slope, was found to be 5.92 x 10^3 M^{-1} for cyclic PS with C_{60}.

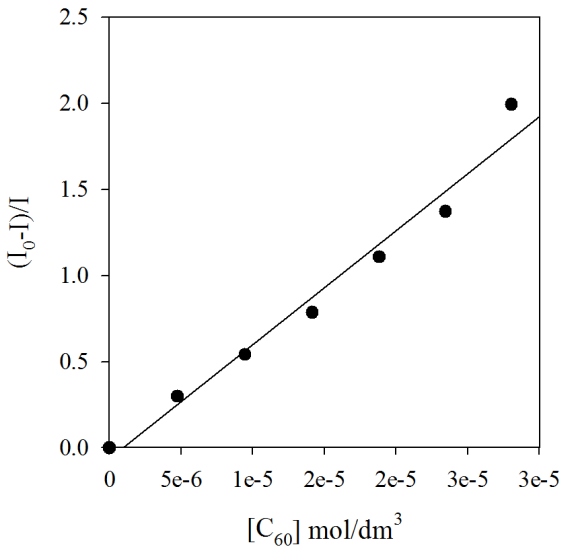

Figure 131. Stern-Volmer plot for linear PS fluorescence quenching by C_{60}. The slope in this case was determined to be 6.63 x 10^4 M^{-1}, equivalent to the Stern-Volmer constant, K_{sv}, containing both static and dynamic quenching components.

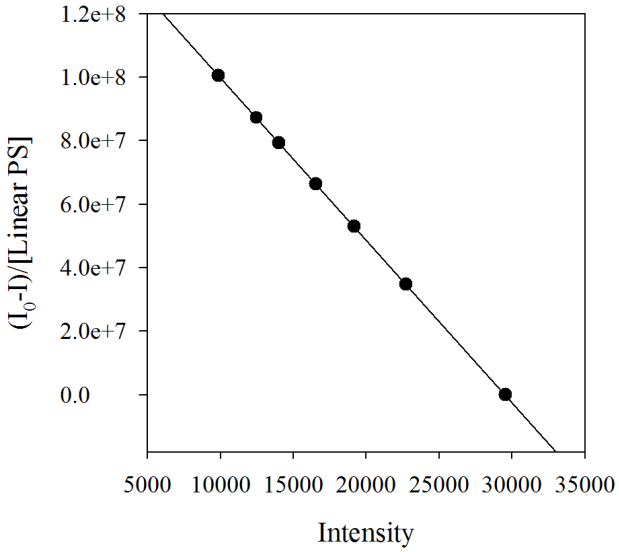

Figure 132. Determination of association constant from fluorescence quenching experiments for linear PS and fullerenes. The association constant for complex formation, determined as the negative of the slope, was found to be 5.11 x 10^3 M^{-1} for linear PS with C_{60}.

The association constant values of 5.92 x 10^3 M^{-1} and 5.11 x 10^3 M^{-1} determined for cyclic and linear PS respectively with C_{60} are not significantly different. While the interaction with cyclic PS is slightly stronger based on the results, the order of magnitude for interaction strength is the same in both cases and the difference is therefore negligible. It is likely that the cyclic PS may interaction stronger with the fullerenes than the linear counterpart of the dimensions of the ring are such that the cyclic polymer can conform to the fullerene cage on all sides. However, in both cases the polymer backbone limits the ability of the interacting vinyl functional groups to all orient optimally with the C_{60} cage to maximize interaction. The method of analysis assumes a one-to-one interaction and this is likely the case based on the quality of the data fits as well as the size of the PS chains investigated.

When the strength of interaction with these materials is compared to that of previous work, we see that the interaction is on the same order of magnitude as that determined by Yamaguchi and coworkers for cyclic polymers with C_{60} [92]. However, the interaction strength is weaker by two orders of magnitude when compared to the PPE-C_{60} systems discussed in Chapter III. Combining what we know about C_{60}-polymer miscibility from WAXS and DFT studies [147, 213] with the difference in binding constants for PS versus PPE systems, it seems probably that we can correlate association constant strength to miscibility behavior with C_{60}. Therefore, it is probable that more C_{60} can be dispersed in PPE-based polymers than in the <1 wt% determined to be miscible in polystyrene.

APPENDIX C: MISCIBILITY OF FULLERENES WITH POLY(4-CHLOROSTYRENE) AS DETERMINED BY WAXS

In addition to the experiments discussed in Chapter III using wide angle x-ray scattering to determine the dispersion limits of fullerenes in vinyl aromatic polymers, we also prepared blends of C60 with a vinyl polymer containing a chlorine functionality, poly(4-chlorostyrene). The chemical structure of poly(4-chlorostyrene) (P4CS) can be seen below in Figure 133; P4CS was selected for investigation as atoms that are much larger than carbon such as chlorine, while electron withdrawing, have been shown to enhance fullerene miscibility with small molecules in previous work [58-69]. We prepared solid blends of P4CS and fullerenes using the method described above by solution mixing and precipitation of the resulting blend. WAXS measurements were made on pressed thin films of blends containing 1, 5, and 10 wt% C_{60} in P4CS, and results were compared to those with polystyrene [147, 213] to determine if higher quantities of fullerenes could be dispersed in P4CS prior to evident aggregation in the 1D WAXS profiles.

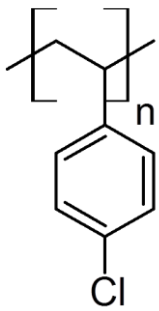

Figure 133. Chemical structure of poly(4-chlorostyrene) investigated with fullerenes for dispersion limits in a solid state blend.

Results of WAXS studies show that the dispersion limit of C_{60} in P4CS is less than 1 wt% (Figure 134), and based on the comparative size of fullerene crystalline peaks at 1 wt% in PS versus P4CS, fullerenes are, unexpectedly, less miscible with poly(4-chlorostyrene) than polystyrene. When considering the differences between chlorobenzene, which shows improved solubility with C_{60} compared to benzene, and P4CS, the reduced miscibility can likely be attributed to the presence of the polymer backbone. Chlorine functional groups are electron withdrawing, and the enhanced negative charge created by this is responsible for the increased solubility between C_{60} and chlorobenzene as fullerenes willing accept electrons (or negative charge). The presence of the polymer backbone at the *para* position to the chlorine functional group likely decreases or even inhibits the electron withdrawing capability of the chlorine group on the phenyl ring. Because fullerenes are electron accepting materials, the interaction with an electron withdrawing group such as the chlorine unit are not preferred without a localized negative charge. The decreased miscibility of C_{60} with P4CS can be attributed to the reduced electron withdrawing capability of the chlorine unit due to the presence of the polymer backbone. Furthermore, as noted for PS, P2VN, and P9VPh interactions with C_{60}, the polymer backbone limits the ability of the vinyl functional group to arrange itself with respect to the fullerene molecule, making conformal geometry a more important factor than any electronic interactions in improving fullerene-polymer miscibility.

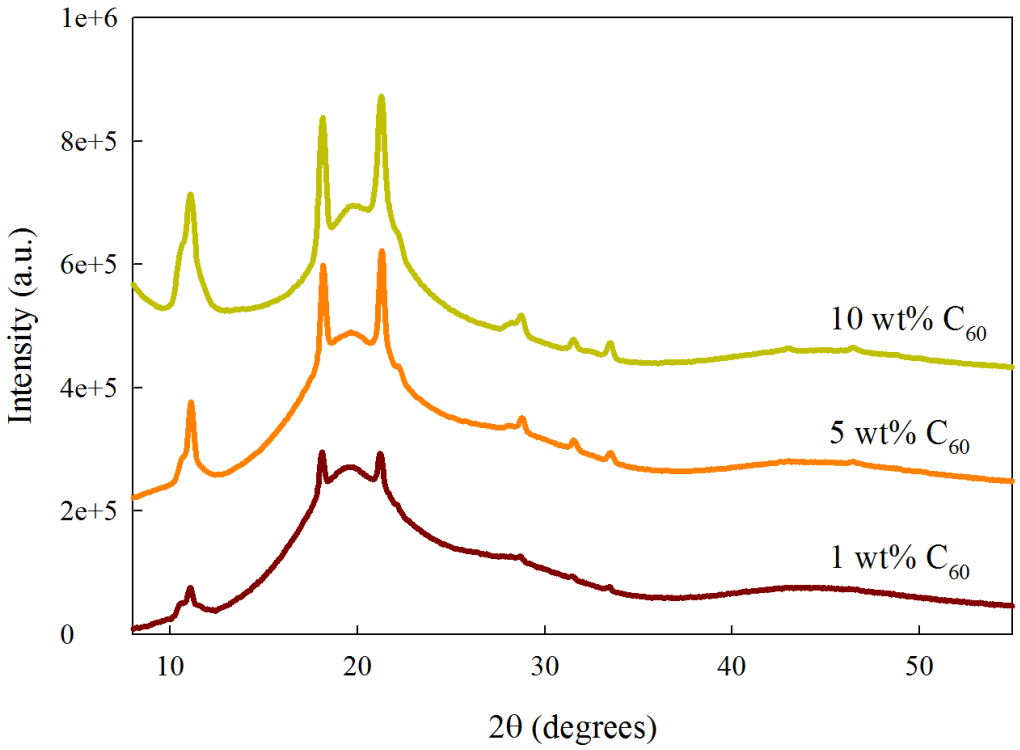

Figure 134. 1D WAXS patterns for P4CS-C_{60} blends prepared at 1, 5, and 10 wt% C_{60} content. As noted, fullerene aggregate peaks at 2θ = 10.8, 17.8 and 20.9° are clearly present even at 1 wt%. The strength of aggregate peaks at this concentration in P4CS further suggests that fullerenes are less soluble with P4CS than even PS polymers.

WAXS studies on P4CS-C_{60} blends indicate that small molecule-fullerene interactions are not always accurate in predicting the behavior of fullerenes with a polymer. The overall size of polymer chains results in differences in the mobility of interacting groups, and the attachment of a polymer backbone alters the electronic structure relative to a comparable small molecule. Both of these factors and the results of polymer-fullerene studies indicate that further understanding is required to characterize the interactions in these blends to optimize dispersion at higher fullerene loadings.

APPENDIX D: POLY(ETHYLENE GLYCOL) FUNCTIONALIZATION OF SUBSTRATES

PEGylation is the covalent attachment of poly(ethylene glycol) chains to a surface. In our case, we attempted to graft short poly(ethylene glycol) (PEG) chains with M_n of 1000 g/mol both silicon and mica surfaces specifically for use with fullerene dimer ***[2]***, having two short PEG ligands attached to the dimer bridge via LB deposition and/or solution casting. However, other dimer systems would also bear investigation with "PEGylated" substrates as they contain one short PEG ligand on the dimer bridge; PEGylated surfaces were prepared to promote non-covalent interaction between functionalized substrates as the covalent interactions between fullerene dimer cages and amine-terminated substrates has the potential to be detrimental to the spin of endohedral systems. The procedure was generically the same for both substrates where PEG was melted and then spin coated at 3000 rpm for 1 minute on a given substrate. The samples were then annealed at 50°C for 4 hours and 100°C for 48 hours to allow sufficient mobility for the –OH terminal groups of the PEG chains to contact the substrate surfaces, and after annealing, films were rinsed with Nanopure water to remove any unreacted PEG and dried in a nitrogen stream. Because the grafting of polymer chains relies on the reaction between –OH end groups on the polymer and –OH terminal groups on the substrates, silicon was piranha cleaned using standard procedure (3:1 H_2SO_4:30% H_2O_2 for 1 hour followed by rinse with Nanopure water and stored in Nanopure water), and mica was hydrated by soaking for 4 hours in Nanopure water, following a similar procedure to that described previously. Substrates were then characterized using contact angle measurements to assess if functionalization was successful. This procedure was modified from that used by Alcantar et al where PEG chains were grafted to silica using plasma-enhanced chemical

vapor deposition (PECVD) at 100°C for 43 hours [262]. Contact angle measurements for silicon substrates treated in this manner were determined to be 24 ± 2°, consistent with literature reports and indicating successful functionalization of the substrate surface [262]. However, the mica contact angle was found to be <5° after treatment with PEG, indicating that the mica was not successfully PEGylated.

REFERENCES

1. Harneit, W., *Fullerene-based electron-spin quantum computer.* Physical Review A, 2002. **65**: p. 032322.

2. Morton, J.J.L., Tyryshkin, A. M., Ardavan, A., Porfyrakis, K., Lyon, S. A.; Briggs, G. A. D., *High Fidelity Single Qubit Operations Using Pulsed Electron Paramagnetic Resonance.* Physical Review Letters, 2005. **95**(20): p. 200501.

3. Knapp, C.W., N.; Kass, K.; Dinse, K. P.; Pietzak, B.; Waiblinger, M.; Weidinger, A., *Electron Paramagnetic Resonance Study of Atomic Phosphorus Encapsulated in [60]Fullerene.* Molecular Physics, 1998. **95**(5): p. 999-1004.

4. Seifert, G.B., A.; Dunsch, L.; Ayuela, A.; Rockenbauer, A., *Electron Spin Resonance Spectra: Geometrical and Electronic Structure of Endohedral Fullerenes.* Applied Physics a-Materials Science & Processing, 1998. **66**(3): p. 265-271.

5. Morton, J.J.L.T., A. M.; Ardavan, A.; Benjamin, S. C.; Porfyrakis, K.; Lyon, S. A.; Briggs, G. A. D., *Bang-Bang Control of Fullerene Qubits Using Ultrafast Phase Gates.* Nature Physics, 2006. **2**(1): p. 40-43.

6. Ardavan, A., Austwick, M., Benjamin, S.C., Briggs, G.A.D., Dennis, T.J.S., Ferguson, A., Hasko, D.G., Kanai, M., Khlobystov, A.N., Lovett, B.W., Morley, G.W., Oliver, R.A., Pettifor, D.G., Porfyrakis, K., Reina, J.H., Rice, J.H., Smith, J.D., Taylor, R.A., Williams, D.A., Adelmann, C., Mariette, H., Hamers, R.J., *Nanoscale solid-state quantum computing.* Phil. Trans. R. Soc. Lond. A, 2003. **361**: p. 1473-1485.

7. Benjamin, S.C., Ardavan, A., Briggs, G.A.D., Britz, D.A., Gunlycke, D., Jefferson, J., Jones, M.A.G., Leigh, D.F., Lovett, B.W., Khlobystov, A.N., Lyon, S.A., Morton, J.J.L., Porfyrakis, K., Sambrook, M.R., Tyryshkin, A.M., *Towards a fullerene-based quantum computer.* J. Phys.:Condensed Matter, 2006. **18**: p. S867-S883.

8. Dietel, E., Hirsch, A., Pietzak, B., Waiblinger, M., Lips, K., Weidinger, A., Gruss, A., Dinse, K-P. , *Atomic Nitrogen Encapsulated in Fullerenes: Effects of Cage Variations.* J. Am. Chem. Soc., 1999. **121**(2432-2437).

9. Harneit, W., Meyer, C., Weidinger, A, Suter, D., Twamley, J., *Architectures for a Spin Quantum Computer Based on Endohedral Fullerenes.* Phys. Stat. Sol. (b), 2002. **233**(3): p. 453-461.

10. Pietzak, B., Waiblinger, M., Murphy, T.A., Weidinger, A., Hohne, M., Dietel, E., Hirsch, A., *Buckminsterfullerene C60: a chemical Faraday cage for atomic nitrogen.* Chem. Phys. Lett., 1997. **279**: p. 259-263.

11. Lloyd, S., *A Potentially Realizable Quantum Computer*. Science, 1993. **261**(5128): p. 1569-1571.

12. Benjamin, S.C., *Quantum Computing Without Local Control of Qubit-Qubit Interactions.* Physical Review Letters, 2002. **88**(1): p. 017904.

13. Benjamin, S.C., *Schemes for Parallel Quantum Computation Without Local Control of Qubits.* Physical Review a, 2000. **6102**(2): p. 020301.

14. Benjamin, S.C.B., S., *Quantum Computing With an Always-on Heisenberg Interaction.* Physical Review Letters, 2003. **90**(24): p. 247901.

15. Raussendorf, R., *Quantum Computation Via Translation-Invariant Operations on a Chain of Qubits.* Physical Review a, 2005. **72**(5): p. 052301.

16. Fitzsimons, J.T., J., *Globally Controlled Quantum Wires for Perfect Qubit Transport, Mirroring, and Computing.* Physical Review Letters, 2006. **97**(9): p. 090502.

17. Fitzsimons, J.X., L.; Benjamin, S. C.; Jones, J. A., *Quantum Information Processing with Delocalized Qubits under Global Control.* Quantum Physics, 2006: p. 0606188.

18. Bates, F.S., Fredrickson, G.H., *Block Copolymers-Designer Soft Materials.* Physics Today, 1999. **52**(2): p. 32-38.

19. Roberts, G., ed. *Langmuir-Blodgett Films*. 1990, Plenum Press: New York.

20. Bonifazi, D., Enger, O., Diederich, F., *Supramolecular [60]fullerene chemistry on surfaces.* Chem. Soc. Rev. , 2007. **36**: p. 390-414.

21. Knill, E., *Quantum computing.* Nature, 2010. **463**: p. 441.

22. Meyer, C., Harnett, W., Weidinger, A., Lips, K., *Experimental Steps Towards the Realisation of a Fullerene Quantum Computer.* Phys. Stat. Sol (b), 2002. **233**: p. 462-466.

23. Moret, R., *Structures, phase transitions and orientational properties of the C60 monomer and polymers.* Acta Crystallographica A, 2005. **A61**: p. 62-76.

24. Harneit, W., Huebener, K., Naydenov, B., Schaefer, S., Scheloska, M., *$N@C_{60}$ quantum bit engineering.* Phys. Stat. Sol. (b), 2007. **244**(11): p. 3879-3884.

25. Kataura, H., Maniwa, Y., Kodama, T., Kikuchi, K., Hirahara, K., Suenaga, K., Iijima, S., Suzuki, S., Achiba, Y., Kratschmer, W., *High-yield fullerene*

encapsulation in single-wall carbon nanotubes. Synthetic Metals, 2001. **121**: p. 1195-1196.

26. Khlobystov, A.N., Britz, D.A., Ardavan, A., Briggs, G.A.D. , *Observation of Ordered Phases of Fullerenes in Carbon Nanotubes.* Phys. Rev. Lett., 2004. **92**(24): p. 245507.

27. Diaconescu, B., Yang, T., Berber, S., Jazdzyk, M., Miller, G.P., Tomanek, D., Pohl, K., *Molecular Self-Assembly of Functionalized Fullerenes on a Metal Surface.* Phys. Rev. Lett., 2009. **102**(5): p. 056102.

28. Bonifazi, D., Spillmann, H., Kiebele, A., de Wild, M., Seiler, P., Cheng, F., Guntherodt, J., Jung, T., Diederich, F., *Supramolecular Patterned Surfaces Driven by Cooperative Assembly of C_{60} and Porphyrins on Metal Substrates.* Angew. Chem. Int. Ed. , 2004. **43**: p. 4759-4763.

29. Nakanishi, T., Miyashita, N., Michinobu, T., Wakayama, Y., Tsuruoka, T., Ariga, K., Kurth, D.G. , *Perfectly Straight Nanowires of Fullerenes Bearing Long Alkyle Chains on Graphite.* J. Am. Chem. Soc., 2006. **128**: p. 6328-6329.

30. Pan, G.-B., Cheng, X-H., Heger, S., Freyland, W., *2D Supramolecular Structures of a Shape-Persistent Macrocycle and Co-deposition with Fullerene on HOPG.* J. Am. Chem. Soc., 2006. **128**(13): p. 4218-4219.

31. Laiho, A., Ras, R.H.A., Valkama, S., Ruokolainen, J., Sterbacka, R., Ikkala, O., *Control of Self-Assembly by Charge-Transfer Complexation between C_{60} Fullerene and Electron Donating Units of Block Copolymers.* Macromolecules, 2006. **39**(22): p. 7648-7653.

32. Schmaltz, B., Brinkmann, M., Mathis, C., *Nanoscale Organization of Fullerenes by Self-Assembly in a Diblock Copolymer Host Matrix.* Macromolecules, 2004. **37**: p. 9056-9063.

33. Yan, C., Dybek, A., Hanson, C., Schulte, K., Cafolloa, A.A., Dennis, J., Moriarty, P., *Langmuir-Blodgett films of C_{60} and $C_{60}O$ on Silicon: Islands, rings and grains.* Thin Solid Films, 2009. **517**(5): p. 1650.

34. Cardullo, F., Diederich, F., Echegoyen, L., Habicher, T., Jayaraman, N., Leblacnk, R.M., Stoddart, J.F., Wang, S., *Stable Langmuir and Langmuir-Blodgett Films of Fullerene-Glycodendron Conjugates.* Langmuir, 1998. **14**: p. 1955-1959.

35. Diederich, F., Effing, J., Jonas, U., Jullien, L., Plesnivy, T., Ringsdork, H., Thilgen, C., Weinstein, D. , *C_{60} and C_{70} in a Basket? Investigations of Mono- and Multilayers from Azacrown Compounds and Fullerenes.* Angew. Chem. Int. Ed Engl., 1992. **31**(12): p. 1599-1602.

36. Gao, Y., Tang, Z., Watkins, E., Majewski, J., Wang, H-L. , *Synthesis and Characterization of Amphiphilic Fullerenes and Their Langmuir-Blodgett Films.* Langmuir, 2005. **21**(1416-1423).

37. Maliszewskyj, N.C., Heiney, P.A., *Langmuir Films of C_{60}, $C_{60}O$, and $C_{61}H_2$.* Langmuir, 1993. **9**(6): p. 1439-1441.

38. Milliken, J., Dominguez, D.D., Nelson, H.H., Barger,W.R., *Incorporation of C_{60} in Langmuir-Blodgett Films.* Chem. Mater., 1992. **4**: p. 252-254.

39. Obeng, Y.S., Bard, A.J., *Langmuir Films of C_{60} at the Air-Water Interface.* J. Am. Chem. Soc., 1991. **113**: p. 6279-6280.

40. Tkachenko, N.V., Vehmanen, V., Nikkanen, J-P., Yamada, H., Imanori, H., Fukuzumi, S., Lemmetyinen, H., *Porphyrin-fullerene dyad with a long linker: formation of charge transfer conformer in Langmuir-Blodgett film.* Chem Phys Lett, 2002. **366**: p. 245-252.

41. Tomioka, Y., Ishibashi, M., Kajiyama, H., Taniguchi, Y., *Preparation and Structural Characterization of Fullerene C_{60} Langmuir Film.* Langmuir, 1993. **9**: p. 32-35.

42. Williams, G., Pearson, C., Bryce, M.R., Petty, M.C., *Langmuir-Blodgett films of C_{60}.* Thin Solid Films, 1992. **209**: p. 150-152.

43. Williams, G., Soi, A., Hirsch, A., Bryce, M.R., Petty, M.C. , *Langmuir-Blodgett films of 1-t-butyl-9-hydrofullerene-60.* Thin Solid Films, 1993. **230**: p. 73-77.

44. Felder, D., del Pilar Carreon, M., Gallani, J-L., Guillon, D., Nierengarten, J-F., Chuard, T., Descheraux, R., *Amphiphilic Fullerene-Cholesterol Derivatives: Synthesis and Preparation of Langmuir and Langmuir-Blodgett Films.* Helvetica Chimica Acta, 2001. **84**: p. 1119-1132.

45. Fendler, J.H., ed. *Nanoparticles and nanostructured films: preparation, characterization, and applications*. 1998, Wiley-VCH Weinheim.

46. Gallani, J.-L., Felder, D., Guillon, D. Heinrich, B., Nierengarten, J-F. , *Micelle Formation in Langmuir Films of C_{60} Derivatives.* Langmuir, 2002. **18**: p. 2908-2913.

47. Guldi, D.M., Zerbetto, F., Georgakilas, V., Prato, M., *Ordering Fullerene Materials at Nanoscale Dimensions.* Acc. Chem . Res., 2005. **38**: p. 38-43.

48. Hawker, C.J., Saville, P.M., White, J.W. , *The Synthesis and Characterization of a Self-Assembling Amphiphilic Fullerene.* J. Org. Chem. , 1994. **59**: p. 3503-3505.

49. Kawai, T., Scheib, S., Cava, M.P., Metzger, R.M., *Langmuir-Blodgett Films of a Thermally Labile 1:1 Adduct of C_{60} Fullerene and 8-(9-Anthryl)-7-oxaoctanoic Acid* Langmuir, 1997. **13**: p. 5627-5633.

50. Maggini, M., Karlsson, A., Pasimeni, L., Scorrano, G., Prato, M., Valli, L., *Synthesis of N-acylated Fulleropyrrolidines: New Materials for the Preparation of Langmuir-Blodgett Films Containining Fullerenes.* Tetrahedron Letters, 1994. **35**(18): p. 2985-2988.

51. Maggini, M., Pasimeni, L., Prato, M., Scorrano, G., Valli, L., *Incorporation of an Acyl Group in Fulleropyrrolidines: Effects on Langmuir Monolayers.* Langmuir, 1994. **10**: p. 4164-4166.

52. Nakamura, E., Isobe, H., *Functionalized Fullerenes in Water. The First 10 Years of Their Chemistry, Biology, and Nanoscience.* Accounts of Chemical Research, 2003. **36**(11): p. 807-815.

53. Nierengarten, J.-F., *Fullerodendrimers: A New Class of Compounds for Supramolecular Chemistry and Materials Science Applications.* Chemistry: A European Journal, 2000. **6**(20): p. 3667-3670.

54. Oh-ishi, K., Okamura, J., Ishi-i, T., Sano, M., Shinkai, S., *Large Monolayer Domain Formed by C_{60}-Azobenzene Derivative.* Langmuir, 1999. **15**: p. 2224-2226.

55. Backer, S.A., Suez, I., Fresco, Z.M., Rolandi, M., Frechet, J.M.J., *Covalent Formation of Nanoscle Fullerene and Dendrimer Patterns.* Langmuir, 2007. **23**: p. 2297-2299.

56. Aldersey-Williams, H., *The Most Beautiful Molecule; The Discovery of the Buckyball*. 1995, New York: John Wiley & Sons, Inc.

57. Baggott, J., *Perfect Symmetry; The Accidental Discover of Buckminsterfullerene*. 1994, New York: Oxford University Press Inc.

58. Kadish, K.M., Ruoff, R.S., *Fullerenes: chemistry, physics, and technology*. 2000: Wiley-IEEE.

59. Hansen, C.M., Smith, A.L., *Using Hansen solubility parameters to correlate solubility of C60 fullerenes in organic solvents and in polymers.* Carbon, 2004. **42**: p. 1591-1597.

60. Huang, J.-C., *Multiparameter solubility model of fullerene C_{60}.* Fluid Phase Equilibria, 2005. **237**: p. 186-192.

61. Ruoff, R.S., Tse, D.S., Malhotra, R., Lorents, D.C., *Solubility of C_{60} in a Variety of Solvents.* J. Phys. Chem., 1993. **97**: p. 3379-3383.

62. Ruoff, R.S., Malhotra, R., Huestis, D.L., Tse, D.S., Lorents, D.C., *Anomalous solubility behaviour of C_{60}.* Nature, 1993. **362**: p. 140-141.

63. Sivaraman, N., Dhamodaran, R., Kaliappan, I., Srinivasan, T.G., Rao, P.R.V., Mathews, C.K., *Solubility of C_{60} in Organic Solvents.* J. Org. Chem. , 1992. **57**: p. 6077-6079.

64. Sivaraman, N., Srinivasan, T.G., Rao, P.R.V. , *QSPR Modeling for Solubility of Fullerene (C_{60}) in Organic Solvents.* J. Chem. Inf. Comput. Sci. , 2001. **41**: p. 1067-1074.

65. Smith, A.L., Walter, E., Korobov, M.V., Gurvich, O.L., *Some Enthalpies of Solution of C_{60} and C_{70}. Thermodynamics of the Temperature Dependence of Fullerene Solubility.* J. Phys. Chem., 1996. **100**(16): p. 6775-6780.

66. Toropov, A.A., Bakhtiyor, F.R., Leszczynska, D., Leszczynski, J. , *Additive SMILES based optimal descriptors: QSPR modeling of fullerene C_{60} solubility in organic solvents.* Chem. Phys. Lett., 2007. **444**: p. 209-214.

67. Toropov, A.A., Leszczynska, D., Leszczynski, J., *QSPR study on solubility of fullerene C_{60} in organic solvents using optimal descriptors calculated with SMILES.* Chem. Phys. Lett., 2007. **441**: p. 119-122.

68. Heymann, D., *Solubility of C_{60} in alcohols and alkanes.* Carbon, 1996. **34**(5): p. 627-631.

69. Tomiyama, T., Uchiyama, S., Shinohara, H. , *Solubility and partial specific volumes of C_{60} and C_{70}.* Chem. Phys. Lett., 1997. **264**: p. 143-148.

70. Ahn, J.S., Suzuki, K., Iwasa, Y., Mitani, T. , *Photoluminescence of C_{60} aggregates in solution.* Journal of Luminescence, 1997. **72-74**: p. 464-466.

71. Alfe, M., Apicella, B., Barbella, R., Bruno, A., Ciajolo, A., *Aggregation and interactions of C_{60} and C_{70} fullerenes in neat N-methylpyrrolidinone and in N-methylpyrrolidinone/toluene mixtures.* Chem. Phys. Lett., 2005. **405**: p. 193-197.

72. Baltog, I., Baibarac, M., Mihut, L., Preda, N., Velula, T., Lefrant, S., *Spectroscopic studies on C_{60} fullerene solutions in binary solvent mixtures.* Romanian Reports in Physics, 2005. **57**(4): p. 837-844.

73. Bensasson, R.V., Bienvenue, E., Dellinger, M., Leach, S., Seta, P., *C_{60} in Model Biological Systems. A Visible-UV Absorption Study of Solvent-Dependent Parameters and Solute Aggregation.* J. Phys. Chem., 1994. **98**: p. 3492-3500.

74. Bezmelnitsin, V.N., Eletskii, A.V., Stepanov, E.V., *Cluster Origin of Fullerene Solubility.* J. Phys. Chem., 1994. **98**(27): p. 6665-6667.

75. Nath, S., Pal, H. Sapre, A.V., *Effect of solvent polarity on the aggregation of fullerenes: a comparison between C_{60} and C_{70}.* Chem. Phys. Lett., 2002. **360**: p. 422-428.

76. Ying, Q., Marecek, J., Chu, B., *Solution behavior of buckminsterfullerene (C_{60}) in benzene.* J. Chem. Phys. , 1994. **101**(4): p. 2665-2672.

77. Bulavin, L.A., Adamenko, I.I., Yashchuk, V.M., Ogul'chansky, T.Y., Prylutskyy, Y.I., Durov, S.S., Scharff, P., *Self-organization C_{60} nanoparticles in toluene solution.* Journal of Molecular Liquids, 2001. **93**: p. 187-191.

78. Torok, G., Lebedev, V.T., Cser, L., *Small-Angle Neutron-Scattering Study of Anomalous C_{60} Clusterization in Toluene.* Physics of the Solid State, 2002. **44**(3): p. 572-573.

79. Nath, S., Pal, H., Palit, D.K., Sapre, A.V., Mittal, J.P., *Aggregation of Fullerene C_{60} in Benzonitrile.* J. Phys. Chem. B, 1998. **102**: p. 10158-10164.

80. Alfe, M., Barbella, R., Bruno, A., Minutolo, P., Ciajolo, A., *Solution behaviour of C_{60} fullerene in N-Methylpyrrolidone/toluene mixtures.* Carbon, 2005. **43**: p. 651-673.

81. Yevlampieva, N.P., Biryulin, Y.F., Melenevskaja, E.Y., Zgonnik, V.N., Rjumtsev, E.I. , *Aggregation of fullerene C_{60} in N-methylpyrrolidone.* Colloids and Surfaces A: Physicochemical and Engineering Aspects, 2002. **209**: p. 167-171.

82. Rudalevige, T., Francis, A.H., Zand, R., *Spectroscopic Studies of Fullerene Aggregates.* J. Phys. Chem. A, 1998. **102**: p. 9797-9802.

83. Nath, S., Pal, H., Sapre, A.V., *Effect of solvent polarity on the aggregation of C_{60}.* Chem. Phys. Lett., 2000. **327**: p. 143-148.

84. Seshadri, R., D'Souza, F., Krishnan, V., Rao, C.N.R., *Electron Donor-Acceptor Complexes of the Fullerenes C_{60} and C_{70} with Amines.* Chemistry Letters, 1993: p. 217-220.

85. Wang, Y., *Photophysical Properties fo Fullerenes and Fullerene/N,N-Diethylaniline Charge-Transfer Complexes.* J. Phys. Chem., 1992. **96**: p. 764-767.

86. Qiao, J.L., Gong, Q.J., Du, L.M., Jin, W.J., *Spectroscopic study on the photoinduced reaction of fullerene C_{60} with aliphatic amines and its dynamics-*

strong short wavelength fluorescence from the adducts. Spectrochimica Acta Part A, 2001. **57**: p. 17-25.

87. Sibley, S.P., Campbell, R.L., Silber, H.B. , *Solution and Solid State Interactions of C_{60} with Substituted Anilines.* J. Phys. Chem., 1995. **99**: p. 5274-5276.

88. Scurlock, R.D., Ogilby, P.R., *Excited-state charge-transfer complexes formed between C_{60} and substitute naphthalenes.* Journal of Photochemistry and Photobiology A: Chemistry, 1995. **91**: p. 21-25.

89. Sibley, S.P., Nguyen, Y.T., Campbell, R.L., Silber. H.B., *Spectrophotometric studies of complexation of C_{60} with aromatic hydrocarbons.* Spectrochimica Acta Part A, 1997. **53**: p. 679-684.

90. Gutierrez-Nava, M., Nierengarten, H., Masson, P., Van Dorsselaer, A., Nierengarten, J.-F., *A supramolecular oligophenylenevinylene-C_{60} conjugate.* Tetrahedron Letters, 2003. **44**: p. 3043-3046.

91. Sapurina, I., Mokeev, M., Lavrentev, V., Zgonnik, V., Trchova, M., Hlavata, D., Stejskail, J., *Polyaniline complex with fullerene C_{60}.* European Polymer Journal, 2000. **36**: p. 2321-2326.

92. Yamaguchi, Y., Kobayashi, S., Amita, N., Wakamiya, T., Matsubara, Y., Sugimoto, K., Yoshida, Z., *Creation of nanoscale oxaarenecyclynes and their C_{60} complexes.* Tetrahedron Letters, 2002. **43**: p. 3277-3280.

93. Mathis, C.S., B., Brinkmann, M. , *Controlled grafting of polymer chains onto C_{60} and thermal stability of the obtained materials.* Comptes Rendus Chimie. **2006**(9): p. 1075-1084.

94. Ederle, Y., Mathis, C., *Palm Tree- and Dumbbell-like Polymer Architectures based on C_{60}.* Macromolecules, 1999. **32**: p. 554-558.

95. Okamura, H., Minoda, M., Fukuda, T., Miyamoto, T., Komatsu, K., *Solubility characteristics of C_{60} fullerenes with two well-defined polystyrene arms in a polystyrene matrix.* Macromolecular Rapid Communications, 1999. **20**: p. 37-40.

96. Benesi, H.A., Hildebrand, J.H., *A Spectrophotometric Investigation of the Interaction of Iodine with Aromatic Hydrocarbons.* J. Am. Chem. Soc., 1949. **71**: p. 2703-2707.

97. Segalman, R.A., *Patterning with block copolymer thin films.* Materials Science and Engineering, 2005. **48**: p. 191-226.

98. Bucknall, D.G., Anderson, H.L., *Polymers Get Organized.* Science, 2003. **302**: p. 1904-1905.

99. Khanna, V., Cochran, E.W., Hexemer, A., Stein, G.E., Fredrickson, G.H., Kramer, E.J., Li, X., Wang, J., Hahn, S.F., *Effect of Chain Architecture and Surface Energies on the Ordering Behavior of Lamellar and Cylinder Forming Block Copolymers.* Macromolecules, 2006. **39**: p. 9346-9356.

100. Knoll, A., Horvat, A., Lyakhova, K.S., Krausch, G., Sevink, G.J.A., Zvelindovsky, A.V., Magerle, R., *Phase Behavior in Thin Films of Cylinder-Forming Block Copolymers.* Physical Review Letters, 2002. **89**(3): p. 035501.

101. Mansky, P., DeRouchey, J., Russell, T., Mays, J., Pitsikalis, M., Morkved, T., Jaeger, H., *Large-Area Domain Alignment in Block Copolymer Thin Films Using Electric Fields.* Macromolecules, 1998. **31**: p. 4399-4401.

102. Morkved, T.L., Lu, M., Urbas, A.M., Ehrichs, E.E., Jaeger, H.M., Mansky, P., Russell, T.P., *Local Control of Microdomain Orientation in Diblock Copolymer Thin Films with Electric Fields.* Science, 1996. **273**: p. 931-933.

103. Angelescu, D., Waller, J., Adamson, D., Deshpande, P., Chou, S., Register, R., Chaikin, P., *Macroscopic Orientation of Block Copolymer Cylinders in Single-Layer Films by Shearing.* Advanced Materials, 2004. **16**(19): p. 1736-1740.

104. Pelletier, V., Adamson, D., Register, R., Chaikin, P., *Writing mesoscale patterns in block copolymer thin films through channel flow of a nonsolvent fluid.* Applied Physics Letters, 2007. **90**: p. 163105.

105. Wu, M.W., Register, R.A., Chaikin, P.M., *Shear alignment of sphere-morphology block copolymer thin films with viscous fluid flow.* Physical Review E, 2006. **74**: p. 040801 (R).

106. Angelescu, D.E., Waller, J.H., Adamson, D.H., Register, R.A., Chaikin, P.M., *Enhanced Order of Block Copolymer Cylinders in Single-Layer Films Using a Sweeping Solidification Front.* Advanced Materials, 2007. **19**(2687-2690).

107. Fukunaga, K., Elbs, H., Magerle, R., Krausch, G., *Large-scale Alignment of ABC Block Copolymer Microdomains via Solvent Vapor Treatment.* Macromolecules, 2000. **33**: p. 947-953.

108. Bang, J., Kim, B.J., Stein, G.E., Russell, T.P., Li, X., Wang, J., Kramer, E.J., Hawker, C.J., *Effect of Humidity on the Ordering of PEO-Based Copolymer Thin Films.* Macromolecules, 2007. **40**: p. 7019-7025.

109. Kim, S.H., Misner, M.J., Xu, T., Kimura, M., Russell, T.P., *Highly Oriented and Ordered Arrays from Block Copolymers via Solvent Evaporation.* Advanced Materials, 2004. **16**(3): p. 226-231.

110. Kim, G.a.L., M., *Morphological Development in Solvent-Cast Polystyrene-Polybutadiene-Polystyrene (SBS) Triblock Copolymer Thin Films.* Macromolecules, 1998. **31**: p. 2569-2577.

111. Cavicchi, K.A.a.R., T.P., *Solvent Annealed Thin Films of Asymmetric Polyisoprene-Polylactide Diblock Copolymers.* Macromolecules, 2007. **40**: p. 1181-1186.

112. Bang, J., Kim, S.H., Drockenmuller, E., Misner, M.J., Russell, T.P., Hawker, C.J., *Defect-Free Nanoporous Thin Films from ABC Triblock Copolymers.* J. Am. Chem. Soc., 2006. **128**: p. 7622-7629.

113. Zhang, M., Yang, L., Yurt, S. Misner, M.J., Chen, J., Coughlin, E.B., Venkataraman, D., Russell, T.P., *Highly Ordered Nanoporous Thin Films from Cleavable Polystyrene-block-poly(ethylene oxide).* Advanced Materials, 2007. **19**: p. 1571-1576.

114. Kim, S.H., Misner, M.J., and Russell, T.P., *Solvent-Induced Ordering in Thin Film Diblock Copolymer/Homopolymer Mixtures.* Advanced Materials, 2004. **16**(23-24): p. 2119-2123.

115. Kimura, M., Misner, M.J., Xu, T., Kim, S.H., Russell, T.P., *Long-Range Ordering of Diblock Copolymers Induced by Droplet Pinning.* Langmuir, 2003. **19**: p. 9910-9913.

116. Park, C., De Rosa, C., Thomas, E.L., *Large Area Orientation of Block Copolymer Microdomains in Thin Films via Directional Crystallization of a Solvent.* Macromolecules, 2001. **34**: p. 2602-2606.

117. Cheng, J.Y., Ross, C.A., Thomas, E.L., Smith, H.I., Vancso, G.J., *Fabrication of nanostructures with long-range order using block copolymer lithography.* Applied Physics Letters, 2002. **81**(19): p. 3657-3659.

118. Cheng, J.Y., Ross, C.A., Thomas, E.L., Smith, H.I., Vancso, G.J., *Templated Self-Assembly of Block Copolymers: Effect of Substrate Topography.* Advanced Materials, 2003. **15**(19): p. 1599-1602.

119. Kim, S.O., Solak, H.H., Stoykovich, M.P., Ferrier, N.J., de Pablo, J.J., Nealey, P.F., *Epitaxial self-assembly of block copolymers on lithographically defined nanopatterned substrates.* Nature, 2003. **424**: p. 411-414.

120. Li, L., Yokoyama, H., *Aligning Single-Layer Cylinders of Block Copolymer Nanodomains using Soft Molding.* Advanced Materials, 2005. **17**: p. 1432-1436.

121. Peng, J., Wei, Y., Wang, H., Li, B., Han, Y. , *Solvent Induced Sphere Development in Symmetric Diblock Copolymer Thin Films.* Macromolecular Rapid Communications, 2005. **26**: p. 738-743.

122. Xuan, Y., Peng, J., Cui, L., Wang, H., Li, B., Han, Y., *Morphology Development of Ultrathin Symmetric Diblock Copolymer Film via Solvent Vapor Treatment.* Macromolecules, 2004. **37**: p. 7301-7307.

123. Peng, J., Xuan, Y., Wang, H., Yang, Y., Li, B., Han, Y., *Solvent-induced microphase separation in diblock copolymer thin films with reversibly switchable morphology.* J. Chem. Phys., 2004. **120**(23): p. 11163-11170.

124. Peng, J., Gao, X., Wei, Y., Wang, H., Li, B., Han, Y., *Controlling the size of nanostructures in thin films via blending of block copolymers and homopolymers.* J. Chem. Phys., 2005. **122**: p. 114706.

125. Peng, J., Kim, D.H., Knoll, W., Xuan, Y., Li, B., Han, Y., *Morphologies in solvent-annealed thin films of symmetric diblock copolymer.* J. Chem. Phys., 2006. **125**: p. 064702.

126. Holoubek, J., Baldrian, J., Lednicky, F., Malkova, S., Lal, J., *Self-assembled Structures in Blends of Block Copolymer A-block-B with Homopolymer A: SAXS and SANS Study.* Macromol. Chem. Phys., 2006. **207**: p. 1834-1841.

127. Matsen, M.W., *Phase Behavior of Block Copolymer/Homopolymer Blends.* Macromolecules, 1995. **28**: p. 5765-5773.

128. Orso, K.A., Green, P.F., *Phase Behavior of Thin Film Blends of Block Copolymers and Homopolymers: Changes in Domain Dimensions.* Macromolecules, 1999. **32**: p. 1087-1092.

129. Stoykovich, M.P., Muller, M., Kim, S.O., Solak, H.H., Edwards, E.W., de Pablo, J.J., Nealey, P.F., *Directed Assembly of Block Copolymer Blends into Nonregular Device-Oriented Structures.* Science, 2005. **308**: p. 1442-1446.

130. de Gennes, P.G., *Conformations of Polymers Attached in an Interface.* Macromolecules, 1980. **13**: p. 1069-1075.

131. Mathis, C., Schmaltz, B., Brinkmann, M. , *Controlled grafting of polymer chains onto C_{60} and thermal stability of the obtained materials.* Comptes Rendus Chimie, 2006(9): p. 1075-1084.

132. Laiho, A., Ras, RHA, Valkama, S., Ruokolainen, J., Osterbacka, R., Ikkala, O., Macromolecules, 2006. **39**(22): p. 7648-7653.

133. Waller, J.H., Bucknall, D.G., Register, R.A., Beckham, H.W., Leisen, J., Campbell, K., Polymer, 2009. **50**: p. 4199-4204.

134. Lin, Y., Boker, A., He, J., Sill, K., Xiang, H., Abetz, C., Li, X., Wang, J., Emrick, T., Long, S., Wang, Q., Balazs, A., Russell, T.P., *Self-directed self-assembly of nanoparticle/copolymer mixtures.* Nature, 2005. **434**: p. 55.

135. Tsutsumi, K., Funaki, Y., Hirokawa, Y., Hashimoto, T., Langmuir, 1999. **15**: p. 5200-5203.

136. Weng, C.-C., Wei, K-H., Chem. Mater. , 2003. **15**: p. 2936-2941.

137. Spatz, J.P., Roescher A., Moller, M., Advanced Materials, 1996. **8**(4): p. 337-340.

138. Lopes, W.A., Jaeger, H.M., Nature, 2001. **414**: p. 735-738.

139. Kim, B.J., Bang, J., Hawker, C.J., Kramer, E.J., *Effect of Areal Chain Density on the Location of Polymer-Modified Gold Nanoparticles in a Block Copolymer Template.* Macromolecules, 2006. **39**: p. 4108-4114

140. Lazzari, M., Lopez-Quintela, M.A., *Block Copolymers as a Tool for Nanomaterial Fabrication.* Advanced Materials, 2003. **15**(19): p. 1583-1594.

141. Mackay, M.E., Tuteja, A., Duxbury, P.M., Hawker, C.J., Van Horn, B., Guan, Z., Chen, G., Krishnan, R.S., *General Strategies for Nanoparticle Dispersion.* Science, 2006. **311**: p. 1740-1743.

142. Tamai, H., Sakurai, H., Hirota, Y., Nishiyama, F., Yasuda, H. J., Appl. Polym. Sci., 1996. **56**: p. 441.

143. Nakao, Y.J., Colloid Interface Sci., 1995. **171**: p. 386.

144. Saito, R.O., S.; Ishizu, K. , Polymer, 1993. **34**: p. 1183-1189.

145. Chan, Y.N.C.C., G. S. W.; Schrock, R. R.; Cohen, R. E., Chem. Mater., 1992. **4**: p. 885.

146. Zehner, R.W.L., W. A.; Morkved, T. L.; Jaeger, H.; Sita,L. R. , Langmuir, 1998. **14**: p. 241.

147. Waller, J.H., Bucknall, D.G. Register, R.A., Beckham, H.W., Leisen, J., Campbell, K., *C_{60} fullerene inclusions in low-molecular-weight polystrene-poly(dimethylsiloxane) diblock copolymers.* Polymer, 2009. **50**: p. 4199-4204.

148. Le, J.Y., Shou, Z., Balazs, A.C., *Modeling the Self-Assembly of Copolymer-Nanoparticle Mixtures Confined between Solid Surfaces.* Phys. Rev. Lett. , 2003. **91**: p. 136103.

149. Kim, B.J., Chiu, J.J., Yi, G., Pine, D.J., Kramer, E.J., *Nanoparticle-Induced Phase Transitions in Diblock-Copolymer Films.* Advanced Materials, 2005. **17**: p. 2618-2622.

150. Lee, J.Y., Thompson, R.B., Jasnow, D., Balazs, A.C., *Effect of Nanoscopic Particles on the Mesophase Structure of Diblock Copolymers.* Macromolecules, 2002. **35**: p. 4855.

151. Yeh, S.-W., Wei, K-H., Sun, Y-S., Jeng, U-S., Liang, K.S., *CdS Nanoparticles Induce a Morphological Transformation of Poly(styrene-b-4-vinylpyrridine) from Hexagonally Packed Cylinders to a Lamellar Structure.* Macromolecules, 2005. **38**: p. 6559.

152. Sun, Y.-S., Jeng, U-S., Liang, K.S., Yeh, S-W., Wei, K-H., *Transitions of domain ordering and domain size in spherical forming polystyrene-block-poly(ethylene oxide) copolymer and its composites with colloidal cadmium sulfate quantum dots.* Polymer, 2006. **47**: p. 1101.

153. Balazs, A.C., Emrick, T., Russell, T.P., *Nanoparticle Polymer Composites: Where Two Small Worlds Meet.* Science, 2006. **314**: p. 1107-1110.

154. Russell, T.P., *X-ray and neutron reflectivity for the investigation of polymers.* Materials Science Reports, 1990. **5**(4): p. 171-271.

155. Pethrick, R.A., Dawkins, J.V., ed. *Modern Techniques for Polymer Characterisation*. 1999, John Wiley & Sons Ltd.: Chichester.

156. Roe, R.-J., *Methods of X-ray and Neutron Scattering in Polymer Science*. Topics in Polymer Science. ed. J.E. Mark. 2000, New York: Oxford University Press, Inc.

157. Schwartz, D.K., *Langmuir-Blodgett film structure.* Surface Science Reports, 1997. **27**: p. 241-334.

158. Petty, M.C., *Langmuir-Blodgett Films: An Introduction*. 1996, Cambridge: Cambridge University Press.

159. Betts, J.J., Pethica, B.A., *The ionization characteristics of monolayers of weak acids and bases.* Trans. Faraday Soc. , 1956. **52**: p. 1581-1589.

160. Gaines Jr., G.L., *Insoluble Monolayers at Liquid-Gas Interaces*. 1966, New York, London, Sydney: Wiley-Interscience.

161. Ries Jr., H.E., Kimball, W.A., *Monolayer structure as revealed by electron microscopy.* J. Phys. Chem. , 1955. **75**: p. 3137-3141.

162. Adam, N.K., *The structure of thin films. Part X1-oxygenated derivatives of benzene.* Proc. R. Soc. London, Ser. A, 1928. **119**: p. 628-644.

163. Kinnunen, P.K.J., Virtanen, J.A., Tulkki, A.P., Ahuja, R.C., Mobius, D., *Pyrene-fatty acid containing phospholipid analogs: Characterization of monolayers and Langmuir-Blodgett assemblies.* Thin Solid Films, 1985. **132**: p. 193-203.

164. Naselli, C., Rabe, J.P., Rabolt, J.F., Swalen, J.D., *Thermally induced order-disorder transitions in Langmuir-Blodgett films.* Thin Solid Films, 1985. **134**: p. 173-178.

165. Steven, J.H., Hann, R.A., Barlow, W.A., Laird, T. , *Influence of chemical structure on the monolayer properties of polycyclic aromatic molecules.* Thin Solid Films, 1983. **99**: p. 71-79.

166. Stewart, F.H.C., *Unimolecular films from certain anthracene derivatives.* Aust. J. Chem. , 1961. **14**: p. 57-63

167. Vincett, P.S., Barlow, W.A., Boyle, F.T., Finney, J.A., Roberts, G.G., *Preparation of Langmuir-Blodgett built-up multilayer films of a lightly substituted model aromatic anthracene.* Thin Solid Films, 1979. **60**: p. 265-277.

168. Vincett, P.S., Barlow, W.A., *Highly organized aromactic molecular systems using Langmuir-Blodgett films; Structure, optical properties and probably epitaxy of anthracene-derivative multilayers.* Thin Solid Films, 1980. **11**: p. 305-326.

169. Ruaudel-Teixier, A., Vandevyver, M., Barraud, A., *Novel conducting Langmuir-Blodgett films.* Mol. Cryst. Liq. Cryst. , 1985. **120**: p. 319-322.

170. Kuhn, H., Mobius, D., *Systems of monomolecular layers-Assembling and physico-chemical behaviour.* Angew. Chem., Int. Ed. Engl., 1971. **10**: p. 620.

171. Kuhn, H., *Electron transfer in monolayer assemblies.* Pure Appl. Chem., 1979. **51**: p. 341-352.

172. Kuhn, H., *Information, electron and energy transfer in surface layers.* Pure Appl. Chem., 1981. **53**: p. 2105-2122.

173. Mobius, D., *Molecular cooperation in monolayer organizates.* Acc. Chem . Res., 1981. **14**: p. 63-68.

174. Bull, R.A., Bulkowski, J.E., *Tetraphenyl porphyrin monolayers: formation at the air water interface and characterization on glass supports by absorption and fluorescence spectroscopy.* J. Colloid Interface Sci., 1983. **92**: p. 1-12.

175. de B. Costa, S.M., Porter, G. , *Model systems for photosynthesis. IV. Photosensitization by chlorophyll a monolayer at a lipid-water interface.* Proc. R. Soc. London, 1974. **341**: p. 167-176.

176. Hopf, F.R., Mobius, D., Whitten, D.G., *Environmental control of reactions; enhancement of μ-oxo dimer formation from iron (III) porphyrins in organised monolayer assemblies as a model for membrane catalysis.* J. Am. Chem. Soc., 1976(98): p. 1584-1586.

177. Jones, R., Tredgold, R.H., O'Mullane, J.E., *Photoconductivity and photovoltaic effects in Langmuir-Blodgett films of chlorophyll-a.* Photochem. Photobiol., 1980. **32**: p. 223-232.

178. Kazantseva, Z.I., Lavrik, N.V, Nabok, A.V., Dimitriev, O.P., Nesterenko, B.A., Kalchenko, V.I., Vysotsky, S.V., Markovskiy, L.N., Marchenko, A.A., *Structure and electronic properties of Langmuir-Blodgett films of calixarene/fullerene composites.* Supramolecular Science, 1997. **4**: p. 341-347.

179. Cadenhead, D.A., Demchak, R.J., *Monolayers of elaidic acid on aqueous glycerol solutions* J. Colloid Interface Sci., 1967. **24**: p. 484-490.

180. Nakagaki, M., Ichihashi, H., *Intermolecular interaction in egg lecithin monolayers spread on aqueous alcohol.* Fac. Pharm. Sci. , 1978. **98**: p. 577-584.

181. Pincus, M., Windreich, S., Miller, I.R., *Preparation of stable mixed monolayers of betacarotene and their transfer to glass slides.* Biochem. Biophys. Acta, 1973. **311**: p. 317-319.

182. Roberts, G.G., Petty, M.C., Baker, S., Fowler, M.T., Thomas, N.J., *Electron devices incorporating stable phthalocyanine Langmuir-Blodgett films.* Thin Solid Films, 1985. **132**: p. 113-123.

183. Bernstein, S., *Comparison of X-ray photographs taken with X and Y built-up films.* J. Am. Chem. Soc., 1938. **60**: p. 1511.

184. Fankuchen, I., *The structure of built up films on metals.* Phys. Rev. , 1938. **53**: p. 909.

185. Peng, J.B., Abraham, B.M., Dutta, P., Ketterson, J.B., Gibbard, H.F., *Langmuir-Blodgett deposition of a ring-shaped molecule (valinomycin).* Langmuir, 1987. **3**(1): p. 104-106.

186. Heiney, P.A., Fischer, J. E., Mcghie, A. R., Romanow, W. J., Denenstein, A. M., McCauley, J. P., Smith, A. B., Cox, D. E., Phys. Rev. Lett., 1991. **66**: p. 2911-2914.

187. Ulman, A., *Formation and Structure of Self-Assembled Monolayers.* Chem. Rev. , 1996. **96**: p. 1533-1554.

188. Love, J.C., Estroff, L.A., Kriebel, J.K., Nuzzo, R.G., Whitesides, G.M., *Self-Assembled Monolayers of Thiolates on Metals as a Form of Nanotechnology.* Chem. Rev., 2005. **105**: p. 1103-1169.

189. Delamarche, E., Michel, B., Biebuyck, H.A., Gerber, C., *Golden Interfaces: The Surface of Self- Assembled Monolayers.* Adv. Mater., 1996. **8**: p. 719-729.

190. Tsukruk, V.V., Lander, L.M., Brittain, W.J., *Atomic Force Microscopy of C_{60} Tethered to a Self-Assembled Monolayer.* Langmuir, 1994. **10**: p. 996-999.

191. Tsukruk, V.V., Everson, M.P., Lander, L.M., Brittain, W.J., *Nanotribological Properties of Composite Molecular Films: C_{60} anchored to a Self-Assembled Monolayer.* Langmuir, 1996. **12**: p. 3905-3911.

192. Zhang, F., Srinivasan, M.P., *Self-Assembled Molecular Films of Aminosilanes and Their Immobilization Capacities.* Langmuir, 2004. **20**: p. 2309-2314.

193. Crampton, N., Bonass, W.A., Kirkham, J., Thomson, N.H., *Formation of Aminosilane-Functionalized Mica for Atomic Force Microscopy Imaging of DNA.* Langmuir, 2005. **21**: p. 7884-7891.

194. Park, B., Paoprasert, P., In, I., Zwickey, J., Colavita, P.E., Hamers, R.J., Gopalan, P., Evans, P.G., *Functional Self-Assembled Monolayers for Optimized Photoinduced Charge Transfer in Organic Field Effect Transistors.* Adv. Mater., 2007. **19**: p. 4353-4357.

195. Chupa, J.A., Xu, S., Fischetti, R.F., Strongin, R.M., McCauley Jr., J.P., Smith III, A.B., Blasie, J.K. , *A Monolayer of C_{60} Tethered to the Surface of an Inorganic Substrate: Assembly and Structure.* J. Am. Chem. Soc., 1993. **115**: p. 4383-4384.

196. Chen, K., Caldwell, W.B., Mirkin, C.A., *Fullerene Self-Assembly onto $(MeO)_3Si(CH_2)_3NH_2$-modified Oxide Surfaces.* J. Am. Chem. Soc., 1993. **115**: p. 1193-1194.

197. Cecchet, F., Rapino, S., Margotti, M., Da Ros, T., Prato, M., Paulucci, F., Rudolf, P., *Structural and electrochemical characterization of fullerene-based surfaces of C_{60} mono- or bis-adducts grafted onto self-assembled monolayers.* Carbon, 2006. **44**: p. 3014-3021.

198. Kadish, K.M., Ruoff, R.S., ed. *Fullerene-Surface interactions*. 2000, Wiley Interscience: New York.

199. Altman, E.I., Colton, R.J., Surf. Sci. , 1993. **295**: p. 13.

200. Tanigaki, K., Kuroshima, S., Ebbesen, T.W., Thin Solid Films, 1995. **257**: p. 154.

201. Shi, X., Caldwell, W.B., Chen, K., Mirkin, C.A., J. Am. Chem. Soc., 1994. **116**: p. 11598.

202. Fibbioli, M., Bandyopadhyay, K., Liu, S-G., Echegoyen, L., Enger, O., Diederich, F., Gingery, D., Buhlmann, P., Persson, H., Suter, U.W., Pretsch, E., Chem. Mater., 2002. **14**: p. 1721.

203. Gu, T., Whitesell, J. K., Fox, M.A., J. Org. Chem., 2004. **69**: p. 4075.

204. Arias, F., Godinez, L.A., Wilson, S.R., Kaifer, A.E., Echegoyen, L., J. Am. Chem. Soc., 1996. **118**: p. 6086.

205. Gulino, A., Bazzano, S., Condorelli, G.G., Giuffrida, S., Minco, P., Satriano, C., Scamporrino, E., Ventimiglia, G., Vitalini, D., Fragala, I., Chem. Mater., 2005. **17**: p. 1079.

206. Hatano, T., Ikeda, A., Akiyama, T., Yamada, S., Sano, M., Kanekiyo, Y., Shinkai, S., J. Am. Chem. Soc., Perkin Trans. 2, 2000. **5**: p. 909.

207. Ikeda, A., Hatano, T., Shinkai, S., Akiyama, T., Yamada, S., J. Am. Chem. Soc., 2001. **123**: p. 4855.

208. Theobald, J.A., Oxtoby, N.S., Phillips, M.A., Champness, N.R., Beton, P.H., Nature (London), 2003. **424**: p. 1029.

209. Theobald, J.A., Beton, P.H., Oxtoby, N.S., Champness, N.R., Dennis, T.J.S., Langmuir, 2005. **21**: p. 2038.

210. Spillmann, H., Kiebele, A., Stohr, M., Jung, T., Bonifazi, D., Cheng, F., Diederich, F., Adv. Mater., 2006. **18**: p. 275.

211. Zhang, S., Palkar, A., Fragoso, A., Prados, P., de Mendoza, J., Echegoyen, L., Chem. Mater., 2005. **17**: p. 2063.

212. Zhang, S., Echegoyen, L., C.R. Chimie, 2006. **9**: p. 1031.

213. Campbell, K., Gurun, B., Sumpter, B.G., Thio, Y.S., Bucknall, D.G., *Role of Conformation in π–π Interactions and Polymer/Fullerene Miscibility.* J. Phys. Chem. B., 2011. ***Submitted 2011***.

214. Skotheim, T.A., Reynolds, J.R., *Conjugated Polymers: Theory, Synthesis, Properties, and Characterization* 2006: CRC Press.

215. Swager, T.M., Gil, C.J., Wrighton, M.S., *Fluorescence Studies of Poly(p-phenyleneethynylene)s: The Effect of Anthracene Substitution.* J. Phys. Chem., 1995. **99**: p. 4886-4893.

216. Bunz, U.H.F., Enkelmann, V., Kloppenburg, L., Jones, D., Shimizu, K.D., Claridge, J.B., zur Loye, H-C., Lieser, G., *Solid-State Structures of Phenyleneethynylenes: Comparison of Monomers and Polymers.* Chem. Mater., 1999. **11**: p. 1416-1424.

217. Zhao, X., Jiang, H., Schanze, K., *Polymer Chain Length Dependence of Amplified Fluorescence Quenching in Conjugated Polyelectrolytes.* Macromolecules, 2008. **41**: p. 3422-3428.

218. Zhou, Q., Swager, T.M., *Methodology for Enhancing Sensitivity of Fluorescent Chemosensors: Energy Migration in Conjugated Polymers.* J. Am. Chem. Soc., 1995. **117**: p. 7017-7018.

219. Lakowicz, J.R., *Principles of Fluorescence Spectroscopy*. 2006: Springer.

220. Boaz, H., Rollefson, G.K., *The Quenching of Fluorescence. Deviations from the Stern-Volmer Law.* J. Am. Chem. Soc., 1950. **72**: p. 3435-3443.

221. Geddes, C.D., *Optical halide sensing using fluorescence quenching: theory, simulations and applications-a review.* Meas. Sci. Technol., 2001. **12**: p. R53-R88.

222. Acquavella, M.F., Evans, M.E., Farraher, S.W., Nevoret, C.J., Abelt, C.J., *Static and Dynamic Fluorescence Quenching of a Dicyanoanthracene-capped β–Χψχλοδεξτριν.* J. Chem. Soc. Perkin Trans. 2, 1995(385-388).

223. Keizer, J., *Nonlinear Fluorescence Quenching and the Origin of Positive Curvature in Stern-Volmer Plots.* J. Am. Chem. Soc., 1983. **105**: p. 1494-1498.

224. Zhou, Q., Swager, T.M., *Fluorescent Chemosensors Based on Energy Migration in Conjugated Polymers: The Molecular Wire Approach to Increased Sensitivity.* J. Am. Chem. Soc. , 1995. **117**: p. 12593.

225. Swager, T.M., *The Molecular Wire Approach to Sensory Signal Amplification.* Acc. Chem. Res., 1998. **31**: p. 201-207.

226. Zhou, Q., Swager, T.M., *Fluorescent Chemonsensors Based on Energy Migration in Conjugated Polymers: The Molecular Wire Approach to Increased Sensitivity.* J. Am. Chem. Soc., 1995. **117**: p. 12593-12602.

227. Kendall, R.A., Apra, E., Bernholdt, D.E., Bylaska, E.J., Dupuis, M., Fann, G.I., Harrison, R.J., Ju, J.L., Nichols, J.A., Nieplocha, J., Straatsma, T.P., Windus, T.L., Wong, A.T., Computer Physics Communications, 2000. **129**(1-2): p. 260-283.

228. Hehre, W.J., Ditchfie, R., Pople, J.A., Journal of Chemical Physics, 1972. **56**(5): p. 2257.

229. Vazquez-Mayagoitia, A., Sherrill, C.D., Apra, E., Sumpter, B.G., J. Chem. Theory Comput. , 2010. **6**(3): p. 727-734.

230. Ringer, A.L., et al., *The Effect of Multiple Substituents on Sandwich and T-Shaped Pi-Pi Interactions.* Chemistry-a European Journal, 2006. **12**(14): p. 3821-3828.

231. Tauer, T.P., Sherrill, C.D. , *Beyond the Benzene Dimer: An Investigation of the Additivity of π–π Interactions.* J. Phys. Chem. A, 2005. **109**(46): p. 10475-10478.

232. Sinnokrot, M.O., Sherrill, C.D., *Substituent Effects in π–π Interactions: Sandwich and T-shaped Configurations* J. Am. Chem. Soc., 2004. **126**: p. 7690-7697.

233. Sygula, A., et al., *A Double Concave Hydrocarbon Buckycatcher.* Journal of the American Chemical Society, 2007. **129**(13): p. 3842.

234. Linton, D., et al., *The importance of chain connectivity in the formation of non-covalent interactions between polymers and single-walled carbon nanotubes and its impact on dispersion.* Soft Matter, 2010. **6**(12): p. 2801-2814.

235. Ederle, Y. and C. Mathis, *Carbanions on grafted C-60 as initiators for anionic polymerization.* Macromolecules, 1997. **30**(15): p. 4262-4267.

236. Edwards, E.W., Muller, M., Stoykovich, M.P., Solak, H.H., de Pablo, J.J., Nealey, P.F., *Dimensions and Shapes of Block Copolymer Domains Assembled on Lithographically Defined Chemically Patterened Substrates.* Macromolecules, 2007. **40**: p. 90-96.

237. Mansky, P., Liu, Y., Huang, E., Russell, T.P., Hawker, C. , *Controlling Polymer-Surface Interactions with Random Copolymer Brushes.* Science, 1997. **275**: p. 1458-1460.

238. Tate, R.S., Fryer, D.S., Pasqualini, S., Montague, M.F., de Pablo, J.J., Nealey, P.F., *Extraordinary elevation of the glass transition temperature of thin polymer*

films grafted to silicon oxide substrates. Journal of Chemical Physics, 2001. **115**(21): p. 9982-9990.

239. Anastasiadis, S.H., Russell, T.P., Satija, S.K., Majkrzak, C.F., *Neutron Reflectivity Studies of the Surface-Induced Ordering of Diblock Copolymer Films.* Phys. Rev. Lett., 1989. **62**(16): p. 1852-1855.

240. Mayes, A.M., Russell, T.P., Deline, V.R., Satija, S.K., Majkrzak, C.F., *Block Copolymer Mixtures As Revealed by Neutron Reflectivity.* Macromolecules, 1994. **27**: p. 7447-7453.

241. Jeong, U., Ryu, D.Y., Kho, D.H., Lee, D.H, Kim, J.K., *Phase Behavior of Mixtures of Block Copolymer and Homopolymers in Thin Films and Bulk.* Macromolecules, 2003. **36**: p. 3626-3634.

242. Likhtman, A.E., Semenor, A.N., *Theory of Microphase Separation in Block Copolymer/Homopolymer Mixtures.* Macromolecules, 1997. **30**: p. 7273-7278.

243. Hamley, I.W., *Ordering in thin films of block copolymers: Fundamentals to potential applications.* Progress in Polymer Science, 2009. **34**(11): p. 1161-1210.

244. Weng, C.-C., Wei, K-H., *Selective Distribution of Surface-Modified TiO_2 Nanoparticles in PS-b-PMMA Diblock Copolymer*. Chem. Mater., 2003. **15**: p. 2936-2941.

245. Tsutsumi, K., Funaki, Y., Hirokawa, Y., Hashimoto, T., *Selective Incorporaton of Palladium Nanoparticles into Microphase-Separated Domains of Poly(2-vinylpyridine)-block-Polyisoprene.* Langmuir, 1999. **15**(5200-5203).

246. Lazzari, M., Lopez-Quintela, M.A., *Block Copolymer for Nanomaterial Fabrication.* Adv. Mater., 2003. **15**(19): p. 1583.

247. Lauter-Pasyuk, V., Lauter, H.J., Ausserre, D., Gallot, Y., Cabuil, V., Hamdoun, B., Kornilov, E.I., *Neutron Reflectivity studies of composite nanoparticle-copolymer thin films.* Physica B, 1998. **248**: p. 243-245.

248. Lauter-Pasyuk, V., Lauter, H.J., Ausserre, D., Gallot, Y., Cabuil, V., Kornilov, E.I., Hamdoun, B., *Effect of nanoparticle size on the internal structure of copolymer-nanoparticles composite thin films studies by neutron reflection.* Physica B, 1998. **241-243**: p. 1092-1094.

249. Hamley, I.W., *Nanotechnology with Soft Materials.* Angew. Chem. Int. Ed., 2003. **42**: p. 1652-1712.

250. Darling, S.B., *Directing the self-assembly of block copolymers.* Progress in Polymer Science, 2007. **32**: p. 1152-1204.

251. Chiu, J.J., Kim, B.J., Kramer, E.J., Pine, D.J., *Control of Nanoparticle Location in Block Copolymers.* J. Am. Chem. Soc., 2005. **127**: p. 5036-5037.

252. Buckstaller, M.R., Mickiewicz, R.A., Thomas, E.L., *Block Copolymer Nanocomposites: Perspectives for Tailored Functional Materials.* Adv. Mater., 2005. **17**: p. 1331-1349.

253. Cohen, Y., Albalak, R.J., Dair,B.J., Capel, M.S., Thomas, E.L., *Deformation of Oriented Lamellar Block Copolymer Films.* Macromolecules, 2000. **33**(17): p. 6502-6516.

254. Listak, J., Bockstaller, M.R., *Stablization of Grain Boundary Morphologies in Lamellar Block Copolymer/Nanoparticle Blends.* Macromolecules, 2006. **39**: p. 5820-5825.

255. Gao, Y., Tang, Z., Watkins, E., Majewski, J., Wang. H-L., *Synthesis and Characterization of Amphiphilic Fullerenes and Their Langmuir-Blodgett Films.* Langmuir, 2005. **21**: p. 1416-1423.

256. McConney, M.E., Singamaneni, Tsukruk, V.V., Polym. Rev., 2010. **in press**.

257. Tsukruk, V.V., Reneker, D.H. , Polymer, 1995. **36**: p. 1791.

258. Tsukruk, V.V., Rubber Chem. Technol., 1997. **70**: p. 430.

259. Janssen, D., De Palma, R.D., Verlaak, S., Heremans, P., Dehaeen, W., *Static solvent contact angle measurements, surface free energy and wettability determination of various self-assembled monolayers on silicon dioxide.* Thin Solid Films, 2006. **515**: p. 1433-1438.

260. Pellerite, E.J., Wood, V.W., Jones, J., J. Phys. Chem. B., 2002. **106**: p. 4746.

261. Caldwell, W.B., Chen, K., Mirkin, C.A., Babinec, S.J. , *Self-Assembled Monolayer Films of C_{60} on Cysteamine-Modified Gold.* Langmuir, 1993. **9**: p. 1945-1947.

262. Alcantar, N.A., Aydil, E.S., Israelachvili, J.N., *Polyethylene glycol–coated biocompatible surfaces.* J. Biomedical Materials Research, 2000. **51**(3): p. 343.

263. Miller, G.P., *Reactions between aliphatic amines and [60]fullerene: a review.* C.R. Chimie, 2006. **9**: p. 952-959.

264. Geckeler, K.E., Hirsch, A., *Polymer-Bound C_{60}.* J. Am. Chem. Soc., 1993. **115**: p. 3850-3851.

265. Tsukruk, V.V., Luzinov, I., Julthongpiput, D. , *Sticky Molecular Surfaces: Epoxysilane Self-Assembled Monolayers.* Langmuir, 1999. **15**: p. 3029-3032.

266. Luzinov, I., Julthongpiput,D., Liebmann-Vinson,A., Cregger,T., Foster, M.D., Tsukruk,V. V., *Epoxy-Terminated Self-Assembled Monolayers: Molecular Glues for Polymer Layers.* Langmuir, 2000. **16**: p. 504-516.

267. Song, X., Zhai, J., Wang, Y., Jiang, L., *Self-assembly of amino-functionalized monolayers on silicon surfaces and preparation of superhydrophobic surfaces based on alkanoic acid dual layers and surface roughening.* Journal of Colloid and Interface Science, 2006. **298**: p. 267-273.

268. Luscombe, C.K., Li, H-W., Huck,W.T.S., Holmes,A.B., *Fluorinated Silane Self-Assembled Monolayers as Resists for Patterning Indium Tin Oxide.* Langmuir, 2003. **19**: p. 5273-5278.

269. Mourougou-Candoni, N., Thibaudau, F., *Formation of Aminosilane Film on Mica.* J. Phys. Chem. B., 2009. **113**(39): p. 13026-13034.

270. Palta, D., *Effect of Nanoparticle Inclusions and Solvent Annealing on Block Copolymer Morphology*, in *Polymer, Textile, and Fiber Engineering*. 2007, Georgia Institute of Technology: Atlanta. p. 173.

271. Gan, Y., Dong, D., Carlotti, S., Hogen-Esch, T.E., *Enhanced Fluorescence of Macrocyclic Polystyrene.* J. Am. Chem. Soc., 2000. **122**: p. 2130-2131.